

THE ANATOMY OF CHROMOSPHERIC FLARES AND ASSOCIATED  
EPHEMERAL BRIGHTENINGS

BY

MICHAEL S. KIRK, B.A., M.S.

A dissertation submitted to the Graduate School

in partial fulfillment of the requirements

for the degree

Doctor of Philosophy

Major Subject: Astronomy

New Mexico State University

Las Cruces New Mexico

February 2013

“The Anatomy of Chromospheric Flares and Associated Ephemeral Brightenings”  
a dissertation prepared by Michael S. Kirk in partial fulfillment of the requirements  
for the degree, Doctor of Philosophy, has been approved and accepted by the  
following:

---

Linda Lacey  
Dean of the Graduate School

---

Jason Jackiewicz  
Chair of the Examining Committee

---

Date

Committee in charge:

Dr. Jason Jackiewicz, Chair

Dr. K. S. Balasubramaniam

Dr. Bernard J. McNamara

Dr. R. T. James McAteer

Dr. Chunpei Cai

## DEDICATION

I affectionately dedicate this work to my parents, Alan and Ann, who have instilled in me a curiosity about and a love of this world.

## ACKNOWLEDGMENTS

I really dislike the phrase “it takes a village.” It evokes an image of a community of people all living in close proximity to each other and all knowing one another. This is never the case with any of us. Maybe one day in the past it was literally a village; but now I, along with everyone else, are supported, encouraged, and cared for by a network of people that literally span the globe. I guess I could start using the phrase “it takes a *global* village,” but this seems trite and therefore I will not. That being said, I have many more people to acknowledge than I have space. It is sad to say, but I will have to leave some people off of this list. If you are reading this and don’t see your name, and you believe that you should be acknowledged for your contribution to my education, I will gladly handwrite your name in the space at the bottom of the page. (Even if this is a library copy – I am the author; I can do that kind of thing.)

Let me start by acknowledging my financial support. These are people and organizations who saw enough promise in my work to literally hand me money so I could keep on doing research. First and foremost is the Air Force Research Laboratory (AFRL) and the Air Force Office of Scientific Research. AFRL’s Space Weather Center of Excellence gave NMSU the initial grant to bring me to New Mexico as a student and has continued to fund my research since. I would like to also recognize the Space Scholars program through AFRL. Space Scholars has provided me with summer employment for the last four summers and allowed me to progress with my PhD without the worry of summer funding. I would like to specifically recognize the contributions of Rich Radick, Misty Crown, and Joel Mozer for helping me succeed with AFRL.

I would also like to recognize the financial support of New Mexico's Space Grant Consortium (NMSGC) and specifically Pat Hynes. The fellowships provided by NMSGC have given me the ability to present my research at conferences around the world. I would also like to say that Pat Hynes' invitation to join them at the dedication of Spaceport America was one of the highlights of my life in Las Cruces. Next time I will try and remember what British Royalty look like and dress more suitably.

Now, I should thank some family. I am using the idea of *family* loosely here. These are people who have helped me with my research in one way or another, but I will remember them foremost because they have been a support to me in my life beyond research. So maybe I will start using the term *research-family*. The first group on this long list, are people from NMSU. My fellow students in the astronomy department have been my coworkers, competition, and above all, friends. Specifically, I would like to thank Paul, Bobby, Kyle, Jillian, Cat, Liz, Chas, Mike, and Maria for putting up with my shenanigans around the office. I would also like to thank Sean, Adam, James, Jeff, Nick, and Ryan for being able to drink 3 martinis and still discuss science. Beyond the students in astronomy, I would like to recognize Tom and Joni for making me more of a booze snob than I already was.

I have realized that I have spent nearly a quarter of my time in New Mexico living and working in Sunspot. I would like to extend my sincere appreciation to all of the staff and residents in Sunspot who have welcomed me into their community. I need to especially thank Steve, Jackie, Han, Ali, Thomas, Friedrich, and Jose for their generosity. I may have never organized a win on the court of the student-staff volleyball game, but I think you can all agree that I won the

propaganda campaign.

I would like to acknowledge the parents of my *research-family*. First my advisor, Jason... seems odd to call Jason a parent... maybe I am taking this family analogy too far. Jason – thank you for letting me take my research where I wanted it to go, even when you thought it wasn't going anywhere. Bernie – thank you for taking a chance on me and bringing me into your research group. James – thank you for your enthusiasm for my project even though it was already my own when you arrived. Bala – thank you for mentoring me through this whole process. You have taught me what it means to be a scientist and pushed me when I needed to be pushed. Dean – you launched my career into solar physics. I am deeply grateful for your faith in me and your encouragement ever since we worked together at Goddard.

Wendy and Lee, thank you for being my surrogate parents in Las Cruces: dinners, oil changes, watching election coverage, finding me a place to live, and so much more. Both of you helped make New Mexico my home. I am still amazed that when you suggested I come down to NMSU way back in 2006, it actually came true.

Mom, I finally know what you went through getting your PhD. Wow. I am impressed you handled it all and were still able to be a great mother. Thank you for all of your encouragement and support during this process and always.

Dad, thank you for being my editor. I hope you know how much I appreciate all of your energy and time. You understood it all, right? Thank you for teaching me how to write when I was in school. You are a big part of the reason I was able to do all of this.

Rebecca, thank you for always being able to see my talents even if I haven't seen them yet. Thank you for blazing a trail through elementary school, high school, and into college for me. It is always nice to have a big sister tell you that it really isn't that scary.

Tia, you have seen me at my worst and my best through this dissertation. Thank you for always being there to listen to me. Thank you for ordering pizza when I am too tired to think about dinner. Thank you for being lazy with me on Sundays. Thank you for celebrating with me and reminding me that life is good.

I probably didn't add you to this list, but that doesn't mean that I have forgotten how much you have helped me. And, if you bring me this copy, I can add you to it.

## VITA

### EDUCATION

- 2008-2010 M.S., Astronomy**  
New Mexico State University  
Las Cruces, New Mexico, USA
- 2009 Heliophysics Summer School**  
NASA International Living With a Star  
Boulder, Colorado, USA
- 2009 Summer School in Solar Physics**  
National Solar Observatory  
Sunspot, New Mexico, USA
- 2002-2006 B.A., Physics and Astronomy**  
Whitman College  
Walla Walla, Washington, USA

## AWARDS AND GRANTS

- 2009-2012 Space Scholar Internship  
Air Force Research Laboratory
- 2011 Zia Research Award, Astronomy Department  
New Mexico State University
- 2009-2011 New Mexico Space Grant Scholarship  
New Mexico State University
- 2009 Honorable Mention, Student Poster Competition  
AAS Solar Physics Division Conference
- 2009 Outstanding Graduate Assistant Award  
New Mexico State University

## PROFESSIONAL ORGANIZATIONS

- American Astronomical Society (& Solar Physics Division)
- American Geophysical Union

## PUBLICATIONS

- Kirk, M.S., Balasubramaniam, K.S., Jackiewicz, J., McAteer, R.T.J., McNamara, B.J.: 2012, **Sequential Chromospheric Brightening: An Automated Approach to Extracting Physics from Ephemeral Brightening**. *Publications of the Astronomy Society of the Pacific*, 463
- Kirk, M.S., Balasubramaniam, K.S., Jackiewicz, J., McAteer, R.T.J., Milligan, R.O.: 2012, **Properties of Sequential Chromospheric Brightenings and Associated Flare Ribbons**. *Astrophysical Journal*, 750, 145
- Kirk, M.S., Balasubramaniam, K.S., Jackiewicz, J., McNamara, B.J., McAteer, R.T.J.: 2011, **An Automated Algorithm to Distinguish and Characterize Solar Flares and Associated Sequential Chromospheric Brightenings**. *Solar Physics*, 345

Kirk, M.S., Pesnell, W.D., Young, C.A., Hess Webber, S.A.: 2009, **Automated Detection of EUV Polar Coronal Holes During Solar Cycle 23.** *Solar Physics*, 257, 99

## CONFERENCE PRESENTATIONS

- “Tracing Transient Chromospheric Features in Flare Eruptions,” Tracing the Connections in Solar Eruptive Events, December 2012, M. S. Kirk, K. S. Balasubramaniam, J. Jackiewicz, and R. T. J. McAteer
- “Identifying Transient Features in the Solar Atmosphere From Multiple Sources,” Solar Information Processing Workshop VI, August 2012, M. S. Kirk, K. S. Balasubramaniam, J. Jackiewicz, and R. T. J. McAteer
- “An Insight Into Atmospheric Structure Through Compact Chromospheric Brightenings,” AAS/SPD Spring Meeting, June 2012, M. S. Kirk, K. S. Balasubramaniam, J. Jackiewicz, and R. T. J. McAteer
- “Chromospheric Explosions: Linking Observations Toward a Physical Model,” AAS Winter Meeting, January 2012, M. S. Kirk, J. Jackiewicz, R. T. J. McAteer, and B. J. McNamara
- “Mapping the Dynamics of Chromospheric Flares,” AGU Fall Meeting, December 2011, M. S. Kirk, K. S. Balasubramaniam, J. Jackiewicz, and R. T. J. McAteer
- “Sequential Chromospheric Brightening: An Automated Approach to Extracting Physics from Ephemeral Brightening,” 2<sup>nd</sup> ATST–EAST Workshop, November 2011, M. S. Kirk, K. S. Balasubramaniam, J. Jackiewicz, R. T. J. McAteer, and B. J. McNamara
- “Connecting Ephemeral Chromospheric Brightenings to Coronal Loops,” 27<sup>th</sup> Annual New Mexico Symposium, October 2011, M. S. Kirk, K. S. Balasubramaniam, J. Jackiewicz, R. T. J. McAteer, and R. O. Milligan
- “Automated Recognition of Solar Features for Developing Data Driven Prediction Models of Coronal Mass Ejections and Space Weather,” AFOSR Space Science Program Review, June 2011, M. S. Kirk, K. S. Balasubramaniam, J. Jackiewicz, R. T. J. McAteer, and B. J. McNamara
- “Connecting Ephemeral Chromospheric Brightenings to Coronal Loops,” AAS/SPD Spring Meeting, 42, June 2011, M. S. Kirk, K. S. Balasubramaniam, J. Jackiewicz, R. T. J. McAteer, and R. O. Milligan
- “Characterizing Chromospheric Flares and Sequential Brightening,” AAS/SPD Spring Meeting, 42, June 2011, M. S. Kirk, K. S. Balasubramaniam, J. Jackiewicz, R. T. J. McAteer, and B. J. McNamara
- “Properties of Solar Flares and Associated Sequential Chromospheric Brightenings,” AGU Fall Meeting, December 2010, M. S. Kirk, K. S. Balasubramaniam, J. Jackiewicz, and B. J. McNamara

“Automated Characterization of Large Flares and Associated Sequential Chromospheric Brightenings,” Solar Image Processing Workshop V, September 2010, M. S. Kirk, K. S. Balasubramaniam, J. Jackiewicz, and B. J. McNamara

“Understanding the Physics of Sequential Chromospheric Brightenings of the Sun Through Automated Recognition,” AAS Winter Meeting, January 2010, M. S. Kirk, K. S. Balasubramaniam, J. Jackiewicz, and B. J. McNamara

“Automated Characterization of Sequential Chromospheric Brightenings,” AGU Fall Meeting, December 2009, M. S. Kirk, and K. S. Balasubramaniam.

“Automated Detection of Polar Coronal Holes in the EUV,” AAS/SPD Spring Meeting, 40, June 2009, M. S. Kirk, and W. D. Pesnell.

## FIELD OF STUDY

Major Field: Heliophysics

## ABSTRACT

### THE ANATOMY OF CHROMOSPHERIC FLARES AND ASSOCIATED EPHEMERAL BRIGHTENINGS

BY

MICHAEL S. KIRK, B.A., M.S.

Doctor of Philosophy  
New Mexico State University  
Las Cruces, New Mexico, 2013  
Dr. Jason Jackiewicz, Chair

Chromospheric flares have been carefully observed and studied for many decades. Ribbons of hot plasma appear, brighten, and separate during the course of a flare. Adjacent to eruptions with associated coronal mass ejections, compact brightenings are observed in the impulsive phase of the flare. What causes these compact brightenings adjacent to flares? What can they tell us about the solar conditions that formed the chromospheric flare?

We present a new automated algorithm to identify, track, and characterize small-scale brightening associated with solar eruptive phenomena observed in  $H\alpha$ . The temporal, spatially localized changes in chromospheric intensities can be separated into two categories: flare ribbons and sequential chromospheric brightenings (SCBs). Within each category of brightening we determine the smallest resolvable locus of pixels, a kernel, and track the temporal evolution of the position and intensity of each kernel. We fully characterize the evolving intensity and morphology of the flare ribbons by observing the tracked flare kernels in aggregate. With the location of SCB and flare kernels identified, they can easily be overlaid on complementary data sets to extract coronal intensities, Doppler velocities, and magnetic-field intensities underlying the kernels.

We then report on the physical properties of SCBs. Following the algorithmic identification and a statistical analysis, we compare and find the following: SCBs are distinctly different from flare brightening in their temporal characteristics of intensity, Doppler structure, duration, and location properties. Within the studied population of SCBs, different classes of characteristics are observed with coincident negative, positive, or both negative and positive Doppler shifts of a few  $\text{km s}^{-1}$ . The appearance of SCBs often precedes peak flare intensity. They are also found to propagate laterally away from flare center in clusters at two distinct velocity groups. Given SCBs' distinctive nature compared to flares, we suggest a physical triggering mechanism relating to SCBs' origin, the associated flare, and coronal mass ejections. We present a heuristic model of SCBs in the chromosphere.

## Contents

<b>LIST OF TABLES</b>	<b>xvi</b>
<b>LIST OF FIGURES</b>	<b>xxviii</b>
<b>1 AN INTRODUCTION TO OUR SUN</b>	<b>1</b>
1.1 The Solar Atmosphere . . . . .	2
1.1.1 Photosphere . . . . .	3
1.1.2 Chromosphere . . . . .	4
1.1.3 Corona . . . . .	7
1.2 Solar Flares . . . . .	8
1.2.1 Morphology of Flares . . . . .	10
1.2.2 Flare Models . . . . .	12
1.2.3 Magnetic Reconnection . . . . .	15
1.3 Coronal Mass Ejections . . . . .	16
1.4 Solar Activity and Space Weather . . . . .	18
1.5 Anatomizing Flares . . . . .	19
<b>2 FLARES IN THE CHROMOSPHERE</b>	<b>21</b>
2.1 Flare Eruption in the Coupled Solar Atmosphere . . . . .	21
2.2 The H $\alpha$ Sun . . . . .	23
2.3 Chromospheric Evaporation . . . . .	26
2.4 Sequential Chromospheric Brightening . . . . .	28
<b>3 OBSERVING THE SUN</b>	<b>31</b>
3.1 Seeing the Sun in Many Different Lights . . . . .	31
3.1.1 Ground-based Observing . . . . .	32
3.1.2 Space-based Observing . . . . .	33
3.2 Improved Solar Observing Optical Network Telescope . . . . .	33
3.3 Extreme Ultraviolet and X-ray Observations . . . . .	36
3.3.1 Atmospheric Imaging Assembly . . . . .	37
3.3.2 Geostationary Operational Environmental Satellites . . . . .	39

3.3.3	Reuven Ramaty High Energy Solar Spectroscopic Imager . . . . .	39
3.4	Polarimetry and Magnetic Fields . . . . .	40
3.4.1	Magnetism and Polarized Light . . . . .	40
3.4.2	Polarimeters . . . . .	41
3.4.3	Potential Field Source Surface Model . . . . .	43
<b>4</b>	<b>INFORMATION PROCESSING IN SEARCH OF EPHEMERAL BRIGHTENINGS</b>	<b>45</b>
4.1	Generalized Detection and Tracking . . . . .	45
4.1.1	General Kernel Position Determination . . . . .	49
4.1.2	General Trajectory Linking . . . . .	52
4.2	Flare Ribbon Extraction . . . . .	54
4.3	Compact Ephemeral Brightenings . . . . .	55
4.4	Creation of Metadata . . . . .	57
<b>5</b>	<b>MEASUREMENTS AND MOTION IN FLARING SYSTEMS</b>	<b>59</b>
5.1	Properties of Flare Ribbons . . . . .	59
5.1.1	Qualities of Individual Kernels . . . . .	73
5.1.2	Derived Flare Quantities . . . . .	74
5.2	Properties of Ephemeral Compact Brightenings . . . . .	88
5.2.1	Qualities of Individual SCBs . . . . .	92
5.2.2	SCBs in Aggregate . . . . .	95
5.2.3	SCBs in AIA . . . . .	110
5.3	The Curious Hyder Flare . . . . .	116
<b>6</b>	<b>INCORPORATING DATA AND PHYSICAL CONTEXT</b>	<b>119</b>
6.1	Two-Ribbon Flares In and Out of the Chromosphere . . . . .	119
6.1.1	Diffusion and Expansion . . . . .	119
6.1.2	Constraints on Reconnection . . . . .	121
6.2	The Root of Sequential Chromospheric Brightenings . . . . .	121
6.2.1	Heuristic Modeling . . . . .	122
6.2.2	PFSS Modeling . . . . .	125

6.2.3	Chromospheric Evaporation . . . . .	126
6.2.4	Implications for Mass Ejection Release . . . . .	128
<b>7</b>	<b>FINDINGS AND FUTURE DIRECTIONS OF THIS WORK</b>	<b>131</b>
7.1	Summary of Results . . . . .	131
7.1.1	Chromospheric Flares . . . . .	131
7.1.2	Sequential Chromospheric Brightening . . . . .	132
7.1.3	Interpretation of Results . . . . .	133
7.2	Extensions and Future Directions . . . . .	134
	<b>REFERENCES</b>	<b>136</b>

## LIST OF TABLES

1.1	GOES flare classification in soft X-rays. . . . .	10
2.1	Statistical results from 18 SCB events studied by Balasubramaniam et al. (2006) showing the relationship between SCBs and CMEs. .	29
3.1	The primary ions observed by AIA, the region of the atmosphere, and their characteristic temperatures (Lemen et al. 2011). . . . .	38
4.1	Metadata generated from applying automated detection and tracking algorithms, the applicable features, and method of generation.	58
5.1	The events used by this work to investigate the automated identification and tracking of SCBs and flare ribbons. The time listed is the start time of the flare. Six of the eleven events were previously identified by Balasubramaniam et al. (2006) while five are new in this study. The data sources utilized for each event are abbreviated as: <u>I</u> SOON, <u>L</u> ASCO, <u>G</u> OES, <u>A</u> IA, <u>H</u> MI, <u>G</u> ONG, and <u>R</u> HESSI .	89
5.2	General physical characteristics of individual flare and SCB kernels. <i>Ensemble Motion</i> refers to the motion of an individual kernel as compared to its nearest neighbors over the kernel’s lifetime. . . . .	89
5.3	Derived physical measurements for SCBs. . . . .	97
6.1	Characteristics of expansion for flare ribbons. . . . .	120
6.2	Characteristics of magnetic loops derived by the PFSS model for the photospheric magnetic field beneath SCBs. . . . .	130

## LIST OF FIGURES

1.1	The dark absorption lines Fraunhofer (1817) discovered in the solar spectrum. . . . .	1
1.2	A schematic diagram of the Sun (Dixon 2007). The three interior regions are shown: core, radiative zone, and convective zone. The three atmospheric layers are also diagrammed: photosphere, chromosphere and corona. The relative size scales of each layer and feature labeled are accurate. . . . .	2
1.3	The solar photosphere observed in visible light by the Helioseismic and Magnetic Imager (Scherrer et al. 2011). Notice sunspots appear as dark regions on the bright solar disk. . . . .	3
1.4	The solar chromosphere observed in H I 6562.8 Å by ISOON (see Section 3.2). Notice active regions appear bright while filaments and sunspots appear dark. . . . .	5
1.5	The solar corona observed in Fe IX 171 Å by AIA (see Section 3.3.1). Magnetic loops are bright because of plasma trapped within them. . . . .	7
1.6	A drawing of the active region observed by Carrington (1859). This active region produced the largest solar flare in recorded history. . . . .	9
1.7	A diagram of the intensity evolution of a solar flare in multiple wavelengths. The flare’s evolution is divided in two four phases: <i>pre-flare</i> , <i>impulsive</i> , <i>flash</i> , and <i>decay</i> (Benz 2008). . . . .	11
1.8	The “Seahorse Flare” occurred on 1972 August 7. The chromosphere was imaged in the blue wing of H $\alpha$ and shows the two-ribbon structure late in the development. Bright H $\alpha$ loops connect each of the ribbons. . . . .	11
1.9	The scale of flares in soft X-rays as observed and classified by the GOES satellite (Grigis 2006). The intensity is logarithmic making an X5 flare an order of magnitude greater energy release than an M5 flare. . . . .	12
1.10	The <i>standard model</i> for flare eruption and CME release (Lin & Forbes 2000). The large scale filament liftoff and subsequent CME release is shown on top. An expanded view of the driving flare is shown on the bottom. The significant features and dynamics in each phase of the flare eruption are noted. . . . .	14
1.11	A diagram of the process of magnetic reconnection along a current sheet (Shibata & Magara 2011). The field lines [ $B_i$ ] are pushed together by a convergent flow [ $v_i$ ]. . . . .	15
1.12	Five different CME release models illustrated by a spring (Klimchuk 2001). <i>Directly driven</i> models are diagrammed in letters A and B. <i>Storage and release</i> models are shown in letters C, D, and E. . . . .	17

2.1	A temperature versus height profile of the chromosphere (Avrett 1985). Overlaid are the approximate locations of chromospheric emission lines. . . . .	22
2.2	A 3-D plot of the modeled $H\alpha$ emission height over a small area of quiet Sun (Leenaarts et al. 2012). The emission height of $H\alpha$ ranges between 0.8–2.8 Mm. . . . .	24
2.3	The $H\alpha$ line response at four distinct times during a flare (Berlicki et al. 2008). The dashed line is the line profile fit to the quiescent $H\alpha$ absorption line. There are two solid lines plotted of the measured $H\alpha$ line, one of which is the unchanging pre-flare line. The other solid line shows the response of $H\alpha$ , changing from an absorption profile to an emission profile. . . . .	25
2.4	Simulated line profiles for $H\alpha$ at four times during a large flare (Allred et al. 2005). The dotted lines indicate the level of the continuum and the line center, while the dashed line is the pre-flare line profile. Notice the distinct red shift of the $H\alpha$ profile as the flare evolves. . . . .	26
2.5	A diagram of the basic model of chromospheric evaporation (Gurman 1987). Electrons injected into the loop at the apex make their way to the footpoints where they heat and subsequently ablate the local plasma, forcing it to rise back up the legs of the loop. . . . .	27
2.6	A phenomenological model for a series of SCBs appearing on 2005 May 6 by Balasubramaniam et al. (2006). $H\alpha$ brightening is shown in red, coronal loops are in blue, and magnetic flux is in green. . . . .	30
3.1	ISOON’s optical diagram. Light paths are traced in red and green lines. . . . .	34
3.2	Measurements along the ISOON $H\alpha$ line profile to calibrate the Doppler velocity to wing intensity. . . . .	35
3.3	Images taken by ISOON from 2003 October 14 generated to calibrate a typical Doppler response. <b>A</b> : $H\alpha$ depth, <b>B</b> : $H\alpha$ width, <b>C</b> : $H\alpha$ intensity, <b>D</b> : derived $H\alpha$ Doppler velocity. . . . .	36
3.4	Examples of an active region on 2011 February 15 imaged with AIA (Lemen et al. 2011). The top row, from left to right, are the 131 Å, 94 Å, and 335 Å channels. The middle row are the 171 Å, 193 Å, and 211 Å channels, and the bottom row are 1600 Å and 304 Å (left and middle). The bottom right corner is an HMI line-of-sight magnetogram showing the same active region. . . . .	37
3.5	A theoretical description of an optical polarizer (top) and retarder (bottom) with an input source $[E]$ (Santiago 2004). . . . .	42

4.1	A flowchart detailing the preprocessing method in preparation for analysis. The green parallelogram represents the database input. Blue trapezoids indicate a feature specific quality that must be manually determined and input. The blue shaded rectangles are individual routines. . . . .	46
4.2	Images representing each of the preprocessing steps outlined in Figure 4.1. . . . .	47
4.3	A flowchart detailing the process in which flare ribbons and SCBs are identified and their physical parameters measured. The green parallelogram represents the database input. Blue trapezoids indicate a feature specific quality that must be determined and input. The gray diamonds are processes that have been defined by a collection of subroutines and are detailed in other flowcharts. The blue shaded rectangles are individual routines. . . . .	48
4.4	A flowchart detailing the process in which flare and SCB kernels are identified. The green parallelogram represents the database input. Blue trapezoids indicate a feature specific quality that must be determined and input. The red diamond is a process that has a conditional result and the blue shaded rectangles are individual routines. . . . .	49
4.5	A diagram of a hypothetical kernel (either flare or SCB) used for classifications in this paper. Each pixel is labeled with a representative intensity $[\mathcal{A}_i]$ . The semi-major axis $[a]$ and semi-minor axis $[b]$ are shown. This kernel has the following properties: total intensity, $m_0 = 43$ , semi-major axis, $a = 4$ , semi-minor axis, $b = 2$ , eccentricity, $e = 0.87$ , centroid, $(x, y) = (0.26, 0.18)$ , and radius of gyration, $R_g = 1.9$ . The maximum intensity, in this case 5, is defined as having pixel coordinates $(0, 0)$ . . . . .	50
4.6	Time series of images showing the evolution of the flare ribbons for the 2005 May 13 event. Each image shows the same flaring region ten minutes after the previous image. The flare peak occurs at 16:49 UT. The top row of images show the $H\alpha$ line-center intensity. The second row of images show the flare after the ribbon isolation and enhancement as described in Section 4.2. The third row of images show the detected flare kernels after the image analysis algorithm is applied. The centroid of each flare kernel is marked by a black circle. Notice how the number of kernels changes as the flare ribbon evolves. A comparison of the first and third row of images show the coverage of detections along the flare ribbons. . . . .	52

4.7	Time series of images showing the evolution of the SCBs for the 2005 May 13 event. Each image shows the same flaring region three minutes after the previous image. The flare peak occurs at 16:49 UT. The top row of images show the $H\alpha$ line-center intensity (same as the top row of Figure 4.6). The second row of images show a binary image of the same flaring region after applying the SCB isolation as described in Section 4.3. The third row of images show the detected SCB kernels after the image-analysis algorithm is applied. Identified SCBs are visually separated into three groups to demonstrate how they appear to move when watching an animation of the flare. The red group propagates quickly while the blue and yellow groups develop more slowly. Notice how the number of kernels peaks before the flare peak and rapidly declines as compared to the flare kernels. . . . .	56
5.1	A histogram of the continuance of detected flare kernels in all 11 events. Flare kernels are tracked for a mean duration of 122 minutes (dot-dashed line) and a median duration of 111 minutes (dashed line).	60
5.2	The 2005 May 13 measured intensities of each flare kernel plotted as points as a function of time. The solid-blue line is the integrated kernel intensities at each time step. Overlaid for comparison in green is the normalized GOES 1.0 – 8.0 Å intensity curve. The vertical dashed line indicates the peak intensity of the $H\alpha$ flare curve. The integrated flare kernels reproduce the shape of the flare curve determined by other methods. . . . .	61
5.3	Time evolution of the 2002 December 19 event. The dashed line in both panels mark the peak flare intensity. Top: the flare area over time as defined by Equation 5.4. Bottom: The blue line is the integrated $H\alpha$ flare kernel intensities at each time step. The red line is the integrated SCB kernel intensities at each time step. Plotted for reference in black is the GOES 1.0 – 8.0 Å intensity curve.	62
5.4	Time evolution of the 2003 March 6 event. The dashed line in both panels mark the peak flare intensity. Top: the flare area over time as defined by Equation 5.4. Bottom: The blue line is the integrated $H\alpha$ flare kernel intensities at each time step. The red line is the integrated SCB kernel intensities at each time step. Plotted for reference in black is the GOES 1.0 – 8.0 Å intensity curve. . . . .	63
5.5	Time evolution of the 2003 May 9 event. The dashed line in both panels mark the peak flare intensity. Top: the flare area over time as defined by Equation 5.4. Bottom: The blue line is the integrated $H\alpha$ flare kernel intensities at each time step. The red line is the integrated SCB kernel intensities at each time step. Plotted for reference in black is the GOES 1.0 – 8.0 Å intensity curve. . . . .	64

- 5.6 Time evolution of the 2003 June 11 event. The dashed line in both panels mark the peak flare intensity. Top: the flare area over time as defined by Equation 5.4. Bottom: The blue line is the integrated  $H\alpha$  flare kernel intensities at each time step. The red line is the integrated SCB kernel intensities at each time step. Plotted for reference in black is the GOES 1.0 – 8.0 Å intensity curve. . . . . 65
- 5.7 Time evolution of the 2003 October 29 event. The dashed line in both panels mark the peak flare intensity. Top: the flare area over time as defined by Equation 5.4. Bottom: The blue line is the integrated  $H\alpha$  flare kernel intensities at each time step. The red line is the integrated SCB kernel intensities at each time step. Plotted for reference in black is the GOES 1.0 – 8.0 Å intensity curve. 66
- 5.8 Time evolution of the 2004 November 9 event. The dashed line in both panels mark the peak flare intensity. Top: the flare area over time as defined by Equation 5.4. Bottom: The blue line is the integrated  $H\alpha$  flare kernel intensities at each time step. The red line is the integrated SCB kernel intensities at each time step. Plotted for reference in black is the GOES 1.0 – 8.0 Å intensity curve. 67
- 5.9 Time evolution of the 2005 May 6 event. The dashed line in both panels mark the peak flare intensity. Top: the flare area over time as defined by Equation 5.4. Bottom: The blue line is the integrated  $H\alpha$  flare kernel intensities at each time step. The red line is the integrated SCB kernel intensities at each time step. Plotted for reference in black is the GOES 1.0 – 8.0 Å intensity curve. . . . . 68
- 5.10 Time evolution of the 2005 May 13 event. The dashed line in both panels mark the peak flare intensity. Top: the flare area over time as defined by Equation 5.4. Bottom: The blue line is the integrated  $H\alpha$  flare kernel intensities at each time step. The red line is the integrated SCB kernel intensities at each time step. Plotted for reference in black is the GOES 1.0 – 8.0 Å intensity curve. . . . . 69
- 5.11 Time evolution of the 2006 December 6 event. The dashed line in both panels mark the peak flare intensity. Top: the flare area over time as defined by Equation 5.4. Bottom: The blue line is the integrated  $H\alpha$  flare kernel intensities at each time step. The red line is the integrated SCB kernel intensities at each time step. Plotted for reference in black is the GOES 1.0 – 8.0 Å intensity curve. 70
- 5.12 Time evolution of the 2010 November 6 event. The dashed line in both panels mark the peak flare intensity. Top: the flare area over time as defined by Equation 5.4. Bottom: The blue line is the integrated  $H\alpha$  flare kernel intensities at each time step. The red line is the integrated SCB kernel intensities at each time step. Plotted for reference in black is the GOES 1.0 – 8.0 Å intensity curve. 71

5.13	Time evolution of the 2010 November 30 event. The blue line is the integrated $H\alpha$ flare kernel intensities at each time step. The red line is the integrated SCB kernel intensities at each time step. Plotted for reference in black is the GOES 1.0 – 8.0 Å intensity curve.	72
5.14	An image from the 2005 May 13 event. Letters A – F point to the locations several SCB kernels that are shown in more detail in Figure 5.15. Letters U – Z point to the locations of a sample of several flare kernels that are also shown in more detail in Figure 5.15. Note that since flare kernels move with the evolving flare ribbon, the locations of these kernels are only accurate for this image. In contrast, SCB kernels are stationary and remain in the same location in any image.	73
5.15	$H\alpha$ normalized intensity curves for each of the kernels indicated in Figure 5.14 by the associated letters. On the left, the tracked flare kernels are shown. The normalized intensity curves for the SCB kernels, shown on the right, are stationary and therefore tracked throughout the flaring window. In both panels, the vertical dashed line indicates the time at which the flare intensity peaks (16:49 UT) derived from integrating all flare kernel intensities at each time step.	74
5.16	A time series of $H\alpha$ images with the apparent lateral velocity of each tracked flare kernel at that time step plotted over the 2005 May 13 flare ribbons. A histogram of the number of flare kernels as a function of unsigned average velocity (speed) corresponding to each time step is plotted underneath.	75
5.17	The number of elements in each apparent instantaneous lateral velocity bin plotted as a function of time for the 2002 December 19 event. The vertical dashed line marks the time of the peak flare intensity. The velocity bins are 5 km s <sup>-1</sup> in width. Velocities, 0 – 0.5 km s <sup>-1</sup> , is excluded because of a base level of noise inherent in the detection routine.	76
5.18	The number of elements in each apparent instantaneous lateral velocity bin plotted as a function of time for the 2003 March 6 event. The vertical dashed line marks the time of the peak flare intensity. The velocity bins are 5 km s <sup>-1</sup> in width. Velocities, 0 – 0.5 km s <sup>-1</sup> , is excluded because of a base level of noise inherent in the detection routine.	77
5.19	The number of elements in each apparent instantaneous lateral velocity bin plotted as a function of time for the 2003 May 9 event. The vertical dashed line marks the time of the peak flare intensity. The velocity bins are 5 km s <sup>-1</sup> in width. Velocities, 0 – 0.5 km s <sup>-1</sup> , is excluded because of a base level of noise inherent in the detection routine.	78

5.20	The number of elements in each apparent instantaneous lateral velocity bin plotted as a function of time for the 2003 June 11 event. The vertical dashed line marks the time of the peak flare intensity. The velocity bins are $5 \text{ km s}^{-1}$ in width. Velocities, $0 - 0.5 \text{ km s}^{-1}$ , is excluded because of a base level of noise inherent in the detection routine. . . . .	79
5.21	The number of elements in each apparent instantaneous lateral velocity bin plotted as a function of time for the 2003 October 29 event. The vertical dashed line marks the time of the peak flare intensity. The velocity bins are $5 \text{ km s}^{-1}$ in width. Velocities, $0 - 0.5 \text{ km s}^{-1}$ , is excluded because of a base level of noise inherent in the detection routine. . . . .	80
5.22	The number of elements in each apparent instantaneous lateral velocity bin plotted as a function of time for the 2004 November 9 event. The vertical dashed line marks the time of the peak flare intensity. The velocity bins are $5 \text{ km s}^{-1}$ in width. Velocities, $0 - 0.5 \text{ km s}^{-1}$ , is excluded because of a base level of noise inherent in the detection routine. . . . .	81
5.23	The number of elements in each apparent instantaneous lateral velocity bin plotted as a function of time for the 2005 May 6 event. The vertical dashed line marks the time of the peak flare intensity. The velocity bins are $5 \text{ km s}^{-1}$ in width. Velocities, $0 - 0.5 \text{ km s}^{-1}$ , is excluded because of a base level of noise inherent in the detection routine. . . . .	82
5.24	The number of elements in each apparent instantaneous lateral velocity bin plotted as a function of time for the 2005 May 13 event. The vertical dashed line marks the time of the peak flare intensity. The velocity bins are $5 \text{ km s}^{-1}$ in width. Velocities, $0 - 0.5 \text{ km s}^{-1}$ , is excluded because of a base level of noise inherent in the detection routine. . . . .	83
5.25	The number of elements in each apparent instantaneous lateral velocity bin plotted as a function of time for the 2006 December 6 event. The vertical dashed line marks the time of the peak flare intensity. The velocity bins are $5 \text{ km s}^{-1}$ in width. Velocities, $0 - 0.5 \text{ km s}^{-1}$ , is excluded because of a base level of noise inherent in the detection routine. . . . .	84
5.26	The number of elements in each apparent instantaneous lateral velocity bin plotted as a function of time for the 2010 November 6 event. The vertical dashed line marks the time of the peak flare intensity. The velocity bins are $5 \text{ km s}^{-1}$ in width. Velocities, $0 - 0.5 \text{ km s}^{-1}$ , is excluded because of a base level of noise inherent in the detection routine. This flare is both spatially and temporally compact as evident in Figure 5.12, which is also reflected in this plot. . . . .	85

5.27	The integrated unsigned propagation speed, acceleration, and energy of flare kernels as a function of time for three events: 2005 May 13, 2005 May 6, and 2004 November 9. The vertical dashed line indicates the maximum flare intensity for the flaring event. The first column shows the integrated speed curves. The second column shows the acceleration of the flare ribbons. The third column shows the integrated kinetic energy, Equation 5.2, as a function of time for each of the three events studied. The 2004 flare had significant noise in the original data and a location on the limb contributing to the inconsistent measurements. . . . .	86
5.28	An $H\alpha$ image of the 2005 May 13 flare at peak intensity is shown with the reconstructed RHESSI 25 – 50 keV pass band integrated between 16:42 – 16:43 UT contoured on top at 10, 30, 50, 70, and 90% of the maximum intensity. The field of view of the RHESSI image [-220:-95, 180:305] is confined within the flaring region. . .	88
5.29	The 2005 May 13 measured intensities of each SCB curve plotted as points as a function of time. The solid yellow line is the integrated kernel intensities at each time step. Here again, the vertical dashed line indicates the peak of the flare curve as shown in Figure 5.10. Notice that the intensity of the integrated SCB curve returns to the continuum level much faster than the integrated flare-kernel curve as shown in Figure 5.2. . . . .	90
5.30	Time series of images showing the evolution of the SCBs for the 13 May 2005 event. Each image shows the same flaring region three minutes after the previous image. The flare peak occurs at 16:49 UT. The top row of images show the $H\alpha$ line-center intensity (same as the top row of Figure 4.6). The second row of images show a binary image of the same flaring region after applying the SCB isolation as described in Section 4.3. The third row of images show the detected SCB kernels after the image-analysis algorithm is applied. Identified SCBs are visually separated into three groups to demonstrate how they appear to move when watching an animation of the flare. The red group propagates quickly while the blue and yellow groups develop more slowly. . . . .	91
5.31	The line center intensity and Doppler velocity measurements for three different types of SCBs observed. The vertical dashed line marks the peak $H\alpha$ intensity of the associated SCB. A negative Doppler velocity is away from the observer and into the Sun. . . .	93
5.32	The $H\alpha$ line-center intensity (black curve) and Doppler velocity (gray curve) measurements of a chromospheric brightening caused by a Moreton wave associated with the 2006 flare. The vertical dashed line marks the peak $H\alpha$ intensity of the associated compact brightening. . . . .	94
5.33	A histogram of the duration (FWHM) of SCB detections in all 11 events. The SCBs have a measured mean duration of 9.1 minutes (dot-dashed line) and a median duration of 6.6 minutes (dashed line).	95

5.34	The distribution of photospheric radial magnetic field intensities beneath SCBs for the 2002 December 19 event. . . . .	96
5.35	The distribution of photospheric radial magnetic field intensities beneath SCBs for the 2003 March 6 event. . . . .	97
5.36	The distribution of photospheric radial magnetic field intensities beneath SCBs for the 2003 May 9 event. . . . .	98
5.37	The distribution of photospheric radial magnetic field intensities beneath SCBs for the 2003 June 11 event. . . . .	98
5.38	The distribution of photospheric radial magnetic field intensities beneath SCBs for the 2003 October 29 event. . . . .	99
5.39	The distribution of photospheric radial magnetic field intensities beneath SCBs for the 2004 November 9 event. . . . .	99
5.40	The distribution of photospheric radial magnetic field intensities beneath SCBs for the 2005 May 6 event. . . . .	100
5.41	The distribution of photospheric radial magnetic field intensities beneath SCBs for the 2005 May 13 event. . . . .	100
5.42	The distribution of photospheric radial magnetic field intensities beneath SCBs for the 2006 December 6 event. . . . .	101
5.43	The distribution of photospheric radial magnetic field intensities beneath SCBs for the 2010 November 6 event. . . . .	101
5.44	The distribution of photospheric radial magnetic field intensities beneath SCBs for the 2010 November 30 event. . . . .	102
5.45	The distance at which the bright point occurs versus time from the $H\alpha$ flare peak for SCB during the 2002 December 19 event. The color of each plotted point is representative of its relative intensity; the dimmest are purple, higher intensity detections are blue and the highest intensity detections are green. The black dashed line shows a weighted regression fit: $84.8 \pm 9.7, 260 \pm 19.4 \text{ km s}^{-1}$ . . .	103
5.46	The distance at which the bright point occurs versus time from the $H\alpha$ flare peak for SCB during the 2003 March 6 event. The color of each plotted point is representative of its relative intensity; the dimmest are purple, higher intensity detections are blue and the highest intensity detections are green. The black dashed line shows a weighted regression fit: $220 \pm 143 \text{ km s}^{-1}$ . . . . .	103
5.47	The distance at which the bright point occurs versus time from the $H\alpha$ flare peak for SCB during the 2003 May 9 event. The color of each plotted point is representative of its relative intensity; the dimmest are purple, higher intensity detections are blue and the highest intensity detections are green. The black dashed line shows a weighted regression fit: $73.9 \pm 10.9, -8.5 \pm 3.6 \text{ km s}^{-1}$ . . . . .	104

5.48	The distance at which the bright point occurs versus time from the $H\alpha$ flare peak for SCB during the 2003 June 11 event. The color of each plotted point is representative of its relative intensity; the dimmest are purple, higher intensity detections are blue and the highest intensity detections are green. The black dashed line shows a weighted regression fit: $95.7 \pm 40, -1684 \pm 1914 \text{ km s}^{-1}$ . . . . .	104
5.49	The distance at which the bright point occurs versus time from the $H\alpha$ flare peak for SCB during the 2003 October 29 event. The color of each plotted point is representative of its relative intensity; the dimmest are purple, higher intensity detections are blue and the highest intensity detections are green. The black dashed line shows a weighted regression fit: $460 \pm -, 2423 \pm - \text{ km s}^{-1}$ . . . . .	105
5.50	The distance at which the bright point occurs versus time from the $H\alpha$ flare peak for SCB during the 2004 November 9 event. The color of each plotted point is representative of its relative intensity; the dimmest are purple, higher intensity detections are blue and the highest intensity detections are green. . . . .	105
5.51	The distance at which the bright point occurs versus time from the $H\alpha$ flare peak for SCB during the 2005 May 6 event. The color of each plotted point is representative of its relative intensity; the dimmest are purple, higher intensity detections are blue and the highest intensity detections are green. The black dashed line shows a weighted regression fit: $63.0 \pm 15.8 \text{ km s}^{-1}$ . . . . .	106
5.52	The distance at which the bright point occurs versus time from the $H\alpha$ flare peak for SCB during the 2005 May 13 event. The color of each plotted point is representative of its relative intensity; the dimmest are purple, higher intensity detections are blue and the highest intensity detections are green. The black dashed line shows a weighted regression fit: $36.3 \pm 7.2, 153 \pm 55.8 \text{ km s}^{-1}$ . . . . .	106
5.53	The distance at which the bright point occurs versus time from the $H\alpha$ flare peak for SCB during the 2006 December 6 event. The color of each plotted point is representative of its relative intensity; the dimmest are purple, higher intensity detections are blue and the highest intensity detections are green. The black dashed line shows a weighted regression fit: $851 \pm - \text{ km s}^{-1}$ . . . . .	107
5.54	The distance at which the bright point occurs versus time from the $H\alpha$ flare peak for SCB during the 2010 November 6 event. The color of each plotted point is representative of its relative intensity; the dimmest are purple, higher intensity detections are blue and the highest intensity detections are green. The black dashed line shows a weighted regression fit: $65.4 \pm 4.8, 465 \pm 206 \text{ km s}^{-1}$ . . .	107

5.55	The distance at which the bright point occurs versus time from the $H\alpha$ flare peak for SCB during the 2010 November 30 event. The color of each plotted point is representative of its relative intensity; the dimmest are purple, higher intensity detections are blue and the highest intensity detections are green. The black dashed line shows a weighted regression fit: $51.0 \pm 4.9 \text{ km s}^{-1}$ . . . . .	108
5.56	A plot showing the RHESSI non-thermal 25–50 keV intensity in black and the $H\alpha$ SCB integrated intensity curve in gray for the 2005 May 13 event. The vertical dashed line indicates the peak of the integrated SCB curve. . . . .	109
5.57	A histogram of the duration (FWHM) of all SCB detections in AIA. The SCBs in AIA have a measured mean duration of 4.9 minutes (dot-dashed line) and a median duration of 4.0 minutes (dashed line). . . . .	110
5.58	An SCB of type Ia. The top plot shows the normalized intensity curves: $H\alpha$ in black, 1600 Å in green, 1700 Å in blue, and 304 Å in red. The bottom panel plots the measured Doppler velocity. . . . .	111
5.59	An SCB of type IIa. The top plot shows the normalized intensity curves: $H\alpha$ in black, 1600 Å in green, 1700 Å in blue, and 304 Å in red. The bottom panel plots the measured Doppler velocity. . . . .	112
5.60	An SCB of type IIb. The top plot shows the normalized intensity curves: $H\alpha$ in black, 1600 Å in green, 1700 Å in blue, and 304 Å in red. The bottom panel plots the measured Doppler velocity. . . . .	113
5.61	An SCB of type III. The top plot shows the normalized intensity curves: $H\alpha$ in black, 1600 Å in green, 1700 Å in blue, and 304 Å in red. The bottom panel plots the measured Doppler velocity. . . . .	114
5.62	An example of a compact brightening in AIA but not in ISOON. The top plot shows the normalized intensity curves: $H\alpha$ in black, 1600 Å in green, 1700 Å in blue, and 304 Å in red. The bottom panel plots the measured Doppler velocity. . . . .	115
5.63	Histograms showing the relative timing of SCB in $H\alpha$ as compared to AIA. The vertical dashed line marks the events coincident with $H\alpha$ peak intensity. Left: timings broken down by wavelength: 1600 Å in green, 1700 Å in blue, and 304 Å in red. Right: Cumulative timing for all events observed in AIA. . . . .	116
5.64	A phenomenological model describing the physical evolution of a Hyder flare (Hyder 1967). . . . .	117

6.1	A phenomenological model of the trigger mechanism for SCBs. A dashed line marks the neutral line in this model. The central loops represent the emerging two ribbon flare arcade. The arches represent field lines connecting outside of the chromospheric flare ribbons (in yellow). The arrows on top of both the loops and arches show the direction trapped plasma flows as the flare begins to erupt, and the stars suggest the location where the plasma is disrupted. Once perturbed, the trapped plasma streams down the loop lines and impacts the chromosphere, causing the $H\alpha$ intensity brightening. The different orientations of off-flare loops accounts for the different propagation speeds of SCB groups observed and indicated by blue and green marks. . . . .	124
6.2	An example of the magnetic field lines above SCBs modeled using a PFSS approach from 2010 November 6. . . . .	125
6.3	A plot of the PFSS modeled magnetic loop lengths versus the associated SCB's measured distance from flare center for all SCBs recorded. . . . .	126
6.4	A diagram of the physical dynamics occurring in a single SCB. Electrons and protons accelerated by magnetic reconfiguration further up in the corona come streaming down the flare loop. Since the mean free path of electrons is significantly less, the electrons deposit energy into the upper chromosphere. Unable to radiate the energy as heat, the chromosphere responds by expanding and sending material back up the flux tube (chromospheric evaporation) and a recoil propagates toward the photosphere. . . . .	127

# 1. AN INTRODUCTION TO OUR SUN

*If you are going to be a physicist, you will have a lot to study: two hundred years of the most rapidly developing field of knowledge that there is.*

– Richard Feynman (1963)

The Sun is the most common and easily accessible celestial object. It is so common, people more readily associate Sunshine with the weather than as an astronomical phenomenon. The Sun has also been worshiped throughout history by every major ancient civilization. For example, the Greeks had their Sun god Helios, Egyptians: Ra, Hindus: Surya, Aztecs: Huitzilopochtli, Hopis: Tawa, and Incas: Inti. Despite the Sun’s commonplace role in our everyday lives, it has also been the inspiration for some of the most significant scientific achievements.

Solar eclipses have been observed for centuries. The oldest records of eclipses are dated back to 1300 B.C. The first recorded observations of sunspots occurred circa 28 B.C. in China during the Han Dynasty when severe dust storms attenuated the Sun’s glare. Galileo used the Sun as a consistent light source to test his new instrument the telescope in 1610, setting the stage for future breakthroughs in physics. Newton passed Sunlight through a prism to deconstruct white light into its color components (Newton 1671).

In 1817 Joseph Fraunhofer used a more sensitive method to disperse Sunlight and discovered hundreds of dark absorption lines, as shown in Figure 1.1, which were later named after him: Fraunhofer Lines (Fraunhofer 1817). Shortly thereafter between 1826 and 1843 Heinrich Schwabe was trying to find a planet interior to the orbit of Mercury and began to make systematic observations of dark spots on the Sun (Schwabe 1843). Although he did not discover a new planet, he did find an  $\approx 11$ -year cycle of variation in the number of sunspots. This sunspot cycle is still observed today.

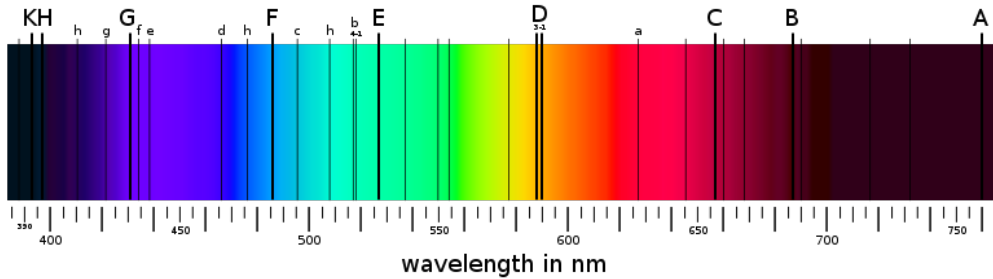


Fig. 1.1.— The dark absorption lines Fraunhofer (1817) discovered in the solar spectrum.

## 1.1. The Solar Atmosphere

The Sun is composed of three interior zones and three atmospheric layers: photosphere, chromosphere, and corona (Figure 1.2). Each layer has its distinct attributes including temperatures, pressures and features observed. The subsections 1.1.1, 1.1.2, and 1.1.3 briefly describe the significant features in each atmospheric layer.

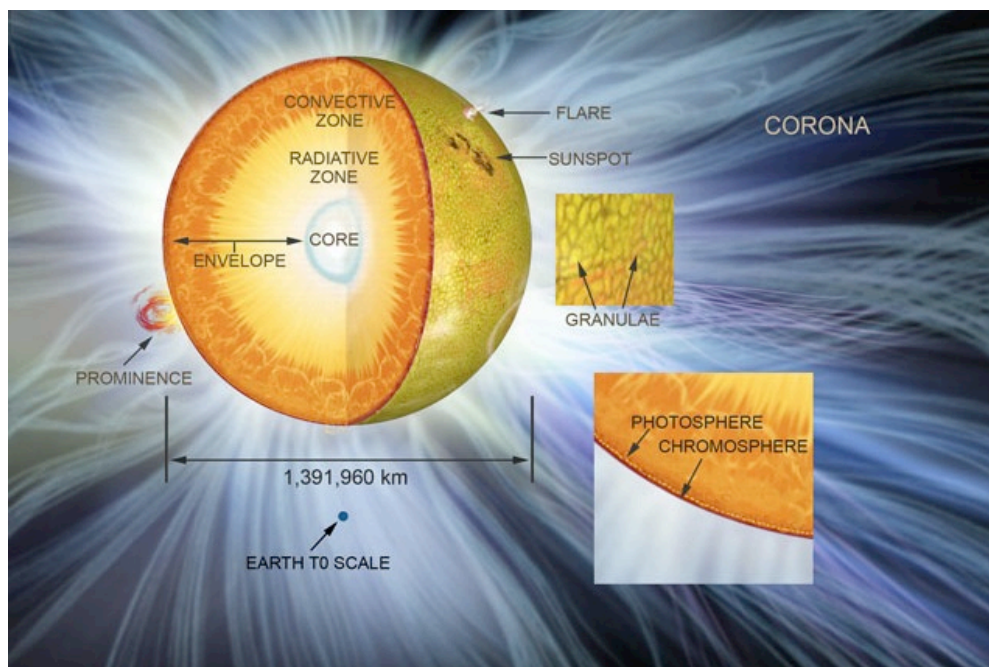


Fig. 1.2.— A schematic diagram of the Sun (Dixon 2007). The three interior regions are shown: core, radiative zone, and convective zone. The three atmospheric layers are also diagrammed: photosphere, chromosphere and corona. The relative size scales of each layer and feature labeled are accurate.

All of the energy from the Sun originates in its core. There, in the inner 25% of the Sun's radius, hydrogen fuses into helium through a series of steps called the proton-proton chain (Salpeter 1952). This nuclear fusion produces an extreme amount of energy ( $10^{26} \text{Js}^{-1}$ ) which then radiates outward to about  $0.7R_{\odot}$ . This is called the radiative zone. The radiative zone has a high density and shallow temperature gradient, enough to suppress convection. At the edge of the radiative zone, a transition region called the tachocline is characterized by a large shear between the rigid-body rotation of the radiative zone and differential rotation of the convective zone. The tachocline is theorized to generate the solar magnetic field which drives many of the features seen in the atmosphere. From  $0.7R_{\odot}$  to the surface, the density of the plasma drops to a point where convection can dominate the heat transfer. This is aptly called the convective zone. The convection cells

that carry heated plasma up to the photosphere are observed as granules in the photosphere.

The 11-year sunspot cycle that Schwabe discovered is magnetic in origin. The magnetic polarity of the global solar magnetic field reverses approximately every 11 years. This 11-year cycle is apparent in the number of sunspots appearing in the photosphere as well as the total radiation output in several wavelengths. A full cycle of 22 years (for example, the northern hemisphere having a positive polarity, shifting to negative, and then back to positive again) is called a Hale cycle. Halfway through the 11-year cycle, the total solar magnetic flux reaches a maximum and begins to decline. This is called solar maximum. During the solar cycle, the magnetic flux varies by a factor of 8 in active regions. Since many radiative processes directly depend on the dissipation of magnetic field energy, the magnetic solar cycle is analogous to a solar activity cycle: the number of flares and total radiative output of the Sun is modulated over an 11-year cycle.

### 1.1.1. Photosphere

The photosphere is the innermost plasma layer and makes up the visible surface of the Sun. This layer is typically defined by an optical depth,  $\tau_\lambda$ , which can be thought of as the number of unobstructed paths traveled by an emerging photon. Typically an optical depth of significantly greater than one is opaque while an optical depth much less than one is transparent. The photosphere is defined as having an optical depth of  $0.1 \leq \tau_\lambda \leq 3.0$  where the majority of the visible photons are emitted. This corresponds to a layer approximately 0.1 Mm thick. Within this region the temperature of the plasma decreases from 6500 K at its base to 4400 K at the outer edge.

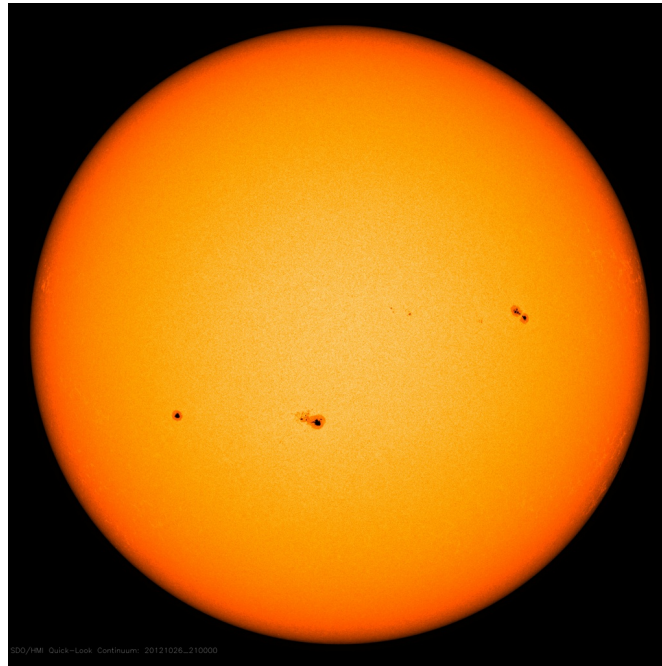


Fig. 1.3.— The solar photosphere observed in visible light by the Helioseismic and Magnetic Imager (Scherrer et al. 2011). Notice sunspots appear as dark regions on the bright solar disk.

The photosphere has several features that are unique to this layer (Figure 1.3). Sunspots appear dark against the quiet Sun, faculae appear bright, and granules cover the entire surface. This granulation is indicative of underlying convective cells where hotter plasma from the solar interior is upwelling in bright areas and returning in the dark lanes surrounding each cell. Granules vary in size but are typically between 0.3 and 2 Mm in diameter, have up flow velocities of  $\approx 1.5 \text{ km s}^{-1}$  and an average lifetime of about 10 minutes. Larger granules – supergranules – also are observed, with an average diameter of  $\approx 35 \text{ Mm}$ . They have an average lifetime of about a day and flow speeds of  $\approx 0.5 \text{ km s}^{-1}$ . The photospheric magnetic field is responsible for several of the features observed in this layer, most notably sunspots. These dark regions are formed from large concentrations of magnetic flux and are about 2000 K cooler than the surrounding plasma.

Sunspots, which interrupt the otherwise consistent photosphere, are areas of high magnetic intensity upward of a few thousand Gauss. Sunspots are classified according to their appearance, complexity, and magnetic structure. The high magnetic flux of a spot suppresses the convection of the photosphere, which in turn inhibits heating; thus they are cooler and appear dark on images taken in the visible continuum. Sunspots typically occur in pairs or clusters of individual spots and consist of a central dark core, the umbra, surrounded by a brighter halo of filaments organized radially outward from the core, the penumbra. The temperature of the umbra is typically  $T_{\text{umbra}}(\tau = 1) = 3500 - 5000 \text{ K}$  as compared with a photospheric temperature of  $T_{\text{photo}}(\tau = 1) = 6000 - 6500 \text{ K}$ . This difference in temperature results in the umbra's dark appearance.

The umbral magnetic field is nearly vertical with respect to the photospheric surface and becomes slightly inclined with respect to the zenith ( $\zeta_{\text{umbra}} = 20^\circ - 40^\circ$ ) near the umbral – penumbral boundary. The magnetic intensity of a sunspot is directly proportional to the size of the spot and ranges between  $B_{\text{umbra}} = 2000 - 3000 \text{ G}$ . Sunspot umbrae show no doppler shifting of their spectral lines and are stationary except for some surface oscillations.

### 1.1.2. Chromosphere

Moving outward from the photosphere, the physical conditions change rapidly. The chromosphere is the region directly above the photosphere and is about 2 Mm thick. In the chromosphere electron density drops by more than a factor of  $\approx 10^7$ . Plasma particle densities are estimated to be  $10^{10} - 10^{13} \text{ cm}^{-3}$  (Fontenla et al. 1990), making the density of the chromosphere about equivalent to a vacuum created on Earth. In contrast to the densities, temperatures jump sharply from 4200 K just above the boundary with the photosphere to over  $2.5 \times 10^4 \text{ K}$  at the outer boundary of the chromosphere. The temperature is not sufficient to fully

ionize the plasma, as chromospheric temperatures span the  $1.1 \times 10^4$  K needed to ionize hydrogen. Thus the plasma is only partially ionized depending on the layer and feature observed. The spectrum of the chromosphere is dominated by  $H\alpha$  emission, giving it a reddish hue when seen during solar eclipses.

All features in the chromospheric layer of the Sun are dominated by the underlying magnetic field. The chromospheric network is a web-like pattern caused by the network outlines of the supergranule cells of the underlying photosphere (Figure 1.4). Sunspots consisting of cooler material appear dark while active regions of hotter material appear as bright features against the quiet Sun. Filaments are also observed as dark ribbons across the solar disk and rise up through the chromosphere from the photosphere. This is the first layer of the Sun in which flares can regularly be seen.

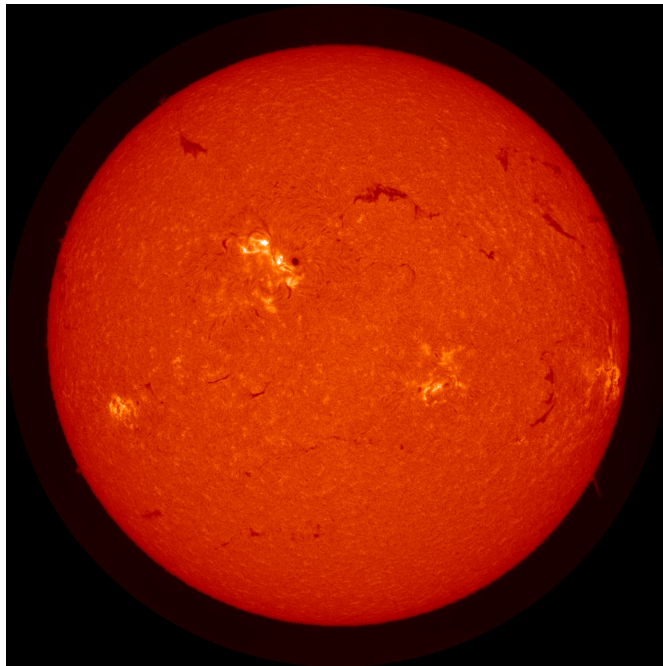


Fig. 1.4.— The solar chromosphere observed in  $H\text{I } 6562.8 \text{ \AA}$  by ISOON (see Section 3.2). Notice active regions appear bright while filaments and sunspots appear dark.

The most common spectroscopic lines to image the chromosphere are  $H\alpha$  ( $H\text{I } 6562.8 \text{ \AA}$ ) and  $\text{CaII H}$  and  $\text{K}$  ( $3968.5 \text{ \AA}$  and  $3933.7 \text{ \AA}$ ). Imaging the chromosphere in the line center as opposed to the wings of the line corresponds to imaging different heights in the atmosphere. Thus, depending on the line, and what part of the line is used, different features will be revealed. Images in the  $\text{CaII K}$  line show alternating bright and dark patches over the surface. The bright features are called mottles. Mottles coalesce to the point where they link together to form a somewhat regular pattern around and above supergranules. The larger bright

features are termed coarse mottles and are sometimes known as flocculi. They visually combine to form the chromospheric network.

Each coarse mottle is made up of several bright fine mottles. These fine mottles are  $\approx 7000$  km in length and  $\approx 700$  km across. Due to the higher excitation energy of  $H\alpha$ , images taken in this line are higher in the atmosphere than  $CaII$  images. In the core of the  $H\alpha$  line, fine mottles at lower heights are bright, while mottles at a height of  $\approx 3000$  km appear dark and sometimes fragmented. Mottles are always dark when imaging in the wing of the line and typically have lifetimes of 12-20 minutes. Fine mottles are regions of upward and downward motions in the chromospheric plasma perpendicular to the disk. They can be simply modeled as cylinders approximately 1000 km thick with a temperatures of 5000 - 15000 K. The difference between the dark and bright contrast is due to an increase in gas pressure at lower heights above the solar surface.

Spicules also appear in the  $H\alpha$  line. They are limb structures with temperatures of  $\approx 10^4$  K and widths up to 1500 km across that extend 10 Mm vertically into the corona. Spicules have a characteristic upward velocity of  $20 \text{ km s}^{-1}$ . This up-flow flux of plasma would entirely replace the mass of the corona in three hours. Thus there is obviously some down-flow associated back into the chromosphere, which is speculated to be related to mottles on the limb. Dark features associated with upward flow are seen in the blue wing of the  $H\alpha$  line. In  $CaII$  lines, bright grains are seen to periodically change in brightness over a few minutes. The brightness may be due to heating after magnetic reconnection.

The chromospheric network has a dynamic timescale of about two hours and is highly spatially-correlated with the underlying photospheric supergranulation. Evolution of the network is similar to photospheric granules: a new field appears in the center, migrates to the boundaries, and resides in the boundaries until its eventual disappearance (Schrijver et al. 1997). The network cell is dominated by the appearance of many smaller up-flowing centers of magnetic field, which are known as the internetwork. Granular buffeting from the photosphere moves internetwork magnetic regions in a random walk. The flow patterns on larger scales, supergranules, have a longer lifetime and eventually collect the magnetic regions into the network and move along it. During this process of flow, regions may interact. Regions of opposite polarities may meet, reconnect, and vanish; or two regions of the same polarity may meet and merge; or a single region can fragment into two or more regions.

Across the chromospheric disk, clusters of increased brightening are found with a somewhat granular structure in the vicinity of active regions. These areas, called plages, have a higher temperature and density than the surrounding quiet Sun and are caused by an enhanced magnetic field in the active region. Similar to a sunspot penumbra in the photosphere, dark fibrils radially extend from a sunspot umbra. These fibrils have a clockwise rotation in the southern hemisphere and a counter-clockwise rotation in the northern hemisphere. Unlike the sunspot penumbra, the chromospheric fibrils are nearly 20 Mm long. Fibrils connect areas of opposite magnetic polarity and are aligned with the local magnetic field.

Long dark filaments are also seen on the chromospheric disk. Filaments mark lines of magnetic inversion. They can be found winding throughout active regions and are often associated with a sunspot. An active region emerges in several

phases: first, brightening begins in the network mottles; next, plage fills in the entire network cell; lastly, sunspots and flares develop. The entire process takes just a few days. If the emerging active region is bipolar, the two regions are connected by low-lying arch filaments. The arch filaments act to bring up denser material from the lower atmosphere into the chromosphere. Gravity, however, is acting to pull the heated plasma down at the foot points of the loops. The down-flow due to gravity is observed as small ephemeral brightenings in the wing of  $H\alpha$  (known in the literature as Ellerman bombs). The random motion of the foot points of the flux tubes causes shearing. Twisting of the tubes in and around active regions also sets up currents along field lines, causing further heating of trapped plasma.

Just beyond the chromosphere, the temperature rises extremely rapidly, increasing from  $\approx 10^4$  to over  $10^6$  K in a few hundred kilometers. This region is known as the transition region and acts as an interface between the cooler chromosphere and the hot outer atmosphere, the corona.

### 1.1.3. Corona

The corona is the outermost layer of the solar atmosphere. It extends from the top of the chromosphere outward for several solar radii. It can even be said that the Earth sits in the extended corona. Because of its high temperature, greater than  $10^6$  K, it is only visible in extreme ultraviolet or X-ray emission. Nearly all of these high energy wavelengths are absorbed by the Earth's upper atmosphere; so observations of the corona must be made from space (Figure 1.5). The particle density of the plasma in the corona ranges from  $10^6$  to  $10^9$   $\text{cm}^{-3}$  in the quiet corona and can reach as high as  $\approx 10^{11}$   $\text{cm}^{-3}$  in flare loops.

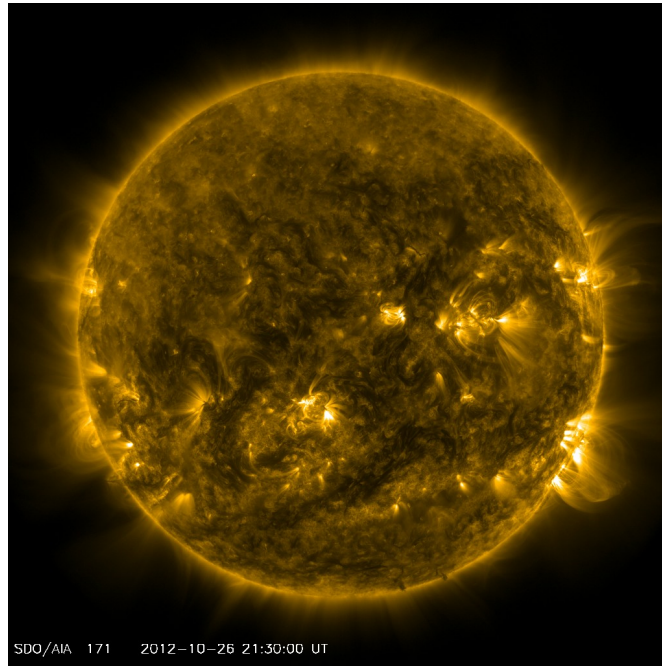


Fig. 1.5.— The solar corona observed in FeIX 171 Å by AIA (see Section 3.3.1). Magnetic loops are bright because of plasma trapped within them.

The coronal plasma is fully ionized and permeated with magnetic fields, which is the source of all features observed. The plasma’s electrical conductivity is nearly uninhibited, so the plasma moves with the magnetic field lines; and the magnetic field dominates, since the field strength  $[B]$  is relatively high compared to the pressure  $[P]$ :

$$\beta \equiv \frac{8\pi P}{B^2} \ll 1. \quad (1.1)$$

This is known as the plasma being “frozen into” the magnetic field. In general, the magnetic field of the corona is dipolar with a multi-pole current sheet forming near the equator. The multi-pole nature of the equatorial current sheet is due to the magnetic field on the solar surface being extremely inhomogeneous. Active regions, and sunspots within them, contour the magnetic field for a few solar radii until a simple potential-field dominates.

The high temperatures, low densities, and frozen-in magnetic field all play a significant role in the features observed in the corona. Bipolar active regions, which appear as sunspots in the photosphere, appear in the corona as bright loops. These coronal loops are fed by heated plasma up-flows from the chromosphere, are characteristically hotter and more dense than the background corona, and emit light in the extreme ultraviolet (EUV) and soft X-rays. Regions of open magnetic field appear dark in the corona, since heated plasma is allowed to stream away unimpeded and is the source of the fast solar wind. The size and location of coronal holes vary with the solar cycle. Polar coronal holes disappear during solar maximum and peak in size at solar minimum (Kirk et al. 2009).

Flare or post-flare loops become bright in soft X-rays as they are filled with chromospheric material. This process is known as chromospheric evaporation and is discussed further in Section 2.3. Occasionally mass erupts out of the corona into interplanetary space. Called coronal mass ejections, they are generally accompanied by large flares and are observed in white-light emission. See Section 1.3 for further discussion of coronal mass ejections.

## 1.2. Solar Flares

A major breakthrough in understanding the connection between the Earth and the Sun occurred in 1859.<sup>1</sup> On September 1 of that year Richard Carrington was monitoring an exceptionally large group of sunspots and visually observed a solar flare (Carrington 1859). His original drawings of this sunspot group is reproduced in Figure 1.6. Carrington’s observation, combined with a simultaneous

---

<sup>1</sup>Charles Darwin published *The Origin of Species* in November 1859 making that year a pivotal year in several fields of science.

terrestrial magnetic disturbance observed in the Kew Observatory magnetometer and a geomagnetic storm seen all over the globe the following day, led Carrington to postulate a connection between the Earth and Sun.

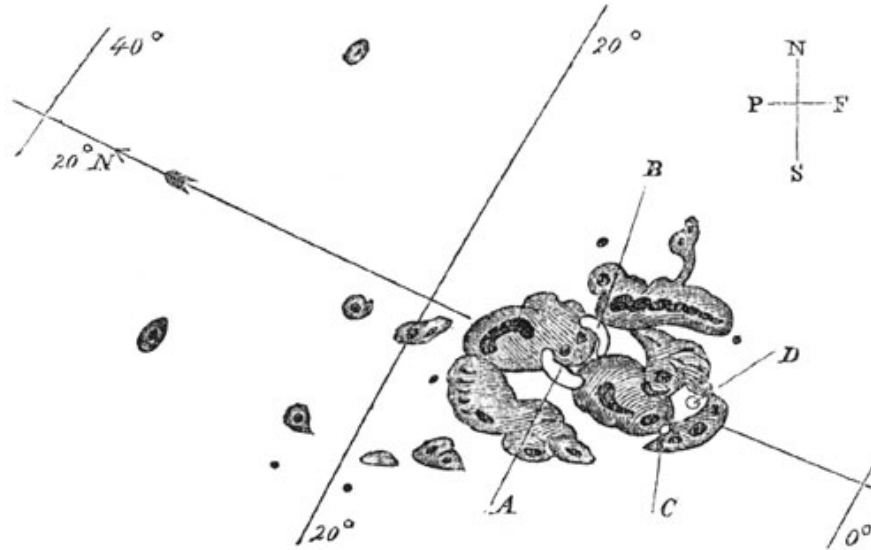


Fig. 1.6.— A drawing of the active region observed by Carrington (1859). This active region produced the largest solar flare in recorded history.

Nearly a half-century later the last piece of the puzzle was put into place, defining the modern field of Heliophysics. George Hale was taking high-resolution spectra of different areas on the Sun and discovered that the absorption lines in sunspots were actually split into three components: Zeeman splitting. His observation of the Zeeman effect led him to the conclusion that there are significant magnetic fields emanating from sunspots (Hale 1908). Hale's discovery showed that the Sun was a much more complicated place than earlier thought. Not only did it have characteristics of a high-temperature fluid described by hydrodynamics, but there was now the influence of magnetic fields as well.

Within a few years of Carrington's discovery, the Sun was studied regularly in  $H\alpha$ . Reports of flares became much more common and increasingly complex. Variations in size, the occasional ejection of plasma blobs, and observations of blast waves further complicated matters (Moreton 1964). As more data about flares was gathered, a consistently observed evolution of a flare was parsed into four phases: *pre-flare*, *impulsive*, *flash*, and *decay* (Benz 2008). These phases are outlined in a diagram in Figure 1.7. In the *pre-flare phase*, coronal plasma heats up in the flaring region, emitting soft X-rays and EUV. Next, magnetic reconnection (see Section 1.2.3) accelerates a large amount of plasma ( $n_e \approx 10^{38}$ ) in a short amount of time. This is the *impulsive phase* when most of the energy is released. In the *flash phase*, thermal soft X-ray and  $H\alpha$  emission reach peak intensity. Energy in this phase is more gently released and further distributed over the growing flaring region. A flare concludes with the *decay phase*. In this phase,

the lower coronal and chromospheric plasma gradually return to their pre-flare state. In the high corona a propagation shock, and possibly mass ejection, can be observed accelerating particles into interplanetary space.

Flares are commonly classified by their X-ray (1–8 Å) emission. This corresponds to the soft-channel in the GOES family of satellites (see Section 3.3.2 for further description of the GOES satellites). Table 1.1 describes the different flare classifications by their peak X-ray flux. Flares are divided into five classes (A, B, C, M, and X) and then further sub-divided into ten sub-classes (1–10) where the number is intended as a multiplicative factor. For example, an M5 flare has ten times the peak emission of a C5 flare and five times the emission of an M1 flare. This scheme is set up such that the peak emission of the smallest class of flare (A1) is almost six orders of magnitude smaller than the largest flare observed in the modern era (X28).

### 1.2.1. Morphology of Flares

Solar flares are often classified into two types: compact flares and two-ribbon flares. In general, two-ribbon flares tend to be larger, more energetic, and more likely to be associated with an eruption. Compact flares usually occur in a pre-existing loop or arch filament system, and little change is seen in the topology of the loops post-flare. Micro-flares are a subset of the compact class, are short-lived, and only slightly brighter than plage. Two-ribbon flares are considerably more violent and longer lived, frequently producing large changes in the structure of the initial loop lines. Two-ribbon flares also have a longer impulse phase, correlating with the amount of energy input into the corona and chromosphere.

Two ribbon flares are called such because they often appear in the chromosphere as two bright bands of emission in H $\alpha$  (Figure 1.8). These ribbons appear to move slowly apart as the flare develops. Before the flare, a prominence is often observed, which disappears at the onset of the flare. If a prominence is observed, the two ribbons form on either side of the prominence. Loop-like structures are seen connecting one ribbon to the other one as the flare evolves and the ribbons

Table 1.1. GOES flare classification in soft X-rays.

Flare Class	Peak Flux 1–8 Å
A1	$10^{-8} \text{ W m}^{-2}$
B1	$10^{-7} \text{ W m}^{-2}$
C1	$10^{-6} \text{ W m}^{-2}$
M1	$10^{-5} \text{ W m}^{-2}$
X1	$10^{-4} \text{ W m}^{-2}$

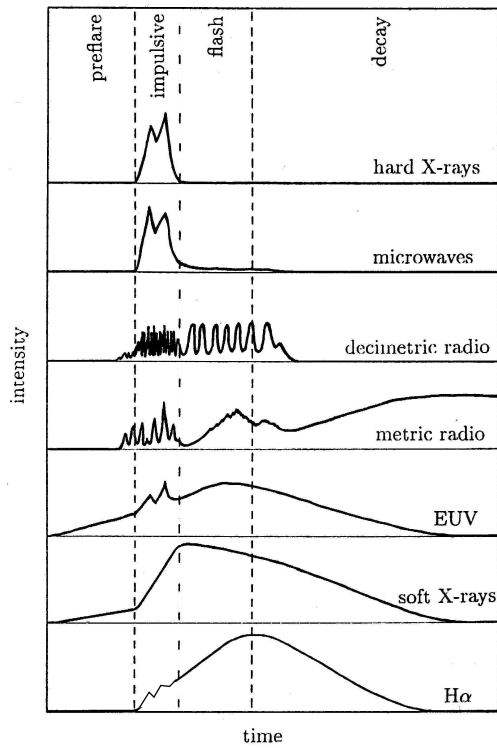


Figure 1.7 A diagram of the intensity evolution of a solar flare in multiple wavelengths. The flare’s evolution is divided in two four phases: *pre-flare*, *impulsive*, *flash*, and *decay* (Benz 2008).

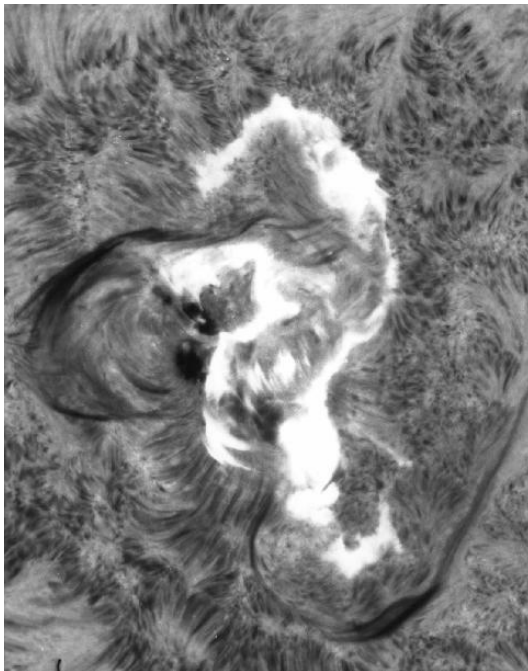


Figure 1.8 The “Seahorse Flare” occurred on 1972 August 7. The chromosphere was imaged in the blue wing of  $H\alpha$  and shows the two-ribbon structure late in the development. Bright  $H\alpha$  loops connect each of the ribbons.

move apart. These post-flare loops are an indication that magnetic reconnection has allowed the coronal magnetic field to relax into a simpler configuration and

lower energy state.

Temporally, flares of different sizes have a range of durations when viewed in soft X-rays (Figure 1.9). This is due to the fact that most of the flare energy is thermalized in the solar atmosphere. In an isolated flare, the plasma cools by thermal conduction into the chromosphere and by radiating high energy photons. At high temperatures and low densities, such as in the corona, conductive cooling dominates. At cooler temperatures and higher densities, in the chromosphere, radiative cooling is predominant (Cargill et al. 1995). Both radiative and conductive cooling have been found to balance approximately over the life of the flare; in the decay phase however, radiative cooling usually dominates (e.g., Milligan et al. 2005).

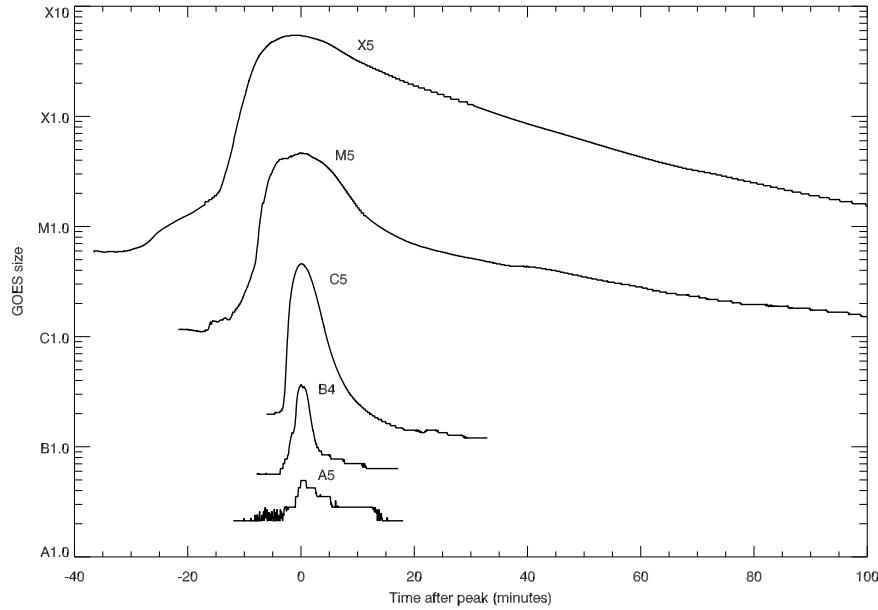


Fig. 1.9.— The scale of flares in soft X-rays as observed and classified by the GOES satellite (Grigis 2006). The intensity is logarithmic making an X5 flare an order of magnitude greater energy release than an M5 flare.

### 1.2.2. Flare Models

In general, flare models can be divided into three different energetic phases: build-up, release, and transport (Shibata & Magara 2011). Typically any given model deals with only one phase and assumes the appropriate initial conditions to account for the other models. Energy build-up in flares is magnetic at its root. Emergence of magnetic fields introduces a distortion to a magnetic structure (e.g., a sunspot group) such that the magnetic field lines tend to be aligned with the boundary between positive and negative polarities (polarity inversion line). This configuration forms a magnetic structure containing free energy; an

observed example is a sigmoid (e.g., Pevtsov et al. 1995). At a certain point, a perturbation causes the stored energy to be released. The release of energy is caused by magnetic reconnection (Section 1.2.3), which changes the topology of the magnetic field such that it is reduced to a state of lower energy than before. The released energy is converted into kinetic and thermal energy. The final phase of flare models is transporting the released energy by radiation, thermal conduction, mass ejection (Section 1.3), wave propagation, and acceleration of particles to high energies. Each energy transport mechanism has its own unique effects on the solar atmosphere and is in itself the generation of several dynamic events such as shock propagation, jet formation, plasma ejection, chromospheric evaporation (Section 2.3), and particle acceleration.

Several different complete models incorporating all three phases for explaining flares have been proposed in some form. The differences between these models are mainly the initial magnetic topologies, which are susceptible to different instabilities or drivers of the flare. The most widely cited model of flares has been in development since the 1960s and is appropriately termed the *standard model* (Figure 1.10). The initial driver of the flare is a rising prominence in an active region. The rising filament stretches a current sheet above oppositely directed open magnetic field lines, which is prone to magnetic reconnection. This induces a magnetic collapse on both sides of the current sheet after the eruption of the prominence. The magnetic collapse triggers the lateral inflow of plasma perpendicular to the current sheet. At this point, an X-type reconnection is assumed to be the major source of energy dissipation. This heats the surrounding plasma and accelerates non-thermal particles toward and away from the solar surface. Precipitating particles heat the chromospheric footprints of the newly formed magnetic loops and cause chromospheric evaporation (Lin & Forbes 2000). For more on chromospheric evaporation see Section 2.3.

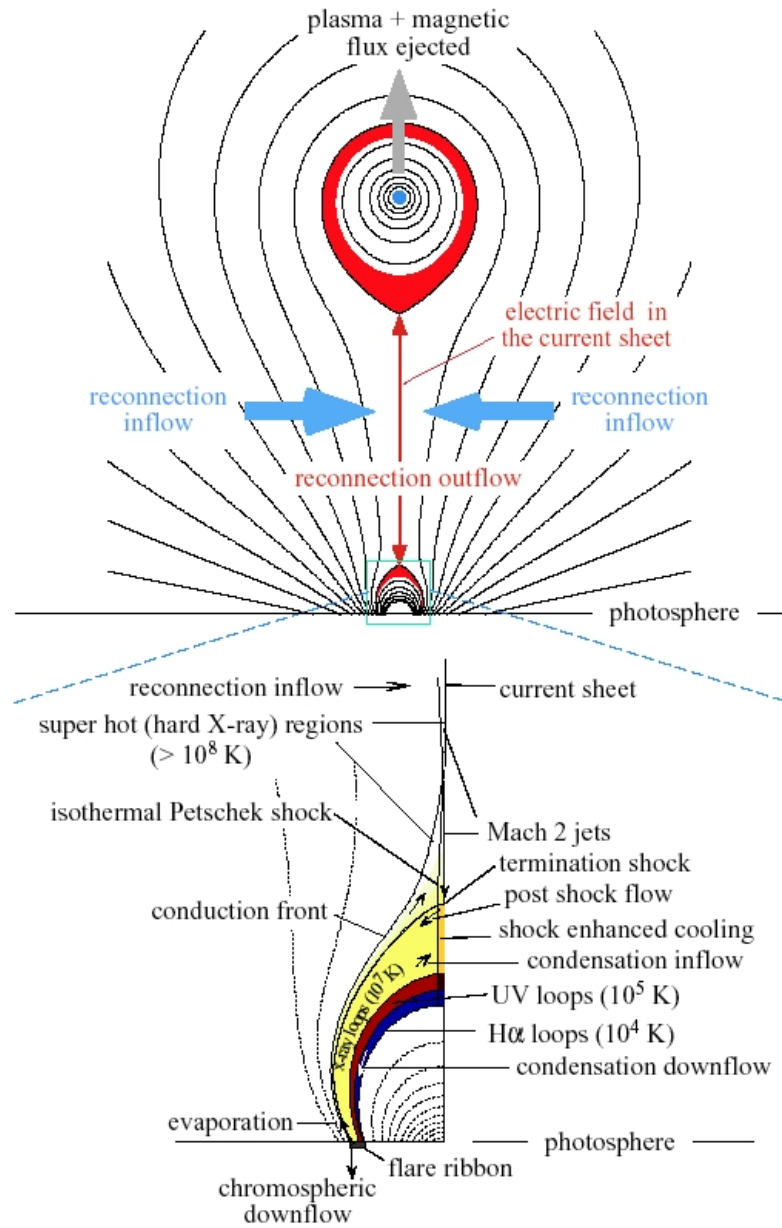


Fig. 1.10.— The *standard model* for flare eruption and CME release (Lin & Forbes 2000). The large scale filament liftoff and subsequent CME release is shown on top. An expanded view of the driving flare is shown on the bottom. The significant features and dynamics in each phase of the flare eruption are noted.

### 1.2.3. Magnetic Reconnection

The solar magnetic field is under constant stress from the generation of new magnetic fields in the interior dynamo, differential rotation, convection, and the changing connectivity with the interplanetary magnetic field. In response to these dynamic conditions, the magnetic field has to constantly change by adjusting its large scale topology. This process of readjustment is called magnetic reconnection. During reconnection, magnetic field lines break and rearrange into a more stable and lower energy state. The energy released is converted into kinetic and thermal energy and is observed as a flare.

Figure 1.11 shows a schematic of the reconnection process in two dimensions. The process begins with magnetic field lines of opposite polarities being pushed together by an external flow. As the field lines approach each other, the magnetic gradient increases, which produces a strong current perpendicular to the plane of the magnetic field lines, called a current sheet, and a diffusion region with a plasma- $\beta$  parameter of  $\beta > 1$ . Within the diffusion region, field lines are broken and reconnect into a lower energy magnetic topology. The energy released by this reconfiguration is converted into heat and a strong outflow perpendicular to the inflow. The stationary outflows are sandwiched between two standing slow shocks which do not propagate. The whole reconnection process is self-propagating and is in a steady state equilibrium as long as there is a continuous externally driven inflow.

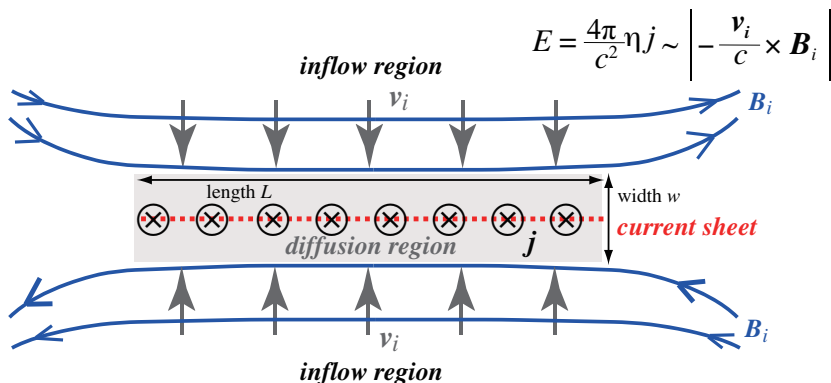


Fig. 1.11.— A diagram of the process of magnetic reconnection along a current sheet (Shibata & Magara 2011). The field lines  $[B_i]$  are pushed together by a convergent flow  $[v_i]$ .

Sweet (1958) and Parker (1957) set about to approximate the timescales at which reconnection could take place, assuming the diffusion region is much longer than it is wide, developing what is called the Sweet-Parker model. This allowed Sweet and Parker to analytically solve the resistive MHD equations for the diffusive region and the ideal MHD equations for the external area. Applying

typical solar values, they found typical reconnection rates

$$M = \sqrt{\frac{\eta}{Lv_a}} = \frac{1}{\sqrt{R_m}} \quad (1.2)$$

where  $[\eta]$  is the magnetic diffusivity,  $[L]$  is a typical lengths scale,  $[v_a]$  is the Alfvén velocity, and  $[R_m]$  is the magnetic Reynolds number. The magnetic Reynolds number quantifies the relative balance of magnetic advection to magnetic diffusion, and is defined as:

$$R_m = \frac{UL}{\eta} \quad (1.3)$$

where  $[\eta]$  is the magnetic diffusivity,  $[L]$  is a typical lengths scale, and  $[U]$  is the characteristic velocity scale of the fluid. When  $R_m \ll 1$  advection is insignificant and the field will relax into a diffusive state, while when  $R_m \gg 1$  diffusion is insignificant and the field will be advected with the fluid flow. In the outer solar atmosphere,  $R_m$  has values between  $10^8$  and  $10^{14}$  which imply reconnection rates much slower than the dissipation timescale. To rectify that situation, Parker proposed that flares are made up of a collection of smaller reconnections, or nanoflares.

### 1.3. Coronal Mass Ejections

Coronal Mass Ejections (CMEs) are the largest and most spectacular eruptions in the solar system, both in energy released and size scale. These eruptions accelerate  $10^{14} - 10^{16}$  g of heated plasma to velocities well beyond the escape velocity of the Sun (e.g., St. Cyr et al. 2000). CMEs leave the Sun’s surface with velocities ranging from  $10^2$  to over  $10^3$  km s<sup>-1</sup> and can reach Earth within hours. They originate from features the size of coronal loops ( $\approx 10^4$  km) in the low corona and expand to sizes up to a solar radius (Chen 2011). A CME structure can have several different visual geometrical shapes: a flux rope, a semi-shell, or a bubble. The exact size and shape of CMEs is debatable because of their optical thinness; a CME can appear to have disparate shapes when viewed from different angles.

Theoretical conceptualizations of CMEs can be grouped into two distinct classes: *storage and release* and *directly driven* models (Klimchuk 2001). These two classes can then in turn be further divided into five distinct types of models with basic physical differences: two models within the *storage and release* class and three within the *directly driven* class. Each type of CME release model has effects on the lower layers of the solar atmosphere and distinct observable phenomena associated with them. All models balance magnetic tension and magnetic pressure in the corona. Regions of strong magnetic fields have high pressure and tend to expand into regions of weaker fields and lower pressure. Filaments observed on the Sun are held in place by magnetic tension, which fixes their foot points in place. In the quiet corona, these forces are held in balance with each other. An eruption occurs when something tips that balance in favor of the outward pressure. This force imbalance usually happens in an erratic way, giving rise to violent eruptions.

The two directly driven models are the *thermal blast* and *dynamo-driven* models. In the *thermal blast* model of CMEs, it is proposed that greatly enhanced thermal pressure produced by a flare is driving the eruption. The pressure is so great, it cannot be contained by the magnetic tension forces and pushes the CME off of the Sun (e.g., Dryer 1982). This model for eruption is analogous to a spring being blown open from its rest state by a pressure blast from a bomb (Figure 1.12A). The *dynamo-driven* type of model involves the rapid generation of magnetic flux and stressing of the coronal magnetic field. The magnetic stress is produced by an external force such as the displacement of magnetic foot points in the solar interior or some other flux injection. A mechanical analogy would be the rapid stretching of a spring with an external crank (Figure 1.12B). Theoretical simulations have demonstrated that a highly sheared coronal arcade yielded a sufficiently fast expansion of magnetic field to produce a CME (Klimchuk 1990).

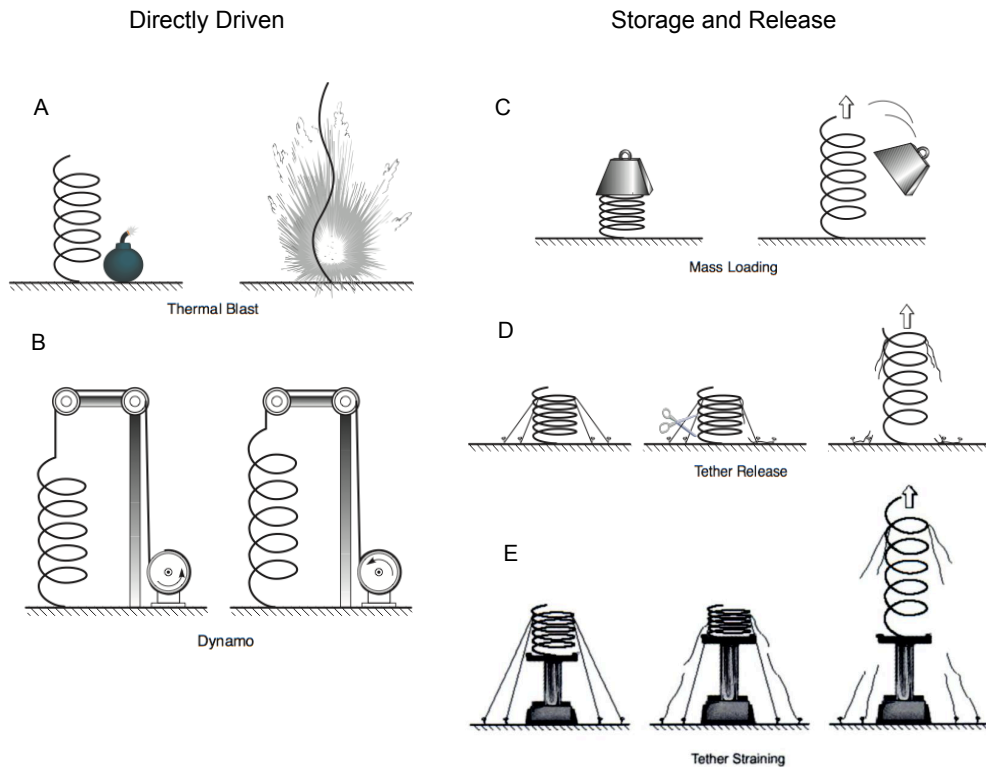


Fig. 1.12.— Five different CME release models illustrated by a spring (Klimchuk 2001). *Directly driven* models are diagrammed in letters A and B. *Storage and release* models are shown in letters C, D, and E.

Three types of storage and release models exist and are the subject of most recent CME modeling: *mass loading*, *tether release*, and *tether straining*. Loading the magnetic field with mass is a way to build up sufficient stress on the system to trigger a CME. The *mass loading* type of model postulates a metastable

magnetic field in which a build-up of significant energy and mass can take place before the system releases (e.g., Low & Smith 1993). An analogue to this would be a spring being compressed by a weight and then explosively uncoiling when the mass is perturbed (Figure 1.12C). Contrary to *mass loading*, *tether release* models do not depend on mass to build stress. The stress from tether release models comes from magnetic tension from field lines called tethers. Magnetic field lines slowly and systematically reconfigure, as illustrated by the ropes holding down the spring in Figure 1.12D. Each time a tether is relaxed, the stress on the remaining tethers grows until a critical point is reached and the pressure is released explosively (Forbes & Isenberg 1991). The last type of model is called *tether straining*. It is similar to the *tether release* models in that a slow evolution of the magnetic environment leads to a cataclysmic release of upward pressure. In *tether straining* the number of tethers remains constant but the pressure increases until a breaking point on all tethers is reached. One example of tether straining is the *breakout* model (Antiochos 1998; Antiochos et al. 1999). This is illustrated by a tethered spring sitting on a platform. The platform slowly raises, increasing the pressure until a breaking point (Figure 1.12E).

#### 1.4. Solar Activity and Space Weather

The term *space weather* refers collectively to the conditions on the Sun, in the solar wind, and in the solar magnetosphere (Schwenn 2006). These conditions directly affect the magnetosphere, ionosphere, and thermosphere of the earth and thereby the performance of space-based technology as well as electronic infrastructure on the ground. As society becomes more dependent on electronic systems, both in space and on earth, the health, safety, and welfare of human populations are more significantly affected by space weather. Space weather is different than *space climate* in that the weather is characterized by individual events on short time scales, while climate addresses the broad effects of the Sun over centuries and millennia.

Space weather can have significant financial consequences on Earth (e.g., Siscoe 2000), since a minor disruption in communication can mean the loss of billions of dollars. These conditions are influenced by explosive events on the Sun:

- Flares produce intense bursts of energy across the electromagnetic spectrum, which can heat the terrestrial atmosphere within minutes, causing drag on satellites and dropping them into lower orbits.
- Solar energetic particles are accelerated to nearly the speed of light in solar storms and can reach the earth in minutes and are a major health concern to all astronauts.
- Coronal mass ejections are clouds of plasma which can traverse the distance from the Sun to the earth from hours to days. These clouds can put enough pressure on the terrestrial magnetic fields that they deform and cause geomagnetic storms.

Flares, energetic particles, and coronal mass ejection events are all pieces of the solar activity jigsaw puzzle. Unfortunately, this is a puzzle in which there are several missing pieces. The ultimate goal of course, is to fit all of the pieces we do have into a coherent picture of how the Sun erupts, mass is ejected off the surface, and how these particles impact the Earth. Here we put forth a *bottom-up* approach where we start with the eruption as deep in the solar atmosphere as visible and extrapolate what we find vertically upwards to draw connections between the atmospheric layers.

Literature analyzing and reviewing flares spans more than a century (Benz 2008). Despite this vast amount of time and effort devoted to the subject, there are still significant gaps in our knowledge about flare eruptions. What is needed are observations that are not only precise and detailed but also systematically applied to several flares. It is also necessary to study flares on multiple scales and in multiple wavelengths simultaneously. This requires a set of robust tools to extract the properties of flares and determine the physical relevance of the various measurements. In this research we develop a specialized image-processing technique to extract useful physical measurements and then incorporate them into the larger body of knowledge on flares.

### 1.5. Anatomizing Flares

Solar features do not purely exist in a single atmospheric layer. Solar flares demonstrate a coupling between the chromosphere and corona that is not observed in the quiet Sun. The interplay between the corona and chromosphere and how they ultimately form one interactive system must be better understood to comprehend the origin of space weather and how the Sun affects the earth. There are several questions about flares that remain without a suitable answer. In this work we will focus on the following topics:

**Flare Ribbons** - How do the chromosphere and the corona interact during a solar flare?

**Mass Ejection** - What changes in the flaring environment when there is a CME versus when there is no mass ejection?

**Flare Environment** - How far away from the flare center can we observe the effects of energized particles?

We propose to investigate these questions by studying sequential chromospheric brightenings and their associated flares. First observed in 2005, solar sequential chromospheric brightenings (SCBs) are observed in the chromospheric layer of the Sun in conjunction with energetic events such as solar flares, prominence eruptions, and coronal mass ejections. SCBs appear as wave-like disturbances propagating away from the site of eruption with increased brightening in chromospheric network elements (Balasubramaniam et al. 2005, 2006). A statistical survey from Pevtsov et al. (2007) suggests that SCBs are relatively rare events. They go on to speculate that SCBs appear only in the presence of significant eruptive events such as coronal mass ejections (CMEs). Of the 17 events

that Pevtsov et al. (2007) looked at, all were associated with filament activity and 71% were associated with CMEs. In cases where SCBs are observed with a CME, the timing of an associated CME is 30 minutes to several hours after the start of the SCBs. It is possible that in cases where SCBs were observed without an associated CME, either the CME was too faint to be seen in a coronagraph or coronal observations were just not available during these periods. This tendency of SCBs to occur in conjunction with a CME presents an opportunity to forecast the emergence of CMEs before they are observed in the corona.

Because of the rarity of SCBs, an automated approach to identifying and tracking SCBs is needed to further study the role of SCBs in the chromosphere and corona. An effective tracking algorithm would identify and track subsections of the flare from pre-flare through the impulsive brightening and the exponential decline. Such tracking would allow measurement of the temporal variation in intensity and position, which could then be combined with other data to infer the photospheric magnetic field, as well as Doppler intensity of the flare. This tracking algorithm would also identify and track the temporal evolution of the ephemeral SCBs associated with the flaring region. In the past, a few different automated methods have been developed to simultaneously analyze flare ribbons across multiple sources of data (e.g., Qu et al. 2003; Maurya & Ambastha 2010; Gill et al. 2010); however, sequential chromospheric brightenings have not been studied in such an automated fashion.

In Chapter 2 we further discuss flares, chromospheric evaporation, and SCBs as they are observed in the chromosphere and specifically in  $H\alpha$ . Chapter 3 describes the different sources of data that are utilized to complete this study of chromospheric flares, including  $H\alpha$ , extreme ultraviolet images, magnetograms, soft X-ray observations, and magnetic field models. Chapter 4 explains our methodology and techniques for identifying and tracking components of the erupting flare. Chapter 5 describes the results of the measurements made on the flares and presents a case study of an atypical long-duration eruption called a Hyder Flare. Chapter 6 incorporates the measurements made of the flaring environment into a regional model of the magnetic field lines as well as into a heuristic model describing how SCBs and flares are related. In Chapter 7 we conclude by summarizing our findings and propose a direction for future work.

## 2. FLARES IN THE CHROMOSPHERE

*He talks about sensible things. He doesn't use long, difficult words...  
He uses short, easy words, like 'What about lunch?'*  
– A.A. Milne (2009)

The solar chromosphere is the subject of several active debates and unanswered questions in solar physics. These unanswered questions are due in large part to the inherent complexity of the region. The plasma- $\beta$  parameter (Equation 1.1) transitions from high to low; the medium is partially ionized; it is optically thin in the UV range; and the temperature jumps three orders of magnitude within a few thousand meters. This complex region is the first layer of the Sun in which flares are observed.

The magnetic field above active regions inextricably joins the chromosphere and corona. In the interplay between these atmospheric layers, we observe magnetic reconnection between twisted field lines leading to solar flares (Priest & Forbes 2002). The spectrum of solar flares peaks in the optical and ultraviolet, which means that the chromosphere is the dominant source of flare radiation (Woods 2004). This means that a majority of the radiative energy that a flare produces is generated in the chromosphere. The chromosphere is the region in which accelerated electrons and protons lose their energy, which in part contributes mass to the corona (e.g., Milligan et al. 2006). For these reasons, it is important to understand flare eruptions in this layer.

We will first discuss the geometry of flare eruption in the coupled solar atmosphere in Section 2.1. Next, we will focus in Section 2.2 specifically on flares observed in  $H\alpha$  and how that absorption line changes as a flare erupts. Section 2.3 discusses the phenomenon of chromospheric evaporation. Lastly, in Section 2.4 we will introduce sequential chromospheric brightenings and present the work previously done on the subject.

### 2.1. Flare Eruption in the Coupled Solar Atmosphere

Current observations of chromospheric flares utilize instruments on mid-sized telescopes in two categories: patrol images that take full-disk measurements ( $H\alpha$ , HeI 10830 Å, and white light) and high-resolution narrow band spectral imaging (e.g.,  $H\alpha$  and CaII 8542 Å). Since each of these wavelength measurements corresponds to a specific emission height in the atmosphere (see Figure 2.1), they can be thought of as a shell-view of the solar atmosphere. This 2D view can be misleading when viewing flares because flares are inherently 3D phenomena. When we observe flares, we are effectively viewing a 2D slice of a complex system.

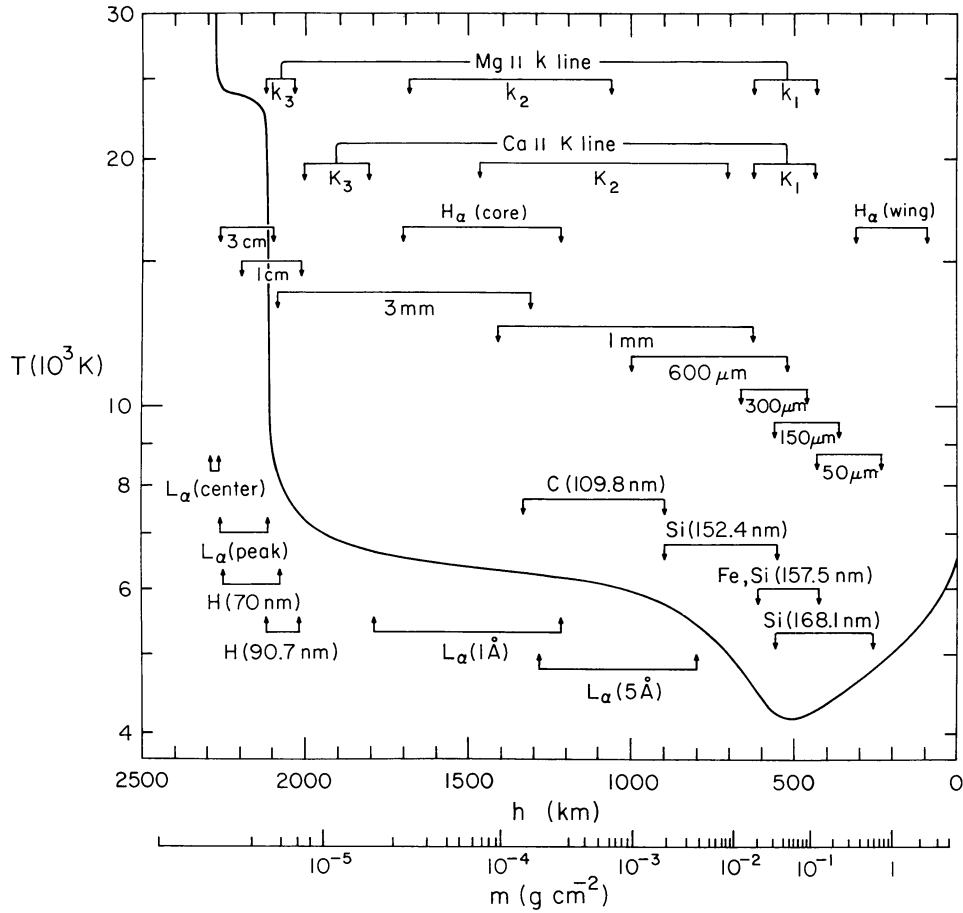


Fig. 2.1.— A temperature versus height profile of the chromosphere (Avrett 1985). Overlaid are the approximate locations of chromospheric emission lines.

Flares in the chromosphere are often observed as two extended ribbon-like structures that brighten, expand, and diverge from each other as the flare erupts (Figure 1.8). The evolution of ribbons reflects the progression of the total flare energy release. These bright ribbons are called the foot-points of the flare. They correspond to the end points of a coronal loop that have reconnected (Sturrock 1968). The ribbons appear bright because they are the location where accelerated particles have propagated down the magnetic field lines and impacted the denser chromosphere, resulting in heating and emission. The ribbons separate two regions of distinct magnetic connectivity; and thus the magnetic field lines associated with the ribbons are known separatrixes and are likely to build up significant current sheets (e.g., Priest & Titov 1996).

Beyond the diverging flare ribbons, chromospheric eruptions produce large scale waves called Moreton waves (Moreton 1960). These waves have been historically identified in the  $H\alpha$  spectral line and derived Dopplergrams. A typical Moreton wave appears as a propagating front of up-down motion (seen as a dark

and bright front in Dopplergrams). The waves usually last for about 3 – 6 minutes, extend over a limited sector ( $60^\circ - 120^\circ$ ), and propagate away from the flare source at  $500 - 2000 \text{ km s}^{-1}$  (Balasubramaniam et al. 2007). In models of Moreton waves, a solar flare initiates a coronal shock or blast disturbance (e.g., Uchida 1968; Chen et al. 2005). The shock propagates as a hydro-magnetic fast-mode wave that has a circular intersection with the chromosphere at which point it is treated as an acoustic wave. More recent models of Moreton waves suggest a significant amount of material from the corona (i.e., in a CME) must be removed to trigger such an acoustic wave propagation in the chromosphere (Balasubramaniam et al. 2007).

## 2.2. The $H\alpha$ Sun

The  $H\alpha$  spectral line is one of the most popular lines used to study the chromosphere. The chromosphere was first defined by the features observed in this line (Lockyer 1868). Despite nearly 150 years of observation and its popularity for observations, there is still a significant amount unknown about the formation of the  $H\alpha$  line and the chromosphere. This lack of knowledge is primarily due to the complicated and often competing physics in this layer.  $H\alpha$  forms the interface between the convection zone of the photosphere and lower chromosphere and the low plasma- $\beta$  environment of the upper chromosphere and corona. Thus, to understand the quiet  $H\alpha$  chromosphere a full 3D non-LTE MHD radiative transfer model is required, which necessitates a significant amount of computational ability (Leenaarts et al. 2012).

Using a state-of-the-art radiation-MHD code paired with high-resolution imaging, some basic properties of  $H\alpha$  can be derived. A relationship between intensity and formation-height of  $H\alpha$  is evident, such that the lower the intensity observed, the higher in the atmosphere the photons are originating, as seen in Figure 2.2 (Leenaarts et al. 2012). The exact relationship between the emission height and the intensity is largely dependent on the thermalization height and density of the chromosphere. This means that, depending on the feature observed (e.g., flare ribbon, network, or plage), a different height in the solar atmosphere is observed. The original approximation of a formation height range using a 1D simulation of between 1.2 and 1.8 Mm (Figure 2.1) is a little narrow and is closer to 0.8–2.8 Mm above the photosphere (Leenaarts et al. 2012). However this simulation was only looking at chromospheric network and plage, which means that in a flare, the formation-height of  $H\alpha$  is most likely as low or lower than 0.8 Mm, assuming a continued negative correlation between formation-height and intensity.

Significantly outside of the line core (more than  $\pm 1 \text{ \AA}$ ),  $H\alpha$  has a distinctly different formation-height in the atmosphere. Avrett (1985) estimated the formation-height of the  $H\alpha$  wing to be between 0.1 and 0.3 Mm above the photosphere. This is largely due to the fact that continuum emission begins to contribute to the total observed intensity. The line wing does not have enough opacity to form the low plasma beta regime ( $\beta \approx 1$ ) and thus the photospheric hydrodynamics contribute to the observed intensity. The end result of a lower formation height of the  $H\alpha$  wing is that more photospheric-type features are visible and the wing strength is sensitive to density perturbations.

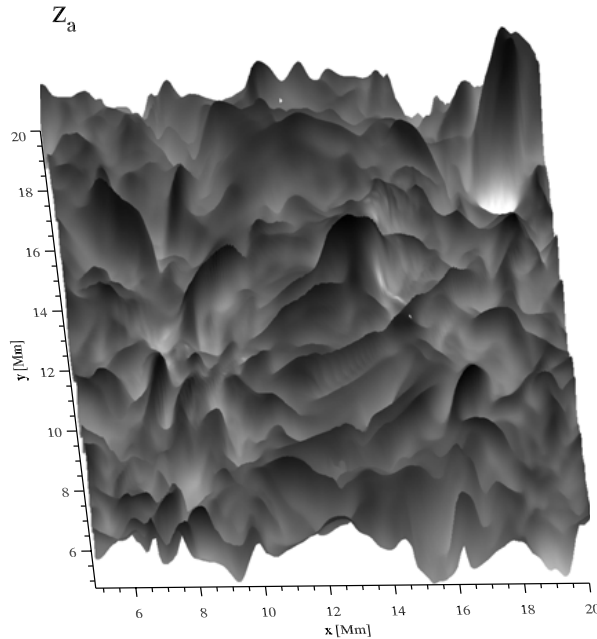


Figure 2.2 A 3-D plot of the modeled  $H\alpha$  emission height over a small area of quiet Sun (Leenaarts et al. 2012). The emission height of  $H\alpha$  ranges between 0.8–2.8 Mm.

The line formation properties of  $H\alpha$  are inherently ambiguous. The opacity of the line is temperature sensitive at heights below 1 Mm due to the excitement of its lower energy levels (Leenaarts et al. 2012). At heights greater than 1 Mm, the temperature sensitivity disappears. At these heights, the opacity is instead sensitive to density, and absorption lines have the ground state as the lower transition level. This means that in the quiet Sun,  $H\alpha$  intensity is an indication of chromospheric mass density, while in active regions and flares  $H\alpha$  intensity corresponds to temperature. Despite this ambiguity,  $H\alpha$  is still a good line to observe the structure of the chromosphere. The line has enough opacity in its core that it forms in the low plasma beta regime ( $\beta < 1$ ) where the magnetic field structures the atmospheric plasma. The low mass of the hydrogen atom broadens the absorption line to the point that a fixed-wavelength intensity measurement in the line core is only weakly influenced by quiescent velocity. The variation of the plasma density caused by the magnetic field, waves, and shocks is what forms the dramatic quiet-sun structures observed in  $H\alpha$ .

The temperature associated with  $H\alpha$  emission is largely dependent on the type of feature observed. In the quiet, inter-granular lanes, temperatures in  $H\alpha$  emission can be as low as 3000 K (Leenaarts et al. 2012). These regions also correspond to high densities and low emission intensities. In active regions and plages, emission temperatures can reach about  $10^4$  K. In this regime, the line core width of  $H\alpha$  is approximately  $1 \text{ \AA}$  due to thermal broadening. In flare ribbons, emission temperatures reach  $1.2 \times 10^4$  K or a little higher. At these temperatures,  $H\alpha$  transitions from an absorption line to an emission line.

Flare ribbons in  $H\alpha$  change the spectral line significantly. As the flare begins to develop, the  $H\alpha$  absorption profile evolves into an emission profile (Figure 2.3). Berlicki et al. (2008) observed the  $H\alpha$  absorption line to transition to an emission

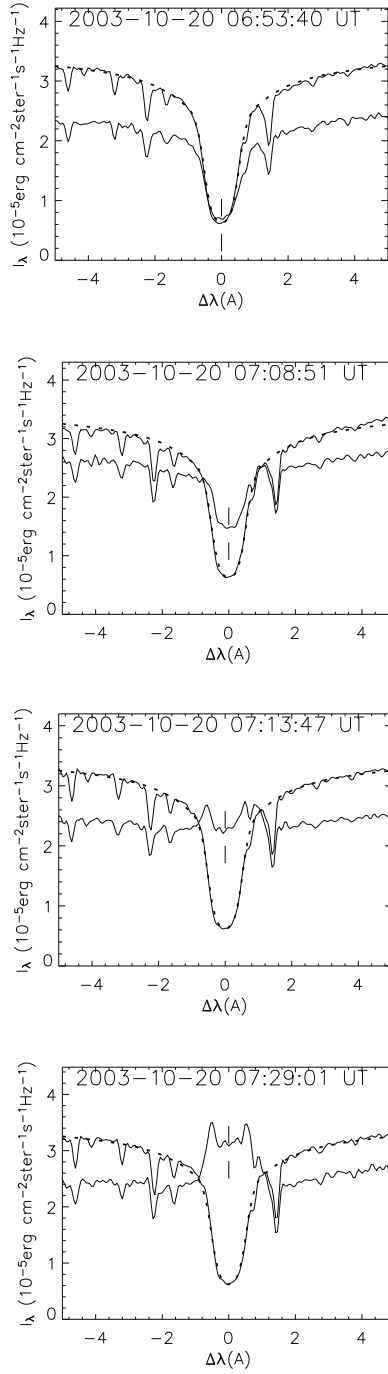


Figure 2.3 The  $H\alpha$  line response at four distinct times during a flare (Berlicki et al. 2008). The dashed line is the line profile fit to the quiescent  $H\alpha$  absorption line. There are two solid lines plotted of the measured  $H\alpha$  line, one of which is the unchanging pre-flare line. The other solid line shows the response of  $H\alpha$ , changing from an absorption profile to an emission profile.

line at the end of the impulsive rise of an M1.9 flare. Through the flash and decay phases of the flare evolution the  $H\alpha$  line remained in emission. Through this evolution, the line profile is not well behaved. The near wings of the line ( $\pm 1 \text{ \AA}$ ) respond to the conductive heating of the chromosphere more readily than the line core. In a 1D hydrodynamic simulation of this conductive heating by the corona,

Allred et al. (2005) was able to model this wing behavior (Figure 2.4). During the flash phase of the flare, material accelerated from the corona into the chromosphere increases the density in the chromosphere, causing  $H\alpha$  to significantly brighten. This coronal heating of the chromosphere also results in  $H\alpha$  blue and redshifts of tens of kilometers per second (e.g. Lites 1980; Canfield et al. 1990).

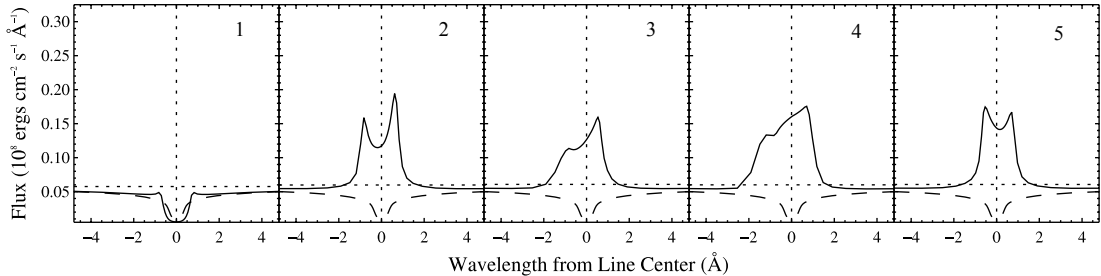


Fig. 2.4.— Simulated line profiles for  $H\alpha$  at four times during a large flare (Allred et al. 2005). The dotted lines indicate the level of the continuum and the line center, while the dashed line is the pre-flare line profile. Notice the distinct red shift of the  $H\alpha$  profile as the flare evolves.

### 2.3. Chromospheric Evaporation

The standard model of a solar flare requires that a significant fraction of the energy released by the flare is used to accelerate electrons to high energies. During the impulsive phase of the flare these heated electrons travel down newly reconnected magnetic field lines from the corona to the underlying chromosphere. The electrons then lose their energy when they collide with the relatively dense plasma of the chromosphere through Coulomb collisions. This collision transfers energy and heats the chromospheric material to tens of millions of degrees. If the over pressure builds high enough, the heated plasma rises up the field lines into the corona and expands to fill the post-flare loop. This is observed in X-ray or extreme ultraviolet images (Figure 2.5). This process is known as chromospheric evaporation and is an important component of flare energetics. The process of expansion of chromospheric plasma was first proposed by Doschek et al. (1980) and Feldman et al. (1980).

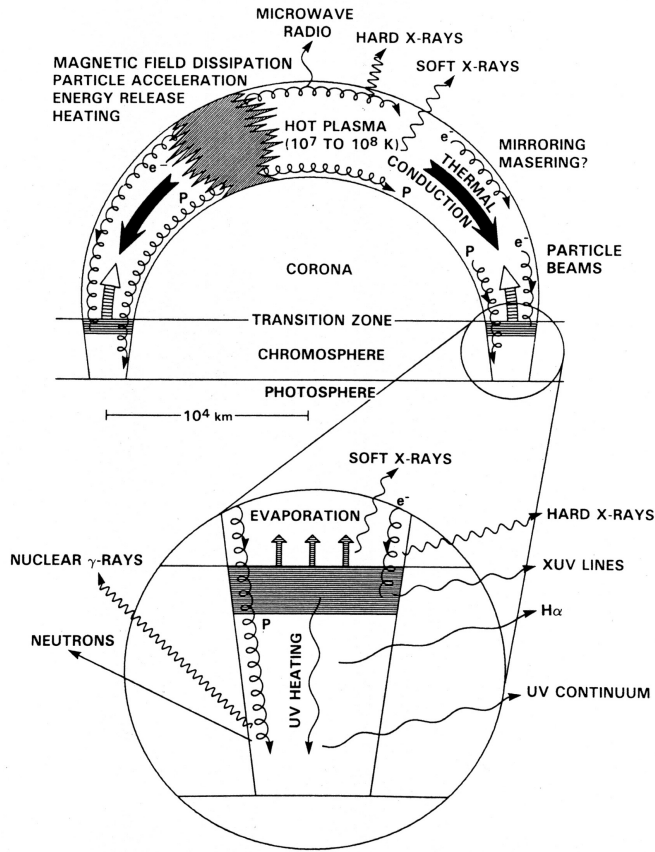


Fig. 2.5.— A diagram of the basic model of chromospheric evaporation (Gurman 1987). Electrons injected into the loop at the apex make their way to the foot-points where they heat and subsequently ablate the local plasma, forcing it to rise back up the legs of the loop.

Chromospheric evaporation was first proposed by Neupert (1968) to explain the delay between the peak of the hard and soft X-ray emission during solar flares. Physically, non-thermal electrons that fall into the chromosphere after reconnection either produce thick-target bremsstrahlung emission in the form of hard X-rays or transfer their energy to the ambient plasma via Coulomb collisions. Coulomb collisions result in intense heating and an increase in pressure and the rapid expansion of the chromospheric plasma into the tenuous corona to fill the overlying flare loops. This emits soft X-ray and EUV emission in the process.

Many simulations have been developed to model the injection of electron beams and the subsequent dynamic response of the lower solar atmosphere. The general result from these simulations is that the amount of energy deposited into the chromosphere by the electrons is directly proportional to the speed at which the evaporated material rises (e.g., Allred et al. 2005). Direct observations have never been made because there is no one instrument that can simultaneously measure both the injected electron spectrum and the velocity of the up-flowing

material.

## 2.4. Sequential Chromospheric Brightening

Sequential chromospheric brightening (SCB) was first observed by Balasubramaniam et al. (2005) in a GOES class M2.7 flare, which occurred on 2002 December 19. Balasubramaniam et al. (2005) used a multi-wavelength data set to analyze the eruption of a large scale transequatorial loop. This eruption manifested itself in the corona as a large scale coronal dimming, flares in both the north and south hemispheres, and a halo CME. In the  $H\alpha$  chromosphere, the loop eruption appeared as flare precursor brightenings, sympathetic flares, and co-spatial propagating chromospheric brightenings. Dubbed sequential chromospheric brightenings (SCBs), the speed of this propagating disturbance was measured to be between 600–800 km s<sup>-1</sup>. Although the disturbance propagated at similar speeds to EIT flare waves, they differed from typical waves observed in  $H\alpha$  (Moreton waves) in that they were not observed in off-band images, they had an angular arc of propagation of less than 30°, and they appeared as distinctly individual points of brightening instead of continuous fronts. The SCBs were also observed to have exclusively one magnetic polarity.

Balasubramaniam et al. (2006) conducted the first statistically motivated study of SCBs. They gathered properties of 18 separate eruptions that had SCBs associated with them (see Table 2.1 for a summary). Balasubramaniam et al. (2006) found that 78% SCB events of the 18 chosen for the survey had a visible CME associated. Also, SCBs are more likely to be associated with a short duration event flare than a long duration event because rapid reconnection is more likely to cause sudden acceleration of particles into the chromosphere. Balasubramaniam et al. (2006) further postulated that the four events that had no observable CME associated may have had a failed eruption associated with them and thus was undetectable by LASCO. They also observed SCBs to originate as few as three minutes after the onset of the associated flare, which corresponds to approximately 30 min before a mass ejection can be detected.

Pevtsov et al. (2007) investigation of the 18 SCB events (Table 2.1), found in some cases that SCBs precede the CME launch. SCBs appear to originate from either end of the flare ribbons and progress outward following the magnetic field topology. Analyzing the magnetic fields around these SCBs reveals them to have mono-polarity as opposed to the network magnetic field which usually has mixed polarity. Pevtsov et al. (2007) asserted that SCB locations exhibit several properties of chromospheric evaporation. The  $H\alpha$  brightening is followed by an associated coronal dimming and the appearance of new loops, suggesting that localized heating creates SCBs, which is enough to expand chromospheric plasma into low lying coronal loops. Pevtsov et al. (2007) postulates that SCBs statistically appear as relatively rare events because of the lack of quality measurements (e.g., low scattered light, high spectral fidelity, and high spatial resolution) and the specific phenomena with which they are associated (e.g., pre-eruptive CME events).

Because of the SCB's single predominate polarity, the relative timing of SCBs

Table 2.1. Statistical results from 18 SCB events studied by Balasubramaniam et al. (2006) showing the relationship between SCBs and CMEs.

Date	Associated Flare Class	Visual CME	LASCO Speed [km s <sup>-1</sup> ]
2002-12-19	M2.7	yes	1092
2003-02-06	none	yes	308
2003-05-09	B6.6	yes	305
2003-05-19	B7.8	yes	900
2003-06-11	M1.8	no	–
2003-10-29	X10.0	yes	2029
2003-10-31	C5.1	yes	605
2003-11-20	C8.6	yes	174
2004-01-05	C4.2	yes	1233
2004-03-16	none	no	–
2004-06-15	C1.1	yes	434
2004-07-20	C8.1	no	–
2004-10-06	C2.5	yes	337
2004-10-07	none	yes	360
2004-11-09	M8.9	yes	462
2004-12-30	M4.2	yes	1035
2005-01-19	none	no	–
2005-05-06	C8.5	yes	624

as compared to the beginning of the associated solar eruption, and the location of the disturbance train with respect to the overall topology of each event, it is hypothesized that SCBs may be caused by high-energy particles cascading away from the magnetic reconnection site. To illustrate the 2005 May 6 SCB event, Balasubramaniam et al. (2006) diagrammed the observed features in the photospheric magnetic field, chromospheric  $H\alpha$ , and coronal EUV emission (Figure 2.6). To explain the dynamics of the May 6 event, Pevtsov et al. (2007) developed a phenomenological model of SCBs. As a result of reconnection between open and closed magnetic field lines, new coronal loops are formed. In doing so, electrons are accelerated into the denser chromosphere, depositing their energy as heat and is observed as an SCB. Therefore SCBs would be expected to form at the beginning of the release of a CME, as they are a byproduct of the CME release mechanism.

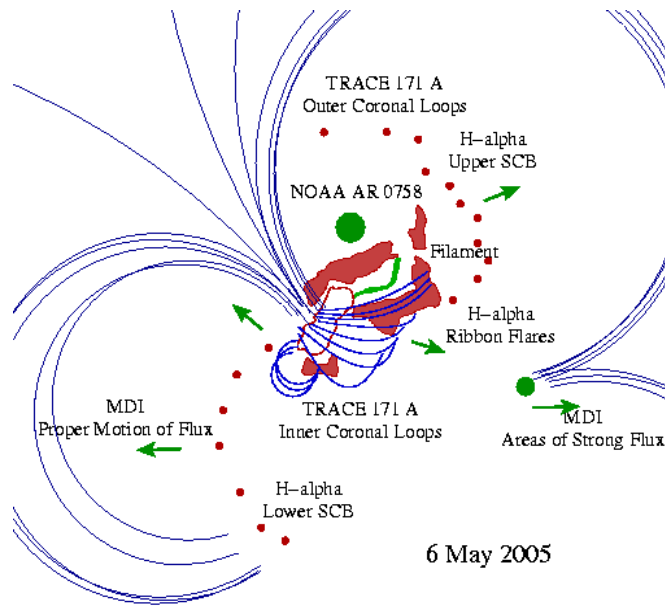


Fig. 2.6.— A phenomenological model for a series of SCBs appearing on 2005 May 6 by Balasubramaniam et al. (2006).  $H\alpha$  brightening is shown in red, coronal loops are in blue, and magnetic flux is in green.

### 3. OBSERVING THE SUN

*Busy old fool, unruly Sun*  
*Why dost thou thus*  
*Through windows, and through curtains, call on us?*  
– John Donne (1896)

Earth’s atmosphere is opaque to most of the electromagnetic spectrum. That, in general, is a very good thing. The small bit of ultraviolet light that does leak through the upper atmosphere is enough to give us sunburns and skin cancer.<sup>1</sup> The visible spectrum of light has historically been our only window on the Sun, since it is one of the few bands of the spectrum that passes unimpeded to the Earth’s surface. Measurements on the space station Skylab provided our first consistent images of the Sun in extreme-ultraviolet (EUV) and soft X-ray (Huber et al. 1974). These images opened up a new world of solar physics by revealing features on the Sun through wavelengths of light that cannot penetrate the atmosphere.

Since the mid-1970’s solar physics has relied on a combination of both ground-based and space-based observations; and this investigation is no different. The challenge comes with connecting features and events through space and time between observations made on the ground with those made in space. Section 3.1 introduces the types of observations used in this work, discusses the general benefits and drawbacks of ground-based and space-based observing, and defines the necessity to use both simultaneously to develop a coherent description of solar features. Section 3.2 discusses the ground-based ISOON telescope and the initial processing performed on the images. Section 3.3 describes the EUV and X-ray measurements taken by three different spacecraft: Atmospheric Imaging Assembly (Section 3.3.1), Geostationary Operational Environmental Satellites (Section 3.3.2), and Reuven Ramaty High Energy Solar Spectroscopic Imager (Section 3.3.3). Section 3.4 introduces the Helioseismic and Magnetic Imager and the models that are built using those measurements (Section 3.4.3).

#### 3.1. Seeing the Sun in Many Different Lights

Solar observations generally fall into two categories: ground-based and space-based. There are benefits and difficulties with both types of observations. No matter where the telescope is gathering photons, there are general difficulties in getting enough of them. This may seem counterintuitive, since the Sun is the brightest object humans can observe, but the limitation lies in contrast. A sunspot in the photosphere has an order of magnitude fewer photons coming from it than from the quiet photosphere. A strong spectral line may have a tenth of the continuum emission, and of those only 1% may be polarized. So it is easy for one

---

<sup>1</sup>Abundant amounts of vitamin D<sub>3</sub> are produced photochemically in the skin of most vertebrate animals with the aid of UV light.

to imagine a situation of looking at polarization in a sunspot’s strong absorption line which could have 0.01% of the light coming from the quiet Sun around it (Stix 2004). Designing an instrument to handle four orders of magnitude in intensity yet be able to detect subtle changes in the solar atmosphere is the challenge. In general, a larger aperture telescope captures more light, allowing the observer to measure small changes in the signal.

### 3.1.1. *Ground-based Observing*

Observing the Sun from the ground is constrained by the Earth’s atmosphere. The image quality of any celestial object is degraded by fluctuations in the reflective index of the light path. These fluctuations are called seeing. The Sun aggravates the problem of seeing by causing thermal convection in the entire troposphere as well as heating of the ground around the observatory and the observatory itself, causing local convection (Stix 2004). Effects of seeing can be mitigated in three ways: site selection, adaptive optics, and image post-processing.

A site with smooth laminar airflow, low atmospheric moisture, and minimal atmospheric density (i.e., high altitudes) is ideal for a large telescope. It is for these reasons, telescopes are often found on mountain tops.

Adaptive optics is a system that physically deforms a mirror in real-time to correct for the atmospheric distortions. These systems take measurements of the optical wave-front and translates perturbations to a matrix of actuators several times per second to correct the image.

Post-processing encompasses several different types of algorithms to correct for seeing effects after the scientific images have been recorded. The images are reconstructed using a statistical understanding of seeing, and the process is computationally intensive.

The benefits of ground-based observing are evident in the storage of data, application of new technologies, and overall cost. In modern solar physics, the rates of collecting data is increasing exponentially, and efficient storage is an issue. Having a storage facility physically connected to the telescope is a major advantage of ground-based observing. As new technologies emerge, they can be integrated into the telescope’s optics, thereby keeping the telescope on the cutting edge of observing. This advantage is evident in the Dunn Solar Telescope, which was built in 1969 yet still remains one of the world’s premiere facilities. The overall cost of ground-based observing is a fraction of the cost of space-based missions. The budget for the ground-based Advanced Technology Solar Telescope, which has yet to be built, is  $\approx$  \$300 million (Keil et al. 2010), while the Solar Dynamics Observatory satellite cost almost \$850 million.

Considering the benefits and drawbacks of ground-based observing, terrestrial telescopes tend to be high-resolution and partial-disk or low-resolution and full-disk configurations. Observations from the ground are constrained to visible, some infrared and radio parts of the electromagnetic spectrum, since Earth’s atmosphere scatters most wavelengths of light. This limits observations to events occurring at cooler temperatures of the photosphere and chromosphere.

### 3.1.2. *Space-based Observing*

Observing the Sun from space has constraints that are unique to it: launching to orbit is expensive; space-ready technologies are often a decade out of date; and data storage and transfer are limited. The current cost of sending a satellite into orbit is tens of millions of dollars, and the expense to build flight-ready hardware is many times the cost of its terrestrial counterpart. Both of these factors combine to inflate the cost of satellite missions to several times what equivalent ground-based observing would cost. Since most satellites are not serviceable once in orbit, the technology designed to fly is limited to what is available at the time of design and is often obsolete at the time of launch. The most limiting factor in space-based observing is the data. Even with dedicated transmitters, sending information from a spacecraft to the ground is several orders of magnitude slower than what can easily be achieved between computers on earth.

On the benefit side, using a satellite to observe the Sun allows measurements of all wavelengths since there is no extinction, full 24-hour coverage since the Sun does not set, and less post-processing of the data because there is no atmosphere intervening. Without an atmosphere, high-temperature events are observed in the chromosphere and corona in several extreme ultraviolet (EUV) and x-ray wavelengths. The continuous coverage of a full solar disk makes it possible to measure the acoustic frequency spectrum in the photosphere – the foundation of helioseismology. Space-based observing also can detect coronal mass ejections out to several solar radii.

## 3.2. Improved Solar Observing Optical Network Telescope

The Improved Solar Observing Optical Network (ISOON) telescope is a semi-autonomous, remotely controllable observatory designed as a joint partnership of the National Solar Observatory (NSO) and the Air Force Research Lab (AFRL) (Neidig et al. 1998). ISOON had its first light in 2002 and was located at the NSO Sacramento Peak, NM until 2012, when it was relocated to Kirtland AFB in Albuquerque, NM. ISOON acquires full solar disk images once per minute in  $H\alpha$  and at  $\pm 0.4 \text{ \AA}$  from line center. It also records continuum images and magnetic field measurements in CaI once every ten minutes. Images are captured on a  $2048 \times 2048$  thermoelectrically cooled CCD with a 12-bit full frame readout, and they are automatically archived on a hard-disk array. ISOON has a photometric accuracy better than 5% over the field of view and records 4096 intensity levels.

Dr. Richard B. Dunn designed the optics for ISOON. The telescope is designed to operate as a narrow band ( $0.1 \text{ \AA}$ ) filtergraph around a telecentral optical axis. This optical configuration is to optimize the performance of the system's two Fabry-Perot filters (Figure 3.1). The entire optical system includes five lenses, none of which are corrected for chromatic aberration, and it is diffraction limited over all wavelengths in the tunable range. The first field lens, magnifier lens, and Cooke triplet lens are all movable to provide a zoom and focus system that corrects for chromatic focus effects and maintains a constant solar diameter throughout the year. The magnifier lens provides a constant spatial resolution of  $1.1 \text{ arcsec}$

per pixel across the full solar disk.

The raw digital images recorded by ISOON are processed in a series of automated steps to produce consistent images. First, dark current is subtracted and a flat-field correction is applied to remove instrumental artifacts. Atmospheric refraction causes the circular Sun to appear as an ellipse. To correct for this aberration, the elliptical disk image is then fitted, the major, minor, and center are calculated, and the Sun is circularized. Next, the image is rotated to account for the position angle between the geocentric north pole and the solar rotational north pole (P-angle correction), and it is resized to a constant solar diameter of 1781 pixels. The image is then standardized over intensity (to correct for varying atmospheric extinction), and any plane tilt aberration is corrected. Finally, the images are compressed into a high-quality JPEG format and are archived.

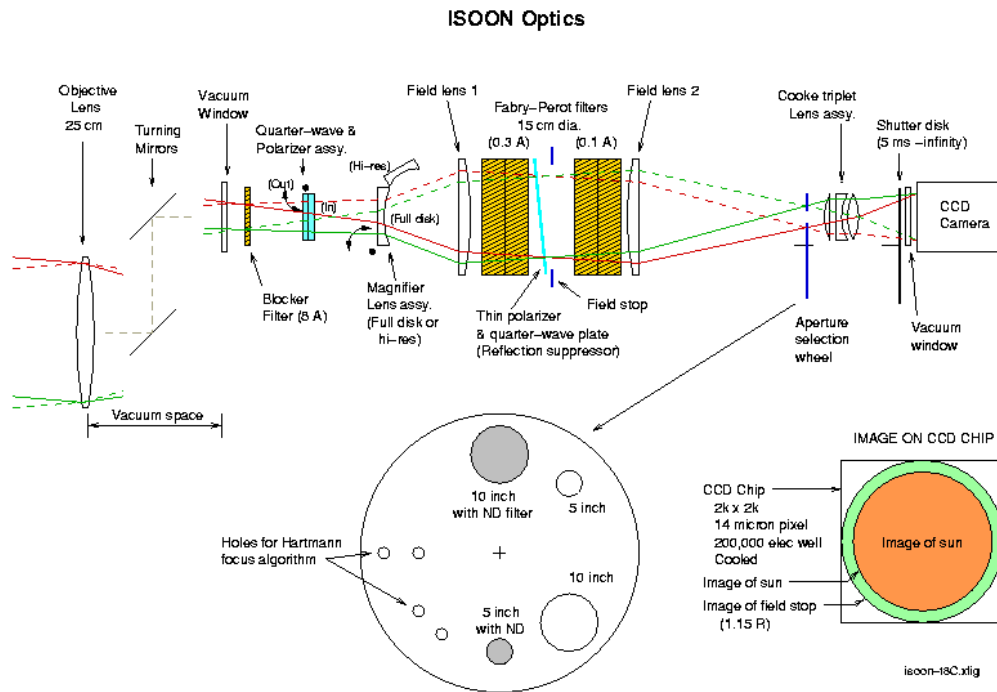


Fig. 3.1.— ISOON’s optical diagram. Light paths are traced in red and green lines.

Since ISOON records images  $\pm 0.4 \text{ \AA}$  from line center, it is possible to translate this measurement into a Doppler velocity. 2003 October 14 was selected to create a standard Doppler profile due to its low solar activity. A total of 14 calibrated images were recorded across 14 wavelengths centered around the  $H\alpha$  absorption line. Next, a separate spectral line profile was obtained for each pixel, and the spectral line center was calculated (Figure 3.2). For each spectral line, the intensity-difference was measured at  $\pm 0.4 \text{ \AA}$  and a Doppler shift calculated by subtracting the calculated line-center for each pixel from the average line-center for the entire image. A characteristic relationship was formed through averaging

the plots of all the points of Doppler shift versus intensity difference (Figure 3.3). Generalizing this measurement for all observations, the measurement of the  $\pm 0.4 \text{ \AA}$  intensity difference can be converted to a Doppler shift by applying the 2003 calibration. This assumes that the line profile is consistent, symmetrical about line center, and the intensity of the line changes symmetrically in both bright and dark features. Since the calibration was calculated for  $H\alpha$  in absorption, the Doppler measurement is not valid when the line changes to emission (e.g., in a flare).

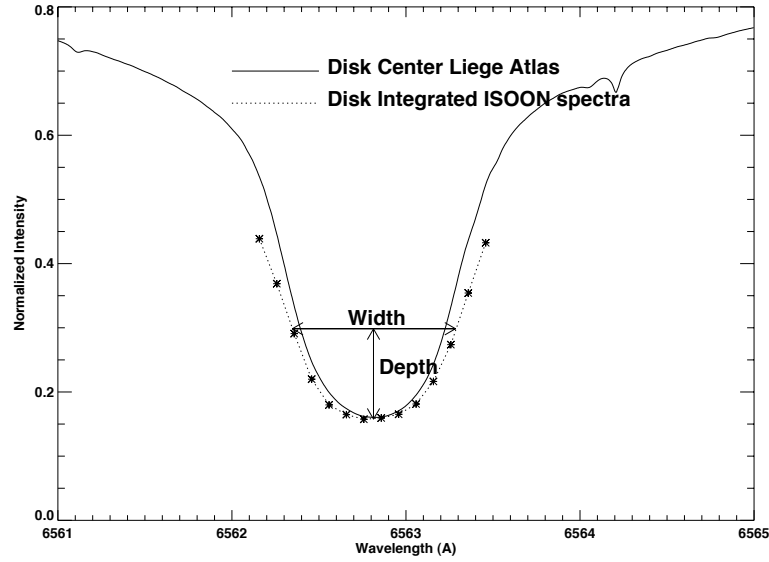


Fig. 3.2.— Measurements along the ISOON  $H\alpha$  line profile to calibrate the Doppler velocity to wing intensity.

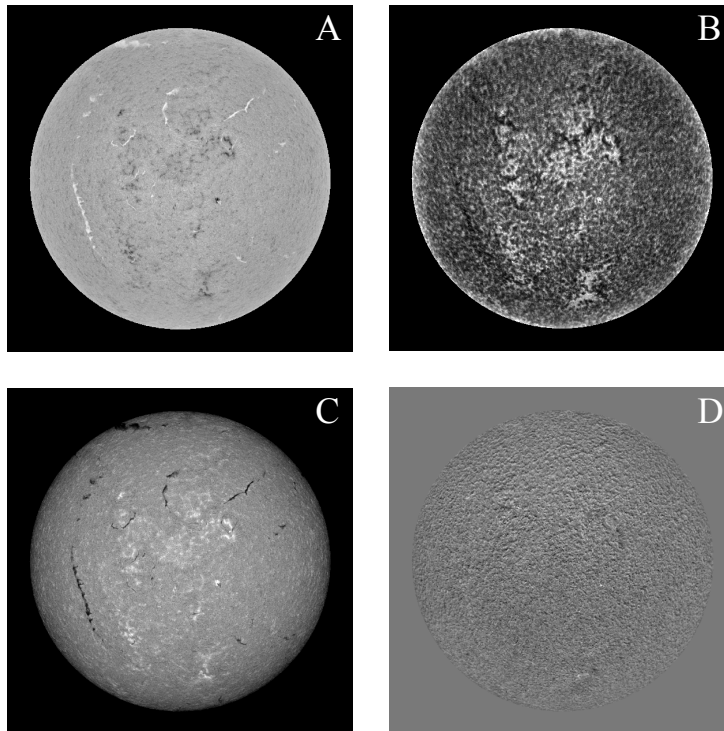


Fig. 3.3.— Images taken by ISOON from 2003 October 14 generated to calibrate a typical Doppler response. **A:**  $H\alpha$  depth, **B:**  $H\alpha$  width, **C:**  $H\alpha$  intensity, **D:** derived  $H\alpha$  Doppler velocity.

### 3.3. Extreme Ultraviolet and X-ray Observations

Extreme Ultraviolet (EUV) and x-ray measurements sample the hottest plasma, which is characteristically rooted in the corona. Nearly all of the activity on the Sun and the majority of the energy for heating Earth's thermosphere and creating Earth's ionosphere occurs between 1 and 1000 Å. To observe this spectral range, the telescope must be outside of the Earth's atmosphere. There have been several satellite and rocket missions to make measurements of this part of the spectrum since about 1950 (Stix 2004). Three current missions to measure high energy wavelengths are the Solar Dynamics Observatory (SDO), Geostationary Operational Environmental Satellites (GOES), and Ramaty High Energy Solar Spectroscopic Imager (RHESSI). NASA launched SDO on 2010 February 11 with an EUV imager to focus on the evolution of the Sun's magnetic environment through its interaction with atmospheric plasma (Section 3.3.1). GOES is an ongoing mission observing solar X-rays with three satellites in current service, 11 decommissioned, and two more planned (Section 3.3.2). RHESSI measures the broadest spectrum of any current instrument, sampling four decades of energies

(Section 3.3.3).

### 3.3.1. Atmospheric Imaging Assembly

The Atmospheric Imaging Assembly (AIA) produces multiple near simultaneous full-disk images of the corona and transition region (Lemen et al. 2011). AIA observes the Sun in EUV up to  $0.5 R_{\odot}$  above the solar limb with a thinned backside illuminated  $4096 \times 4096$  CCD where each pixel spatially corresponds to 0.6 arcsec. AIA employs four telescopes that image seven EUV narrow band passes centered on specific ions' emission lines at a 12-second cadence. Additionally, one of the four telescopes observes the transition region in the UV ( $1600 \text{ \AA}$ ), the nearby UV continuum ( $1700 \text{ \AA}$ ), and the continuum visible-light photosphere using a broad-band filter ( $\approx 500 \text{ \AA}$  full-width half-max). The visible light images are taken to aid in co-alignment with images from other telescopes. Table 3.1 lists the wavelengths, primary ions, types of solar features, and associated temperature for each of the AIA band-passes. As a whole, AIA samples solar temperatures that span the range from  $5 \times 10^3 \text{ K}$  to  $2 \times 10^7 \text{ K}$  and all three layers of the solar atmosphere. Figure 3.4 shows an active region from February 15, 2011 in the seven EUV wavelengths, the  $1600 \text{ \AA}$  channel, and an HMI line-of-sight magnetogram. (For a further description of magnetograms, see Section 3.4.)

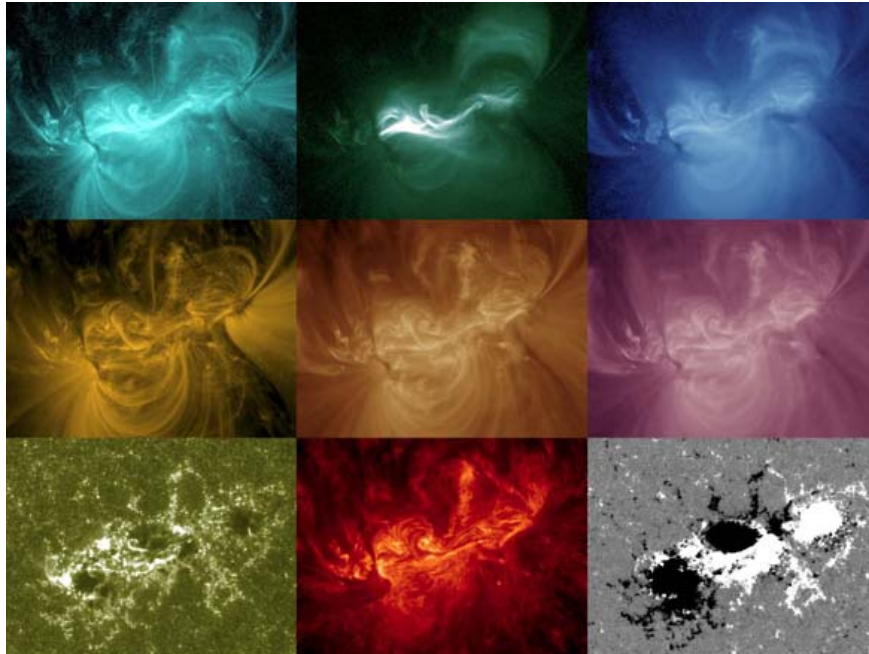


Fig. 3.4.— Examples of an active region on 2011 February 15 imaged with AIA (Lemen et al. 2011). The top row, from left to right, are the  $131 \text{ \AA}$ ,  $94 \text{ \AA}$ , and  $335 \text{ \AA}$  channels. The middle row are the  $171 \text{ \AA}$ ,  $193 \text{ \AA}$ , and  $211 \text{ \AA}$  channels, and the bottom row are  $1600 \text{ \AA}$  and  $304 \text{ \AA}$  (left and middle). The bottom right

Table 3.1. The primary ions observed by AIA, the region of the atmosphere, and their characteristic temperatures (Lemen et al. 2011).

Channel [ $\text{\AA}$ ]	Primary Ions	Region of Atmosphere	Assoc. $\log(T)$ [K]
4500	continuum	photosphere	3.7
1700	continuum	temperature minimum, photosphere	3.7
304	HeII	chromosphere, transition region	4.7
1600	CIV & cont.	transition region, upper photosphere	5.0
171	FeIX	quiet corona, upper transition region	5.8
193	FeXII, FeXXIV	corona, hot flare plasma	6.2, 7.3
211	FeXIV	active-region corona	6.3
335	FeXVI	active-region corona	6.4
94	FeXVIII	flaring corona	6.8
131	FeVIII, FeXX, FeXXIII	transition region, flaring corona	5.6, 7.0, 7.2

corner is an HMI line-of-sight magnetogram showing the same active region.

SDO does not record science data onboard the satellite but transmits Level 0 data continuously to two Ka-band radio receivers located near White Sands, New Mexico (Lemen et al. 2011). A Level 1 calibrated data product is created in several steps. First, the overscan regions on the Level 0 images are removed and dark current is subtracted. Next, a flat-field correction, which is unique for each telescope, is applied. Flat-field images are constructed routinely to account for the changing CCD charge-collection efficiency. The AIA images are then processed to remove “bad” pixels and “spikes” where charged particles interact with the CCD. In the last step, images are flipped so solar North is at the top of the array. To achieve a higher level of consistency between calibrated Level 1 images, three further corrections are made in a single step. The images are rotated so that solar north is at exactly  $0^\circ$ , the plate-scale is adjusted to exactly 0.6 arcsecs per pixel, and realigning is done so that the Sun’s center is at the middle of the image. Applying these corrections produce a Level 1.5 data product, which is archived as a 16-bit FITS file.

### *3.3.2. Geostationary Operational Environmental Satellites*

The Geostationary Operational Environmental Satellites (GOES) are a series of satellites that have operated continuously since July 1974 (Ludwig & Johnson 1981). Administered by the National Oceanic and Atmospheric Administration (NOAA), the GOES mission is primarily tasked with observing the atmospheric conditions on Earth and is currently operating its 15<sup>th</sup> satellite in the series. In addition to terrestrial weather, GOES monitors the space environment through a suite of instruments: magnetometer, energetic particle detector, soft X-ray irradiance sensor (XRS), and soft X-ray imager. XRS consists of ion chamber detectors which provide full-disk X-ray fluxes in two wavelength bands: 0.5 to 3 Å (hard channel) and 1 to 8 Å (soft channel). GOES’s XRS has been consistent and successful in detecting solar flares to the extent that the classification of flare size is currently based on the total flux measured in the soft X-ray channel (see Table 1.1). The ion chamber detectors are also sensitive to bremsstrahlung radiation from energetic particles in the outer radiation belts of the Earth and SEPs strikes which are detected because of their distinct local particle pitch-angle distribution and removed in data post-processing.

### *3.3.3. Reuven Ramaty High Energy Solar Spectroscopic Imager*

Reuven Ramaty High Energy Solar Spectroscopic Imager (RHESSI) is a NASA small explorer mission satellite designed to explore particle acceleration and energy release in solar flares. Launched in 2002, it observes solar x-ray and gamma ray flux in the range of 3 keV to 17 MeV with an energy resolution of about 1 keV (Lin, R. P. et al. 2002). RHESSI has 9 identical detectors with a

pair of grids in front of each which are used for imaging. The satellite rotates at about 15 revolutions per minute, changing the orientation of the grids and thereby modulating the signal recorded. It is then possible to reconstruct an image from the modulated patterns. The theoretical resolution limit of RHESSI is  $2.3''$ ; however, a strong source and long integration time are required for maximum energy resolution; thus the practical spatial resolution is routinely less.

RHESSI covers a broad spectrum, smoothly stretching from thermal emission (Maxwell-Boltzmann distribution) to entirely non-thermal (power-law distribution), showing a distinct separation between the two. Because flares have such a large dynamic emission range during eruption, RHESSI employs thin aluminum attenuators that are automatically placed in front of the detectors and absorb low-energy photons. These attenuators cause discontinuous jumps in the measured lower-energy emission and have to be removed in post-processing algorithms. RHESSI is especially adept in detecting bremsstrahlung, recombination, and bound-bound emission in flares. Since bremsstrahlung and recombination are more efficient with heavier ions, these types of emissions predominately come from partially ionized atomic iron.

### 3.4. Polarimetry and Magnetic Fields

Magnetic fields are known to be the dominant factor driving the dynamics of the solar atmosphere. These fields can be detected through Zeeman splitting of spectral lines. However, Zeeman splitting is only evident in relatively strong fields. For weaker fields, polarization of the Zeeman components is utilized to make measurements (Stix 2004). Spectropolarimetry is the technique of measuring the polarization of light as it interacts with matter and magnetic fields. To fully make sense of how light interacts with matter, an understanding of the theory of spectral line formation in a magnetized solar atmosphere is necessary. There is a complex theoretical interpretation needed to connect polarimeter output and solar magnetic field measurements, ultimately producing magnetograms. Below is a sketch of this theory (Section 3.4.1), an outline of polarimeters used in this work (Section 3.4.2), and the theory of reconstructing field lines from magnetograms (Section 3.4.3).

#### 3.4.1. Magnetism and Polarized Light

The theory of how magnetism affects light begins with a quasi-monochromatic electromagnetic plane wave propagating in the  $z$ -direction with a given frequency  $[\nu]$ , wavelength  $[\lambda]$ , and amplitude  $[a]$  (Stokes 1852). The electric field vector,  $\vec{E}$ , rotates orthogonally to the direction of propagation, in this case the  $x$  and  $y$ -directions over a given time  $[t]$ .  $\vec{E}$  can be described as a superposition of both the  $x$  and  $y$  components:

$$E_x(t) = a_x(t) \exp i \left( \phi_x(t) - 2\pi\nu t + \frac{2\pi z}{\lambda} \right) \quad (3.1)$$

$$E_y(t) = a_y(t) \exp i \left( \phi_y(t) - 2\pi\nu t + \frac{2\pi z}{\lambda} \right). \quad (3.2)$$

Let  $\delta$  be defined as the rotation of the electric field in the  $x$ - $y$  direction:  $\delta = \phi_x - \phi_y$ . Thus, if  $\sin(\delta) < 0$  then the rotation is counterclockwise, and if  $\sin(\delta) > 0$  then the rotation is clockwise. The Stokes parameters are defined as averages over some time period:

$$I = \langle a_x^2 \rangle + \langle a_y^2 \rangle \quad (3.3)$$

$$Q = \langle a_x^2 \rangle - \langle a_y^2 \rangle \quad (3.4)$$

$$U = 2 \langle a_x a_y \cos \delta \rangle \quad (3.5)$$

$$V = 2 \langle a_x a_y \sin \delta \rangle \quad (3.6)$$

Expressed as a vertical vector,  $S = (I, Q, U, V)^\top$ , these four parameters are collectively known as the Stokes vector (superscript  $\top$  means transposition). In general, it can be said that  $I$  represents the total intensity of the original beam,  $Q$  represents how much of the beam is vertical or horizontal ( $0^\circ$  or  $90^\circ$ ),  $U$  represents how much of the beam is diagonal ( $\pm 45^\circ$ ), and  $V$  represents how much of the beam is circularly polarized (left or right handed). Since  $I$  represents the total intensity of the polarized light, it naturally follows that:

$$I^2 \geq Q^2 + U^2 + V^2. \quad (3.7)$$

The equality condition is only achieved with a perfectly monochromatic beam of light.

The Radiative Transfer Equation (RTE) describes how polarized light is transmitted through a medium with a magnetic field and describes how the magnetic field changes the polarization state of the light. The work of Unno (1956) derived a detailed solution to the RTE as it relates to the Stokes parameters as a vector description of line to continuum absorption coefficient. In general the RTE is written as:

$$\frac{d\mathbf{I}}{dz} = -\hat{\kappa}(\mathbf{I}(z) - \mathbf{S}(z)) \quad (3.8)$$

where  $\mathbf{I}$  is the Stokes vector  $\mathbf{I} = (I, Q, U, V)$  emerging from the solar atmosphere and  $\mathbf{S}(z)$  is the Plank function assuming local thermodynamic equilibrium (LTE). The matrix  $\hat{\kappa}$  is known as the absorption matrix, which describes both continuum and line contributions to absorption. Solutions to the RTE are tedious at best and oftentimes can only be solved numerically.

### 3.4.2. Polarimeters

A polarimeter is used to measure the polarization state of an incident beam of light. A polarimeter measures the direction of motion of  $\vec{E}$  and the phase

difference between each component (through  $a_x$  and  $a_y$ ). In practicality, this is done with two optical devices: a linear polarizer and a linear retarder. A linear polarizer is a device that transmits all of the light along a given direction, the optical axis, while reflecting or absorbing light along the perpendicular direction. For example, let the incident electric field be defined by  $\vec{E} = E_x \hat{i} + E_y \hat{j}$  and the linear polarizer has an optical axis rotated to an angle  $\theta$  with respect to the  $x$ -axis. The resultant electric field after the passing through the linear polarizer will be:

$$\vec{E}' = (E_x \cos \theta + E_y \sin \theta) \hat{\theta}; \quad (3.9)$$

illustrated in the top panel of Figure 3.5. A linear retarder introduces a phase lag,  $\delta$ , to one of the components of the incoming beam of light. The component retarded is called the slow axis, while the unperturbed axis is called the fast axis. In this case, the outgoing components of the electric field would be:  $E'_x = E_x$  and  $E'_y = E_y e^{i\delta}$  (see the bottom panel of Figure 3.5).

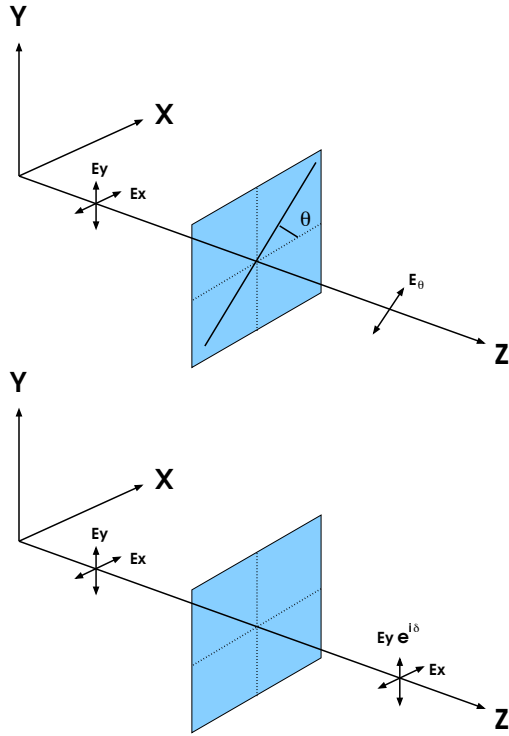


Figure 3.5 A theoretical description of an optical polarizer (top) and retarder (bottom) with an input source  $[E]$  (Santiago 2004).

After passing an incident light beam through both of the optical devices, we can measure the intensity of the resultant beam as a function of the rotation of the polarizer optical axis,  $\theta$ , and the phase shift in the slow axis of the retarder,  $\delta$ :

$$I_{mes}(\theta, \delta) = \langle E_{\theta}(\theta, \delta) E_{\theta}^*(\theta, \delta) \rangle. \quad (3.10)$$

After some manipulation, this allows us to write the Stokes parameters in terms of the measured intensity:

$$I = I_{mes}(0, 0) + I_{mes}\left(\frac{\pi}{2}, 0\right) \quad (3.11)$$

$$Q = I_{mes}(0, 0) - I_{mes}\left(\frac{\pi}{2}, 0\right) \quad (3.12)$$

$$U = I_{mes}\left(\frac{\pi}{4}, 0\right) - I_{mes}\left(\frac{3\pi}{4}, 0\right) \quad (3.13)$$

$$V = I_{mes}\left(\frac{\pi}{4}, \frac{\pi}{2}\right) - I_{mes}\left(\frac{3\pi}{4}, \frac{\pi}{2}\right) \quad (3.14)$$

(del Toro Iniesta, José Carlos 2003).

The Helioseismic and Magnetic Imager (HMI), and Michelson Doppler Imager (MDI) are both space-based instruments, while the Global Oscillation Network Group (GONG) is a series of ground-based telescopes at seven locations around the world; but in principle they all operate in essentially the same way to measure the Stokes parameters (as described above).

GONG is based upon an instrument similar to a Michelson interferometer called a Fourier Tachometer and is supported by a portable and automated installation which records a magnetogram every minute (Harvey et al. 1996). A 1.0 Å passband filter isolates the photospheric Ni I line at 6768 Å and images the Sun on a 1024 × 1024 pixel CCD with a spatial correlation of 2.5 arcsec per pixel. GONG's distributed approach to imaging achieves an 89% duty cycle.

MDI images the same Ni I line every 96 minutes on a 1024 × 1024 pixel CCD with a spatial mapping of 2 arcsec per pixel using a pair of tunable Michelson interferometers (Scherrer et al. 1995).

HMI has significantly higher spatial and temporal resolution than GONG or MDI. HMI uses a photospheric Fe I line at 6173.3 Å and images the Sun on a 4096 × 4096 pixel CCD with a spatial correlation of 0.6 arcsec per pixel (Scherrer et al. 2011). Images are recorded at a cadence of 45 seconds and have a 10 G precision. All images are pre-processed to a Level 1 state using a similar process as described for AIA (Section 3.3.1).

### 3.4.3. Potential Field Source Surface Model

Polarimeters measure magnetic fields exclusively in the photosphere because that is the only place in the solar atmosphere with adequate flux to measure polarization. To extrapolate the measured photospheric magnetic field [ $\mathbf{B}$ ] into the rest of the atmosphere, a model is needed. The simplest model is the Potential Field Source Surface (PFSS) which assumes a potential atmosphere that is current-free:

$$\nabla \times \mathbf{B} = 0. \quad (3.15)$$

Since

$$\mathbf{B} = \nabla\Phi, \quad (3.16)$$

where  $\Phi$  is the magnetic scalar field, the assumption of a potential atmosphere means that

$$\nabla^2\Phi = 0 \quad (3.17)$$

given that  $\nabla \cdot \mathbf{B} = 0$ . The problem for any model is to find the scalar potential  $[\Phi]$  that satisfies Equation 3.17 in a spherical geometry.

Schrijver & De Rosa (2003) developed an assimilation PFSS model to solve Equation 3.17 in a spherical volume between  $r = 1 R_{\odot}$  and  $r = 2.5 R_{\odot}$ .<sup>2</sup> The model derives a unique solution for a given domain and boundary conditions both the top ( $r = 2.5 R_{\odot}$ ) and bottom ( $r = 1 R_{\odot}$ ). At the upper boundary condition the field is assumed to be purely radial. The lower boundary condition field is derived from an evolving surface-flux transport model (Schrijver 2001). Synoptic magnetograms from MDI or HMI are used to anchor the model in the photosphere. The flux transport model then assimilates the photospheric field through the entire domain by advecting the flux stepwise vertically across the full solar surface. It empirically determines differential rotation, meridional flow, and convective dispersal profiles from the input data, using a non-linear algorithm to account for fragmentation and collision of flux. The result of the PFSS model is a 3D projection of the magnetic field in which field lines can be drawn. This model is limited to locations where the field is potential, which is most accurate in the quiet Sun and least in flaring regions where a significant current sheet is generated.

---

<sup>2</sup>DeRosa's PFSS model software package is available at [www.lmsal.com/~derosa/pfsspack/](http://www.lmsal.com/~derosa/pfsspack/)

## 4. INFORMATION PROCESSING IN SEARCH OF EPHEMERAL BRIGHTENINGS

*Through half-closed eyes, for the light would otherwise be overpowering, I consider the tree, the lonely cloud, the sandstone bedrock of this part of the world and pray – in my fashion – for a vision of the truth. I listen for signals from the sun – but the distant music is too high and pure for the human ear.*

– Edward Abbey (1988)

When viewing a sequential time series of images covering an erupting flare, several physical characteristics of the evolving ribbons are immediately apparent: the ribbons separate, brighten, and change their morphology. Along with the erupting flare, SCBs can be observed brightening and dimming in the vicinity of the ribbons. This section describes the techniques and methods used to extract quantities of interest such as location, velocity, and intensity of the flare ribbons and SCBs. Section 4.1 describes the technique used to identify and track bright kernels in a set of images. In this context, we are defining a kernel to be a small matrix of pixels that are associated with each other through increased intensity as compared with the immediately surrounding pixels. Each kernel has a local maximum, must be separated from another kernel by at least one pixel, and does not have any predetermined size or shape. Section 4.2 describes some of the image processing required to extract characteristics of flare kernels; Section 4.3 describes the technique for SCB kernels; and Section 4.4 summarizes the measured properties of each kernel.

### 4.1. Generalized Detection and Tracking

Before the kernel detection analysis is applied, each image is preprocessed (see Figure 4.1). Preprocessing of line-center  $H\alpha$  images begins by removing limb darkening from the calibrated full-disk ISOON image. This is accomplished by subtracting a standard limb-darkening profile determined by the spherical geometry of the solar surface (Hestroffer & Magnan 1998; Neckel & Labs 1994). The images are then de-projected into conformal coordinates using a Guyou projection (an oblique aspect of the Peirce projection, Peirce 1879), which removes the projection effects of imaging the solar sphere. As a consequence, latitudes above 85 degrees North or South are significantly distorted and are cropped. In this cylindrical projection, the entire solar limb is distorted. Any region of interest at the limb is significantly distorted as well, leading to added noise in the analysis. The de-projected image is then normalized to the mean background level of the quiet Sun so that any flare brightening is comparable between images. Next, the full-disk de-projected image is cropped down to isolate the flaring region (Figure 4.2). The flaring regions in each image are aligned using a cross-correlation algorithm. This eliminates the rotation effects of the Sun so the flare can be observed as if it were stationary on the solar surface.

An algorithm to de-stretch each image is applied to the image cube to co-align subsections of the image. The mean displacement of any given subsection due to de-stretching over time is nearly zero. A net zero displacement implies the algorithm is not removing any proper motion observed in the time series. A discussion of the methodology behind the de-stretching algorithm can be found in November & Simon (1988). The entire image preprocessing of a flare is automated up to this point, given a library of ISOON images and the coordinates of the active region that is of interest. The last step in preprocessing is removing bad frames. Images that contain peculiar observations due to clouds or other factors are discarded interactively.

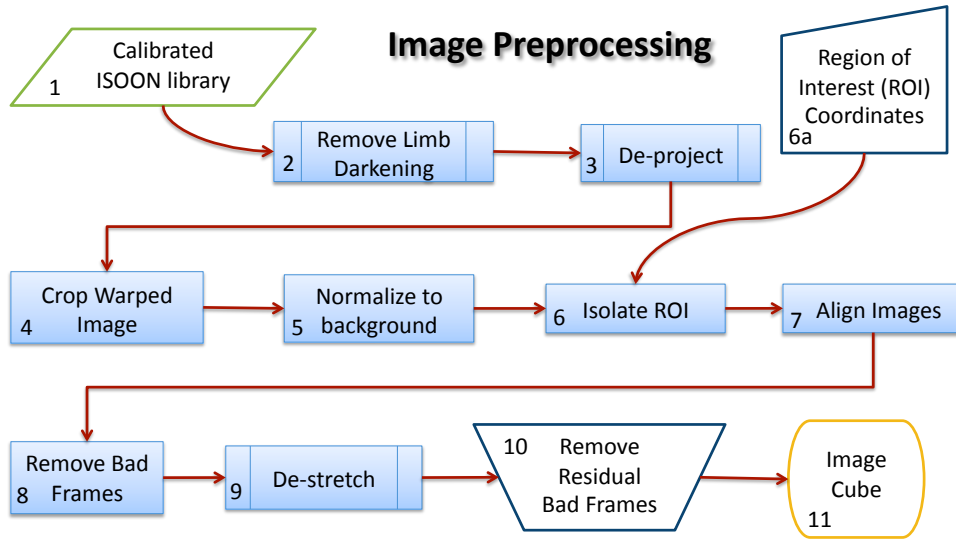


Fig. 4.1.— A flowchart detailing the preprocessing method in preparation for analysis. The green parallelogram represents the database input. Blue trapezoids indicate a feature specific quality that must be manually determined and input. The blue shaded rectangles are individual routines.

## Image Preprocessing

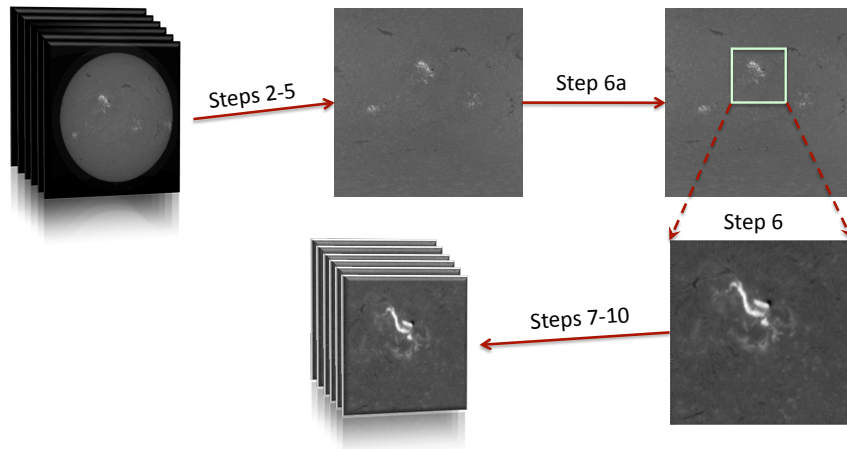


Fig. 4.2.— Images representing each of the preprocessing steps outlined in Figure 4.1.

The algorithm developed to identify, track and extract physical quantities in the ISOON dataset does so in seven logical steps: thresholding, feature isolation, feature enhancement, locating the position of candidate kernels, eliminating “false” kernels, linking time-resolved kernels together into trajectories, and extracting physical quantities by overlaying the trajectories over other datasets (numbers 3 – 9 in Figure 4.3). To aid in this detection, tracking software developed by Crocker, Grier and Weeks (Crocker 1996) was used as a foundation and modified to fit the needs of this project<sup>1</sup>.

---

<sup>1</sup>Crocker’s software is available online at [www.physics.emory.edu/~weeks/idl/](http://www.physics.emory.edu/~weeks/idl/)

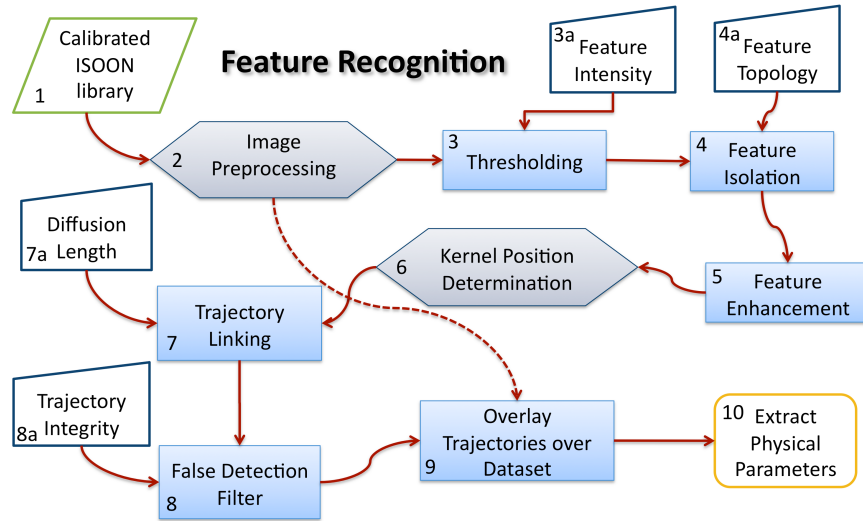


Fig. 4.3.— A flowchart detailing the process in which flare ribbons and SCBs are identified and their physical parameters measured. The green parallelogram represents the database input. Blue trapezoids indicate a feature specific quality that must be determined and input. The gray diamonds are processes that have been defined by a collection of subroutines and are detailed in other flowcharts. The blue shaded rectangles are individual routines.

Analysis begins with thresholding the preprocessed  $H\alpha$  images. A threshold is taken of the background-normalized images, eliminating any features that are dimmer than a specified intensity. Because the mean intensity of the flare ribbons is significantly brighter than SCBs, the specific thresholding level is different for each feature extraction. Section 4.2 describes the process for flares and Section 4.3 for SCBs.

Next, to isolate features a spatial bandpass filter is applied to suppress pixel noise with a characteristic length scale of a pixel. A pixel with a value much different from its neighbors is considered as having high spatial frequency. Using the average of a small local region in the image suppresses large jumps in intensity and is equivalent to low-pass filtering in the spatial frequency domain. Noise reduction is necessary to remove the smallest changes in brightening while preserving the general structure of the images. Selecting the length scale for the bandpass filter requires prior knowledge of the features' characteristics. With ISOON images, flare ribbons appear as  $\approx 10$  pixels wide and  $\approx 100$  pixels long – significantly larger than the bandpass filter. SCBs appear characteristically smaller in ISOON images with diameters of a few (3 – 8) pixels. The noise filter eliminates some of the smallest SCBs but is a worthwhile tradeoff for reduced noise levels.

The process of feature enhancement differs between flare ribbons and SCBs. In either case, it is a process of folding a processed image back into the original to enhance either the flare ribbon or the SCB. Section 4.2 describes the process for flare tracking and Section 4.3 for SCB tracking.

#### 4.1.1. General Kernel Position Determination

Determining the location of kernels is an iterative process. A flowchart corresponding to this process is described in Figure 4.4. The process begins by identifying local intensity maxima within the enhanced image,  $\mathcal{I}'$ , as candidate kernels. Figure 4.5 diagrams a hypothetical kernel. A pixel is considered a candidate centroid of a kernel if a brighter pixel does not exist within a radius of  $\omega$  pixels of the candidate. In general,  $\omega$  is the characteristic radius of the kernel the algorithm is looking for. We require an  $\omega$  to maximize the number of detections along a flare ribbon as well as the number of frames in which a detection could be tracked. Without specific knowledge of what size a flare kernel or SCB kernel could be,  $\omega$  is iterated until both of the conditions are met. A mask with an 8 pixel radius ( $\omega = 8$ ) was found to maximize the number of detection regions and reduce the number of untraceable kernels.

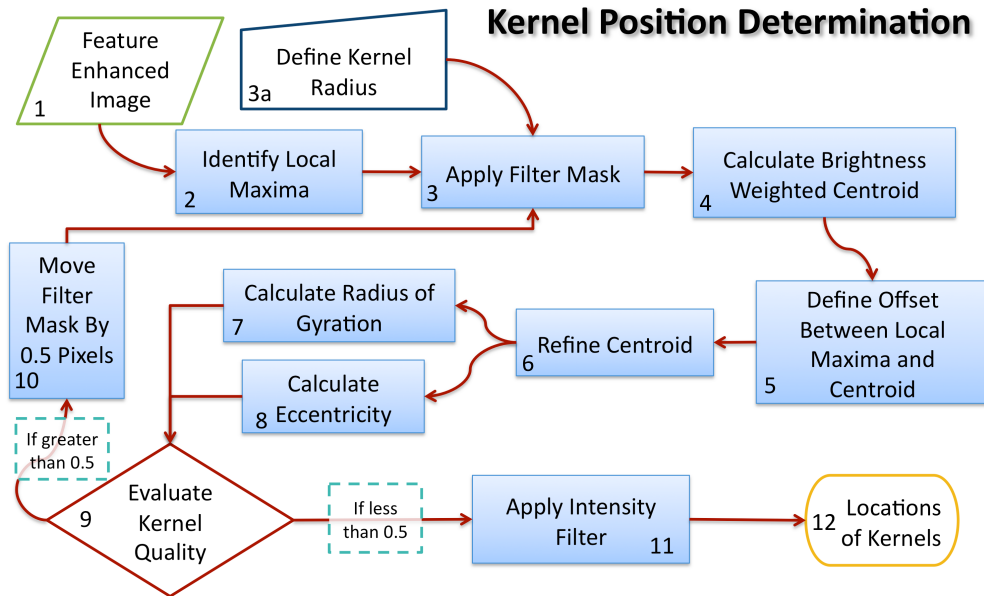


Fig. 4.4.— A flowchart detailing the process in which flare and SCB kernels are identified. The green parallelogram represents the database input. Blue trapezoids indicate a feature specific quality that must be determined and input. The red diamond is a process that has a conditional result and the blue shaded rectangles are individual routines.

Next, the brightness-weighted centroid of pixels,  $(\mathbf{x}, \mathbf{y})$ , for each candidate kernel is calculated with the local maxima having pixel coordinates  $(\bar{x}, \bar{y})$  and intensity  $\mathcal{A}(\bar{x}, \bar{y})$ :

$$\begin{pmatrix} \mathbf{x} \\ \mathbf{y} \end{pmatrix} = \frac{1}{m_0} \sum_{i^2+j^2 \leq \omega^2} \begin{pmatrix} \bar{x} \\ \bar{y} \end{pmatrix} \mathcal{A}(\bar{x} + i, \bar{y} + j). \quad (4.1)$$

$m_0$  is the integrated intensity of the candidate kernel:

$$m_0 = \sum_{i^2+j^2 \leq \omega^2} \mathcal{A}(\bar{x} + i, \bar{y} + j) \quad (4.2)$$

and  $\omega$  is the radius of the mask which was defined above (Crocker 1996). Improper background subtraction can bias the centroid toward the center of the mask and away from the kernel's brightness center by adding weight to pixels that are not part of the features being identified.

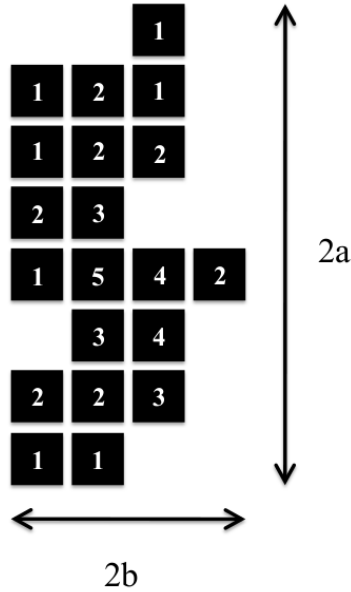


Figure 4.5 A diagram of a hypothetical kernel (either flare or SCB) used for classifications in this paper. Each pixel is labeled with a representative intensity  $[\mathcal{A}_i]$ . The semi-major axis  $[a]$  and semi-minor axis  $[b]$  are shown. This kernel has the following properties: total intensity,  $m_0 = 43$ , semi-major axis,  $a = 4$ , semi-minor axis,  $b = 2$ , eccentricity,  $e = 0.87$ , centroid,  $(x, y) = (0.26, 0.18)$ , and radius of gyration,  $R_g = 1.9$ . The maximum intensity, in this case 5, is defined as having pixel coordinates  $(0, 0)$ .

An offset between the brightness weighted centroid and the local maxima is then defined by subtracting the position of the brightness centroid from the position of the local intensity maximum:

$$\begin{pmatrix} \epsilon_x \\ \epsilon_y \end{pmatrix} = \begin{pmatrix} \bar{x} \\ \bar{y} \end{pmatrix} - \begin{pmatrix} \mathbf{x} \\ \mathbf{y} \end{pmatrix}. \quad (4.3)$$

Next, a refined centroid of the candidate kernel is calculated by:

$$(x', y') = \left( \bar{x} + \frac{\epsilon_x}{2}, \bar{y} + \frac{\epsilon_y}{2} \right). \quad (4.4)$$

This refined centroid is located halfway between the local intensity maximum and the brightness-weighted centroid.

To evaluate the quality of the candidate kernel, the discrepancy between the local maximum and centroid is examined. If either  $|\epsilon_x|$  or  $|\epsilon_y|$  (the offset as described by Equation 4.3) is greater than 0.5 pixels from the local maximum,

the filtering mask is shifted by 0.5 pixels in the direction of  $(\epsilon_x, \epsilon_y)$  and the new kernel is characterized. This iteration has the effect of guaranteeing that the local maximum and the centroid of the kernel are within half a pixel of each other.

To characterize the size of the kernel, the radius is measured to be the radius of gyration. A radius of gyration  $[R_g]$  is related to the moment of inertia  $[I]$  by using:

$$I = \sum_k m_k r_k^2 = m R_g^2, \quad (4.5)$$

$$r = (a + b)/2, \quad (4.6)$$

where  $m_k$  is the mass of particle  $k$ ,  $m$  is the total mass of the system, and  $r$  is the distance to the rotation axis. In this context, we interpret the radius of gyration to be

$$R_g^2 = \sum_k \frac{\mathcal{A}_k r_k^2}{m} \quad (4.7)$$

where  $m$  is the integrated intensity as defined in Equation 4.2 (Crocker 1996). See Figure 4.5 for a pictorial description.

The final step in determining the kernel's position is to eliminate unwanted kernel detections or "false kernels." A threshold is applied to the integrated intensity of each candidate kernel. This intensity filter is intended to eliminate large, dim detections that may have a local maximum but are not part of the features in which we are interested. The threshold for this filter was determined empirically to eliminate marginal detections while retaining the bulk of the detections. Each detection now has position  $(x'_i, y'_i)$  and an integrated intensity  $m_{0,i}$  to characterize the kernel. The results of this detection process can be seen in the lower panels of Figure 4.6. The total number of flare kernels detected in an image is typically between 100 – 400, while the number of SCB kernels detected is typically three to four times that number.

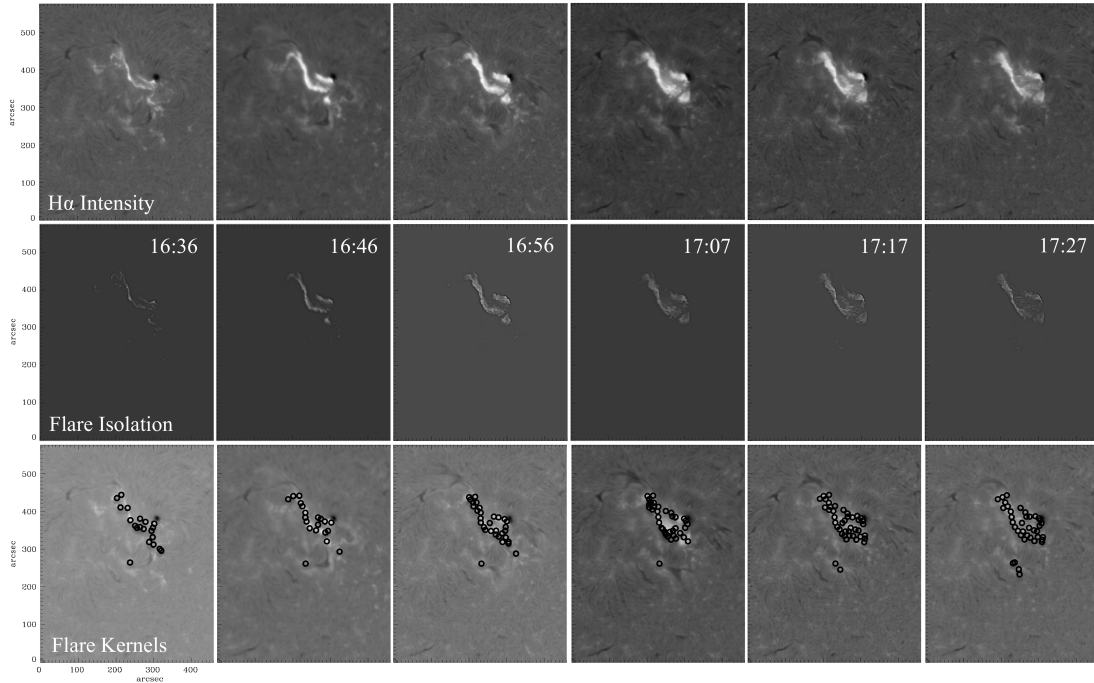


Fig. 4.6.— Time series of images showing the evolution of the flare ribbons for the 2005 May 13 event. Each image shows the same flaring region ten minutes after the previous image. The flare peak occurs at 16:49 UT. The top row of images show the  $H\alpha$  line-center intensity. The second row of images show the flare after the ribbon isolation and enhancement as described in Section 4.2. The third row of images show the detected flare kernels after the image analysis algorithm is applied. The centroid of each flare kernel is marked by a black circle. Notice how the number of kernels changes as the flare ribbon evolves. A comparison of the first and third row of images show the coverage of detections along the flare ribbons.

#### 4.1.2. General Trajectory Linking

After the positions of all kernels within the series of images have been located, the next step is to associate kernels between frames to form trajectories. Frames recorded by ISOON are spaced one minute apart, but the following process is generalized for any series of images regularly spaced in time. This presents a problem in determining which kernel in image  $\mathcal{I}'_{n+1}$  is most likely to correspond to a given kernel in the preceding image,  $\mathcal{I}'_n$ . It is complicated by the number of particles that are being tracked simultaneously. We simplify the problem by requiring that each kernel be identified with at most one kernel in the previous image. Since kernels are nominally indistinguishable from each other, a pair of kernels' physical proximity between frames is a reasonable way to establish a correlation between the two. The following algorithm for trajectory linking is

motivated by the dynamics of noninteracting Brownian particles (see Crocker 1996, for a more complete discussion).

The probability that a single particle with Brownian motion will diffuse a distance  $\delta$  in time  $\tau$  is

$$P(\delta|\tau) = \frac{1}{4\pi\mathcal{D}\tau} \exp\left(-\frac{\delta^2}{4\mathcal{D}\tau}\right) \quad (4.8)$$

where  $\mathcal{D}$  is the self-diffusion coefficient of each particle (Crocker 1996). For a system of  $N$  noninteracting particles, the diffusion probability distribution is the product of the distribution for each single particle:

$$P(\{\delta_i\}|\tau) = \left(\frac{1}{4\pi\mathcal{D}\tau}\right)^N \exp\left(-\sum_{i=1}^N \frac{\delta_i^2}{4\mathcal{D}\tau}\right). \quad (4.9)$$

Thus the best assignment of trajectories is one that maximizes  $P(\{\delta_i\}|\tau)$  or minimizes  $\sum \delta_i^2$  (Crocker 1996). While merging or converging kernels result in a loss of tracking memory, we are able to visually discern any such occurrences by animating the trajectories.

Calculating  $P(\{\delta_i\}|\tau)$  for every possible combination of trajectories would require  $O(N!)$  computations, which is unfeasible and not necessary in this case. We know that a flare or SCB is going to stay fairly localized and not jump sporadically from one location to another. Thus we can define a characteristic diffusion length  $L$  to be the maximum distance a kernel can travel between frames. This diffusion length is different between flares and SCBs. (See Sections 4.2 and 4.3 for the specific differences.) With a small enough diffusion length, most kernels have only one possible association between two frames.

If the number of kernels remained constant throughout the series of images, then associating trajectories would be trivial. Unfortunately this is not the case at all, since we are interested in tracking the flare from its inception through decay. To account for a kernel disappearing and reappearing, “missing” links are assigned to a kernel that does not have a counterpart in the next frame. A diffusion distance of  $\delta = L$  is assigned for the purposes of calculating  $P(\{\delta_i\}|\tau)$ . The last known location of a “missing” particle is retained for a predetermined number of frames. That number of frames is different for flares and SCBs. (See Sections 4.2 and 4.3 for the specific differences.)

Linking detections into trajectories is only possible if the diffusion distance  $\delta$  is significantly smaller than the typical spacing between kernels  $a$ . If  $\delta$  is greater than  $\approx \frac{a}{2}$  then trajectories are inextricably confused between images. This property of confusion provides an upper bound for kernel motion, which provides insights into physical properties (see Chapter 5).

Linking the initial kernel detections into trajectories provides another opportunity to filter out inconsistent or unsustainable detections. A kernel lasting only one or two frames is a weak detection and can be filtered out. A temporal trajectory filter eliminates fleeting bright points that appear in a few frames but are

not associated with the features being tracked. The specifics of this filter appears in Sections 4.2 and 4.3.

The last step in the kernel identification and tracking algorithm is to extract physical properties from the data. To accomplish this extraction, the locations and parameters of the kernel trajectories are placed over the preprocessed dataset. Since the original  $H\alpha$  images were modified to aid in the detection process in thresholding and feature enhancement, the tracked kernels are placed over the un-enhanced  $H\alpha$  images to extract the intensity underneath the each kernel.

## 4.2. Flare Ribbon Extraction

Within the general feature detection and tracking framework presented above and outlined in Figure 4.3, there are several situations where the algorithm is customized to the features that it is trying to extract. This subsection will explain the specifics for extracting flare ribbons from the  $H\alpha$  data set.

The first flare-specific customization is applying a threshold level of 1.35 to the preprocessed images, where quiet Sun disk center intensity is set to unity. This eliminates any features that are approximately less than one standard deviation above background intensity. This corresponds to keeping features with a 35% increase in brightening over the background intensity, and since all images are normalized to their background intensity, the threshold value holds true for any ISOON data set.

Next, the flare ribbons are isolated and enhanced. To isolate flare ribbons, a Laplacian operator is applied to the thresholded images. In this application, the Laplacian operator acts as an edge enhancement algorithm, making smooth transitions on the image disappear while rapid changes in intensity stand out. The images operated upon are then added back into the original image,

$$\mathcal{I}' = \mathcal{I} + \nabla^2 \mathcal{I}, \quad (4.10)$$

where  $\mathcal{I}$  is the image after thresholding and the bandpass filter, and  $\mathcal{I}'$  is the resultant image used for the detection of flare kernels (Figure 4.6). By adding the Laplacian image back to the original, the edges and peaks in the flare ribbons are enhanced, while the physical dimensions of the active regions stay the same.

When linking flare kernels into trajectories, we define a characteristic diffusion length  $L$  as the maximum distance a kernel can travel between frames. For flare kernels,  $L = 4$  pixels. This diffusion length was empirically found to be the maximum distance a flare kernel could travel, to minimize the confusion of tags when associating kernels between images. The typical spacing between flare kernels,  $a$ , is approximately 8 pixels, thus  $L \approx \frac{a}{2}$ .

Last, a filter is applied to remove unwanted trajectories by evaluating their temporal integrity. The previous 40 frames are considered when linking flare kernels into trajectories. This means that a kernel can go “missing” for 40 images and be associated together. Using the fact that flare ribbons are relatively long-lived phenomena, lasting more than an hour, a filter is applied to eliminate short-lived detections. Any trajectories that last less than 20 frames are eliminated.

This filter eliminates several off-ribbon detections which are associated with the eruption but do not characterize the evolution of the flare ribbons.

### 4.3. Compact Ephemeral Brightenings

SCB detections are completely eliminated in the flare detection and tracking process. A separate process is required to extract SCB kernels and characterize this different type of brightening that occurs during a flare eruption. This subsection details the customizations to the detection algorithm needed to extract SCBs.

To expose the SCBs from the original background normalized images, a threshold of 1.2 is taken. This threshold eliminates all features except where intensities greater than 20% above background level. The SCB threshold level is 15% dimmer than what was used for flare ribbons.

To isolate the SCB features in a series of  $H\alpha$  images, a running difference image series is created. In general, a running difference image series eliminates long-lived features while enhancing rapidly changing intensities. In this case, a binary image is created which collapses all non-zero pixel values to 1. The binary image is necessary to force all brightening above the threshold to a uniform value and includes both SCBs as well as the associated flare ribbons. Next, a median image cube is created by taking a series of 11 frames and creating one image in which each pixel is the median of the corresponding pixels in the series of images. The running difference image is then calculated by subtracting the median image from the current binary image,

$$\mathcal{I}'_n = \mathcal{I}_n - \tilde{\mathcal{I}}_{n-11:n-1}, \quad (4.11)$$

where  $\mathcal{I}$  is the binary image and  $\mathcal{I}'$  is the running difference image. As the running difference window is increased from one image to 40, the number of detections reaches a maximum and then decays with a longer window. The 11 minute duration of the running difference image was empirically determined to best maximize the number of SCBs detected over the three training cases examined. The results of this process expose the locations of the SCBs while filtering out the longer-lived flare ribbons (Figure 4.7).

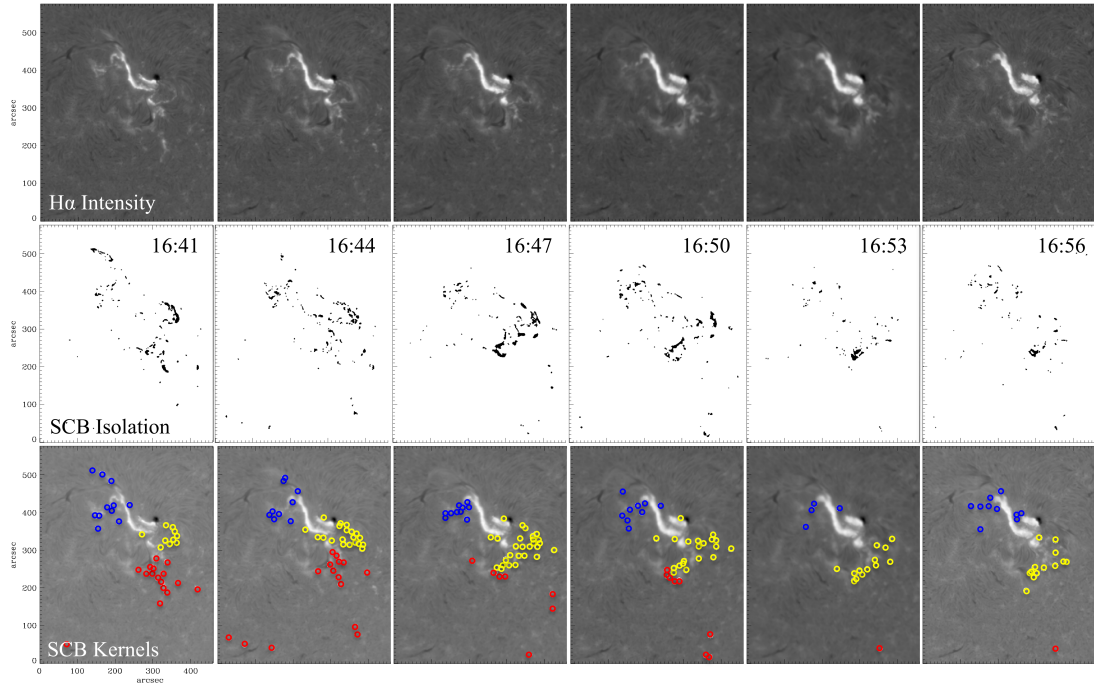


Fig. 4.7.— Time series of images showing the evolution of the SCBs for the 2005 May 13 event. Each image shows the same flaring region three minutes after the previous image. The flare peak occurs at 16:49 UT. The top row of images show the  $H\alpha$  line-center intensity (same as the top row of Figure 4.6). The second row of images show a binary image of the same flaring region after applying the SCB isolation as described in Section 4.3. The third row of images show the detected SCB kernels after the image-analysis algorithm is applied. Identified SCBs are visually separated into three groups to demonstrate how they appear to move when watching an animation of the flare. The red group propagates quickly while the blue and yellow groups develop more slowly. Notice how the number of kernels peaks before the flare peak and rapidly declines as compared to the flare kernels.

The isolated SCBs are then enhanced through a morphological transform. The transform performs an erosion operation followed by a dilation operation using a diamond-shaped operating kernel with a 3-pixel diameter. This transform has the effect of removing small regions of noise in the running difference image while preserving the size and shape of the features in the image.

Using the binary running difference images, the SCB's local maxima are identified as outlined in Section 4.1.1. However, since the images being analyzed are binary images, the local maximum is coincident with the centroid of the bright points within the mask, which significantly decreases processing time. The kernels are then run through the trajectory linking algorithm with a diffusion length  $L = 10$ . This diffusion length allows the centroid of the SCB kernel to move no more than 10 pixels between frames.

When correlating SCB kernels between frames into trajectories, only the previous image is searched. A temporal filter is also applied to the trajectories, requiring at least two frames. What remains are kernels that last at least two minutes and do not “go missing” at any time. Last, a spatial filter is applied to eliminate any SCB kernels that are identified as within the “flaring region.” This region is defined by co-adding 80 of the thresholded images used in the identification of flare kernels centered around the peak of the flare intensity. All non-zero pixels are flagged as the “flaring region.” The spatial filter guarantees that any SCB kernels that are detected are not associated with the flare ribbons. The resulting detections are shown in Figure 4.7.

#### 4.4. Creation of Metadata

The application of the algorithms described in the previous sections results in a large amount of information about the solar event dissected. These descriptive metrics of the event are collectively called metadata. Metadata in this context refers to the *content about the event* (as opposed to *data about the data container*, e.g., size of file, compression, and location). This concept is useful for describing how one event is distinct from a library of events and further characterizing patterns in the entire library. The use of metadata efficiently reduces the amount of data needed to describe an event by several orders of magnitude. In this project, the size of the image-data is more than four orders of magnitude greater than the metadata.

Specifically, a systematic set of metadata is generated by the application of the automated detection and tracking routines. Table 4.1 lists this set generated in each flare event. Not all of the metrics apply to every characteristic in each image. Also not all metadata are generated in the same way; some are measured, some are derived, and some are assigned. Thus, Table 4.1 also lists the applicable features that each metadata tag applies to and the method by which it is generated.

Generating metadata is not only useful for efficient cataloguing of flares, but it is also immensely useful in understanding the complex physical processes driving solar eruptions. Humans are arguably better than computers at recognizing visual patterns but have shortcomings in consistently observing objectively. Characterizing a solar eruption using metadata products can literally and figuratively change the way in which scientists see flares. For example, flares are typically observed in four dimensions: two spatial dimensions, intensity, and time. Using metadata products enables us to visualize events as they evolve in other measured dimensions such as feature velocity,  $H\alpha$  intensity, coronal intensity, and time. Of course, some sets of measurements are products of the same physical process, while some are truly independent of each other. Because the measurements are consistent between events, patterns and consistencies in metadata are illustrative of the physics driving the eruptive event.

Table 4.1. Metadata generated from applying automated detection and tracking algorithms, the applicable features, and method of generation.

Data Product	Feature	Method
Flare Center	All Events	Derived
Pixel Coordinates	All Kernels	Direct Measurement
H $\alpha$ Intensity	All Kernels	Direct Measurement
Relative H $\alpha$ Intensity	All Kernels	Direct Measurement
Photospheric Intensity	All Kernels	Direct Measurement
Coronal Intensity	All Kernels	Direct Measurement
Eccentricity	All Kernels	Direct Measurement
Time	All Kernels	Direct Measurement
Particle ID	All Kernels	Assigned
Radius of Gyration	All Kernels	Derived
Heliographic Coordinates	All Kernels	Derived
Group ID	Flare Kernels	Derived
Instantaneous Velocity	Flare Kernels	Derived
Doppler Velocity	SCB Kernels	Direct Measurement
Magnetic Polarity	SCB Kernels	Direct Measurement
PFSS Field Line	SCB Kernels	Derived
Duration	SCB Kernels	Derived
Distance from Center	SCB Kernels	Derived

## 5. MEASUREMENTS AND MOTION IN FLARING SYSTEMS

*Like a life without music, art or literature, a life without science is bereft of something that gives experience a rich and otherwise inaccessible dimension.*

– Brian Greene (2008)

We chose to demonstrate the brightening detection and tracking algorithm suite outlined in the previous chapter by applying it to eleven different events (Table 5.1). A variety of eruptive events were chosen to demonstrate the versatility as well as the limitations of the detection code. Six of the eleven events were previously studied by Balasubramaniam et al. (2006), while the remaining five are new in this study.

Nine events had flares associated with them, ranging in X-ray intensity from B6.6 to X10. All of the events selected except two had a two-ribbon configuration and an associated halo CME. One of the events that had no CME was a compact M1.8 flare (2003-06-11), while the other had no flare associated (2003-03-06). The 2006 December 6 event had an associated Moreton wave previously characterized by Balasubramaniam et al. (2010).

Data from several different sources were utilized for each event: ISOON (both  $H\alpha$  line center and Doppler), LASCO (C2), GOES, GONG (magnetograms), RHESSI, AIA, and HMI (magnetograms). Table 5.1 details which data sources were utilized in each case. Data covering the entire flaring event both spatially and temporally were extracted. This yielded data cubes with 250 – 1600 images, depending on the data source and duration of the event. The region of interest (ROI) extracted was also dependent on the physical size of the event. The ROI's ranged from  $3.2 \times 10^5$  arcsec<sup>2</sup> in the 2010 November 30 event to  $2.0 \times 10^6$  arcsec<sup>2</sup> in the 2003 December 29 event.

An animated series of images of the ROIs reveals several well known physical characteristics of evolving ribbons: the ribbons separate, brighten, and change their morphology. In most of the events examined, SCBs can be observed brightening and dimming in the region adjacent to the ribbons. The 30 November 2010 event was a significantly different type of event. This event was identified as a Hyder Flare and had a CME associated with the eruption but no X-ray emission to identify it as a typical flare. For this reason, the 30 November 2010 event is treated separately in Section 5.3. The derived properties of flare ribbons are discussed in Section 5.1, followed by a discussion of the measured properties of SCBs in Section 5.2.

### 5.1. Properties of Flare Ribbons

In the detection algorithm, we define a characteristic diffusion length [ $L$ ] for flare kernels to maximize the length of trajectories formed while minimizing confusion between kernel tags (see Chapter 4). This parameter [ $L$ ] corresponds to

the maximum distance a kernel can travel between frames. A parameter of  $L = 4$  pixels is found to be the best diffusion length for flare kernels. Thus, the maximum physical distance that a flare kernel can travel between frames translates to 3200 km. Since  $L \approx a/2$ , where  $a$  is the characteristic distance between kernels, the diameter of the smallest resolvable kernel along the flare ribbon is approximately 6400 km with the ISOON dataset (Table 5.2).

After flare kernels are associated between frames into trajectories, the temporal integrity of flare kernels can be exposed. Flare kernels are temporally fairly robust, lasting on average  $\approx 120$  minutes each (Figure 5.1). Generally, large flares take a few hours to evolve from the impulsive phase, through peak intensity, and return to pre-flare brightness. Also, the number of detectable kernels declines as the flare’s intensity decays from its peak, implying that there are fewer resolvable components in the flare ribbons as the flare evolves. This change in detectable kernels means that the majority of kernels cannot be tracked from pre-flare to post-flare, suggesting a dynamic substructure to the flare ribbons when bright points appear and disappear as the flare erupts.

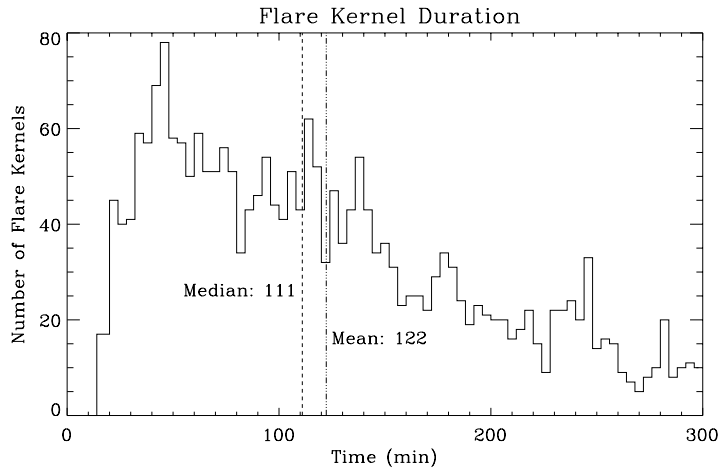


Fig. 5.1.— A histogram of the continuance of detected flare kernels in all 11 events. Flare kernels are tracked for a mean duration of 122 minutes (dot-dashed line) and a median duration of 111 minutes (dashed line).

Because flare kernels do not last for the entirety of the flare, individual kernels are not a good indication of overall flare behavior. However when taken in aggregate, flare kernels reproduce the overall topology of the flare. Figure 5.2 shows the intensities of all of the tracked flare kernels, plotted as points as a function of time in the 2005 May 13 event. Integrating these intensities over each time step yields an aggregate intensity curve that reproduces the GOES X-ray flare intensity curve shown in Figure 5.10. The aggregate flare intensity curves as compared to the associated GOES X-ray intensity for all the studied events can be seen in Figures 5.3 – 5.13.

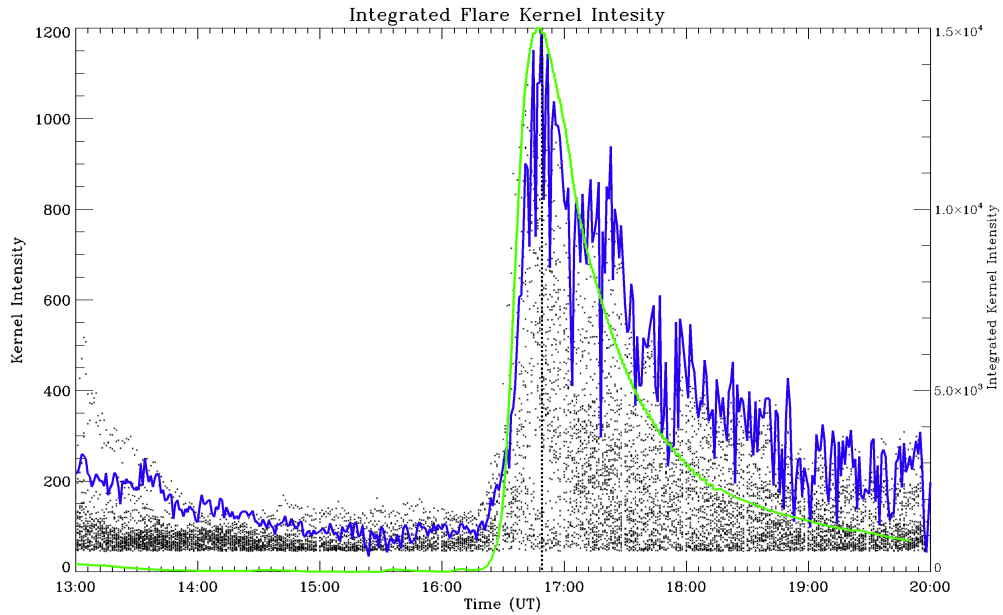


Fig. 5.2.— The 2005 May 13 measured intensities of each flare kernel plotted as points as a function of time. The solid-blue line is the integrated kernel intensities at each time step. Overlaid for comparison in green is the normalized GOES 1.0 – 8.0 Å intensity curve. The vertical dashed line indicates the peak intensity of the H $\alpha$  flare curve. The integrated flare kernels reproduce the shape of the flare curve determined by other methods.

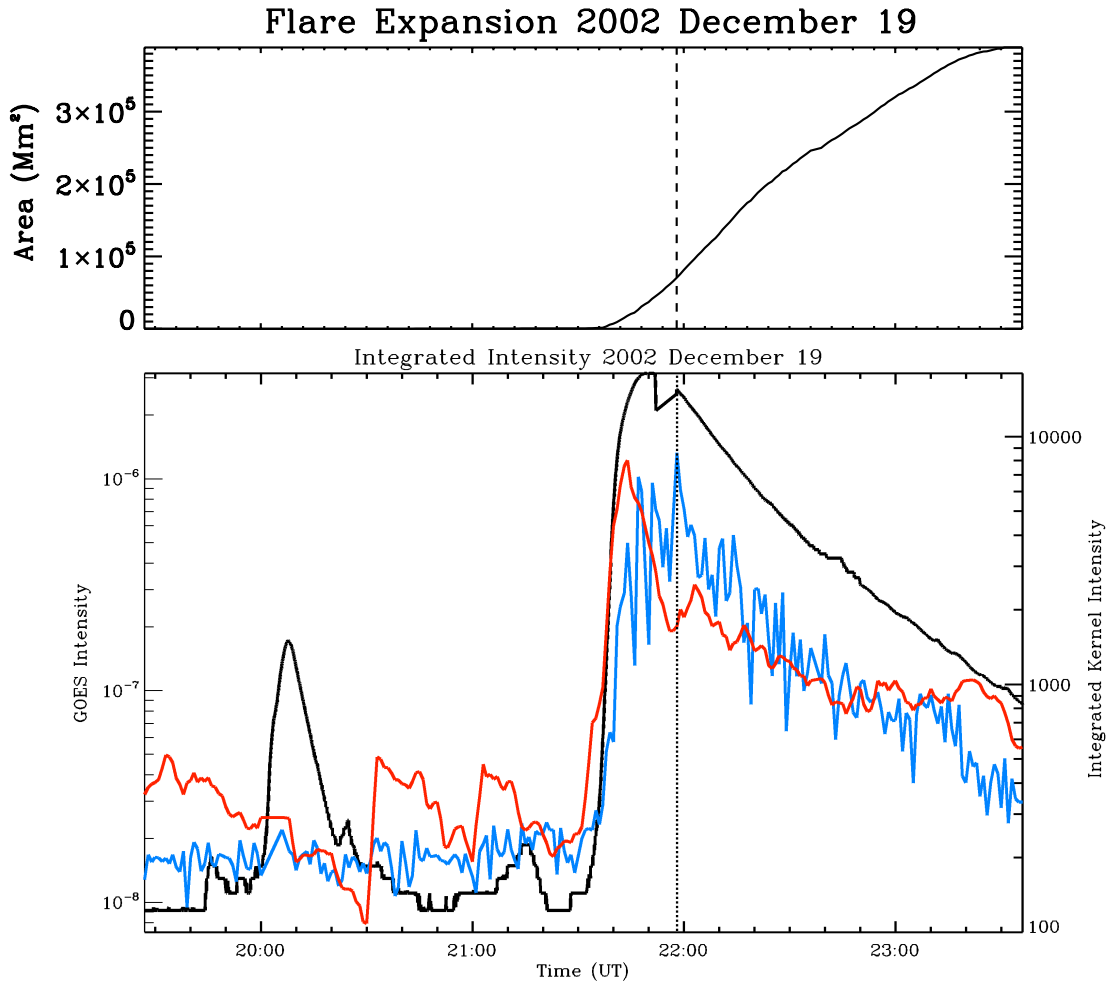


Fig. 5.3.— Time evolution of the 2002 December 19 event. The dashed line in both panels mark the peak flare intensity. Top: the flare area over time as defined by Equation 5.4. Bottom: The blue line is the integrated  $H\alpha$  flare kernel intensities at each time step. The red line is the integrated SCB kernel intensities at each time step. Plotted for reference in black is the GOES 1.0 – 8.0 Å intensity curve.

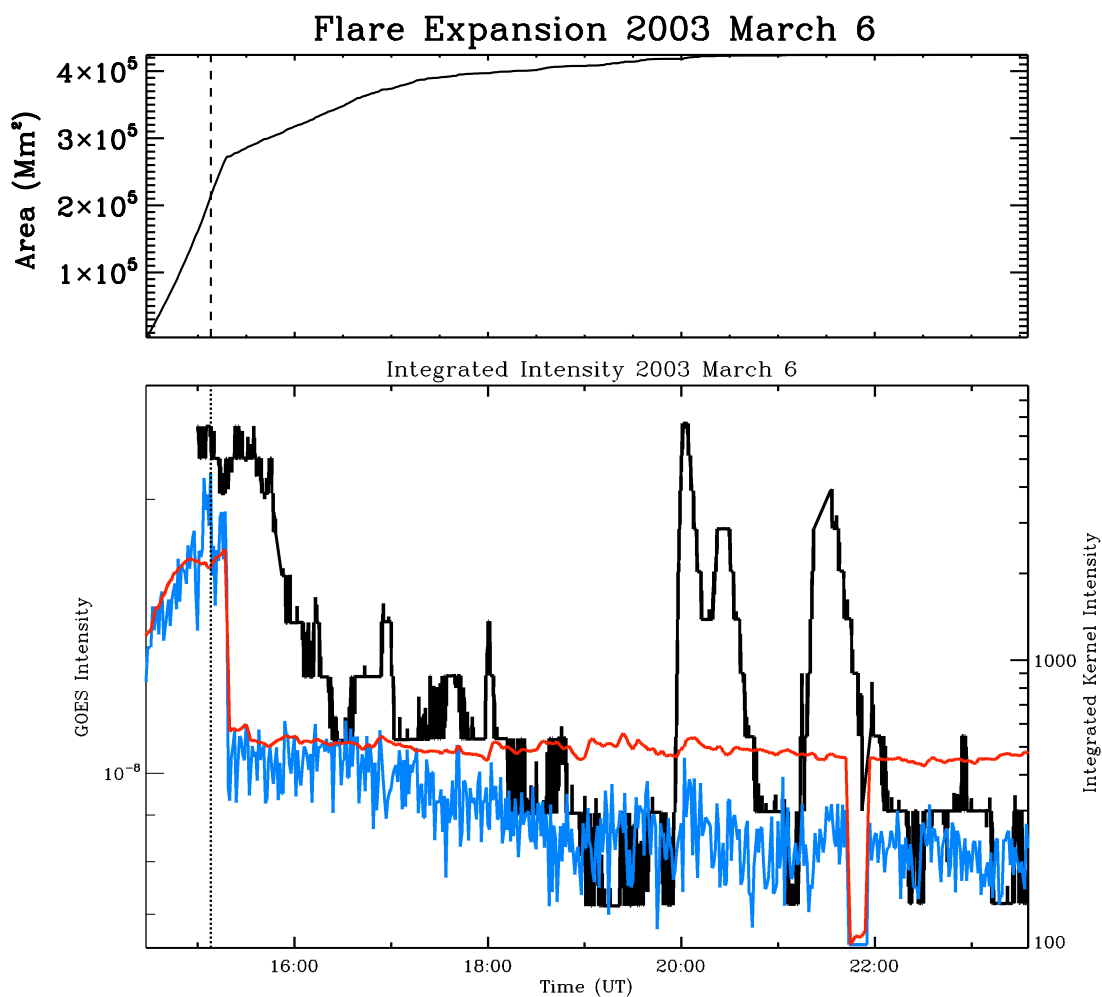


Fig. 5.4.— Time evolution of the 2003 March 6 event. The dashed line in both panels mark the peak flare intensity. Top: the flare area over time as defined by Equation 5.4. Bottom: The blue line is the integrated  $H\alpha$  flare kernel intensities at each time step. The red line is the integrated SCB kernel intensities at each time step. Plotted for reference in black is the GOES 1.0 – 8.0  $\text{\AA}$  intensity curve.

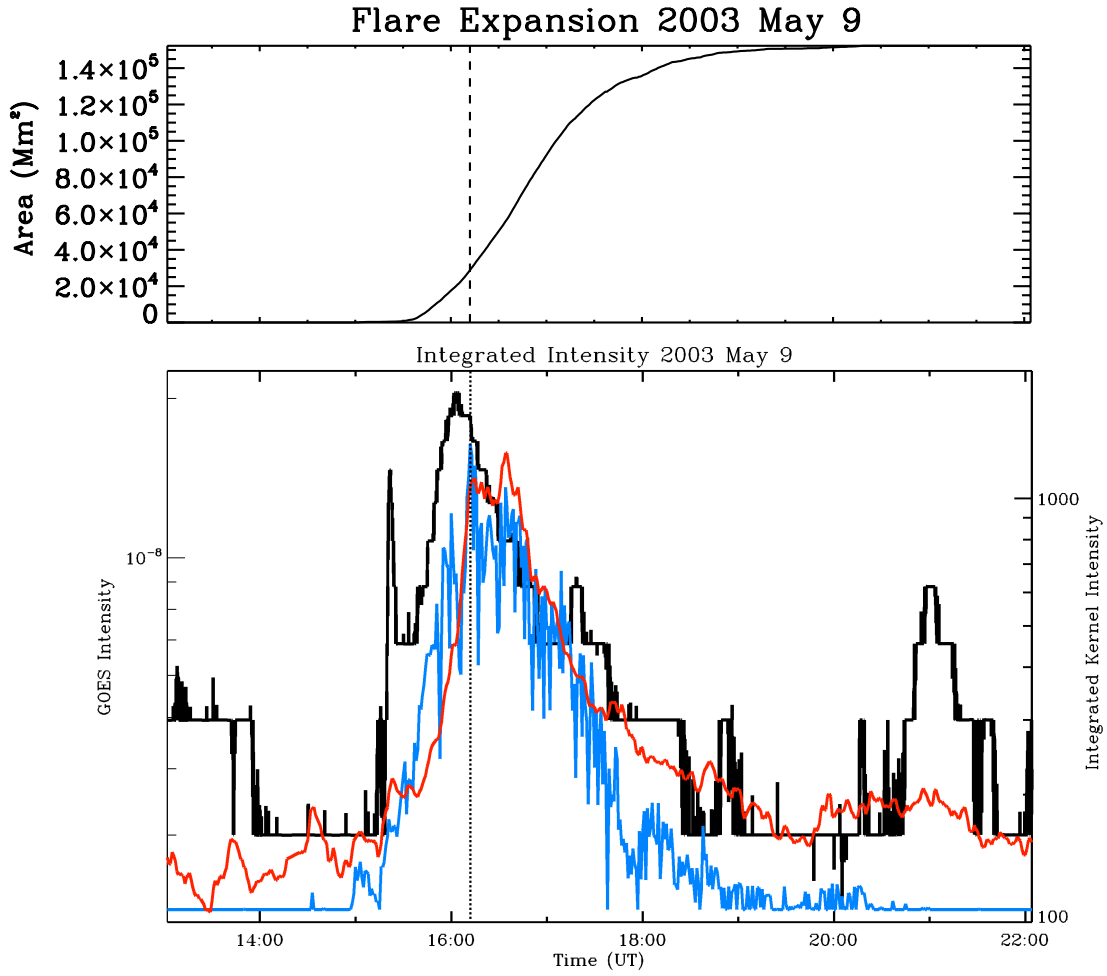


Fig. 5.5.— Time evolution of the 2003 May 9 event. The dashed line in both panels mark the peak flare intensity. Top: the flare area over time as defined by Equation 5.4. Bottom: The blue line is the integrated  $\text{H}\alpha$  flare kernel intensities at each time step. The red line is the integrated SCB kernel intensities at each time step. Plotted for reference in black is the GOES 1.0 – 8.0  $\text{\AA}$  intensity curve.

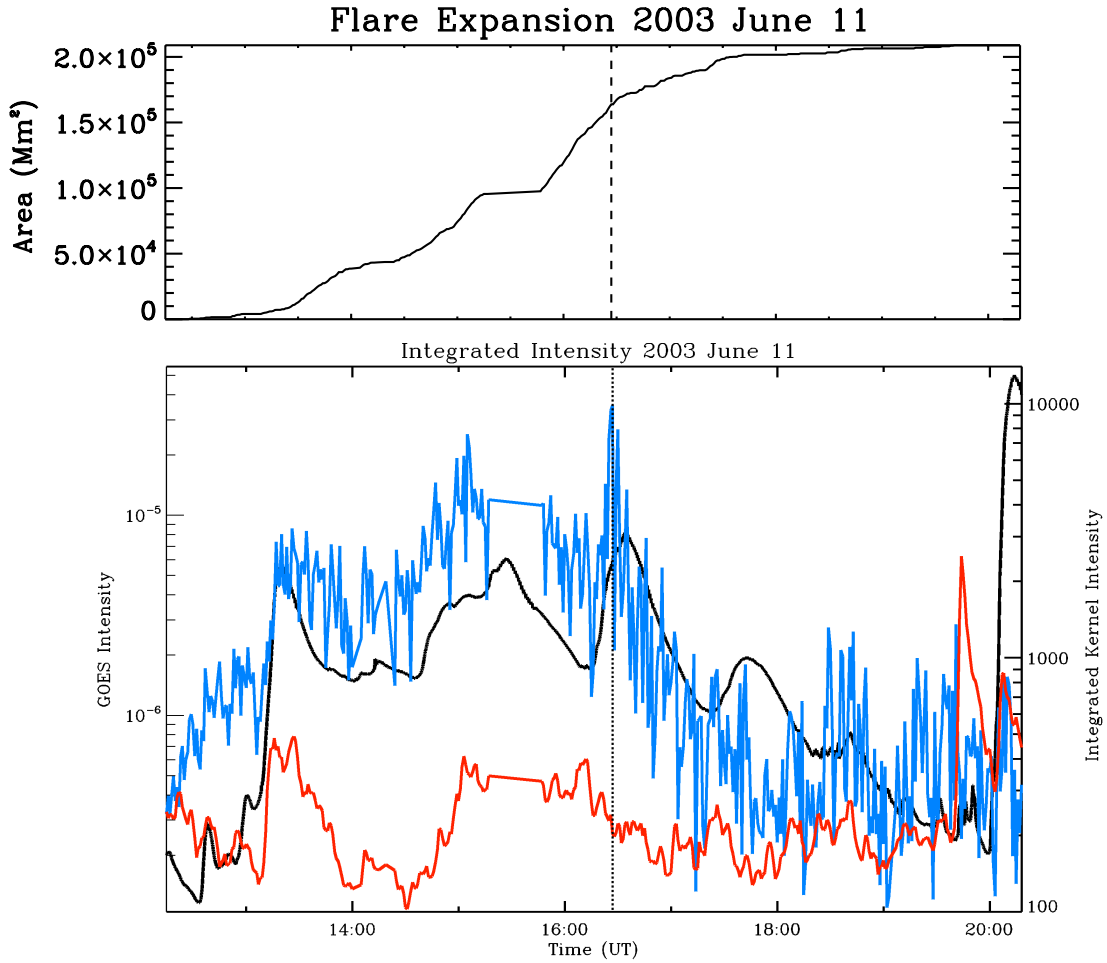


Fig. 5.6.— Time evolution of the 2003 June 11 event. The dashed line in both panels mark the peak flare intensity. Top: the flare area over time as defined by Equation 5.4. Bottom: The blue line is the integrated  $H\alpha$  flare kernel intensities at each time step. The red line is the integrated SCB kernel intensities at each time step. Plotted for reference in black is the GOES 1.0 – 8.0 Å intensity curve.

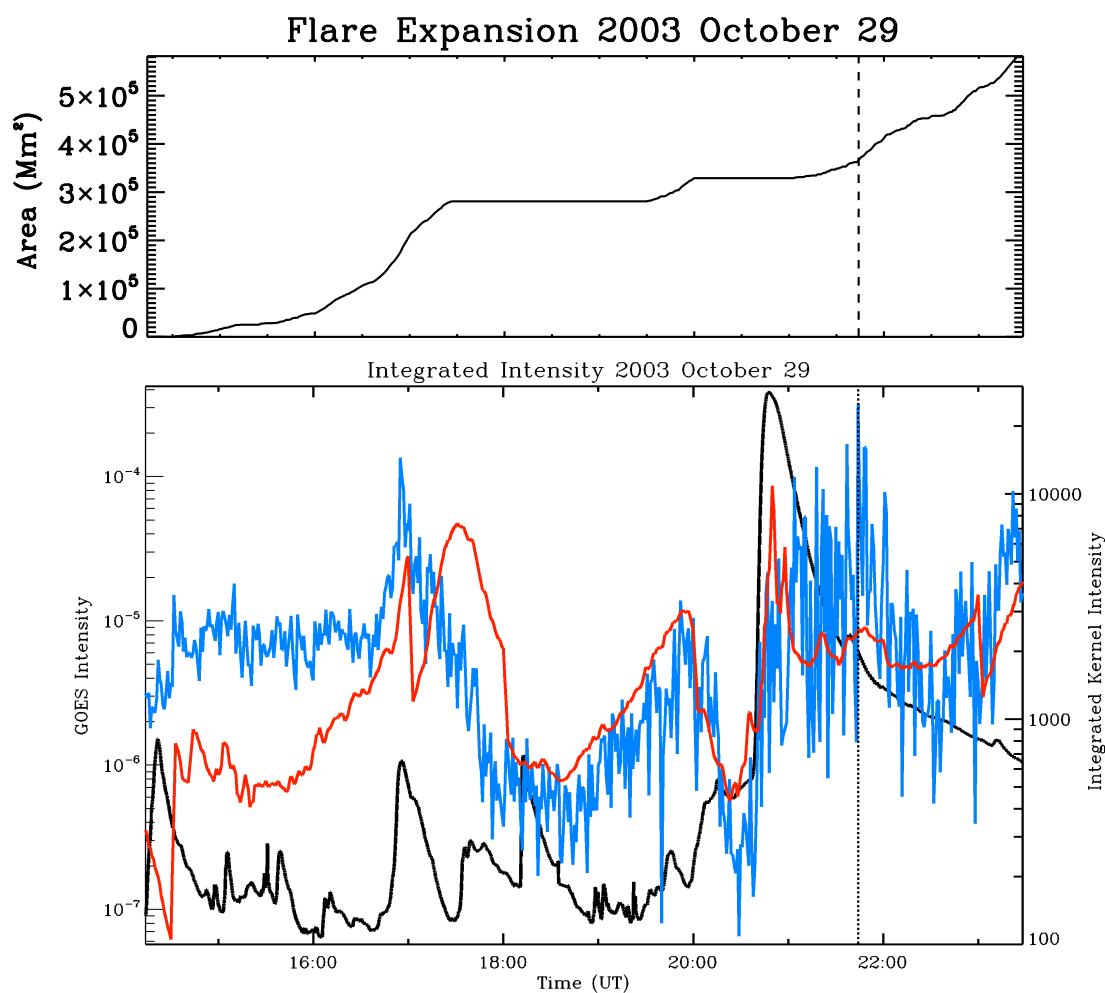


Fig. 5.7.— Time evolution of the 2003 October 29 event. The dashed line in both panels mark the peak flare intensity. Top: the flare area over time as defined by Equation 5.4. Bottom: The blue line is the integrated  $\text{H}\alpha$  flare kernel intensities at each time step. The red line is the integrated SCB kernel intensities at each time step. Plotted for reference in black is the GOES 1.0 – 8.0 Å intensity curve.

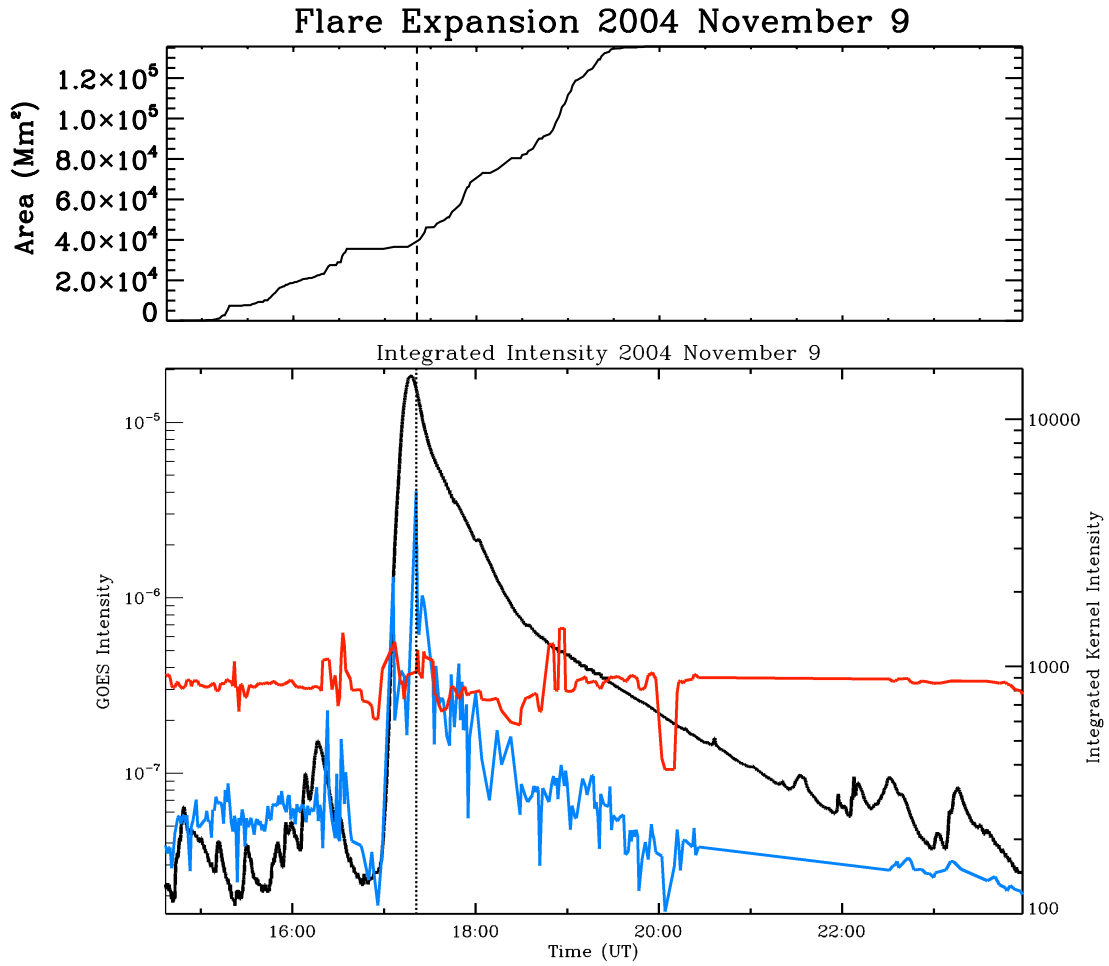


Fig. 5.8.— Time evolution of the 2004 November 9 event. The dashed line in both panels mark the peak flare intensity. Top: the flare area over time as defined by Equation 5.4. Bottom: The blue line is the integrated  $\text{H}\alpha$  flare kernel intensities at each time step. The red line is the integrated SCB kernel intensities at each time step. Plotted for reference in black is the GOES 1.0 – 8.0 Å intensity curve.

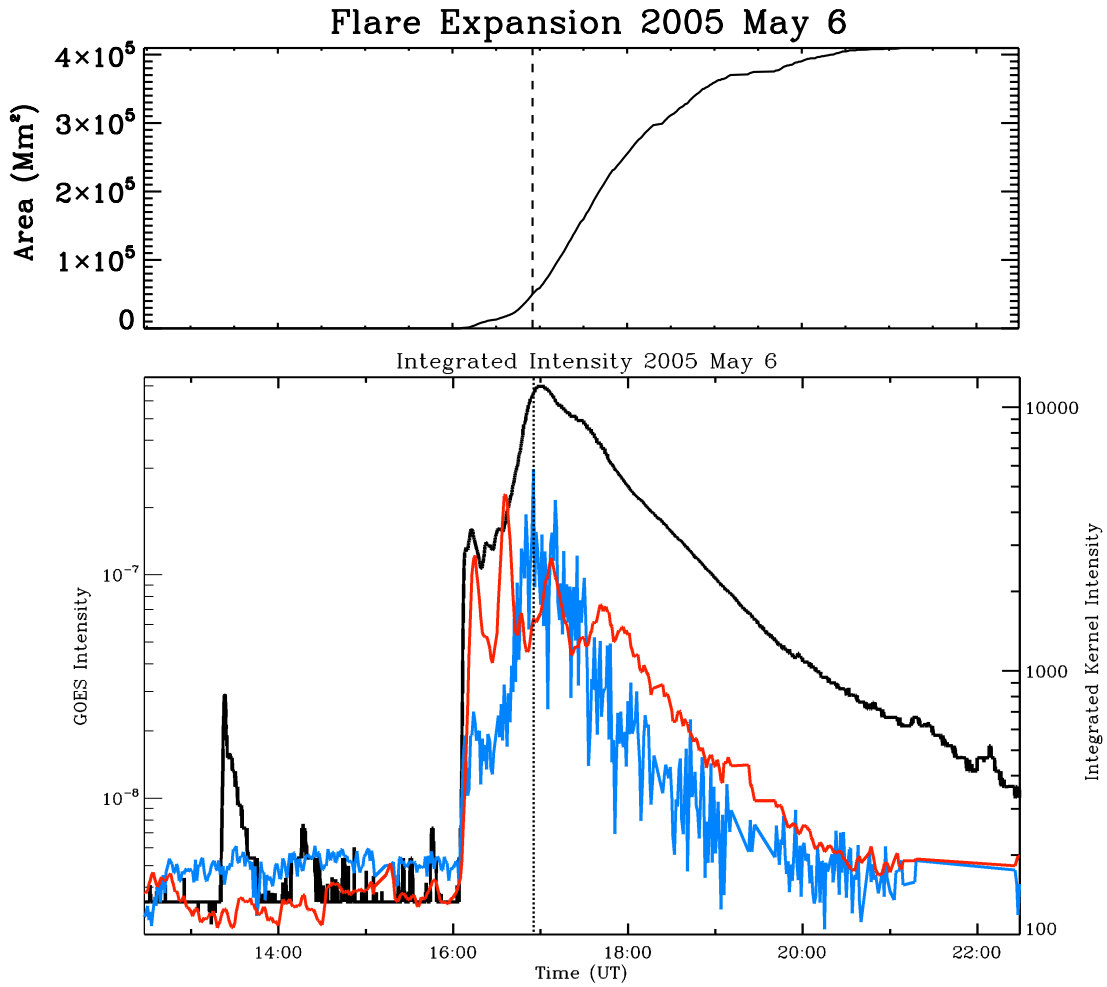


Fig. 5.9.— Time evolution of the 2005 May 6 event. The dashed line in both panels mark the peak flare intensity. Top: the flare area over time as defined by Equation 5.4. Bottom: The blue line is the integrated  $H\alpha$  flare kernel intensities at each time step. The red line is the integrated SCB kernel intensities at each time step. Plotted for reference in black is the GOES 1.0 – 8.0 Å intensity curve.

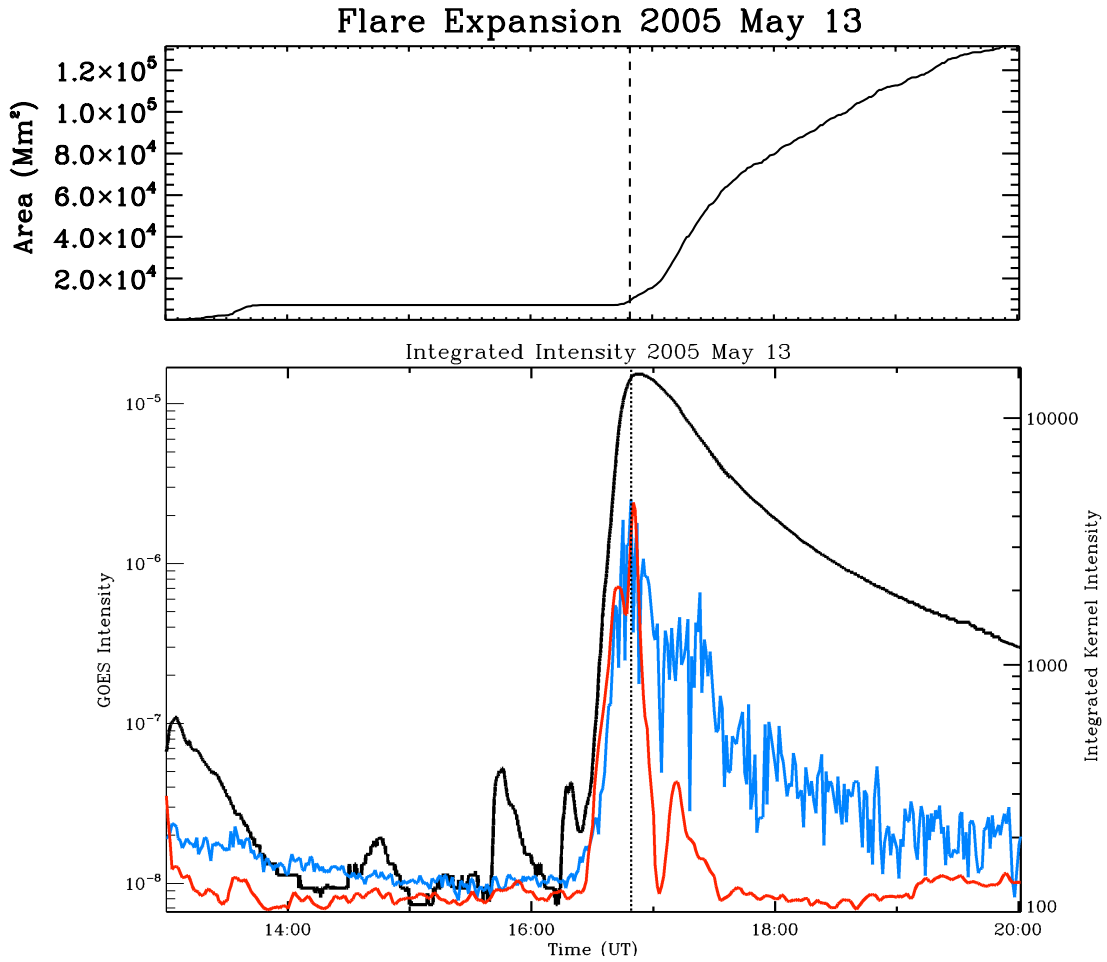


Fig. 5.10.— Time evolution of the 2005 May 13 event. The dashed line in both panels mark the peak flare intensity. Top: the flare area over time as defined by Equation 5.4. Bottom: The blue line is the integrated H $\alpha$  flare kernel intensities at each time step. The red line is the integrated SCB kernel intensities at each time step. Plotted for reference in black is the GOES 1.0 – 8.0 Å intensity curve.

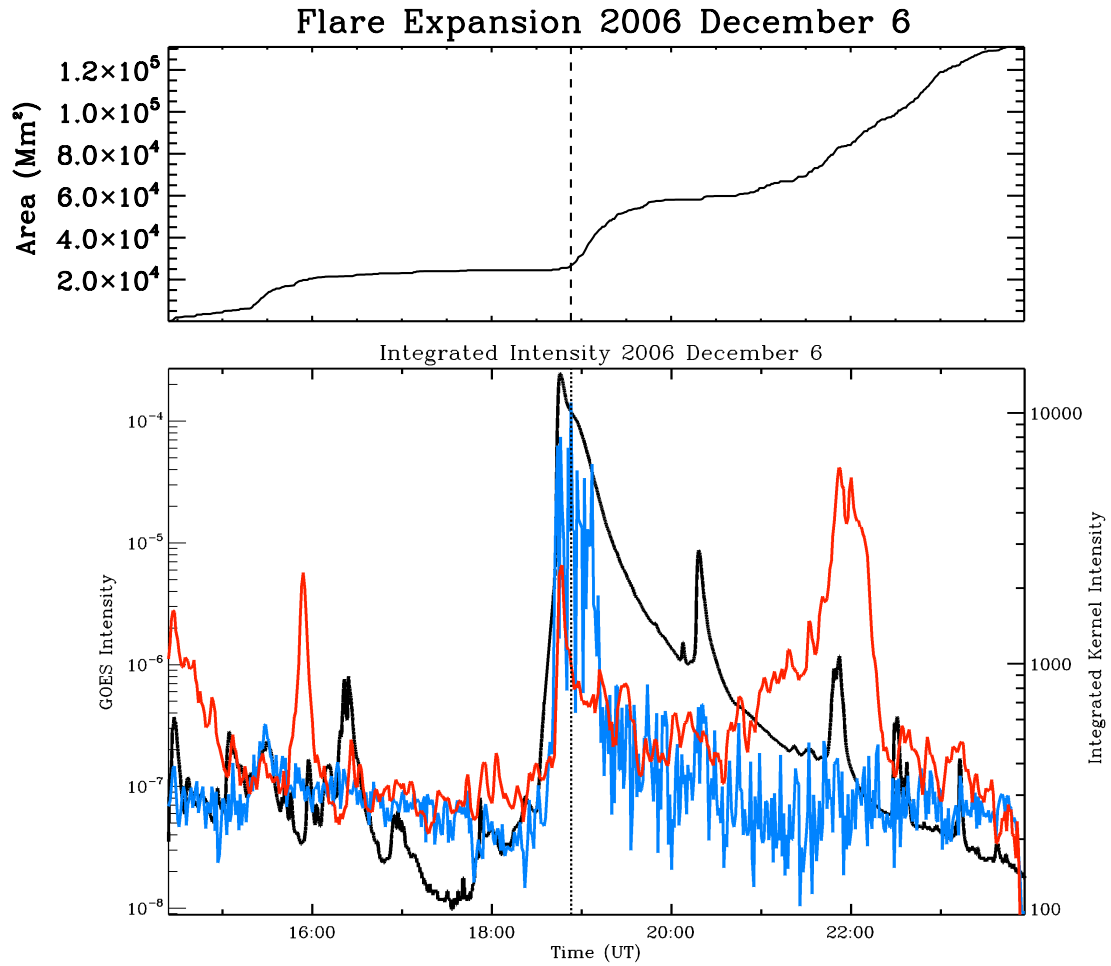


Fig. 5.11.— Time evolution of the 2006 December 6 event. The dashed line in both panels mark the peak flare intensity. Top: the flare area over time as defined by Equation 5.4. Bottom: The blue line is the integrated  $H\alpha$  flare kernel intensities at each time step. The red line is the integrated SCB kernel intensities at each time step. Plotted for reference in black is the GOES 1.0 – 8.0 Å intensity curve.

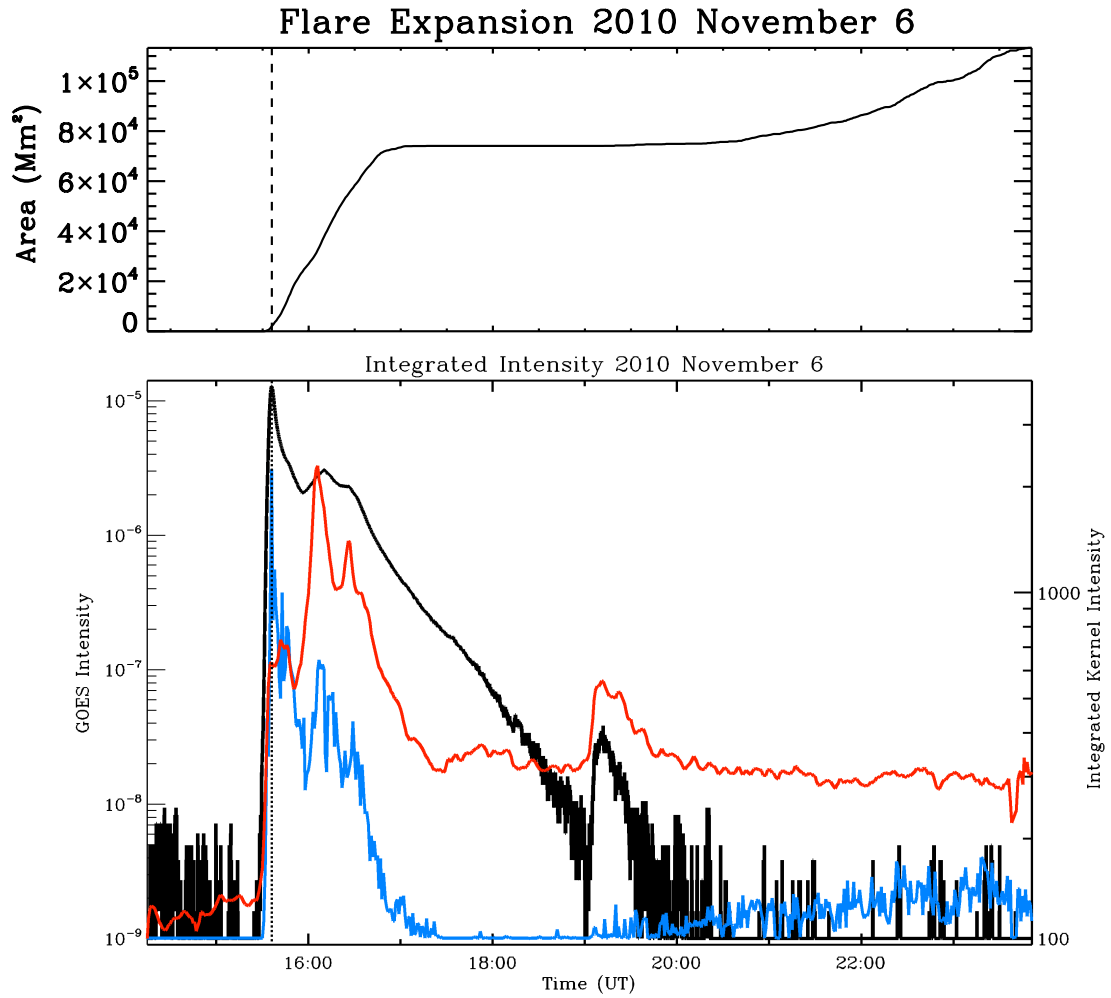


Fig. 5.12.— Time evolution of the 2010 November 6 event. The dashed line in both panels mark the peak flare intensity. Top: the flare area over time as defined by Equation 5.4. Bottom: The blue line is the integrated  $H\alpha$  flare kernel intensities at each time step. The red line is the integrated SCB kernel intensities at each time step. Plotted for reference in black is the GOES 1.0 – 8.0 Å intensity curve.

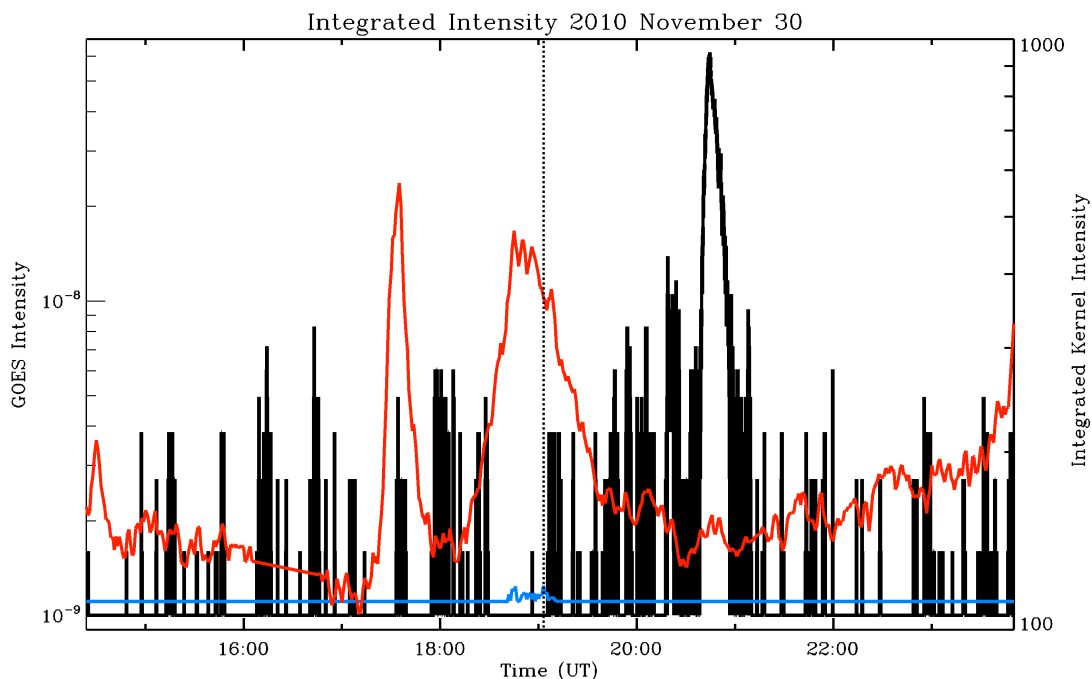


Fig. 5.13.— Time evolution of the 2010 November 30 event. The blue line is the integrated  $H\alpha$  flare kernel intensities at each time step. The red line is the integrated SCB kernel intensities at each time step. Plotted for reference in black is the GOES 1.0 – 8.0  $\text{\AA}$  intensity curve.

Each flare examined for this study has its unique features but also display similarities that transcend flare class and duration. Noticeable in all curves, flares are not smooth processes (Figures 5.3 – 5.13). Intensities impulsively change from minute to minute in the GOES curve, flare kernel curve, and the SCB kernel curve. The GOES X-ray intensity curve generally follows features evident in both the SCB kernel and flare kernel curves; appearing visually as almost a linear combination of the two. The size of the flare also does not smoothly grow in every flare. This sporadic growth in flare-area is indicative of the complicated active region that exists before, during, and after the flare erupts. Qualitatively, the more “starts and stops” in the flare growth curve, the more complicated the active region the in which the flare is imbedded.

The properties of kernels identified in flare ribbons can be examined in two ways: (i) each kernel can be considered as an independent aggregation of compact brightenings; or (ii) kernels can be considered as dependent on each other as fragments of a dynamic system. Each category brings about contrasting properties. If one considers the kernels as independent elements, this provides a way to examine changes to subsections of the flare and is discussed in Section 5.1.1. Associating kernels with their contextual surroundings allows a way to examine the total evolution of the flare without concern for how individual kernels behave. This type of examination is addressed in Section 5.1.2.

### 5.1.1. Qualities of Individual Kernels

A sample of six kernels from the 2005 May 13 event, letters U - X in Figure 5.14, is representative of the majority of flare kernels tracked. The kernels were selected from three different regions of this flare. The normalized  $H\alpha$  intensity of each of these kernels is shown in Figure 5.15. In contrast to the integrated flare light curve, an individual flare kernel often has a shorter lifetime. This is because an individual kernel may first appear in the impulsive phase of the flare (as demonstrated in kernels W - Y), while other kernels may disappear as the flare begins to decay (as in kernels U and Z). Most likely these kernels merged with one another, at which point their unique identity was lost. Kernels W and X are the only two that show the characteristic exponential dimming found in the reference curves in Figure 5.10. All of these kernels have peak intensities within a few minutes of the peak of the total flare intensity and have sustained brightening above background levels for up to an hour.

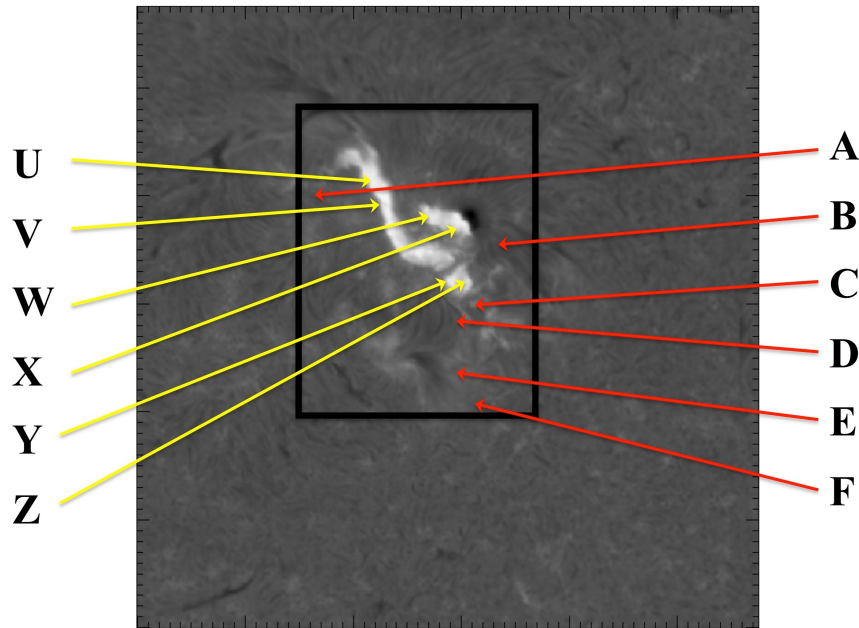


Fig. 5.14.— An image from the 2005 May 13 event. Letters A – F point to the locations several SCB kernels that are shown in more detail in Figure 5.15. Letters U – Z point to the locations of a sample of several flare kernels that are also shown in more detail in Figure 5.15. Note that since flare kernels move with the evolving flare ribbon, the locations of these kernels are only accurate for this image. In contrast, SCB kernels are stationary and remain in the same location in any image.

The integrated speed of displaced kernels provides context to the evolution of intensities. We define the integrated speed of displacement to be the sum

over all time steps of the measured velocity of an individual kernel; thus small velocity perturbations are minimized by the sum. The integrated speed measured for each kernel peaks at  $\approx 2.3 \text{ km s}^{-1}$  and has a mean of  $\approx 0.2 \text{ km s}^{-1}$ . There is significant motion along the flare ribbons as well as outflow away from the flare center. The motions are complex but generally diverge. The total spatial (angular) displacement of each flare kernel peaks at  $\approx 20.7 \text{ Mm}$  and has a mean of  $\approx 5.0 \text{ Mm}$ . Flare kernels that exhibit the greatest speeds do not necessarily have the greatest displacements. As the flare develops, most of the motion in flare ribbons indicated is synchronous with the separation of the ribbons. A few tracked kernels indicate motion along flare ribbons. These flows along flare ribbons are consistently observed in all two-ribbon morphologies.

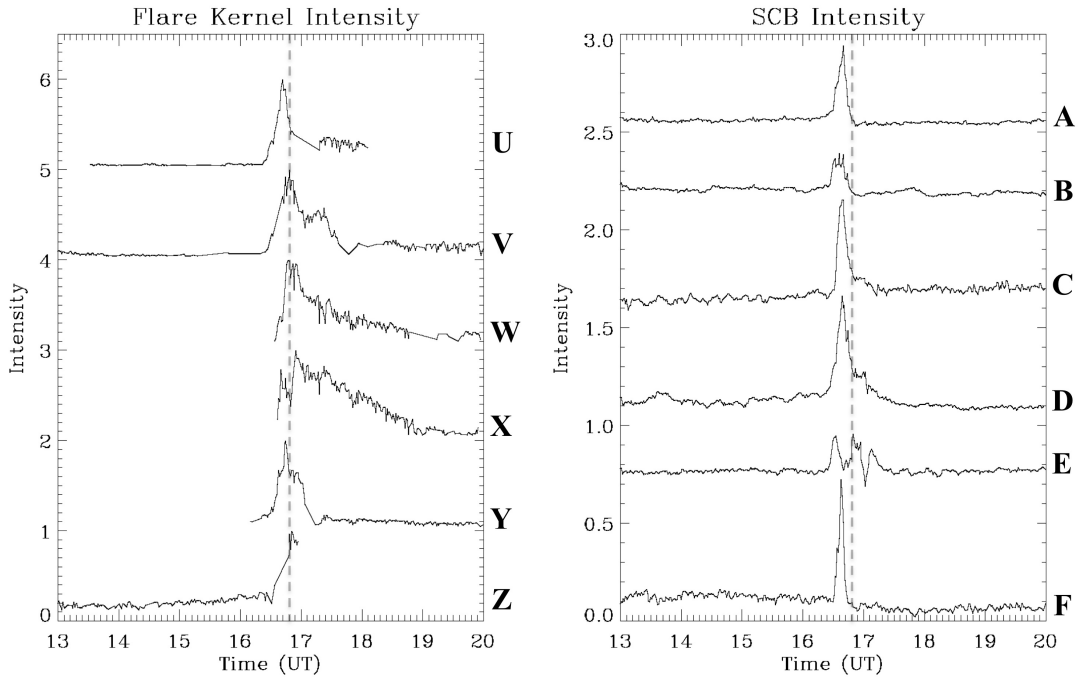


Fig. 5.15.—  $H\alpha$  normalized intensity curves for each of the kernels indicated in Figure 5.14 by the associated letters. On the left, the tracked flare kernels are shown. The normalized intensity curves for the SCB kernels, shown on the right, are stationary and therefore tracked throughout the flaring window. In both panels, the vertical dashed line indicates the time at which the flare intensity peaks (16:49 UT) derived from integrating all flare kernel intensities at each time step.

### 5.1.2. Derived Flare Quantities

Examining trajectories of flare kernels offers insight into the motions of the flare ribbons as they evolve through the eruption. Figure 5.16 shows a time series of images for the 2005 May 13 event centered about the peak-time of the flare.

The velocities of the detected flare kernels are superposed as vectors. Notice the initial outflow of the two ribbons near the flare peak at 16:49 UT. But as the flare continues to evolve, there is more motion along the flare ribbons. This is probably a result of the over-arching loops readjusting after the reconnection event. Beneath each image is a histogram of the distribution of velocities at each time step. The mean apparent lateral velocity of each kernel remains below  $0.5 \text{ km s}^{-1}$  throughout the flare, even though the total velocity changes significantly. Qualitatively, the bulk of the apparent motion appears after the flare peak intensity at 16:49 UT.

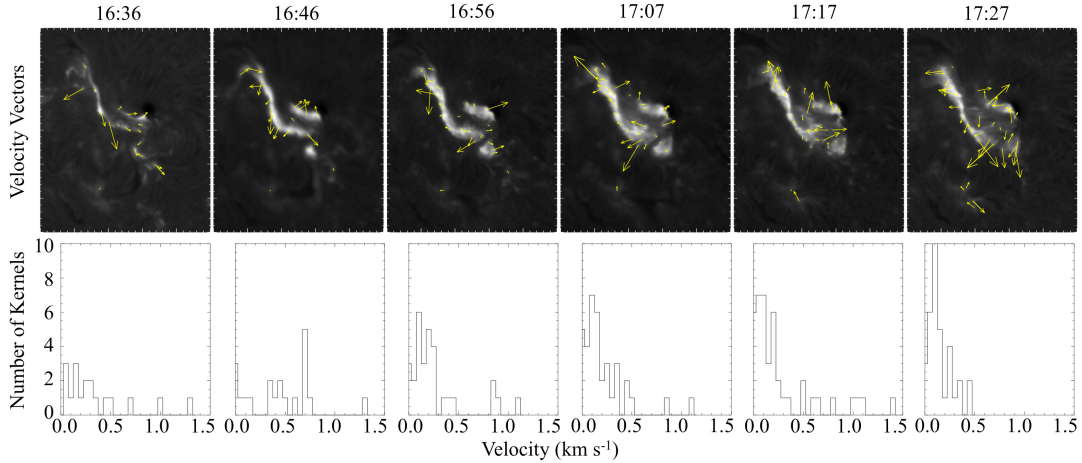


Fig. 5.16.— A time series of H $\alpha$  images with the apparent lateral velocity of each tracked flare kernel at that time step plotted over the 2005 May 13 flare ribbons. A histogram of the number of flare kernels as a function of unsigned average velocity (speed) corresponding to each time step is plotted underneath.

The instantaneous speed of the kernels provides another way to analyze the dynamics of the flare (Figures 5.17 – 5.26 bottom panel). The instantaneous speed is significantly more sensitive to the accuracy of the alignment and tracking code than the average speed of a tracked kernel, resulting in higher measured speeds. Grouping the kernels' velocities into five distinct bins yields some interesting trends. The kernels with apparent lateral speeds above  $15 \text{ km s}^{-1}$  are highly coincident with the impulsive phase and peak intensity of the flare. The number of these fast moving kernels peaks within a couple minutes of the onset of the impulsive phase and then quickly decays back to quiet levels near flare-peak. The velocity bins between  $0.5$  and  $15 \text{ km s}^{-1}$  show a different substructure. These velocity bins are at maximum between  $\approx 5 - 30$  minutes after the peak of the flare intensity. They show a much slower decay rate, staying above the pre-flare velocity measured throughout the decay phase of the H $\alpha$  flare curve. The number of tracked kernels decreases with the increased velocity bin. There are about ten times the number of flare kernels moving  $0.5 - 10 \text{ km s}^{-1}$  than  $> 25 \text{ km s}^{-1}$  in every case study.

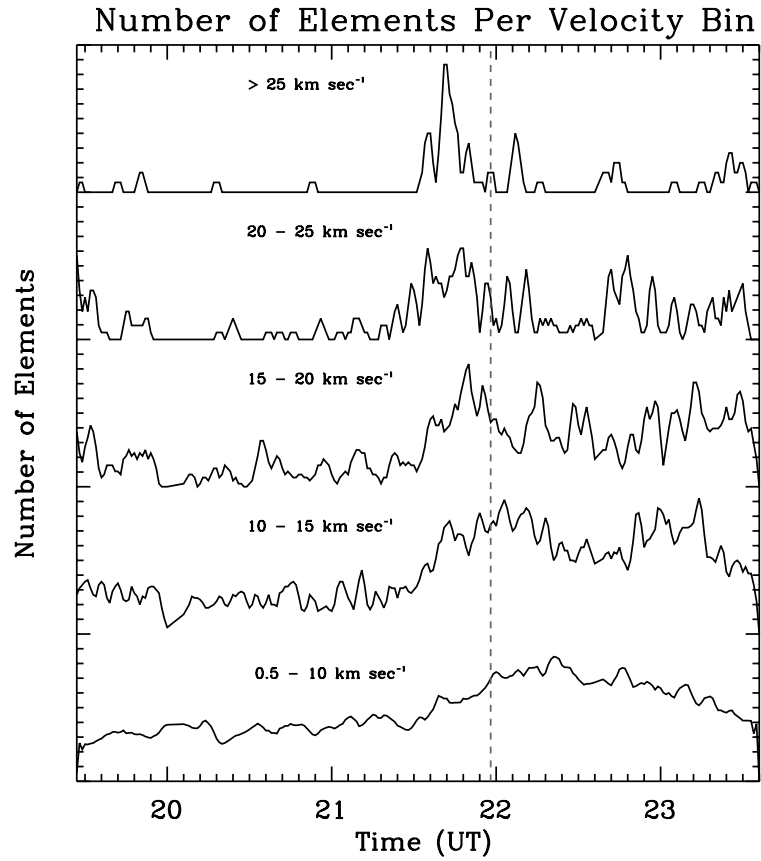


Fig. 5.17.— The number of elements in each apparent instantaneous lateral velocity bin plotted as a function of time for the 2002 December 19 event. The vertical dashed line marks the time of the peak flare intensity. The velocity bins are  $5 \text{ km s}^{-1}$  in width. Velocities,  $0 - 0.5 \text{ km s}^{-1}$ , is excluded because of a base level of noise inherent in the detection routine.

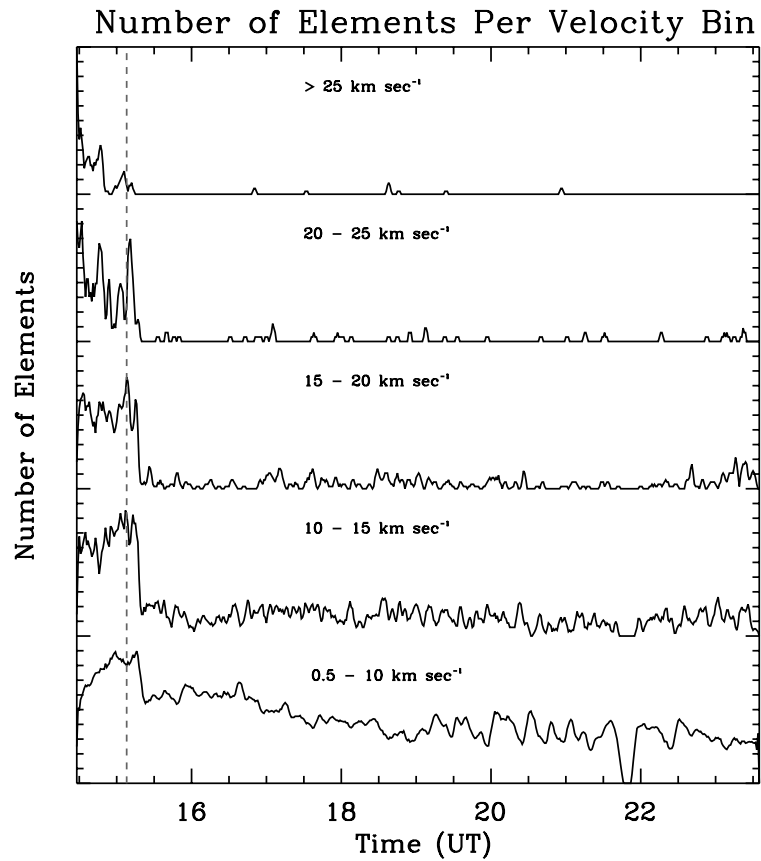


Fig. 5.18.— The number of elements in each apparent instantaneous lateral velocity bin plotted as a function of time for the 2003 March 6 event. The vertical dashed line marks the time of the peak flare intensity. The velocity bins are  $5 \text{ km s}^{-1}$  in width. Velocities,  $0 - 0.5 \text{ km s}^{-1}$ , is excluded because of a base level of noise inherent in the detection routine.

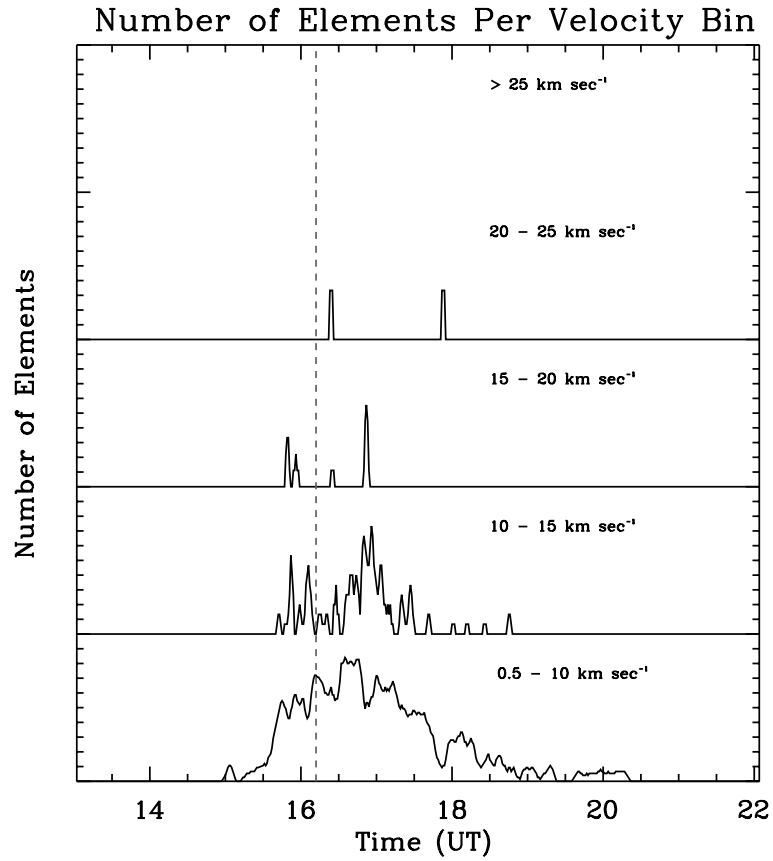


Fig. 5.19.— The number of elements in each apparent instantaneous lateral velocity bin plotted as a function of time for the 2003 May 9 event. The vertical dashed line marks the time of the peak flare intensity. The velocity bins are  $5 \text{ km s}^{-1}$  in width. Velocities,  $0 - 0.5 \text{ km s}^{-1}$ , is excluded because of a base level of noise inherent in the detection routine.

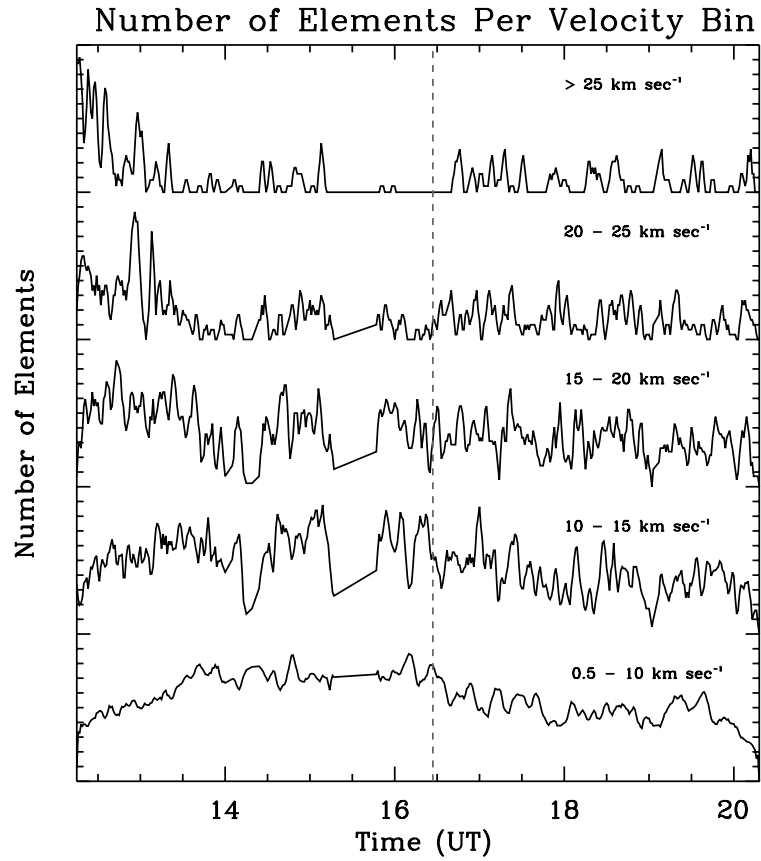


Fig. 5.20.— The number of elements in each apparent instantaneous lateral velocity bin plotted as a function of time for the 2003 June 11 event. The vertical dashed line marks the time of the peak flare intensity. The velocity bins are  $5 \text{ km s}^{-1}$  in width. Velocities,  $0 - 0.5 \text{ km s}^{-1}$ , is excluded because of a base level of noise inherent in the detection routine.

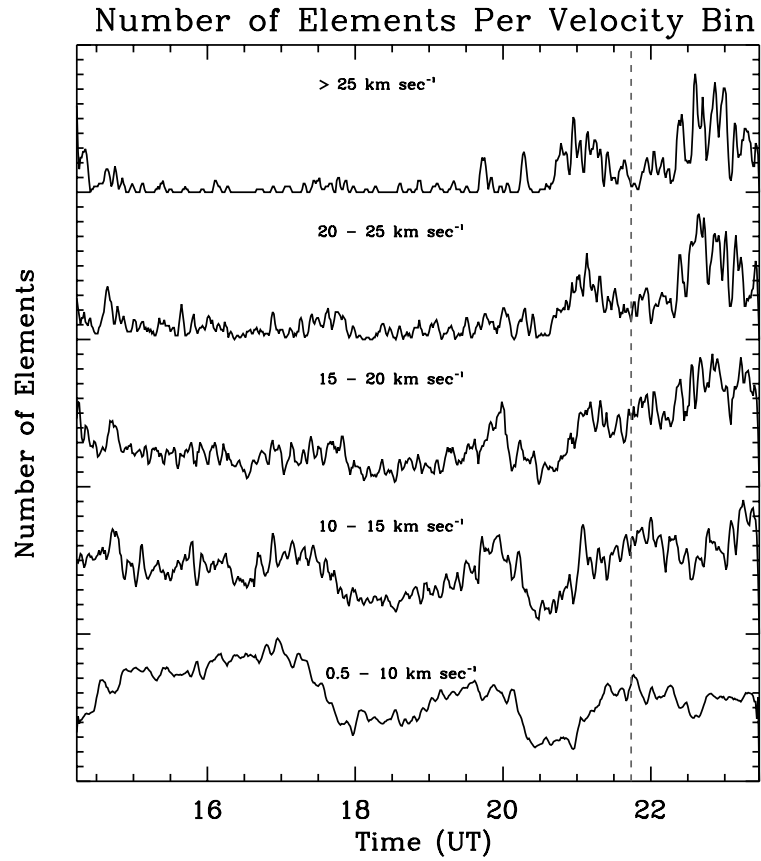


Fig. 5.21.— The number of elements in each apparent instantaneous lateral velocity bin plotted as a function of time for the 2003 October 29 event. The vertical dashed line marks the time of the peak flare intensity. The velocity bins are  $5 \text{ km s}^{-1}$  in width. Velocities,  $0 - 0.5 \text{ km s}^{-1}$ , is excluded because of a base level of noise inherent in the detection routine.

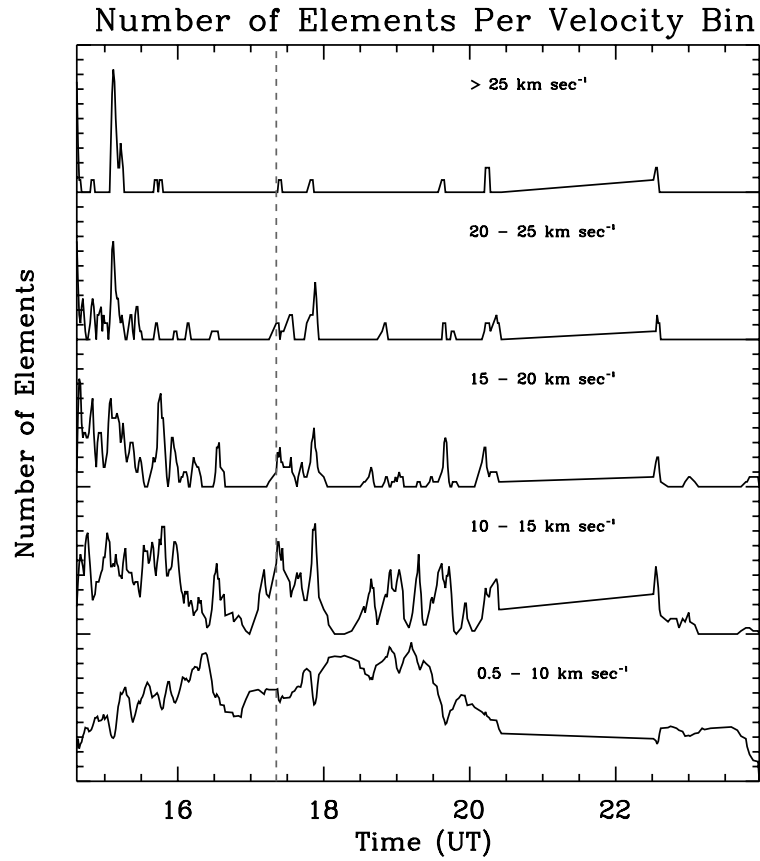


Fig. 5.22.— The number of elements in each apparent instantaneous lateral velocity bin plotted as a function of time for the 2004 November 9 event. The vertical dashed line marks the time of the peak flare intensity. The velocity bins are  $5 \text{ km s}^{-1}$  in width. Velocities,  $0 - 0.5 \text{ km s}^{-1}$ , is excluded because of a base level of noise inherent in the detection routine.

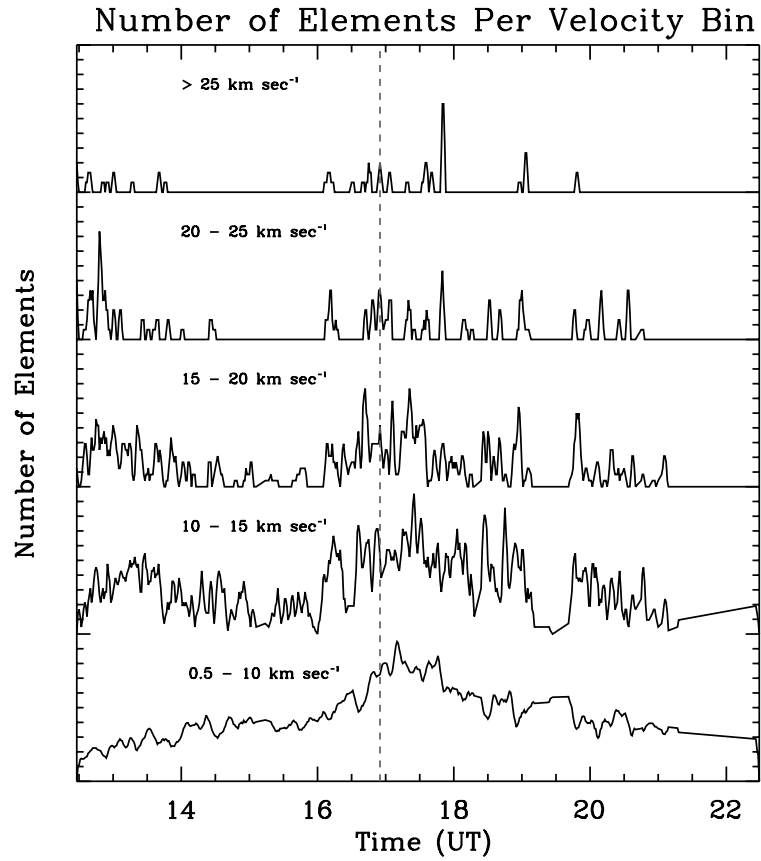


Fig. 5.23.— The number of elements in each apparent instantaneous lateral velocity bin plotted as a function of time for the 2005 May 6 event. The vertical dashed line marks the time of the peak flare intensity. The velocity bins are  $5 \text{ km s}^{-1}$  in width. Velocities,  $0 - 0.5 \text{ km s}^{-1}$ , is excluded because of a base level of noise inherent in the detection routine.

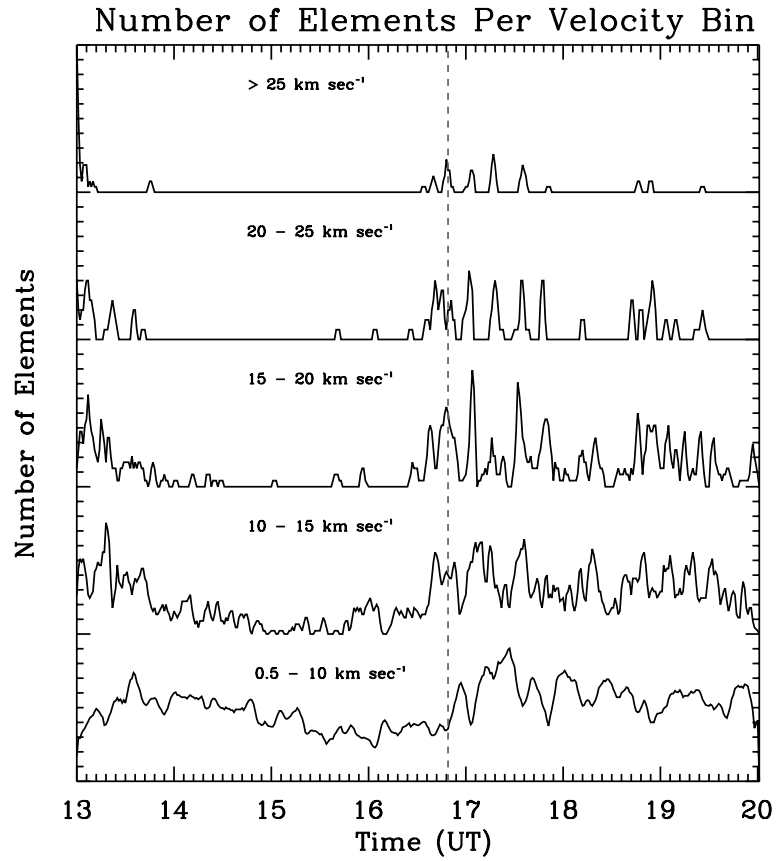


Fig. 5.24.— The number of elements in each apparent instantaneous lateral velocity bin plotted as a function of time for the 2005 May 13 event. The vertical dashed line marks the time of the peak flare intensity. The velocity bins are  $5 \text{ km s}^{-1}$  in width. Velocities,  $0 - 0.5 \text{ km s}^{-1}$ , is excluded because of a base level of noise inherent in the detection routine.

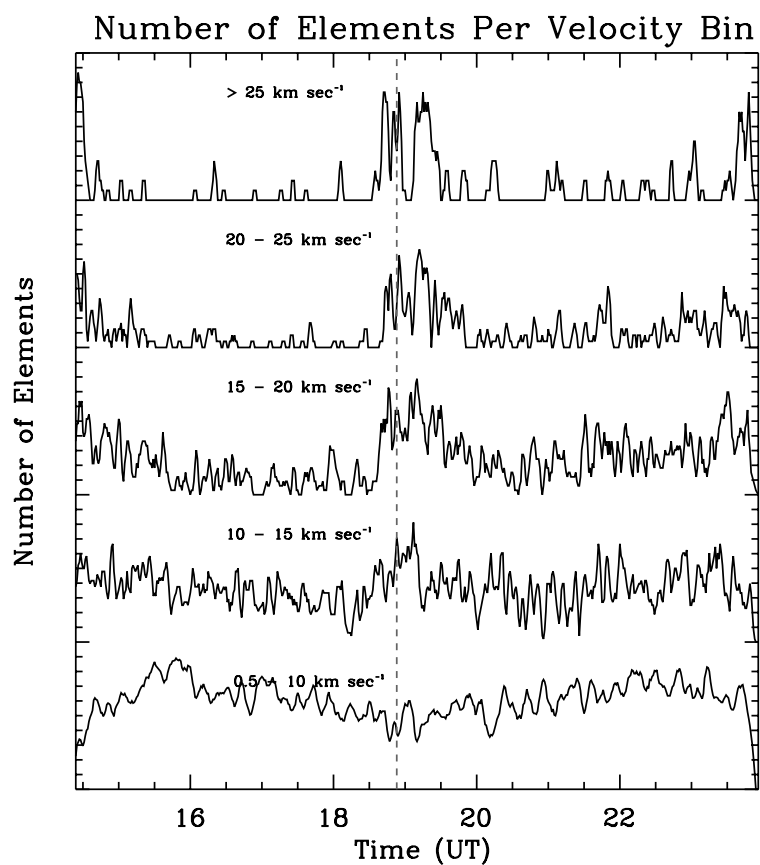


Fig. 5.25.— The number of elements in each apparent instantaneous lateral velocity bin plotted as a function of time for the 2006 December 6 event. The vertical dashed line marks the time of the peak flare intensity. The velocity bins are  $5 \text{ km s}^{-1}$  in width. Velocities,  $0 - 0.5 \text{ km s}^{-1}$ , is excluded because of a base level of noise inherent in the detection routine.

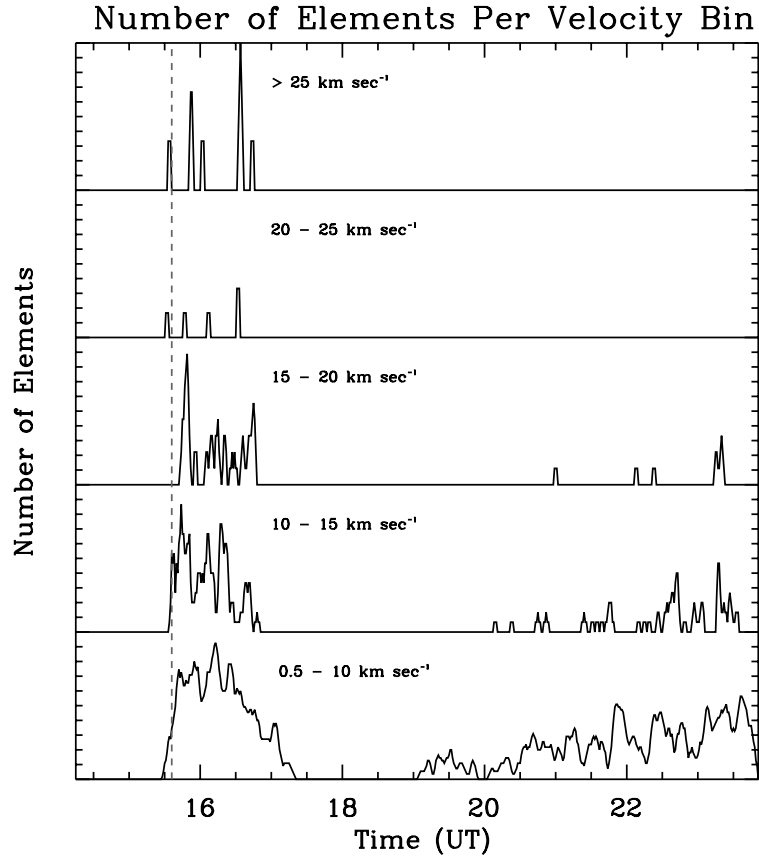


Fig. 5.26.— The number of elements in each apparent instantaneous lateral velocity bin plotted as a function of time for the 2010 November 6 event. The vertical dashed line marks the time of the peak flare intensity. The velocity bins are  $5 \text{ km s}^{-1}$  in width. Velocities,  $0 - 0.5 \text{ km s}^{-1}$ , is excluded because of a base level of noise inherent in the detection routine. This flare is both spatially and temporally compact as evident in Figure 5.12, which is also reflected in this plot.

Figure 5.27 (left column) shows the integrated kernel velocity for a sample of three events: 2005 May 13, 2005 May 6, and 2004 November 9. In general, the evolution of the integrated kernel speed has a shape similar to the intensity curve. For the 2005 May 6 event, the speed curve is more similar to the GOES x-ray intensity curve than to the  $\text{H}\alpha$  curve. For the November 9 event, the limb geometry of the flare, as well as the noise in the original dataset, contribute to a noisy curve. Despite these difficulties, a clear increase in total speed is apparent near the peak of the flare. A continuum integrated velocity level of  $1\text{--}2 \text{ km s}^{-1}$  is consistent in each event, indicating the quality of data and of the tracking software. The peak integrated velocity is about  $15 \text{ km s}^{-1}$  for the three flares sampled.

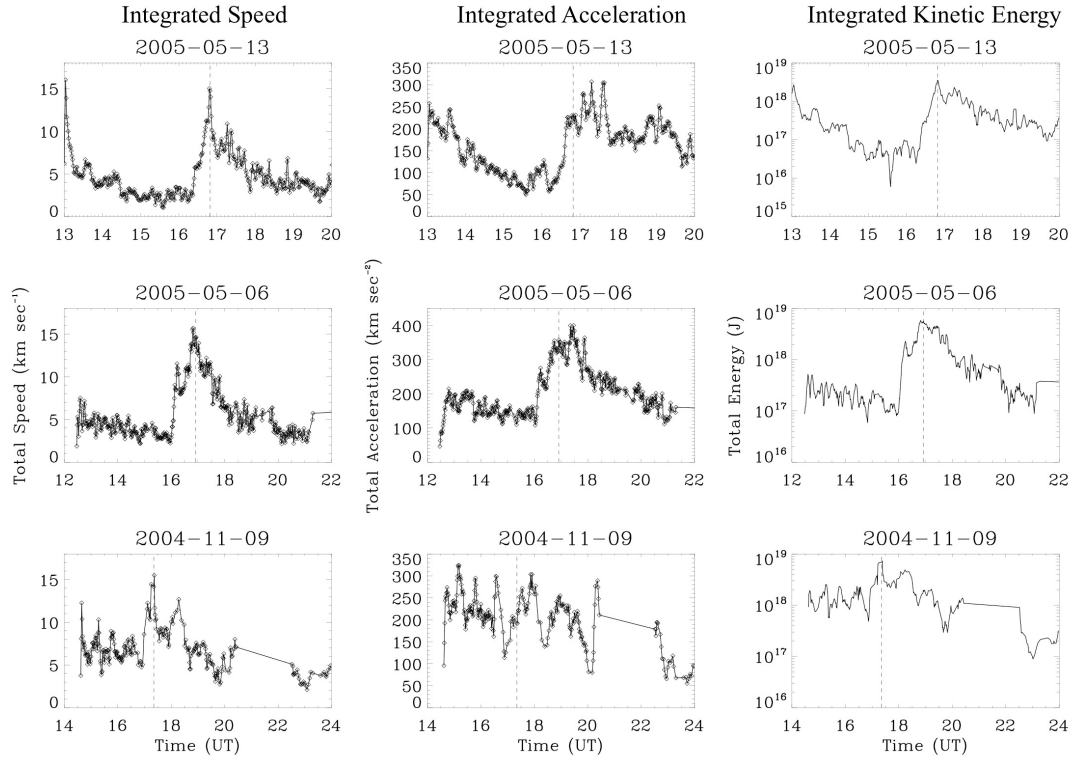


Fig. 5.27.— The integrated unsigned propagation speed, acceleration, and energy of flare kernels as a function of time for three events: 2005 May 13, 2005 May 6, and 2004 November 9. The vertical dashed line indicates the maximum flare intensity for the flaring event. The first column shows the integrated speed curves. The second column shows the acceleration of the flare ribbons. The third column shows the integrated kinetic energy, Equation 5.2, as a function of time for each of the three events studied. The 2004 flare had significant noise in the original data and a location on the limb contributing to the inconsistent measurements.

Examining the change in the speed of each kernel between successive images yields a derived acceleration for each tracked kernel. The integrated unsigned acceleration is plotted in Figure 5.27 (middle column). The overall shape of the acceleration curve is influenced by flare kernels coming into existence and disappearing during the flare. Both the 2005 May 13 and 2005 May 6 events show peak acceleration after the peak of the intensity curve. Hence the majority of the acceleration in the apparent motion of the flare comes in the decay phase of  $H\alpha$  emission, in concert with the formation of post-peak flare loops, as seen in movies of AIA images of other flares. The peak acceleration appears uncorrelated with the strength of the flare: the peak of the M class May 13 event is just over  $300 \text{ km s}^{-2}$ , while the peak of the C class flare on May 6 is nearly  $400 \text{ km s}^{-2}$ . The acceleration curve for the November 9 flare has too much noise associated with it to decisively determine the peak value.

The right column of Figure 5.27 shows a derived kinetic energy associated with the measured motion of the flare kernels. This was accomplished by assuming a chromospheric density  $[\sigma]$  of  $10^{-5} \text{ kg m}^{-3}$  and a depth  $[h]$  of 1000 km. The mass contained in each volume is then calculated by

$$m = \pi h \sigma R_g^2 \sqrt{1 - e^2} \quad (5.1)$$

where  $R_g$  is defined in Equation 4.7 and  $e$  is the measured eccentricity. The kinetic energy under a kernel is defined in the standard way to be

$$E_n = \frac{1}{2} m v^2 \quad (5.2)$$

where  $v$  (speed) is a measured quantity for each kernel. The derived kinetic energy curves show a  $\approx 30$  fold increase in kinetic energy during the flare with a decay time similar to the decay rate of the  $\text{H}\alpha$  intensity. The measure of a kernel's kinetic energy is imprecise, because the measured motion is apparent motion of the underlying plasma. In the model of two ribbon solar flares put forth by Priest & Forbes (2002), the apparent velocity is a better indicator of rates of magnetic reconnection rather than of plasma motion. Despite this caveat, the derived kernel kinetic energy is a useful measure, because it combines the size of the kernels with their apparent velocities to characterize the flare's evolution, thus representing the two in a quantitative way.

Similar to the derived kinetic energy, we can characterize the expansion rate of the flare. This requires finding the area  $[A]$  of the flare at a given frame number  $[\mathcal{I}]$ :

$$A_{\mathcal{I}} = \sum_n R_g^2 \sqrt{1 - e_n^2} \quad (5.3)$$

where the radius of gyration  $[R_g]$  (defined in Equation 4.7) and the measured eccentricity  $[e]$  are used to calculate an area of the flare kernel  $[k]$  and the flare area is the sum of all the kernels. The expansion of the flare  $[A_{ex}]$  can then be calculated by summing the derived areas from the beginning of the event:

$$A_{ex} = \sum_0^{\mathcal{I}} A_{\mathcal{I}} - A_{\text{base}}. \quad (5.4)$$

Since the flare areas are co-added from previous frame numbers, a base area  $[A_{\text{base}}]$  representing the quiescent area of the region pre-flare is subtracted from each image before calculating the expansion. The results of this measurement can be seen in the top panels of Figures 5.17 – 5.26. Each of these expansion rates shows a consistent functional form similar to a hyperbolic tangent that begins in the impulsive phase of the flare and persists through the decay phase. Complex flare dynamics are simplified in this view. An example of a flare with complicated flare dynamics is the 2003 October 29 event (Figure 5.21) where several smaller eruptions are apparent before the X10 flare.

To characterize the non-thermal emission during the May 13 event, RHESSI 25 – 50 keV emission between 16:42 – 16:43 UT from RHESSI is contoured in

Figure 5.28 over an  $H\alpha$  image taken at 16:42 UT. The high-energy emission is centered over the flare ribbons but is discontinuous across the ribbon. There are three localized points from which the majority of the X-ray emission comes. The parts of the flare ribbons exhibiting the most displacement show generally lower X-ray intensity than the more stationary segments of the flare ribbons.

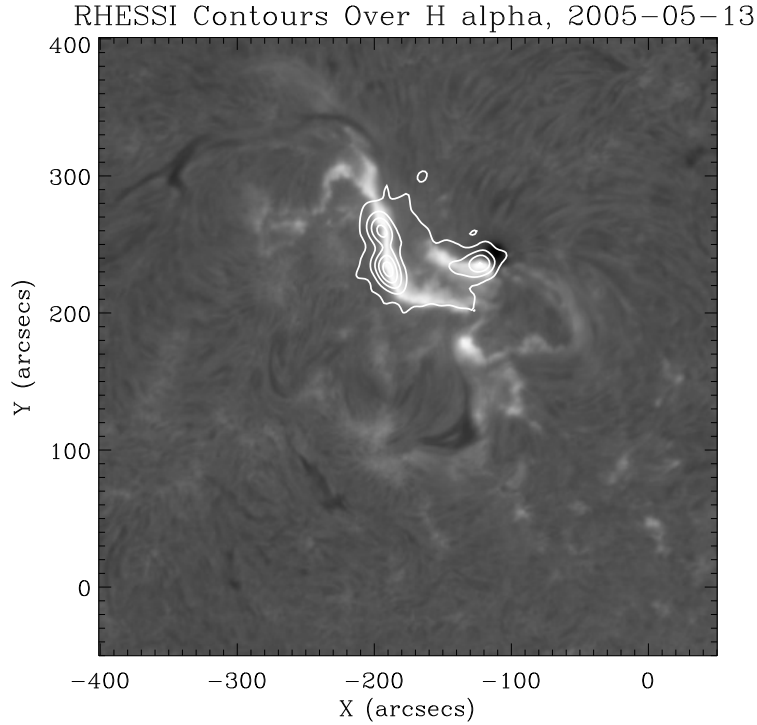


Fig. 5.28.— An  $H\alpha$  image of the 2005 May 13 flare at peak intensity is shown with the reconstructed RHESSI 25 – 50 keV pass band integrated between 16:42 – 16:43 UT contoured on top at 10, 30, 50, 70, and 90% of the maximum intensity. The field of view of the RHESSI image [-220:-95, 180:305] is confined within the flaring region.

## 5.2. Properties of Ephemeral Compact Brightenings

Sequential chromospheric brightenings, although related to the erupting flare ribbons, are distinctly different from the flare kernels. Figure 5.29 plots the aggregated intensity of the entire population of SCBs versus time in the 2005 May 13

Table 5.1. The events used by this work to investigate the automated identification and tracking of SCBs and flare ribbons. The time listed is the start time of the flare. Six of the eleven events were previously identified by Balasubramaniam et al. (2006) while five are new in this study. The data sources utilized for each event are abbreviated as: ISOON, LASCO, GOES, AIA, HMI, GONG, and RHÉSSI

Date	Time UT	GOES Class	Visual CME	Data Sources	Previously Studied	Flare Curve Figure	Velocity Histogram
2002-12-19	21:34	M2.7	yes	I, L, G, N	yes	5.3	5.17
2003-03-06	15:08	None	no	I, L, G, N	no	5.4	5.18
2003-05-09	15:18	B6.6	yes	I, L, G, N	yes	5.5	5.19
2003-06-11	17:27	M1.8	no	I, L, G, N	yes	5.6	5.20
2003-10-29	20:37	X10.0	yes	I, L, G, N	yes	5.7	5.21
2004-11-09	16:59	M8.9	yes	I, L, G, N	yes	5.8	5.22
2005-05-06	16:03	C8.5	yes	I, L, G, N	yes	5.9	5.23
2005-05-13	16:13	M8.0	yes	I, L, G, N, R	no	5.10	5.24
2006-12-06	18:29	X6.5	yes	I, L, G, N	no	5.11	5.25
2010-11-06	15:30	M5.4	yes	I, L, G, A, H	no	5.12	5.26
2010-11-30	17:35	None	yes	I, L, G, A, H	no	5.13	–

Table 5.2. General physical characteristics of individual flare and SCB kernels. *Ensemble Motion* refers to the motion of an individual kernel as compared to its nearest neighbors over the kernel’s lifetime.

Kernel Type	Minimum Diameter	Peak Intensity Increase	Average Lifetime	Ensemble Motion
Flare	6.4 Mm	1000%	≈ 120 min	Directional Consistency
SCB	1.6 Mm	250%	≈ 10 min	Random Walk

event. It shows a relatively short period of time when SCBs occur before returning to pre-flare intensities. In a typical two-ribbon flare, SCBs begin brightening in the impulsive phase of the flare, about 30 minutes before flare peak, and return to a quiet intensity in the early decay phase, about 30 minutes after peak. In contrast, the flare intensity curve remains above pre-flare levels for several hours. The peak of the aggregate SCB intensity curve occurred before or concurrent with the flare in 72% (representing 8 of 11) of the cases studied.

Similar to the flare kernels discussed in Section 5.1, the aggregate SCB curve is plotted in Figures 5.3 – 5.13. Another result that is well demonstrated when plotting SCB kernel intensities is that SCBs never have a peak intensity greater than their host flare (except in the 2010 Hyder flare discussed below). An SCB has a peak intensity 1.2 – 2.5 times above the background intensity level. In contrast, flares can brighten an order of magnitude or more above the pre-flare brightness (Table 5.2). Individual SCBs are also much more fleeting than the flare ribbons. They increase to their peak brightness and return to background intensities in a much shorter timescale than the flare ribbons are observed to do. When isolated, these ephemeral phenomena have intensity curves that are impulsive with a sharp peak and then a return to background intensities in the span of a few minutes. A typical SCB lasts less than 10 frames (corresponding to 10 minutes) above the detection thresholds in ISOON’s  $H\alpha$ .

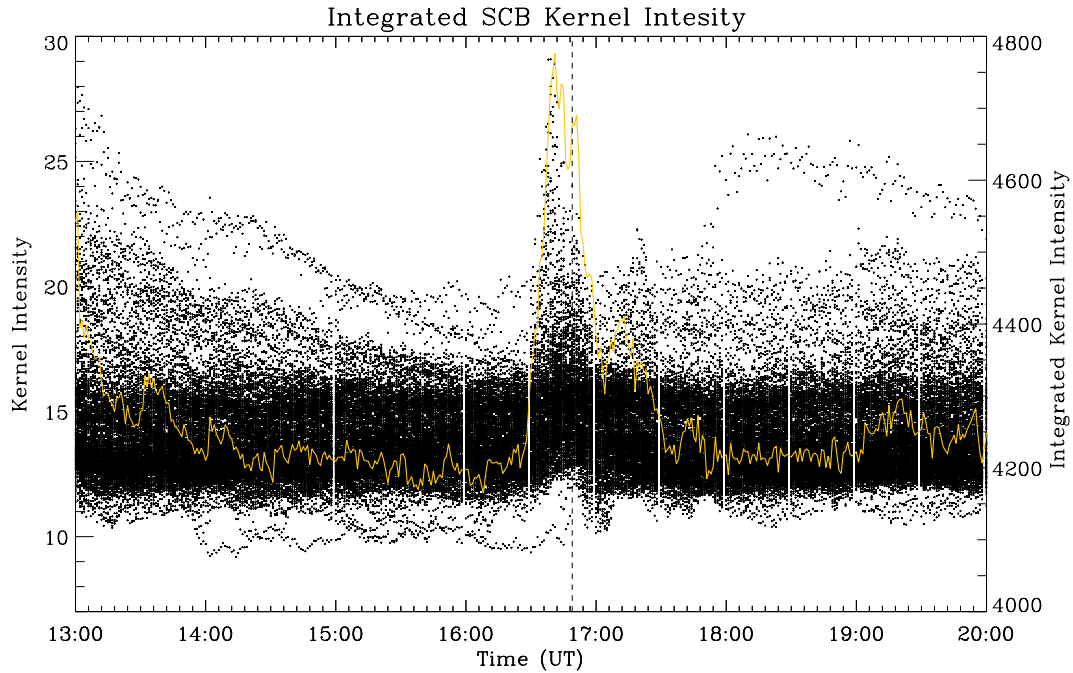


Fig. 5.29.— The 2005 May 13 measured intensities of each SCB curve plotted as points as a function of time. The solid yellow line is the integrated kernel intensities at each time step. Here again, the vertical dashed line indicates the peak of the flare curve as shown in Figure 5.10. Notice that the intensity of the integrated SCB curve returns to the continuum level much faster than the integrated flare-kernel curve as shown in Figure 5.2.

When the tracks of SCB kernels are examined, they do not show any progressive motion. The centroid of an SCB kernel randomly walks around within about six pixels of its starting location for the duration of the trajectory. Although SCBs' sequential nature of point brightening gives the appearance of a progressive traveling disturbance, the plasma beneath each brightening does not follow the disturbance and remains in the same location (Table 5.2). Similar to a wave, the medium in which SCBs are measured is not displaced with the apparent propagation of the brightenings. This result confirms the findings of Balasubramaniam et al. (2005). The third row of images in Figure 5.30 are manually color-coded to reflect this traveling disturbance that is seen in an animation of the detections. The red group of detections matures quickly and dissipates, while the yellow and blue groups take more time to develop. This suggests that there may be more than one population of SCBs.

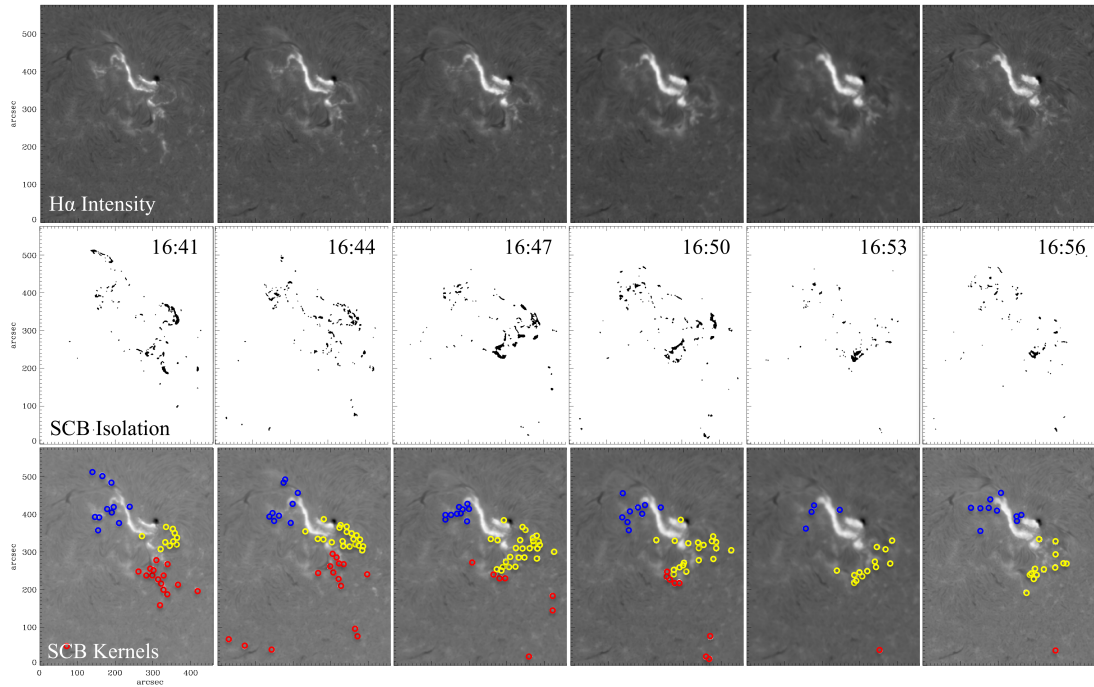


Fig. 5.30.— Time series of images showing the evolution of the SCBs for the 13 May 2005 event. Each image shows the same flaring region three minutes after the previous image. The flare peak occurs at 16:49 UT. The top row of images show the H $\alpha$  line-center intensity (same as the top row of Figure 4.6). The second row of images show a binary image of the same flaring region after applying the SCB isolation as described in Section 4.3. The third row of images show the detected SCB kernels after the image-analysis algorithm is applied. Identified SCBs are visually separated into three groups to demonstrate how they appear to move when watching an animation of the flare. The red group propagates quickly while the blue and yellow groups develop more slowly.

To more thoroughly understand the nature of SCBs, their measured properties can be studied using two scenarios: (i) each SCB kernel can be considered as an independent and isolated compact brightening; and (ii) each compact brightening can be considered to be fragments of a dynamic system that has a larger structure. This is similar to the approach used for flares. Again, considering both scenarios has its benefits. Identifying kernels as independent elements reveals structural differences in compact brightenings and is discussed in Section 5.2.1. Associating kernels with their contextual surroundings provides some insight into the physical structure causing SCBs. An aggregate assessment of SCBs is addressed in Section 5.2.2. To mitigate the effects of false or marginal detections, only SCBs with intensities two standard deviations above the mean background intensity are considered for characterizing the nature of the ephemeral brightening.

### 5.2.1. Qualities of Individual SCBs

SCBs, although related to erupting flare ribbons, are distinctly different from the flare kernels discussed in Section 5.1. Six SCBs are chosen from the 2005 May 13 event as an example of these ephemeral phenomena. The locations of these six events are letters A - F in Figure 5.14. The  $H\alpha$  normalized intensity of each of these kernels is shown in Figure 5.15. The SCB intensity curve is significantly different from the flare kernel curves shown on the left side of the figure. SCB curves are impulsive; they have a sharp peak and then return to background intensity in the span of about 12 minutes. Nearly all of the SCBs shown here peak in intensity before the peak of the flare intensity curve, shown as a vertical dashed line in Figure 5.15. SCBs B and E both appear to have more internal structure than the other SCBs and last noticeably longer. This is most likely caused by several individual unresolved brightening events occurring in succession.

Over the eleven different events studied, a total of 4,095 unique SCBs were identified and characterized (Table 5.3). Nearly all SCB locations had  $H\alpha$  line center intensities above the mean chromospheric intensity before the brightening event occurred. Commonly intensity enhancements as high as 40 – 60% above the mean quiet chromospheric intensity were observed (an example of which is seen in Figure 5.31). SCBs then brightened to intensities 75 – 130% above that increased initial intensity.

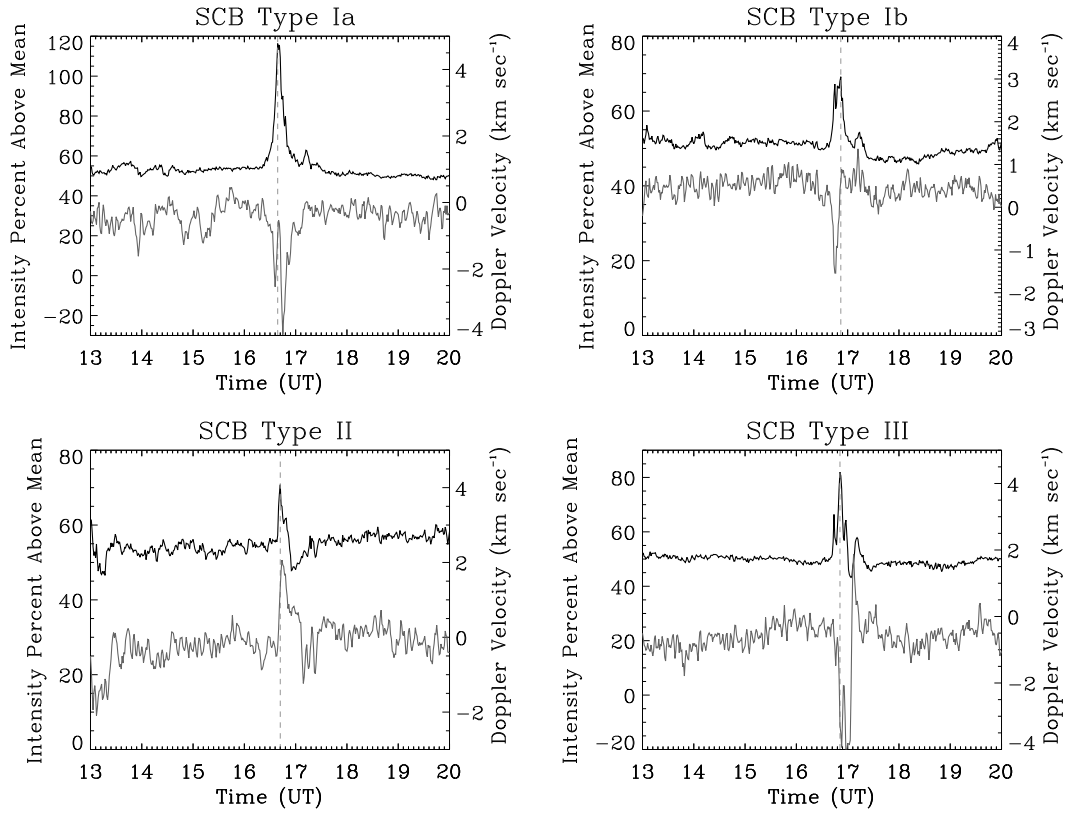


Fig. 5.31.— The line center intensity and Doppler velocity measurements for three different types of SCBs observed. The vertical dashed line marks the peak H $\alpha$  intensity of the associated SCB. A negative Doppler velocity is away from the observer and into the Sun.

Examining the Doppler velocity measurements underneath several SCB locations reveals three distinct types of SCBs (I, II, and III) and two variations within types (*a* and *b*) as defined by Kirk et al. (2012). Figure 5.31 shows examples of each of the types of SCBs and their variations. A type I SCB has an impulsive intensity profile and an impulsive negative Doppler shift of  $1 - 6 \text{ km s}^{-1}$  that occurs close in time to the peak brightening (simultaneously or a few minutes before or after the peak). A negative velocity is defined here as motion away from the observer and into the Sun.

The subtype variations of *a* and *b* describe the timing of the Doppler shift relative to the line center intensity peak. A Doppler type Ia SCB has an impulsive intensity profile as well as an impulsive negative doppler profile which occur simultaneously or a few minutes after the peak brightening. A Doppler type Ib SCB has a similar intensity and Doppler profile as a type Ia, but the timing of the impulsive negative velocity occurs several minutes before the peak intensity of the SCB. The type Ib SCB shown in Figure 5.31 has a negative velocity which peaks 10 minutes before the line center peak intensity.

In contrast to the negative Doppler velocity of a type I, a type II SCB has a positive Doppler velocity perturbation. This velocity is measured to be between  $1 - 4 \text{ km s}^{-1}$  and often lasts longer than the emission in the  $\text{H}\alpha$  intensity profile. The timing of the Doppler shift and intensity peak in type II SCBs are most often coincidental; however, they do exhibit both subtypes *a* and *b*. (Section 5.2.3 shows examples of the subtypes of type II SCBs.) See Figure 5.31 for an example of a type II SCB.

A Doppler type III SCB initially has an impulsive  $\text{H}\alpha$  intensity increase and negative Doppler velocity perturbation much like a type I. As the negative velocity perturbation decays back to continuum levels, there is a dramatic positive velocity shift within a minute or two with a second distinct  $\text{H}\alpha$  brightening. The typical velocity perturbation in a type III SCB is similar to the first two types. Doppler velocity is measured between  $-1$  and  $-5 \text{ km s}^{-1}$  for the initial shift and between  $0.8$  and  $2 \text{ km s}^{-1}$  for the rebound. The positive velocity shift in a type III is always less than the initial negative shift.

The intensity and Doppler profile of a previously identified Moreton wave on 2006 December 6 was characterized to distinguish a type III SCB from wave propagation. The Moreton wave demonstrates variable dynamics similar to SCBs. As it passes over a location, it has an impulsive  $\text{H}\alpha$  intensity line center like other SCBs; however, the Doppler profile of the Moreton wave is distinct. The Moreton wave begins with a positive Doppler shift; then there is an impulsive negative velocity shift, followed by a shift back to a positive velocity before it decays to background levels (Figure 5.32). This ‘M’ shape velocity shift identifies the wave separate from SCBs. Also the magnitude of Doppler velocities associated with the Moreton wave decays as a function of distance from the flare from  $\approx 10 \text{ km s}^{-1}$  near the flare center down to  $\approx 2 \text{ km s}^{-1}$  at the limits of detection. SCBs do not show such a regular intensity decline.

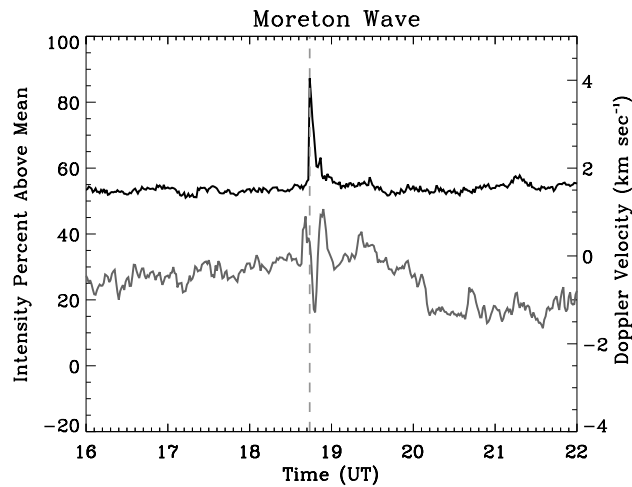


Fig. 5.32.— The  $\text{H}\alpha$  line-center intensity (black curve) and Doppler velocity (gray curve) measurements of a chromospheric brightening caused by a Moreton wave associated with the 2006 flare. The vertical dashed line marks the peak  $\text{H}\alpha$  intensity of the associated compact brightening.

Of all off-flare compact brightenings detected using the automated techniques, on average only 47% of brightenings have a discernible Doppler velocity and are characterized as an SCB. Out of the SCBs that do have an associated Doppler velocity, 42% appear as type I, 45% are type II, and 13% are type III. Both line center brightenings and Doppler velocities are filtered such that positive detections have at least a two standard deviation peak above the background noise determined in the candidate detection. Because of this detection stringency, Doppler measurements with a better signal to noise ratio could produce significantly different statistics.

### 5.2.2. SCBs in Aggregate

Looking at SCBs as a dynamic system gives context to how the eruption evolves. Figure 5.33 shows a duration histogram of all the SCBs measured. The mean duration of an SCB is 9.1 minutes and the median 6.6 minutes. The duration is characterized by the full-width half-maximum of the SCB intensity curve (examples of these curves are shown in Figure 5.15). The most common duration of SCBs is 2 minutes. A histogram of the distribution of the number of SCB events as a function of duration shows an exponential decline in the number of SCB events between 1 and 9 minutes and then a linear decline between 10 and 25 minutes. This suggests the possibility of two populations of brightenings detected: one population that decays quickly and one that has sustained brightening. The duration of SCBs is uncorrelated with both distance from flare center and the peak intensity of the SCB.

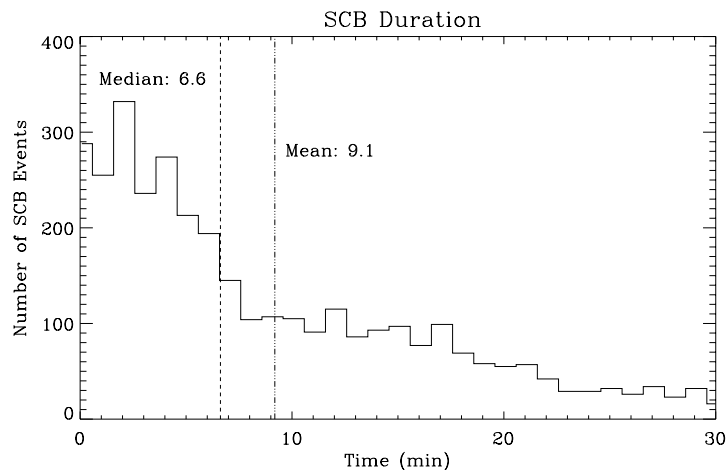


Fig. 5.33.— A histogram of the duration (FWHM) of SCB detections in all 11 events. The SCBs have a measured mean duration of 9.1 minutes (dot-dashed line) and a median duration of 6.6 minutes (dashed line).

Both Balasubramaniam et al. (2006) and Pevtsov et al. (2007) find that SCBs have a strong mono-polarity. To test these findings, photospheric radial magnetic field measurements were taken at the locations of the identified SCBs in GONG magnetograms. Histograms of these magnetic measurements are plotted for each event in Figures 5.34 – 5.44. The means of the magnetic field measurements are also reported in Table 5.3, ranging from  $-6.7$  gauss in the 2003 October 29 event to  $12.7$  gauss in the 2005 May 13 event. If SCBs did exhibit strong mono-polarity, a histogram of magnetic field measurements should have the peak value of the distribution biased toward one polarity. The population of measurements observed did show a weak bias toward one polarity; however, the most common measurement was always  $\pm 0.5$  gauss from 0 in every event except 2005 May 6.

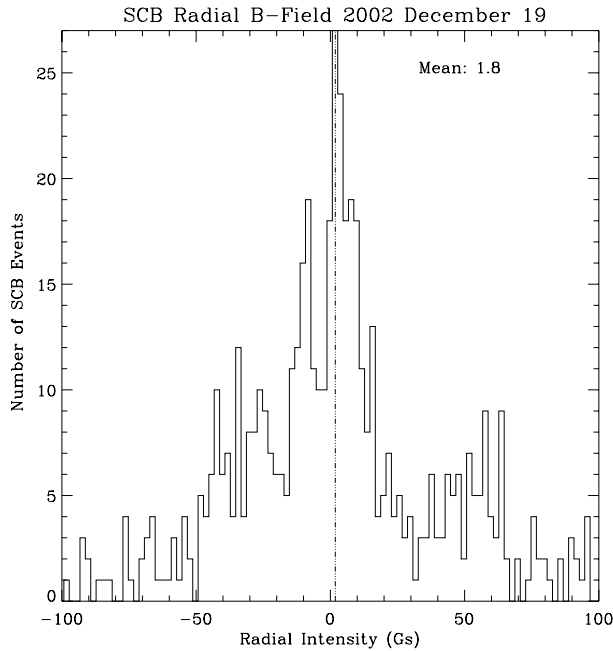


Figure 5.34 The distribution of photospheric radial magnetic field intensities beneath SCBs for the 2002 December 19 event.

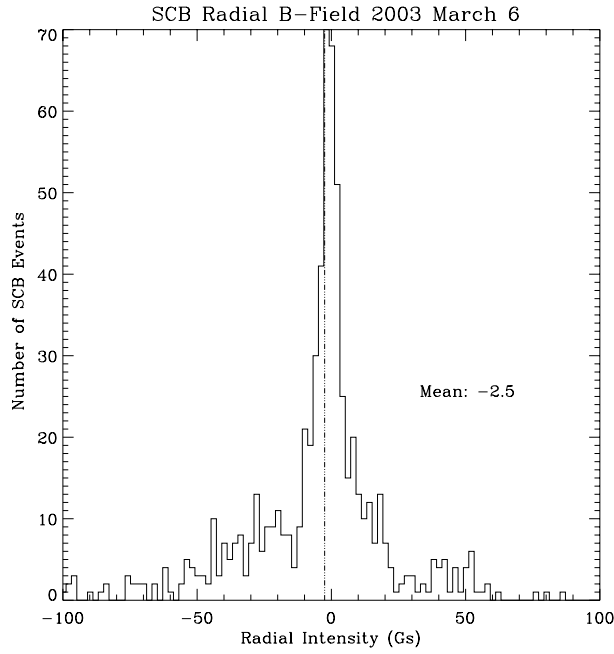


Figure 5.35 The distribution of photospheric radial magnetic field intensities beneath SCBs for the 2003 March 6 event.

Table 5.3. Derived physical measurements for SCBs.

Date	Number of SCBs	Propagation Velocity ( $\text{km s}^{-1}$ )	Aggregate Timing Compared to Flare	B-Field Bias (gauss)
2002-12-19	562	$84.8 \pm 9.7, 260 \pm 19.4$	Before	1.8
2003-03-06	684	$220 \pm 143$	Coincident	-2.5
2003-05-09	57	$73.9 \pm 10.9, -8.5 \pm 3.6$	After	-0.5
2003-06-11	281	$95.7 \pm 40.0, -1684 \pm 1914$	After	1.7
2003-10-29	1335	460, 2423	Coincident	-6.7
2004-11-09	302	–	Before	5.9
2005-05-06	171	$63.0 \pm 15.8$	Before	-4.7
2005-05-13	154	$36.3 \pm 7.2, 153 \pm 55.8$	Coincident	12.2
2006-12-06	291	851	Before	0.5
2010-11-06	210	$65.4 \pm 4.8, 465 \pm 206$	After	-5.9
2010-11-30	48	$51.0 \pm 4.9$	Before	3.6

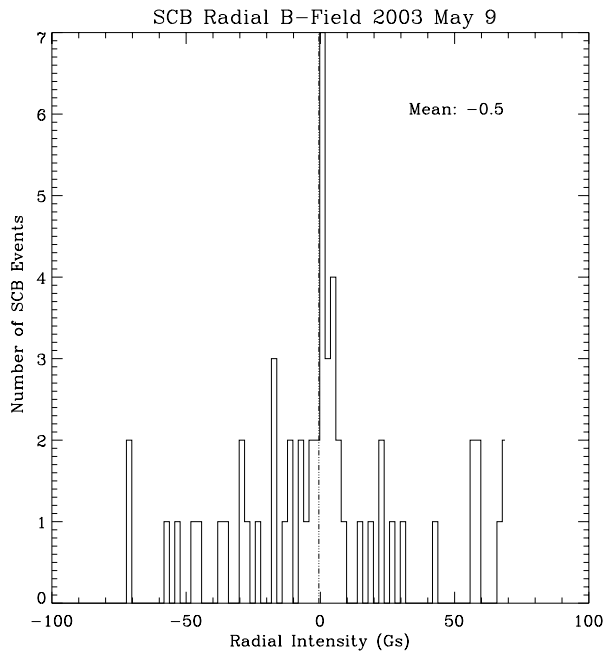


Figure 5.36 The distribution of photospheric radial magnetic field intensities beneath SCBs for the 2003 May 9 event.

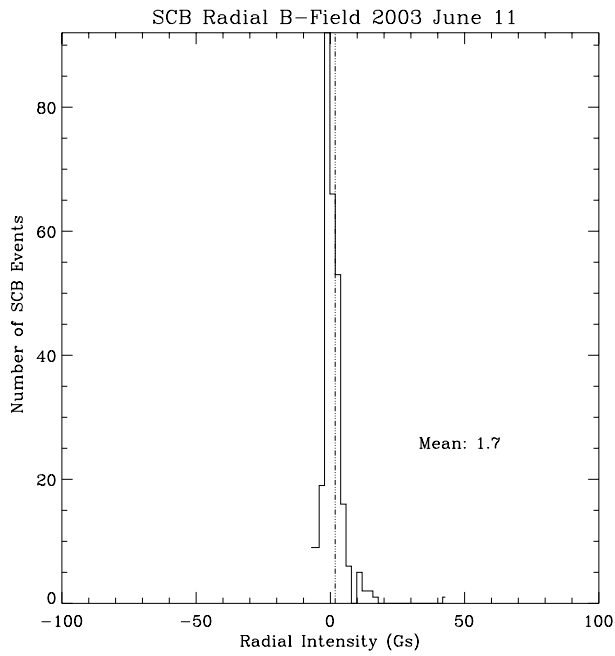


Figure 5.37 The distribution of photospheric radial magnetic field intensities beneath SCBs for the 2003 June 11 event.

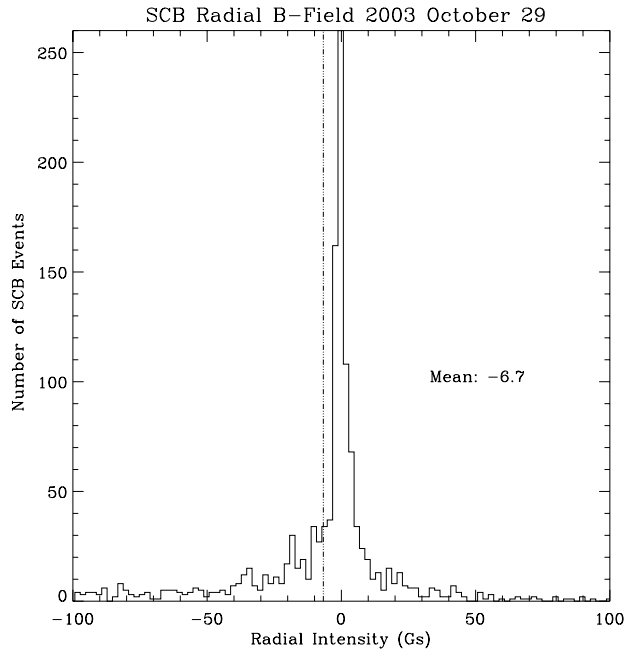


Figure 5.38 The distribution of photospheric radial magnetic field intensities beneath SCBs for the 2003 October 29 event.

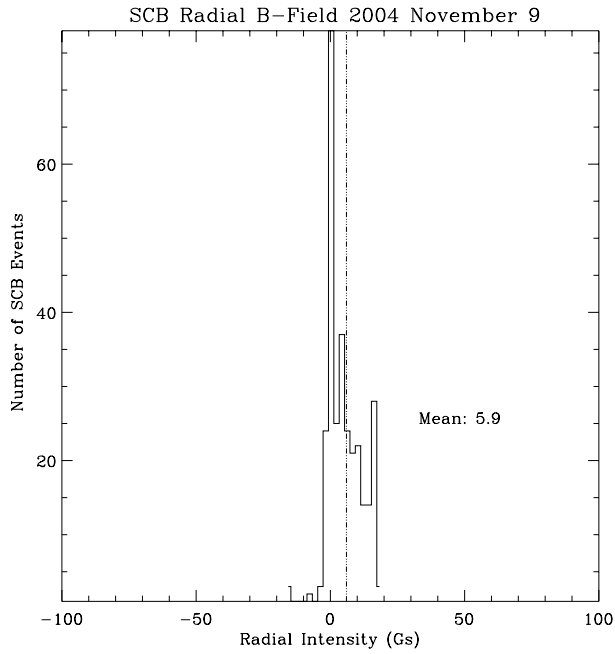


Figure 5.39 The distribution of photospheric radial magnetic field intensities beneath SCBs for the 2004 November 9 event.

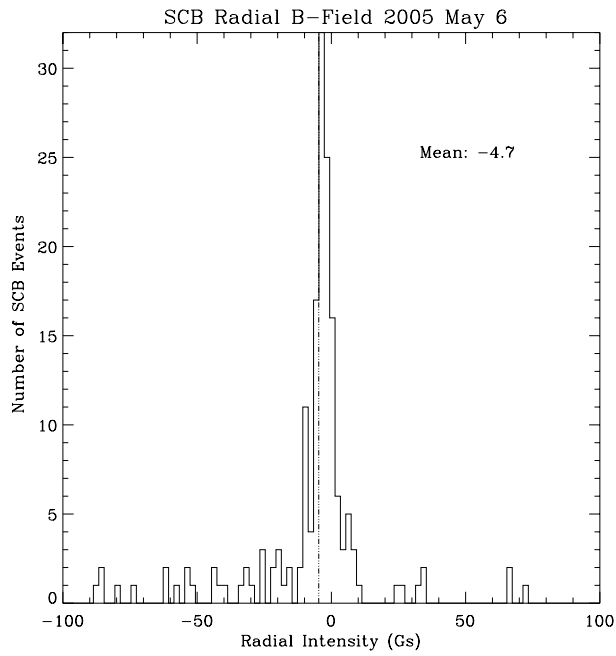


Figure 5.40 The distribution of photospheric radial magnetic field intensities beneath SCBs for the 2005 May 6 event.

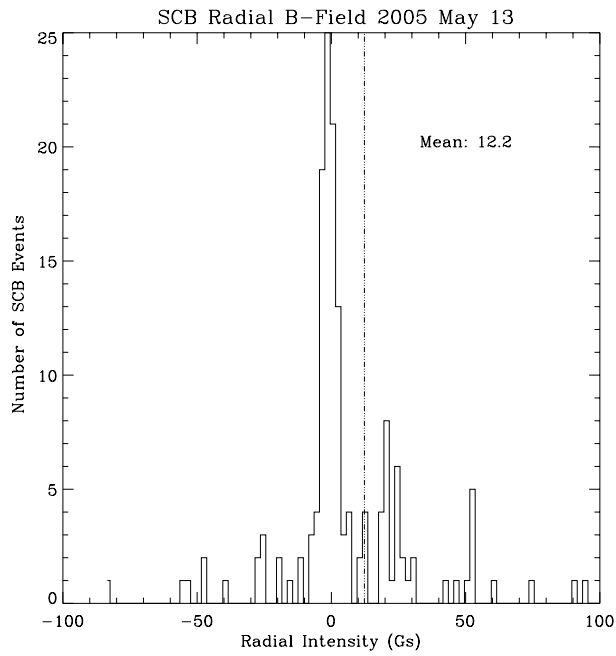


Figure 5.41 The distribution of photospheric radial magnetic field intensities beneath SCBs for the 2005 May 13 event.

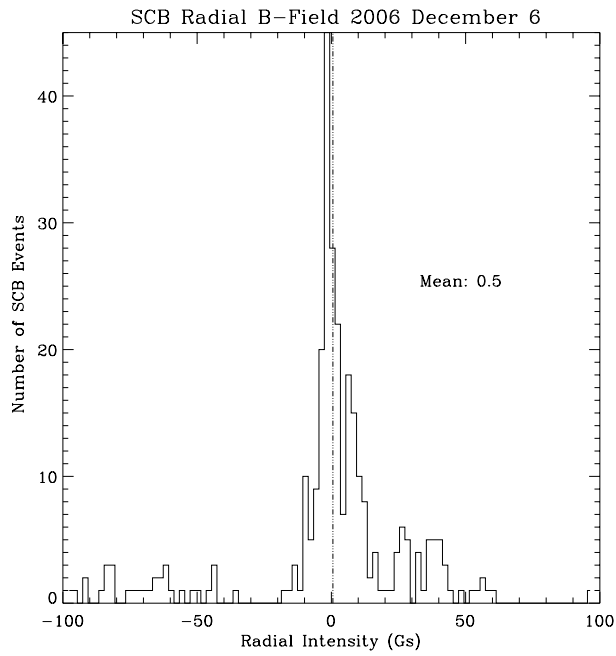


Figure 5.42 The distribution of photospheric radial magnetic field intensities beneath SCBs for the 2006 December 6 event.

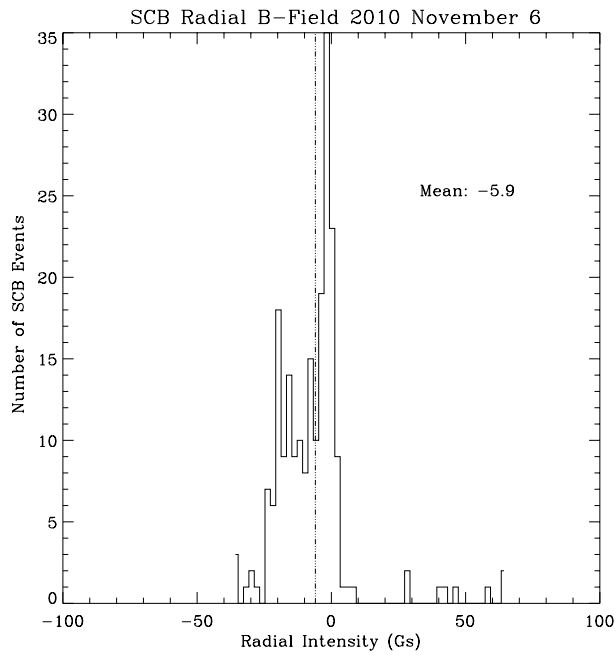


Figure 5.43 The distribution of photospheric radial magnetic field intensities beneath SCBs for the 2010 November 6 event.

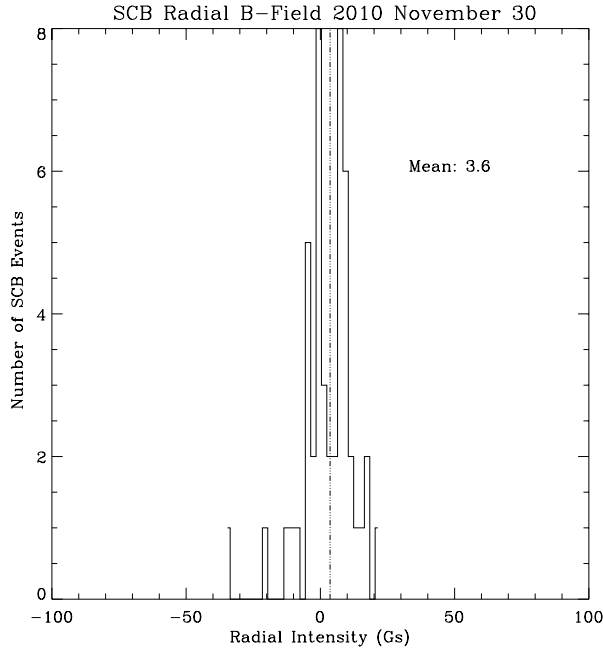


Figure 5.44 The distribution of photospheric radial magnetic field intensities beneath SCBs for the 2010 November 30 event.

The lack of a strong magnetic bias suggests SCBs have a weak mono-polarity. However, the weak bias could also be a result of the quality of the magnetograms. The magnetograms used in this study had one quarter the resolution of the  $H\alpha$  images. The temporal alignment between SCBs and magnetograms was at times several hours different. Also, since the magnetograms only measure line-of-sight magnetic field, the locations of the SCBs on the solar disk have a strong influence on the measured magnetic intensity. The closer the measurements are to the limb, the more tangential the magnetic field measured in the magnetogram and thus closer to zero. A highly inclined magnetic field might also skew measurements, since the magnetic polarity directly beneath the SCB would then not represent the strength of the field line connecting the photosphere to the chromosphere.

Examining individual SCBs' distances from the flare center as a function of time provides a way to extract the propagation trends of SCBs around the flare (Figures 5.45 – 5.55). The bulk of SCBs appears between 50 and 200 Mm away from the associated flare's center in a 1-hour time window around peak flare intensity. At the extremes, SCBs are observed at distances up to  $\approx 600$  Mm from flare center, a solar radius, and  $\approx 2$  hours after the associated flare's intensity maximum. The center of the flare is determined by first retaining pixels in the normalized dataset at least 35% above the mean disk intensity. The filtered images covering the flare eruption are then co-added, and the center of mass of that co-added image is determined to be the "flare center."

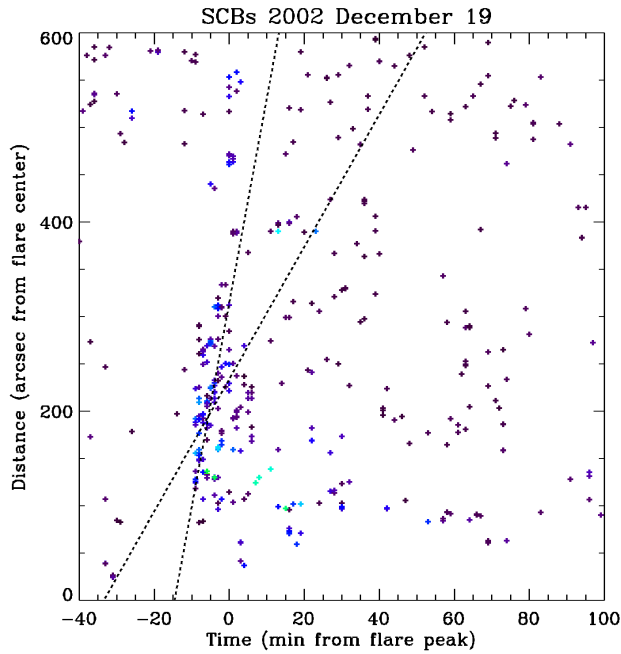


Figure 5.45 The distance at which the bright point occurs versus time from the  $H\alpha$  flare peak for SCB during the 2002 December 19 event. The color of each plotted point is representative of its relative intensity; the dimmest are purple, higher intensity detections are blue and the highest intensity detections are green. The black dashed line shows a weighted regression fit:  $84.8 \pm 9.7$ ,  $260 \pm 19.4 \text{ km s}^{-1}$ .

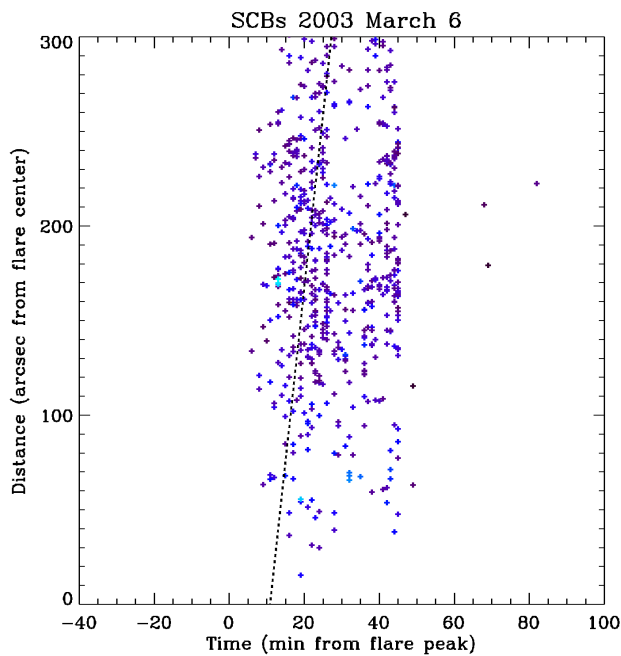


Figure 5.46 The distance at which the bright point occurs versus time from the  $H\alpha$  flare peak for SCB during the 2003 March 6 event. The color of each plotted point is representative of its relative intensity; the dimmest are purple, higher intensity detections are blue and the highest intensity detections are green. The black dashed line shows a weighted regression fit:  $220 \pm 143 \text{ km s}^{-1}$ .

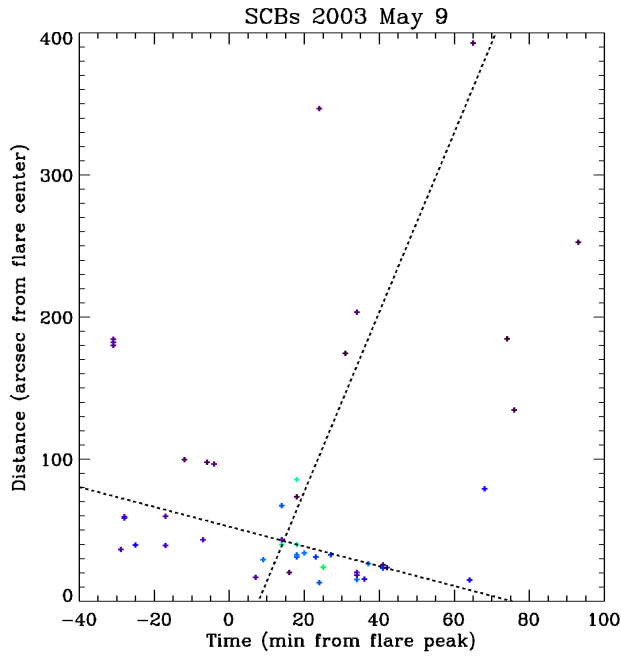


Figure 5.47 The distance at which the bright point occurs versus time from the  $H\alpha$  flare peak for SCB during the 2003 May 9 event. The color of each plotted point is representative of its relative intensity; the dimmest are purple, higher intensity detections are blue and the highest intensity detections are green. The black dashed line shows a weighted regression fit:  $73.9 \pm 10.9, -8.5 \pm 3.6 \text{ km s}^{-1}$ .

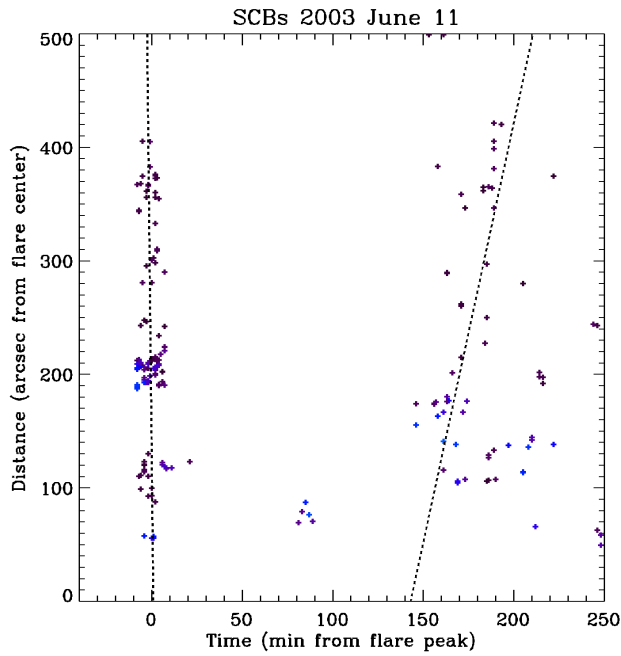


Figure 5.48 The distance at which the bright point occurs versus time from the  $H\alpha$  flare peak for SCB during the 2003 June 11 event. The color of each plotted point is representative of its relative intensity; the dimmest are purple, higher intensity detections are blue and the highest intensity detections are green. The black dashed line shows a weighted regression fit:  $95.7 \pm 40, -1684 \pm 1914 \text{ km s}^{-1}$ .

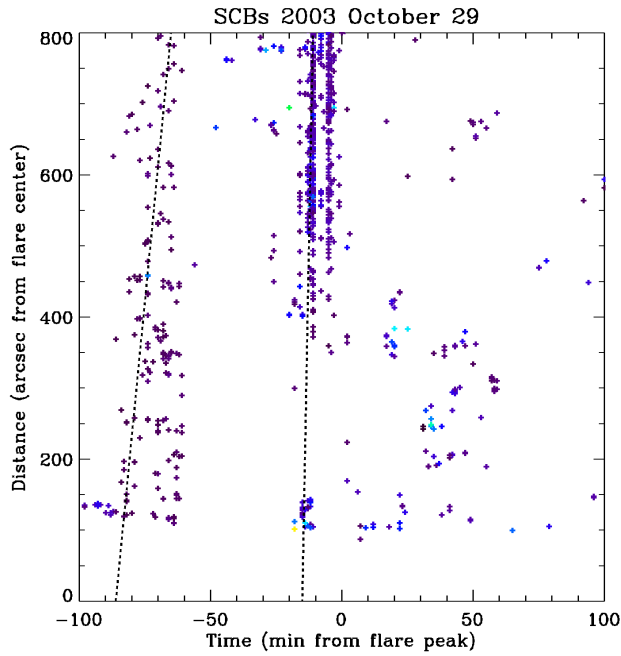


Figure 5.49 The distance at which the bright point occurs versus time from the  $H\alpha$  flare peak for SCB during the 2003 October 29 event. The color of each plotted point is representative of its relative intensity; the dimmest are purple, higher intensity detections are blue and the highest intensity detections are green. The black dashed line shows a weighted regression fit:  $460 \pm \dots, 2423 \pm \dots \text{ km s}^{-1}$ .

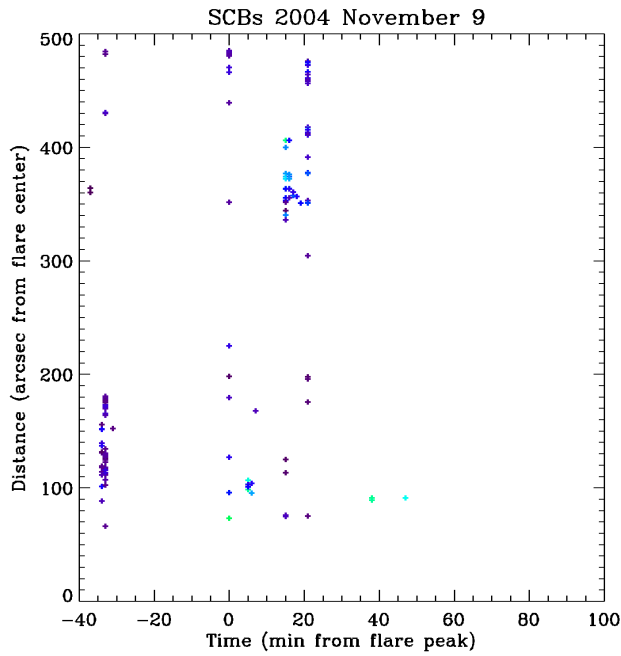


Figure 5.50 The distance at which the bright point occurs versus time from the  $H\alpha$  flare peak for SCB during the 2004 November 9 event. The color of each plotted point is representative of its relative intensity; the dimmest are purple, higher intensity detections are blue and the highest intensity detections are green.

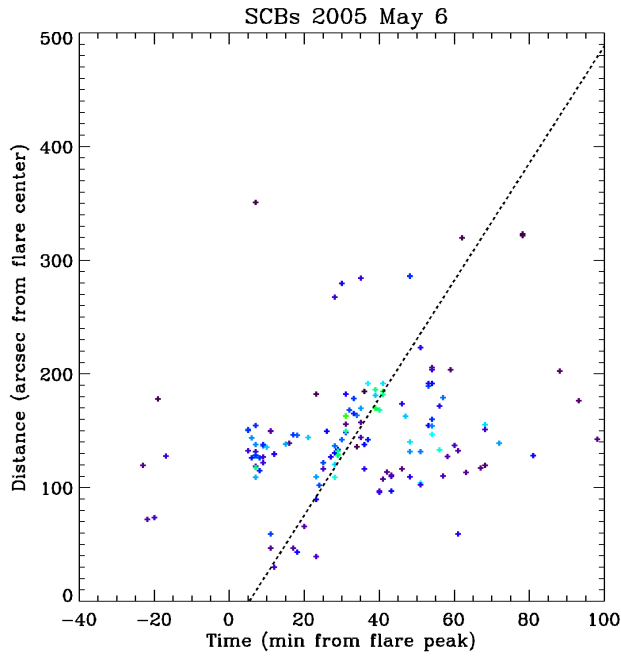


Figure 5.51 The distance at which the bright point occurs versus time from the  $H\alpha$  flare peak for SCB during the 2005 May 6 event. The color of each plotted point is representative of its relative intensity; the dimmest are purple, higher intensity detections are blue and the highest intensity detections are green. The black dashed line shows a weighted regression fit:  $63.0 \pm 15.8 \text{ km s}^{-1}$ .

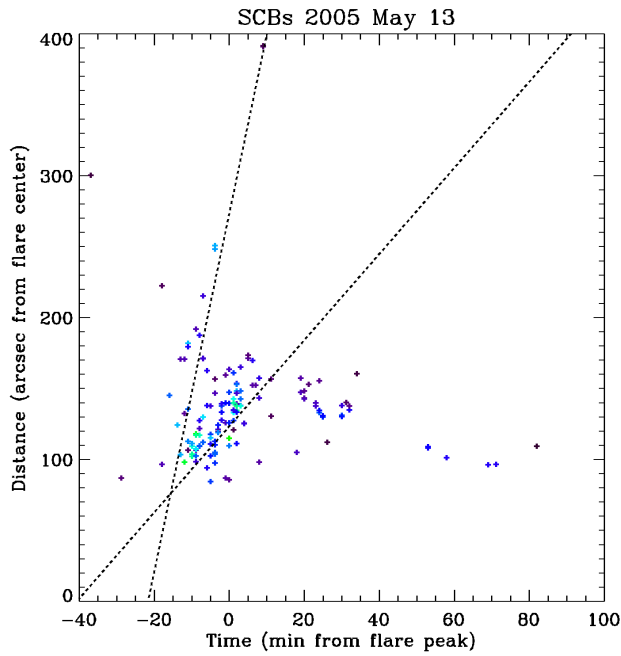


Figure 5.52 The distance at which the bright point occurs versus time from the  $H\alpha$  flare peak for SCB during the 2005 May 13 event. The color of each plotted point is representative of its relative intensity; the dimmest are purple, higher intensity detections are blue and the highest intensity detections are green. The black dashed line shows a weighted regression fit:  $36.3 \pm 7.2, 153 \pm 55.8 \text{ km s}^{-1}$ .

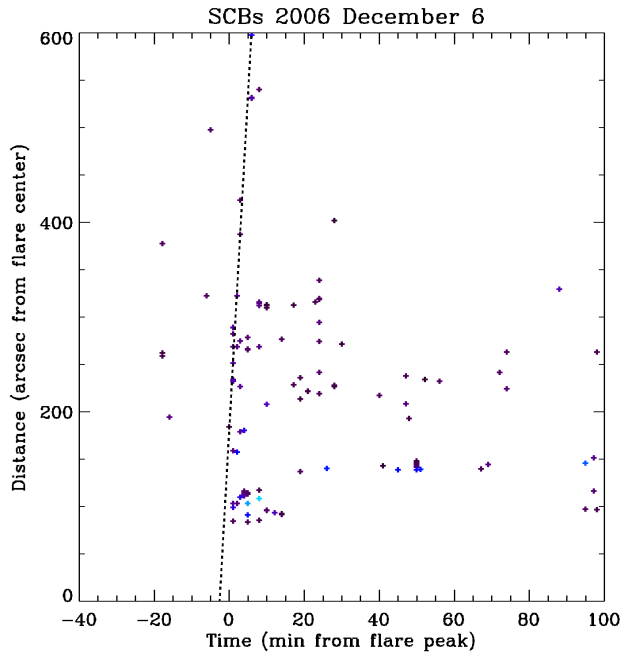


Figure 5.53 The distance at which the bright point occurs versus time from the  $H\alpha$  flare peak for SCB during the 2006 December 6 event. The color of each plotted point is representative of its relative intensity; the dimmest are purple, higher intensity detections are blue and the highest intensity detections are green. The black dashed line shows a weighted regression fit:  $851 \pm - \text{ km s}^{-1}$ .

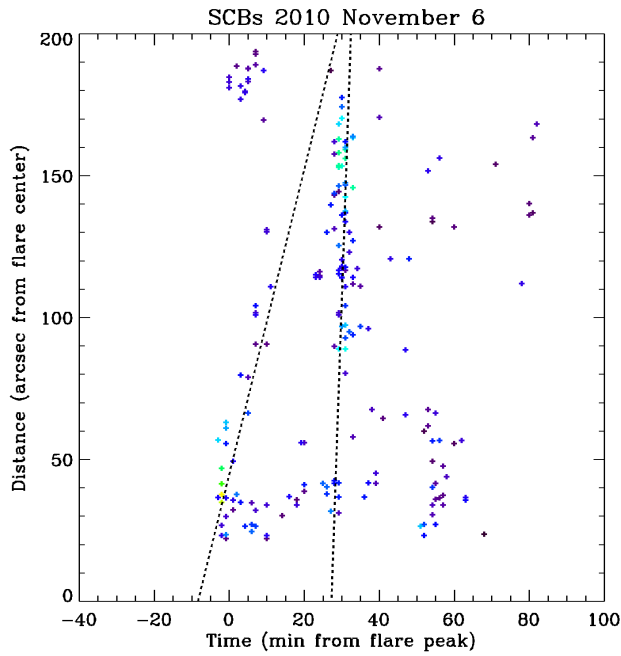


Figure 5.54 The distance at which the bright point occurs versus time from the  $H\alpha$  flare peak for SCB during the 2010 November 6 event. The color of each plotted point is representative of its relative intensity; the dimmest are purple, higher intensity detections are blue and the highest intensity detections are green. The black dashed line shows a weighted regression fit:  $65.4 \pm 4.8, 465 \pm 206 \text{ km s}^{-1}$ .

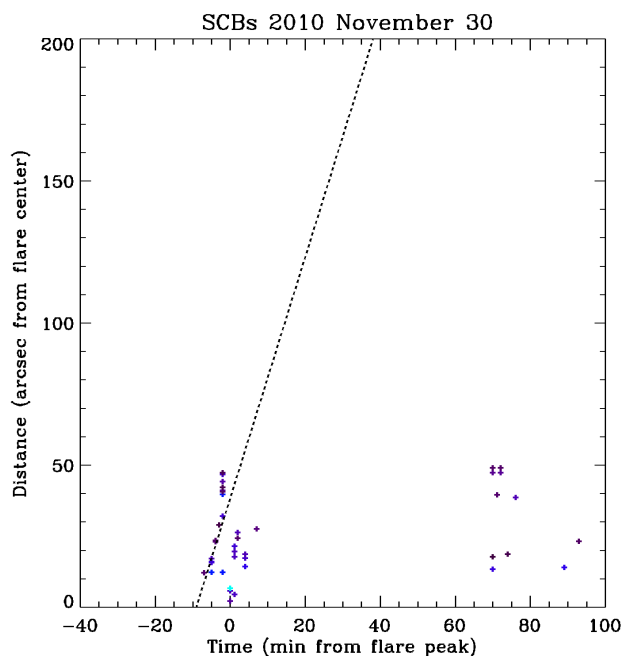


Figure 5.55 The distance at which the bright point occurs versus time from the  $H\alpha$  flare peak for SCB during the 2010 November 30 event. The color of each plotted point is representative of its relative intensity; the dimmest are purple, higher intensity detections are blue and the highest intensity detections are green. The black dashed line shows a weighted regression fit:  $51.0 \pm 4.9 \text{ km s}^{-1}$ .

SCBs tend to cluster together in time-distance plots in all events. In Figures 5.45 – 5.55 the shade of the mark (from violet to red) corresponds to the intensity of the SCB measured. The closer the color of the mark is to red, the brighter the SCB. Generally, the brighter SCBs are physically closer to the flare and temporally occur closer to the flare peak. This intensity correlation is weak and more closely related to distance rather than time of brightening. Statistics from 2003 March 6, 2003 October 29, and 2004 November 9 events are dominated by noise.

To identify each group and characterize its propagation, a slope is fit to these time-distance SCB populations. For this a forward-fitting technique is employed similar to a linear discriminate analysis. This method requires the user to visually identify the number of groups to be fitted and the approximate location of each group. The forward-fitting routine then searches all linear combinations of features for the next “best point” to minimize the chi-square to a regression fit of the candidate group. Repeating this method over all the points in the set produces an ordered set of points that when sequentially fit, have an increasing chi-square value. The derivative of the chi-square curve is then taken. The point in which this curve increases to beyond one standard deviation is selected to divide the candidate group from the rest of the population.

Selecting the groups in the chi-squared curve has the effect of identifying where the goodness of fit begins to decrease dramatically. Running this routine several times, each time selecting the same groups, minimizes the effect of the user and provides an estimate of the error associated with the group identification. This method has two caveats. First, this fitting method relies on the detections having Poissonian noise. This is not necessarily correct, since the detection process of compact brightenings introduces a selection bias. Second, the fitting method makes the assumption that no acceleration occurs in the propagation of SCBs.

This is a reasonable approximation but from studies of Moreton waves in the chromosphere, a constant velocity is unlikely in wave propagation.

Applying the forward-fitting technique to these data sets yields three propagation speeds: slow propagation, fast propagation, and unphysical propagation. The dashed lines in Figures 5.45 – 5.55 visually show the groups identified and Table 5.3 lists the results. Slow propagation of less than  $100 \text{ km s}^{-1}$  was measured in 64% (7 of 11) of the events. Their velocities ranged from  $36.3$  to  $84.8 \text{ km s}^{-1}$  (a tenuous velocity of  $95.7 \pm 40 \text{ km s}^{-1}$  occurred in the 2003 June 11 event). A fast propagation was measured in 55% (6 of 11) of the events. Just two events demonstrated fast propagation without a slow group as well. These fast speeds ranged from  $153$  to  $851 \text{ km s}^{-1}$  and typically had large relative errors associated with them. Two events (2003 June 11 and 2003 October 29) had unphysical propagation groups identified. Both of these measurements were much higher than  $1000 \text{ km s}^{-1}$  and had errors larger than the measurement. The October 29 event was measured at almost 1% the speed of light. The 2003 May 9 event was the only event measured to have a negative propagation velocity, meaning that SCBs were approaching the flare. The implications of these statistics are discussed in Chapter 6.

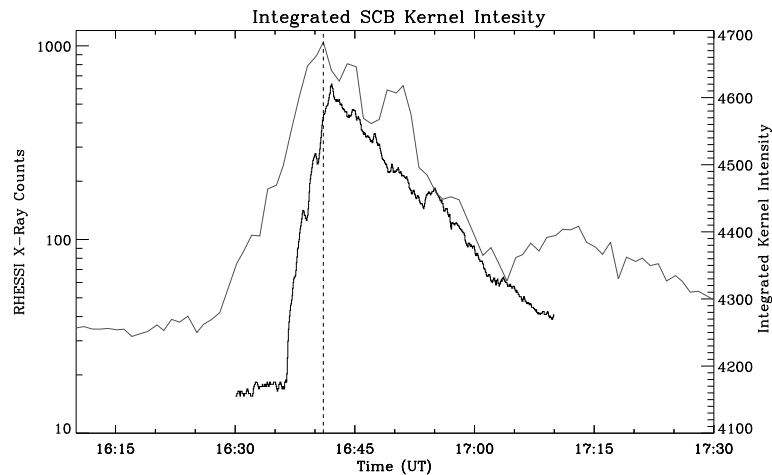


Fig. 5.56.— A plot showing the RHESSI non-thermal 25–50 keV intensity in black and the  $H\alpha$  SCB integrated intensity curve in gray for the 2005 May 13 event. The vertical dashed line indicates the peak of the integrated SCB curve.

The RHESSI satellite measures a spectrum of X-ray intensities that are associated with non-thermal electron emission. On the 2005 May 13 event, RHESSI data coverage begins at 16:37 UT during the impulsive phase of the flare. Comparing the integrated X-ray intensity curve between 25 and 50 keV to the aggregate of SCB intensities integrated over each minute yields some similarities (Figure 5.56). The X-ray intensity peaks about a minute after the integrated SCBs reach their maximum intensity. The decay of both the X-ray intensity and the SCB integrated curves occur approximately on the same time-scale of  $\approx 50$  minutes. The

substructure in the SCB intensity curve is not reproduced by the RHESSI measurements.

### 5.2.3. SCBs in AIA

SDO was launched in early 2010 and is currently providing us with images of the Sun in unprecedented clarity. We selected three wavelengths of AIA to study SCBs from the chromosphere up to the lower corona: 304 Å, 1600 Å, and 1700 Å. A more detailed description of AIA can be found in Section 3.3.1. These wavelengths were selected because of their small emission scale height and coverage of the chromosphere, transition region, and lower corona. Because of the relatively recent launch of SDO, only two events in this study were also observed by AIA: 2010 November 6 and 2010 November 30. The November 30 event is treated separately, since it did not have an associated flare and is discussed further in Section 5.3.

To make the high-resolution images of AIA comparable to ISOON, the AIA images were condensed so that their solar diameter was 1781 pixels, the diameter of the Sun in ISOON. Each of the wavelengths was quiet Sun normalized and de-projected in the same manor as ISOON images. Because of their higher cadence, 1600 Å and 1700 Å images had two and a half times the number of frames as ISOON; and 304 Å had five times as many. Of the 210 SCBs identified in ISOON during the November 6 event, 23% were observed in all four wavelengths ( $H\alpha$ , 304 Å, 1600 Å, and 1700 Å). Figure 5.57 shows a duration histogram of the 49 SCBs measured in AIA. The mean duration of an SCB in AIA is 4.9 minutes and the median is 4.0 minutes – significantly shorter than SCBs observed in  $H\alpha$ .

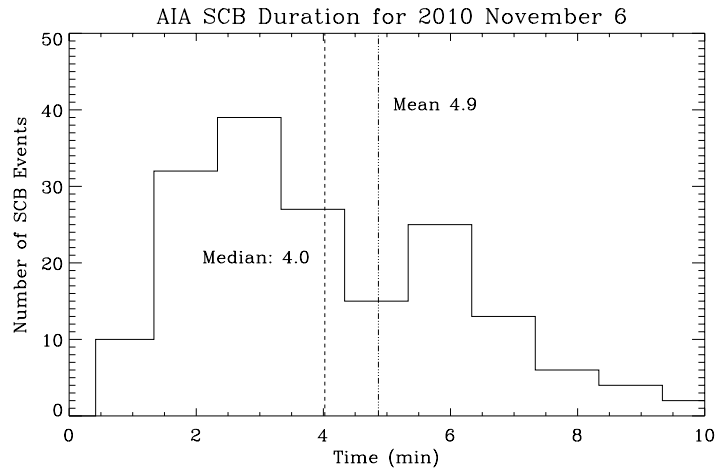


Fig. 5.57.— A histogram of the duration (FWHM) of all SCB detections in AIA. The SCBs in AIA have a measured mean duration of 4.9 minutes (dot-dashed line) and a median duration of 4.0 minutes (dashed line).

All three types and both subtypes were observed in the group of AIA SCBs. Figure 5.58 shows an SCB of type Ia. All three of the AIA wavelengths show much higher contrast than their ISOON counterpart. In this case, all wavelengths have sustained intensity enhancement significantly after the SCB, which is also mirrored by an increase in noise by the Doppler signal.

Figures 5.59 and 5.60 show a type II SCB and both subtypes. In Figure 5.59 all wavelengths as well as the Doppler signal peak within a minute of each other, again highlighting the better contrast in AIA. In contrast, Figure 5.60 shows a type IIb SCB with the Doppler signal peaking two minutes before the intensity peak in 304 Å and six minutes before the peak in H $\alpha$ , 1600 Å, and 1700 Å. It is worth noting that in this case the H $\alpha$  intensity is double peaked: one synchronous with the 304 Å intensity and the second with both 1600 Å and 1700 Å.

Figure 5.61 shows an SCB of type III with a complicated substructure. The Doppler signal abruptly changes from a negative velocity to a positive one; however, the H $\alpha$  intensity is not double peaked as defined in Section 5.2.1. The AIA signals are double peaked with 1600 Å intensity having an absolute maximum first while 304 Å and 1700 Å have local maxima. Six minutes later 304 Å and 1700 Å intensities have absolute maxima while 1600 Å has a local maximum.

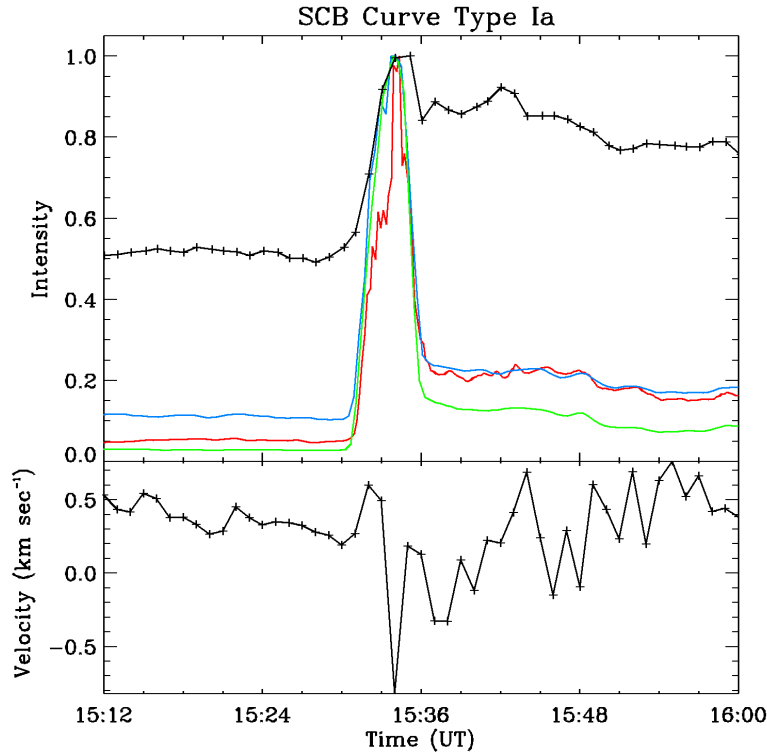


Fig. 5.58.— An SCB of type Ia. The top plot shows the normalized intensity curves: H $\alpha$  in black, 1600 Å in green, 1700 Å in blue, and 304 Å in red. The bottom panel plots the measured Doppler velocity.

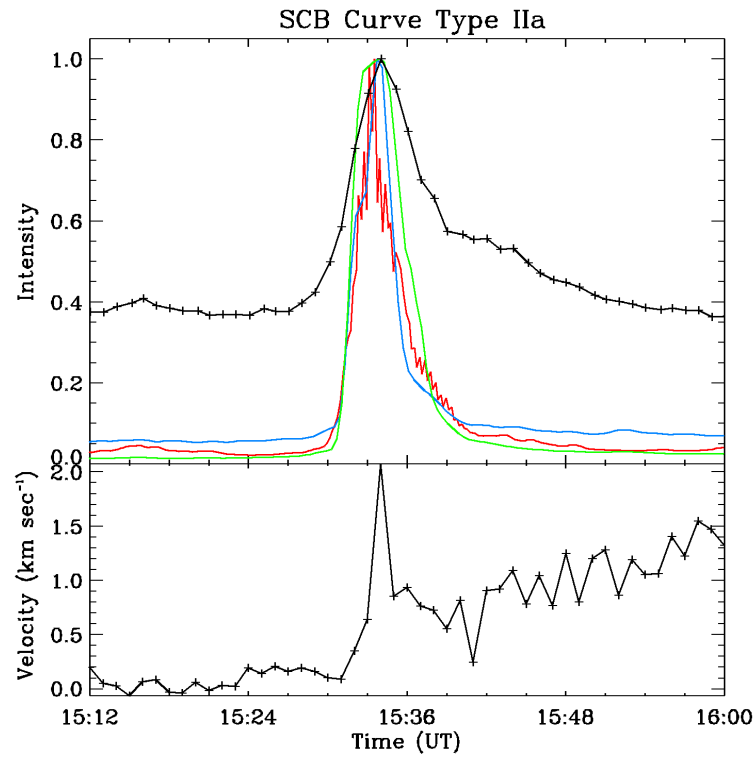


Fig. 5.59.— An SCB of type IIa. The top plot shows the normalized intensity curves: H $\alpha$  in black, 1600 Å in green, 1700 Å in blue, and 304 Å in red. The bottom panel plots the measured Doppler velocity.

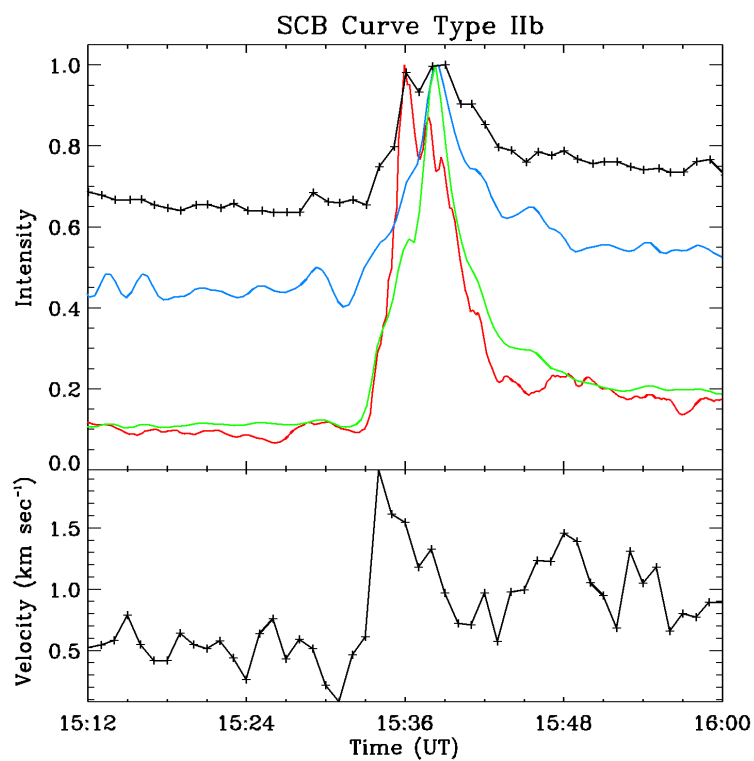


Fig. 5.60.— An SCB of type IIb. The top plot shows the normalized intensity curves:  $H\alpha$  in black,  $1600 \text{ \AA}$  in green,  $1700 \text{ \AA}$  in blue, and  $304 \text{ \AA}$  in red. The bottom panel plots the measured Doppler velocity.

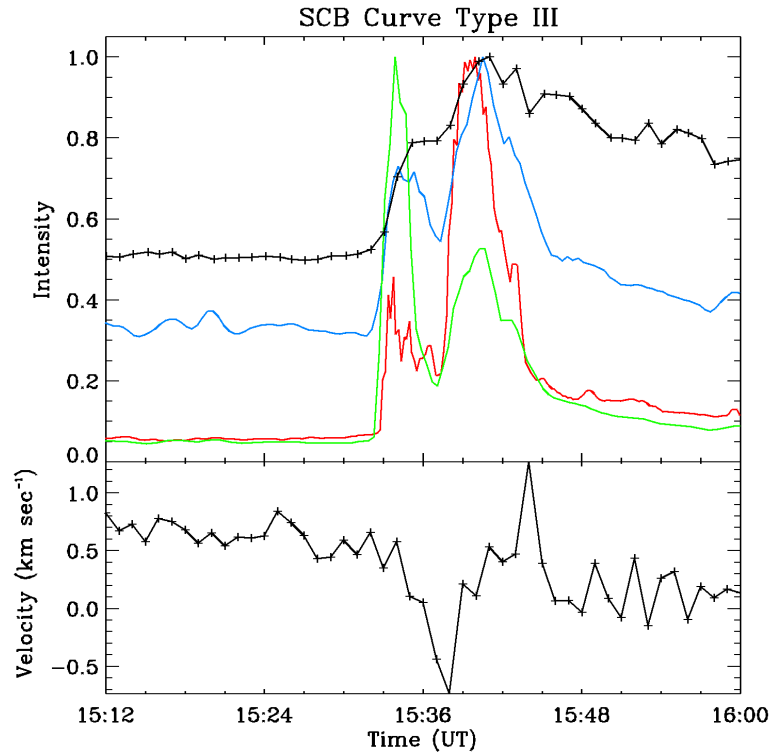


Fig. 5.61.— An SCB of type III. The top plot shows the normalized intensity curves:  $H\alpha$  in black,  $1600 \text{ \AA}$  in green,  $1700 \text{ \AA}$  in blue, and  $304 \text{ \AA}$  in red. The bottom panel plots the measured Doppler velocity.

Not all bright points seen in AIA are also recorded in ISOON. Figure 5.62 shows an example where all three wavelengths observed in AIA show an impulsive brightening lasting 2 – 3 minutes, yet there is no concurrent signal in ISOON’s  $H\alpha$  or Doppler intensities. Spurious bright points in the AIA CCD were accounted for in the preprocessing of AIA data. This bright point has the longest duration in  $1600 \text{ \AA}$ , then  $1700 \text{ \AA}$ , and the most impulsive is  $304 \text{ \AA}$ .

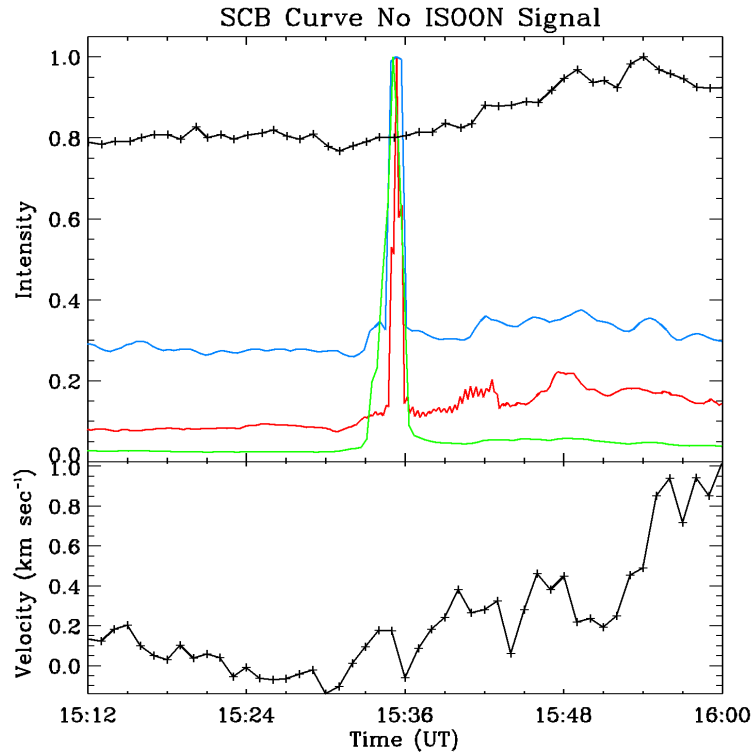


Fig. 5.62.— An example of a compact brightening in AIA but not in ISOON. The top plot shows the normalized intensity curves:  $H\alpha$  in black,  $1600 \text{ \AA}$  in green,  $1700 \text{ \AA}$  in blue, and  $304 \text{ \AA}$  in red. The bottom panel plots the measured Doppler velocity.

The timing of SCBs in AIA are slightly delayed from those measured in ISOON. A histogram of the delay between the peak intensity of  $H\alpha$  and the peak intensity of AIA wavelengths is shown in Figure 5.63. The average delay between AIA and ISOON is slightly different depending on wavelength:  $304 \text{ \AA}$  has a delay of 1.5 minutes;  $1600 \text{ \AA}$  a 1.6 minute delay; and  $1700 \text{ \AA}$  a 1.0 minute delay. The median delay is almost the same:  $304 \text{ \AA}$  is 1.3 minutes,  $1600 \text{ \AA}$  is 1.3 minutes, and  $1700 \text{ \AA}$  is 0.7 minutes. A given SCB in all three AIA wavelengths exhibits an intensity maximum occurring typically between one and two frames later than the ISOON  $H\alpha$  intensity maximum.

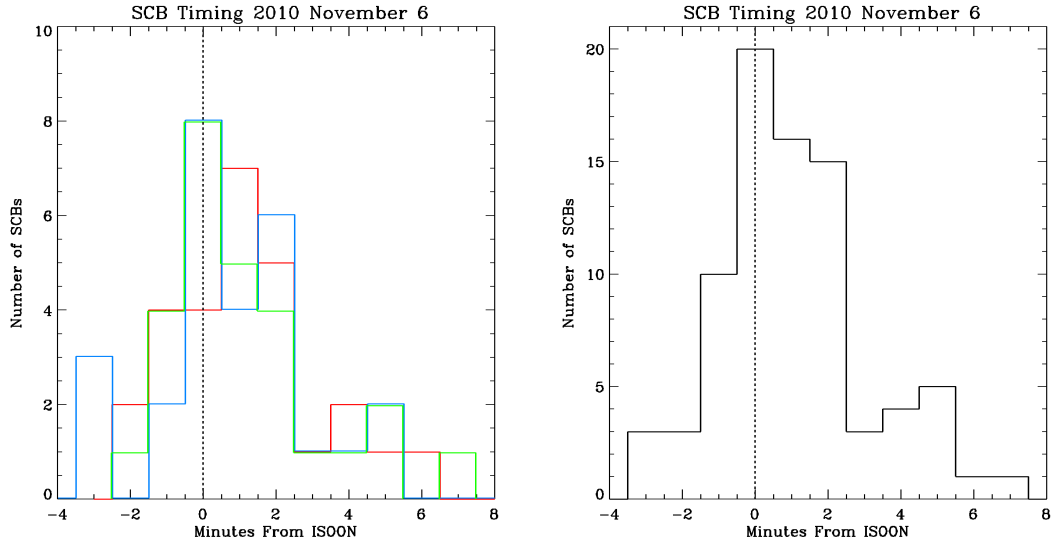


Fig. 5.63.— Histograms showing the relative timing of SCB in  $H\alpha$  as compared to AIA. The vertical dashed line marks the events coincident with  $H\alpha$  peak intensity. Left: timings broken down by wavelength:  $1600 \text{ \AA}$  in green,  $1700 \text{ \AA}$  in blue, and  $304 \text{ \AA}$  in red. Right: Cumulative timing for all events observed in AIA.

### 5.3. The Curious Hyder Flare

Originally termed a *disparition brusque*, Hyder (1967) proposed a phenomenological model for a flare-like brightening seen after a filament eruption that occurs away from an active region. These events are now called Hyder flares and represent a class of low-energy eruptions which brighten the solar atmosphere yet do not have the high energetics of a solar flare. Hyder flares can range in appearance from a string of bright knots to a two-ribbon flare. In all cases the brightening appears parallel to and on one or both sides of the filament channel. Differing from typical flares, Hyder flares develop much more slowly, taking from 30 to 60 minutes to rise to peak intensity. In some cases they also sustain an enhanced intensity level for several hours.

The physical mechanism for producing a Hyder flare begins with initially stable filaments lying in a magnetic trough (Figure 5.64). Through a perturbation and reconfiguration of the magnetic field, the magnetic trough becomes a magnetic ridge, and the filamentary material is accelerated into the corona. However, a portion of the filament's material is not ejected and falls down, impacting the lower atmosphere. The symmetry of the resultant chromospheric brightening reflects the symmetry of the infall process. This infall can therefore produce a double parallel ribbon, single ribbon, or only bright knots if the infall is sporadic. From this model, the falling material is estimated to reach speeds of  $50 - 215 \text{ km s}^{-1}$ , which is sufficient to provide the required energy for the brightening (Hyder 1967).

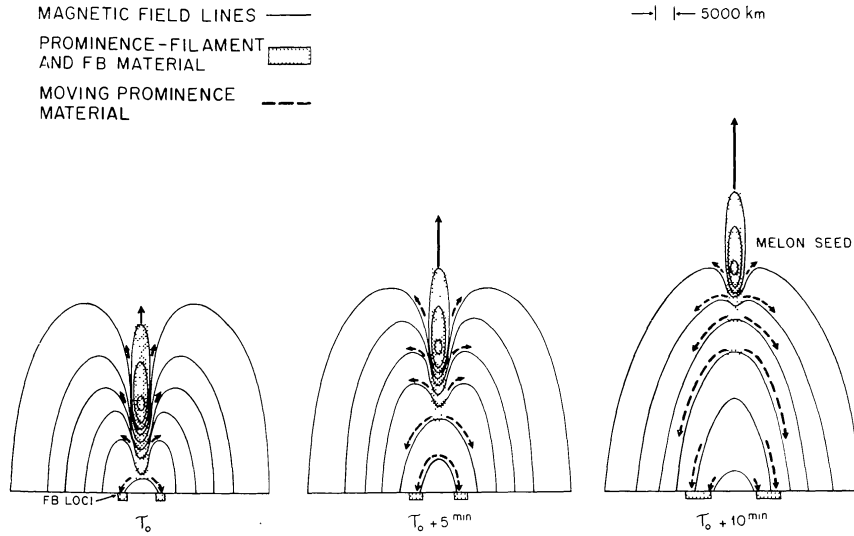


Fig. 5.64.— A phenomenological model describing the physical evolution of a Hyder flare (Hyder 1967).

ISOON and AIA observed an event on 2010 November 30 that had the characteristics of a Hyder flare. A filament eruption began at 17:35 UT in a quiet region of the Sun and appeared to evolve like a slow two-ribbon flare over the following two hours (Table 5.1). A CME was observed in LASCO concurrent with the timing and angle of the filament eruption. To characterize the November 30 Hyder flare, the bright point algorithm was applied to identify and track the evolving ribbons. Figure 5.13 shows the aggregated flare and SCB intensity curves over-plotted on GOES X-ray intensity. It is immediately apparent that neither GOES or the flare tracking observes much more than noise. The SCB curve has a double peaked structure, reflecting the visual evolution of the Hyder flare. Brightening is first observed with the liftoff of the filament at 17:35 UT and then a second peak, reflecting two-ribbon separation, which follows an hour later.

Individual brightenings tracked during the November 30 event appeared similar to SCBs. The observed SCBs were of type I and II, had Doppler perturbations between  $-0.4 \text{ km s}^{-1}$  and  $0.6 \text{ km s}^{-1}$ , and a 3.6 gauss radial magnetic field bias (Figure 5.44). They had a radial extent of about 35 Mm from the center of the Hyder flare. Using the same forward-fitting analysis described in Section 5.2.2, we measured a ribbon propagation velocity of  $51 \pm 4.9 \text{ km s}^{-1}$  (Figure 5.55). These measurements are summarized in Table 5.3 and are consistent with the other SCB measurements made.

The November 30 event in AIA wavelengths looked remarkably similar to the event in  $H\alpha$ . The Hyder flare can be observed in every AIA wavelength except 1700 Å and 4500 Å both of which have strong continuum contributions. The AIA 94 Å channel images plasma at  $10^{6.8}$  K, and the 131 Å channel has contributions of  $10^{7.2}$  K plasma but lower temperatures as well. Both of these images show enhanced intensity due to the Hyder flare. However GOES does not measure any

emission in  $1 - 8 \text{ \AA}$  soft X-ray channel. Assuming a purely thermal emission of plasma, we can use Wein's displacement law to estimate that the infalling material had an emission temperature of 6 and 8 MK and reached depths well into the chromosphere.

## 6. INCORPORATING DATA AND PHYSICAL CONTEXT

*The fringe benefits are priceless: clean air to breath (after the spring sand storms); stillness, solitude and space; an unobstructed view every day and every night of the Sun, sky, stars, clouds, mountains, moon, cliff rock and canyons; a sense of time enough to let thought and feeling range from here to the end of the world and back; the discovery of something intimate – though impossible to name – in the remote.*

– Edward Abbey (1988)

From the results of the tracking method, we can gain insight into the physical processes at the root of SCBs and chromospheric flares. The method itself contributes new insights into how flares evolve. The flare ribbons studied are both spatially and temporally separated into discrete kernels. The relatively smooth ribbon motions observed in  $H\alpha$  and the nearly ideal exponential decay characterized in X-ray flux measurements belie the substructure that makes up a two-ribbon flare. The substructure of the measured flares is discussed in Section 6.1. The measurements of SCBs imply that the brightening in the flare ribbons is caused by a distinctly different physical process than the one causing SCBs. In other words, SCBs are not micro-flares and should be examined on their own. Our interpretation of the physical origin of SCBs is addressed in Section 6.2.

### 6.1. Two-Ribbon Flares In and Out of the Chromosphere

Flare kernels are observed to appear and disappear as the underlying flare ribbons evolve, as discussed in Section 5.1.1. Examining individual kernel structure suggests there is substructure within a flare ribbon whose elements impulsively brighten and dim within the brightness that encompasses the intensity curve. These results support the premise that flares are made up of several magnetic field lines reconnecting (e.g., Priest & Forbes 2002). There is no evidence to claim an individual flare kernel is directly tracking a loop footpoint. Within a tracked flare kernel, multiple coronal reconnection events are superimposed to produce the observed asymmetries of a single flare kernel’s light curve. To investigate the underlying physical dynamics of flares, we characterize the diffusion and expansion of flare ribbons in Section 6.1.1, and then we use that knowledge to constrain reconnection in Section 6.1.2.

#### 6.1.1. Diffusion and Expansion

Maurya & Ambastha (2010) tracked subsections of an X17 flare occurring on 2003 October 28. They reported peak speeds ranging from  $\approx 10 - 60 \text{ km s}^{-1}$  (depending on the spatially tracked part of the flare) over the observed span of 13 minutes. Maurya & Ambastha (2010) also reported that the total apparent distances the ribbons traveled were  $\approx 10^4 \text{ km}$ . The October 28 flare is almost

an order of magnitude greater in X-ray intensity than the largest flare considered for this study. In the present study, despite this difference, peak speeds of flare kernels observed in this work are measured between  $34.0 - 53.7 \text{ km s}^{-1}$  and the mean velocity of kernels is between  $6.2 - 7.9 \text{ km s}^{-1}$ . The velocity of the flare kernels did not correlate with GOES flare class. The maximum distance that an individual flare kernel traversed was  $\approx 4 \times 10^4 \text{ km}$ , and the average distance traveled was  $\approx 5 \times 10^3 \text{ km}$ ; both of these values are similar to the X17 flare studied. The velocities of the flare ribbons studied here are very similar to the velocities measured by Maurya & Ambastha (2010). It is worth noting that the one to four orders of magnitude difference in the GOES peak intensity between the October 28 flare and the flares studied here implies that the apparent velocities and distance traveled by flare ribbons are not dependent on the energy released in the eruption.

Ignoring the complex physics that generate and govern solar flares, they are simply nonlinear energy dissipation processes. They can be characterized by their spatiotemporal evolution, or in other words, comparing their changing apparent geometric size over time. Knowledge of this evolution provides insights relating scaling laws to the physical parameters that govern the evolving system. The tracking algorithm outlined in Section 4.1.2 makes use of this to probabilistically determine the most likely location an identified particle has moved to. To characterize the flaring system as a whole, we can conceptualize the flare as an expanding circle with an area equivalent to that of the flare. This conceptualization gives us a hypothetical radius of the flare [ $\mathcal{R}$ ] as a function of an arbitrary time step [ $\tau$ ]:

$$\mathcal{R}(\tau) \propto \tau^{\beta_d/2} \quad \begin{cases} \beta_d < 1 & \text{(sub-diffusion)} \\ \beta_d = 1 & \text{(classical diffusion)} \\ \beta_d > 1 & \text{(super-diffusion)}, \end{cases} \quad (6.1)$$

where  $\beta$  is called the diffusive exponent (Aschwanden 2012). The diffusive exponent defines the type of diffusion the system experiences. A diffusive exponent equal to one is classical diffusion (i.e., Brownian motion); less than one is sub-diffusive (i.e., diffusion through a porous medium); and greater than one is considered super-diffusive or a Lévy flight where Brownian motion is interrupted by large

Table 6.1. Characteristics of expansion for flare ribbons.

Event Date	GOES Class	Peak Expansion $\text{Mm}^2 \text{ s}^{-1}$	Mean Expansion $\text{Mm}^2 \text{ s}^{-1}$	Radial Expansion $\text{Mm s}^{-1}$	Diffusive Exponent [ $\beta$ ]
2002-12-19	M2.7	89.4	26.8	2.9	0.78
2003-03-06	None	110.6	12.9	2.0	0.90
2003-05-09	B6.6	25.2	4.8	1.2	0.60
2003-06-11	M1.8	35.7	7.9	1.6	1.42
2003-10-29	X10.0	93.1	17.6	2.4	1.32
2004-11-09	M8.9	35.0	8.7	1.7	0.58
2005-05-06	C8.5	64.8	14.6	2.2	0.42
2005-05-13	M8.0	28.4	5.3	1.3	0.28
2006-12-06	X6.5	18.5	3.9	1.1	0.74
2010-11-06	M5.4	22.2	3.3	1.0	0.54

jumps. In this case, the surface area of the flare is calculated through summing the tracked flare kernels described in Equation 5.4. The peak and mean expansion rates of the flare derived by calculating the flare area is listed in Table 6.1.

We were able to derive the diffusive parameter  $[\beta_d]$  for each of the events studied (Table 6.1). All of the flares studied were sub-diffusive except two: 2003-06-11 and 2003-10-29. Both of these events are imbedded in a complex active region where one eruption can trigger sympathetic flaring in other regions of the field of view (Figures 5.6 and 5.7). This causes a condition well characterized by a Lévy flight where individual cases of classical diffusion or sub-diffusion are driven by electromagnetic flows, in this case occurring in the corona. Excluding these two super-diffusive cases, the mean diffusive parameter is  $\beta_d = 0.61 \pm 0.20$ . This finding agrees with that of Aschwanden (2012) that most flares operate in the sub-diffusive regime with  $\beta_d = 0.53 \pm 0.27$ . The sub-diffusive characteristic is likely to reflect chains or clusters of energy release during the flare and anisotropic plasma heating in the low plasma- $\beta$ , magnetically dominated coronal plasma.

### 6.1.2. Constraints on Reconnection

The bulk of the apparent motion and acceleration in the flare ribbons is observed after the peak of the flare intensity. Integrating this into the dynamical model of a two-ribbon flare (Demoulin & Priest 1988) implies that the peak energy release of the flare occurs in the low lying arcade and loses intensity as the X-point reconnection progresses vertically to higher levels (Baker et al. 2009). The measured divergence of the ribbons dominates the motion of the kernels, but there is significant measured flow tangential to the flare ribbons. This measured flow is almost certainly not a physical flow of material but suggests that there is lateral propagation to the X-point as well as vertical propagation.

The quiescent solar corona is highly anisotropic due to the dominance of the magnetic field in the low plasma  $\beta$  regime. In a solar flare, we are observing a 2-D projection of the heated plasma caused by an X-point reconnection diffusing through 3-D space. If the flare was imagined to be diffusive throughout an isotropic 1-D volume, then  $\mathcal{R}(\tau) \propto \tau^{1/4}$  or  $\beta_d = 1/2$  (Aschwanden 2012). Our observational result of sub-diffusion ( $\beta_d \approx 0.6$ ) in the 2-D projection of the flare suggests that the triggering of subsequent magnetic reconnection events occurs along anisotropic 1-D paths. In other words, the X-point follows 1-D paths in 3-D space as it propagates. Since Aschwanden (2012) measured the diffusion in coronal flares and found the diffusion exponent to be roughly the same as this study, we can surmise that the motion of the X-point dominates the overall diffusion of the flare process from the corona down through the chromosphere, regardless of the changing environment.

## 6.2. The Root of Sequential Chromospheric Brightenings

The results of Chapter 5 suggest tracking kernels through the evolution of the erupting flare can characterize several different physical phenomena that make

up the evolving active region. We confirm the results of Kirk et al. (2011) that tracking ephemeral brightenings surrounding the flare aggregates several different physical phenomena. To separate these different events, we use Doppler velocities. This kernel tracking technique is also able to follow a wavefront progression with a sufficient number of detections to characterize its deceleration. Section 6.2.1 incorporates the measured data into a phenomenological model of how SCBs originate in flares. Section 6.2.2 discusses using a PFSS model to extrapolate SCB locations into the corona. Measurements of SCBs in the context of chromospheric evaporation is covered in Section 6.2.3. Finally in Section 6.2.4, we use the quantitative measurements and modeling of SCBs to constrain the CME release mechanism in the cases studied.

### 6.2.1. Heuristic Modeling

The simplest conceptual model of an SCB is a volume of heated chromospheric plasma. Combining this idea with the physical parameters measured, it is possible to calculate how long this volume would take to radiatively cool from its heated state back down to its quiescent state. Let us imagine an SCB to be a cylinder of plasma with a radius of  $1.6 \times 10^6$  m and a height of  $3 \times 10^5$  m. This gives it a surface area  $[A]$  of  $1.9 \times 10^{13}$  m<sup>2</sup>. The rate of radiative emission from a hot surface is given by the Stephan-Boltzmann law:

$$\frac{dE}{dt} = \epsilon \sigma A (T_{\text{hot}}^4 - T_{\text{ambient}}^4) \quad (6.2)$$

where  $\epsilon$  is the emissivity of the body and  $\sigma$  is the Stephan-Boltzmann constant. If we assume the energy of the SCB is purely translational kinetic energy and integrate the Stephan-Boltzmann law, we can derive the cooling time:

$$t_{\text{cooling}} = \frac{Nk_B}{2\epsilon\sigma A} \left( \frac{1}{T_{\text{final}}^3} - \frac{1}{T_{\text{hot}}^3} \right) \quad (6.3)$$

where  $N$  is the number of particles in the system. Let us further assume that the SCB is made up of a fully ionized plasma and that the electrons are responsible for the bulk of the heat. Thus, we can treat the SCB as a volume of electrons with a chromospheric density of  $10^{-8}$  kg m<sup>-3</sup> that has been heated. If the SCB is heated to  $10^4$  K, it would take  $\approx 35$  seconds for it to cool back down to  $5 \times 10^3$  K. The radiative cooling curve is so steep near the beginning, if we imagined the SCB to be heated to  $10^7$  K, it would only take  $\approx 45$  seconds to radiatively cool to  $5 \times 10^3$  K. This calculation is neglecting the ambient temperature; however, ambient temperature has little impact on the result, since the hot temperature is orders of magnitude greater than the ambient temperature.

This simplistic model is far from physical because the chromosphere is not completely ionized; electrons are not singularly responsible for the temperature of an SCB; thermal conductivity is not infinite; and other heat transfer processes are ignored. This model does provide a lower bound to the cooling time of SCBs. Antiochos & Sturrock (1978) take a more nuanced approach to cooling times,

accounting for both radiative and thermal cooling in evaporative plasma. They find a chromospheric cooling time to be  $\approx 30$  seconds. Separately, Giovanelli (1978) calculates a chromospheric relaxation time of  $\approx 1.5$  minutes in the low chromosphere up to  $\approx 6$  minutes in the upper chromosphere. In our simplistic model as well as two more careful calculations, we find that chromospheric hot spots should dissipate in  $0.5 - 1.5$  minutes –significantly shorter than the 8.3 minute median SCB duration. This means that SCBs are actively heated over a significant portion of their lifetime and not caused by one isolated heating event.

The slopes plotted in Figures 5.45 – 5.55 show two different groups of propagation speeds for SCBs: ‘slow’ ( $36 - 85 \text{ km s}^{-1}$ ) and ‘fast’ ( $> 150 \text{ km s}^{-1}$ ). The sound speed in the chromosphere is approximately  $c_s \approx 10 \text{ km s}^{-1}$  (Nagashima et al. 2009), while the Alfvén speed in the upper chromosphere is approximated to be  $v_A \approx 10 - 100 \text{ km s}^{-1}$  (Aschwanden 2006). Both of the SCB propagation speeds are significantly above the approximated sound speed. The ‘slow’ propagation speeds fall reasonably well into the range of the chromospheric Alfvén speed; however, the ‘fast’ propagation is higher than the Alfvénic velocity. Because a propagating wave front is not observed, and ‘fast’ propagating SCBs appear to move at speeds much faster than Alfvénic velocity, the driving mechanism for SCBs most likely originates and propagates in the corona.

Assuming the propagation speed of non-thermal plasma along the loop line is consistent between flare loops, the different propagation speeds would then imply different populations of loops being heated as the flare erupts. A simple loop configuration without localized diffusion or anomalous resistance implies that the length of the loop is directly proportional to the travel time of the electron beam. Thus the ‘slow’ and ‘fast’ propagation groups result from different physical orientations of over-arching loops. The time it takes to observe a chromospheric brightening can therefore be described as:

$$\tau_{\text{SCB}} = \gamma \frac{L}{v_e}, \quad (6.4)$$

where  $\tau_{\text{SCB}}$  is the time it takes for accelerated plasma to travel from its origin in the corona, along the magnetic loop lines, impact the chromosphere, and produce a brightening;  $L$  is the length of the magnetic loop before perturbation;  $v_e$  is the electron velocity along the loop line; and  $\gamma$  is a function of changing diffusion and resistance between chromosphere and corona. In physical scenarios,  $v_e$  is a function of the specific environment.

On 1971 October 22, Hyder et al. (1973) observed flare-like intensity enhancements in the line core of Ca II and H $\alpha$  without any continuum enhancement. The brightenings were observed to have a diameter of about 1 arcsec, a rise to peak intensity of about 5 seconds and a duration of about 20 seconds. To explain these events, Hyder et al. (1973) used a model invoking the precipitation of high-energy particles from the corona. They go on to state that “it may be an increase or decrease in the number of these flare-points that defines ordinary flare characteristics.” Although these observations were not in the vicinity of an erupting flare, they provide context to the SCB events. SCBs are measured to have a size and duration approximately two to three times greater than these events but otherwise have a similar behavior implying a similar origination.

A useful model must incorporate the precipitation of high-energy particles, origination of SCBs in the corona, the coronal propagation of SCBs, and the appearance of SCBs from the chromosphere ( $H\alpha$ ) to the transition region ( $HeII$  and  $CIV$ ). Figure 6.1 is a proposed phenomenological model of the overlying physical topology. SCBs are hypothesized to be caused by electron beam heating confined by magnetic loop lines overarching flare ribbons. As the flare erupts, magnetic reconnection begins in a coronal X-point and propagates vertically on a 1-D path. As the flare reaches its maximum intensity, the CME generated is accelerated into the outer corona, the remaining loop arcade produces a two ribbon flare, and the overarching loops reconfigure to a new equilibrium position. This reconfiguration accelerates plasma trapped within the loops, impacting the denser chromosphere and causing observed brightening. Thus the ‘slow’ and ‘fast’ propagation groups are formed from different populations of loops having differing lengths. The longer loops contribute to the ‘slow’ propagation groups, while the ‘fast’ propagation groups are dominated by shorter loops, possibly driven by other mechanisms such as Moreton waves.

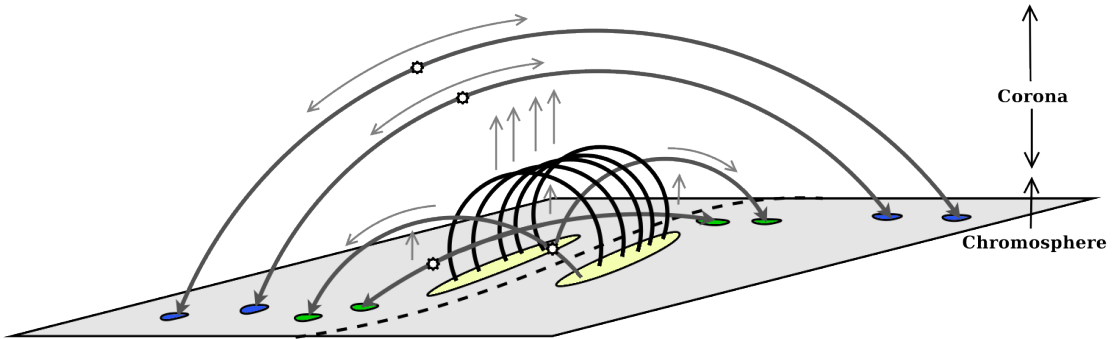


Fig. 6.1.— A phenomenological model of the trigger mechanism for SCBs. A dashed line marks the neutral line in this model. The central loops represent the emerging two ribbon flare arcade. The arches represent field lines connecting outside of the chromospheric flare ribbons (in yellow). The arrows on top of both the loops and arches show the direction trapped plasma flows as the flare begins to erupt, and the stars suggest the location where the plasma is disrupted. Once perturbed, the trapped plasma streams down the loop lines and impacts the chromosphere, causing the  $H\alpha$  intensity brightening. The different orientations of off-flare loops accounts for the different propagation speeds of SCB groups observed and indicated by blue and green marks.

Timing differences between  $HeII$  and  $CIV$  as compared with  $H\alpha$  are significant, as they can give us clues as to how the chromosphere is heated in an SCB. The peak intensity of SCBs observed in  $304 \text{ \AA}$  and  $1600 \text{ \AA}$  both occur on average  $\approx 1.5$  minutes later than the  $H\alpha$  intensity peak. The duration of SCBs in the transition region are also significantly shorter: 4.3 minutes in the transition region as compared with 8.3 minutes in the chromosphere. While some of the difference could be accounted for through the higher temporal resolution and better contrast of AIA, the difference in duration suggests a chromospheric phenomenon propagating from chromosphere upward to the corona. Since the brightening originates

near the line formation height of  $H\alpha$ , it takes time to propagate upwards to the corona, leading to a shorter duration and a delay in time in the transition region lines. The relatively few events (23% of ISOON) observed in AIA also points to this process, since only a portion of SCB events have enough energy to propagate vertically to the transition region.

### 6.2.2. PFSS Modeling

We used a potential field source surface (PFSS) model from Schrijver & De Rosa (2003) to investigate the coronal magnetic field above SCBs (see Section 3.4.3 for the theoretical foundation of the PFSS model). The locations of SCBs are identified on photospheric magnetograms and used as the starting point for the model. The result is a localized map of the magnetic field lines around SCBs (Figure 6.2). The results of this modeling are in Table 6.2. An average field line derived from an SCB was a relatively consistent length of  $0.20 \pm 0.09 R_{\odot}$ , and the maximum line length averaged  $0.96 \pm 0.32 R_{\odot}$  and never exceeded  $1.45 R_{\odot}$ .

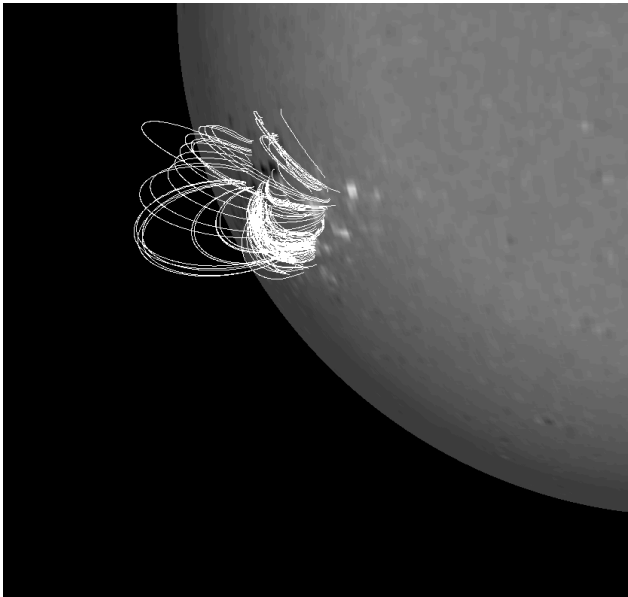


Figure 6.2 An example of the magnetic field lines above SCBs modeled using a PFSS approach from 2010 November 6.

Although a PFSS model of coronal magnetic field is not an accurate predictor for the local magnetic field lines surrounding a dynamically changing eruption for reasons discussed in previous chapters, some general conclusions can be made from this model. First, over 99% of the lines modeled were closed, and of the closed lines, none reached beyond  $1.45 R_{\odot}$ . This means that the mechanism for driving SCBs is most likely in the lower corona between  $0.1$  and  $0.3 R_{\odot}$ . Second, there is no correlation between field line length and intensity or duration of SCB. This lack of correlation means that the strength of the magnetic field is not driving the intensity or duration of brightening. Third, only a loose correlation is observed between the distance of SCB from the flare center and field line length (Figure 6.3). No long field lines are found close to flare center, and short field lines are most

likely to be found near the flare. This lack of strong correlation between distance and line length suggests that the heuristic model presented in Figure 6.1 is most likely an over-simplified schematic of the eruption.

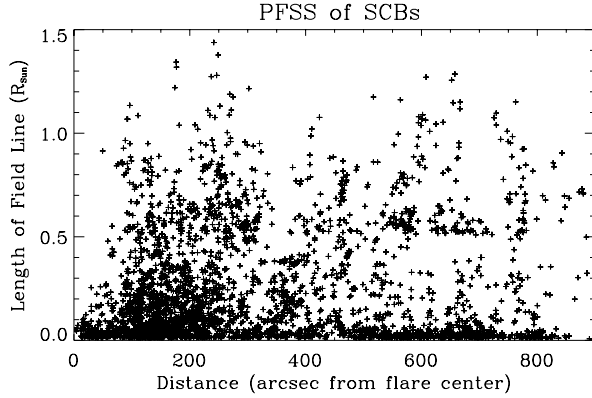


Figure 6.3 A plot of the PFSS modeled magnetic loop lengths versus the associated SCB's measured distance from flare center for all SCBs recorded.

### 6.2.3. Chromospheric Evaporation

Examining single SCBs, the coincident Doppler recoil with the  $H\alpha$  intensity presents a contradiction. If an SCB is an example of compact chromospheric evaporation (e.g., Dennis & Schwartz 1989), then the only Doppler motion should be outward – the opposite of what is observed. Figure 6.4 presents a possible solution to this. Since the scattering length of electrons is significantly smaller than that of protons, the electron beam impacts the mid-chromosphere and deposits energy into the surrounding plasma, while the protons penetrate deeper. This deposited heat cannot dissipate effectively through conduction or radiation and thus expands upward into the flux tube. To achieve an expansion with rates of a few  $\text{km s}^{-1}$  as observed, the chromospheric heating rate must be  $E_H \leq 10^{10} \text{ erg cm}^{-2} \text{ s}^{-1}$  (Fisher et al. 1984). As a reaction to this expansion, a reaction wave propagates toward the solar surface in the opposite direction of the ejected plasma. Since the Doppler measurements are made in the wings of the  $H\alpha$  line, the location of the Doppler measurement is physically closer to the photosphere than the  $H\alpha$  line center. Thus the observer sees the heating of the  $H\alpha$  line center and coincidentally observes the recoil in the lower chromosphere.

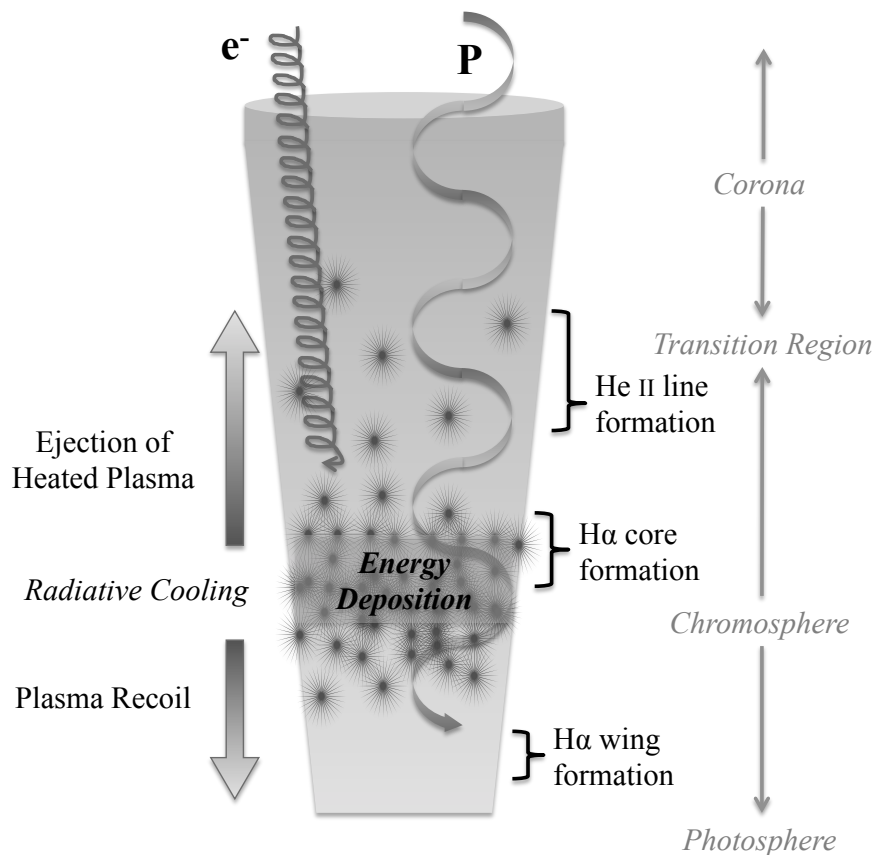


Fig. 6.4.— A diagram of the physical dynamics occurring in a single SCB. Electrons and protons accelerated by magnetic reconfiguration further up in the corona come streaming down the flare loop. Since the mean free path of electrons is significantly less, the electrons deposit energy into the upper chromosphere. Unable to radiate the energy as heat, the chromosphere responds by expanding and sending material back up the flux tube (chromospheric evaporation) and a recoil propagates toward the photosphere.

In type II SCBs an up-flow is observed. This is an example of a classic chromospheric evaporation, where the heated plasma in the bulk of the chromosphere is heated and ablated back up the flux tube to a quasi-stable state in the newly reconfigured magnetic loop. In contrast, the type III class of SCB shown in Figure 5.31 presents an interesting anomaly to both the other observed SCBs and the model proposed in Figure 6.4. Since there is an initial down-flow, the beginning state of type III SCBs is similar to type I SCBs. As the recoil is propagated, a continual bombardment of excited plasma (both protons and electrons) impacts the lower chromosphere, causing ablation and changing the direction of flow.

As an alternative to the scenarios proposed above, a low energy model is also plausible. In this model, like the last, an incident beam of high energy

particles heats a volume of plasma to a temperature hotter than its surroundings. Unable to radiate the input energy as heat, the density of the heated plasma decreases. In contrast to the ablation scenario of the other model, this heating smoothly expands the volume of the plasma vertically, confined by the magnetic flux tube. Eventually the plasma is able to radiate the additional energy and the material condenses back down to its original position. If the expansion takes place below the formation height of  $H\alpha$ , we observe an outward velocity. However if the expansion takes place above the height of the  $H\alpha$  line, we would observe a negative velocity as the expanding material pushes downward. The velocity reversal in a type III SCB is a product of cooler material ‘filling in’ after the hot material dissipates. This model would also explain the shorter duration of SCBs observed in the transition region as the material expands through the chromosphere to reach the transition region and then condenses out of it while still significantly hotter than the chromosphere.

#### 6.2.4. Implications for Mass Ejection Release

Nine of the eleven events in this study had visible CMEs associated with the eruptions. Balasubramaniam et al. (2006) also found a strong correlation between CMEs and the presence of SCBs, with 14 out of 18 events having measurable CMEs. This high correlation between CMEs and SCBs suggests that the release mechanism for CMEs and the origin of SCBs are causally connected. This supposition is bolstered by the case study of the Hyder flare (Section 5.3). The Hyder flare produced a CME and SCBs without an active region or conventional flare eruption. The topological model proposed in Figure 6.1 supports the *storage and release* mechanisms of CMEs release while contradicting the *directly driven* models.

Figure 6.1 hypothesizes highly sheared magnetic field lines enclosing the active region at the initiation of the flare. These overarching loops are analogous to the higher lying, unshredded tethers in the *tether release* and *tether straining* CME models. As the flare erupts, the CME escapes into interplanetary space, the remaining loop arcade produces a two ribbon flare, and the tethers reconfigure to a new equilibrium position through either reconnection or relaxation. The tether reconfiguration releases trapped plasma to impact the chromosphere. The other *storage and release* model, *mass loading*, necessitates a build up of mass above the CME to be perturbed thus releasing the CME. SCBs are the chromospheric impact of the mass loaded into the metastable magnetic fields in the *mass loading* model. This description implies the driver of SCBs is equivalent to the driver of a CME. The Hyder flare is an example of this model where the mass-loaded metastable field is perturbed and a CME released without a flare as a catalyst.

The correlation of CMEs and SCBs does not support the two *directly driven* models. In the *thermal blast* model, thermal pressure is the driver of a CME. In that case, we would expect to see a correlation between the strength and propagation velocity of SCBs to scale with the energy release of flares. We observe no such connection between the energy released in the flare and propagation speed of SCBs. The *dynamo-driven* model uses buildup of magnetic fields to stress the corona into releasing a CME. In that scenario we would expect correlation between

the measured parameters of SCBs and localized magnetic field strength. We do not observe such a correlation between the magnetic strength in SCBs and the release of a CME.

Table 6.2. Characteristics of magnetic loops derived by the PFSS model for the photospheric magnetic field beneath SCBs.

Event Date	Mean Length ( $R_{\odot}$ )	Maximum Length ( $R_{\odot}$ )	Minimum Length ( $R_{\odot}$ )
2002-12-19	0.25	1.19	0.009
2003-03-06	0.30	1.44	0.010
2003-05-09	0.13	0.81	0.014
2003-06-11	0.18	0.91	0.012
2003-10-29	0.21	1.28	0.005
2004-11-09	0.26	0.86	0.011
2005-05-06	0.13	0.94	0.010
2005-05-13	0.19	1.09	0.009
2006-12-06	0.39	1.13	0.009
2010-11-06	0.10	0.33	0.012
2010-11-30	0.09	0.53	0.011

## 7. FINDINGS AND FUTURE DIRECTIONS OF THIS WORK

*It matters to me  
Took a long time to get here  
But if it would have been easy  
I would not have cared*  
– Jim James (2011)

In the preceding chapters we have first discussed the current understanding of eruptions on the Sun, how they affect the Earth, and the methods used to observe differing phenomena in the solar atmosphere. Next, we have outlined a software suite designed to identify and track bright kernels in and around flares. We have then applied that software to eleven eruptive events to make measurements of how the dynamic environment changes in the midst of a flare. The amount of energy released in these events spanned several orders of magnitude. Finally, we have incorporated the data extracted from the flares into statistical and phenomenological models of how flares erupt and the physical origin of SCBs. In this chapter Section 7.1 summarizes these results and formalizes the properties of a typical SCB. Section 7.2 concludes with a brief discussion of extensions for, and a future direction to, the study of SCBs.

### 7.1. Summary of Results

Solar flares have been studied in  $H\alpha$  by several generations of researchers. The community has long understood that two-ribbon flares expand and compact brightenings exist along the side of them. What sets this work apart from the accomplishments of the past is the use of automated tools to make precise measurements. Automated analysis has the ability to objectively search a large set of data and extract an overwhelming amount of metadata about the evolution of that data. This allows the researcher to better remove the human bias from generating statistics about tracked phenomena. Both the large amount of data, combined with an objective tracking method, allows this work to begin to create assimilation models that bridge data from  $H\alpha$  flares and compact brightenings into a better theoretical understanding of solar eruptions.

#### 7.1.1. Chromospheric Flares

Tracking flare kernels through the evolution of the erupting flare can characterize the evolving active region. We also demonstrate that a sum of the components of the flare ribbon reproduces the total intensity curve of the flare. Although it is not possible to say that any given kernel is tracking one specific flare loop, the flare kernels dissect the flare into its smallest visibly resolvable components in the ISOON  $H\alpha$  dataset. Since the number of detectable kernels declines as the

flare’s intensity decays, the overall intensity of the flare is related to the number of ribbon components discernible at any given time.

The velocities and distance traveled by the tracked ribbons are measured to be  $6.2 - 7.9 \text{ km s}^{-1}$  and  $5 \times 10^3 \text{ km}$ , which are consistent with previous measurements. The distance and velocity measurements do not scale with the X-ray intensity of the flare. The magnitude of the instantaneous velocity of the flare ribbons is coincident with the intensity peak, but the bulk of the apparent motion in the flare ribbons appears in the declining phase. These results suggest that X-ray intensity is not a good measure of energy released in the flare despite its ubiquity in flare size classifications.

Analyzing the spatiotemporal evolution of flare ribbons, we find most events to expand at a sub-diffusive rate. The diffusive exponent is found to be  $\beta_d = 0.61 \pm 0.20$ , which is consistent with diffusive measurements made of flares in the corona. The sub-diffusive result suggests that the triggering of magnetic reconnection in flares occurs along anisotropic 1-D paths that propagate horizontally as well as vertically. Since the diffusive nature of flares is not dependent on the atmospheric layer in which the flares are observed, the propagation of the reconnection point dominates the overall diffusion of the flare.

### 7.1.2. *Sequential Chromospheric Brightening*

SCBs are a special case of chromospheric compact brightenings that occur in conjunction with flares. The distinct nature of SCBs arises from their impulsive brightenings, unique Doppler velocity profiles, rapid dispersal, and origin in the impulsive phase of flare eruption. SCBs have a non-localized area of influence appearing up to half a solar radius away from the host flare and are indicative of the conditions of the entire flaring region. SCBs in aggregate often precede the  $H\alpha$  flare peak and have evolutions that more closely mirror the high-energy, non-thermal component of the flare spectrum than the low-energy, thermal component. The heated plasma in tracked SCB kernels does not physically progress in one direction, although the appearances of SCBs are sequential and propagate out from the flare ribbon.

A typical SCB has a radius of about 5 arcsec and a nearly circular geometry. The intensity of an SCB has a characteristic impulsive rise and decay, a median duration in  $H\alpha$  of 6.6 minutes, and a median duration in both CIV and HeII of 4.0 minutes. The derived Doppler velocity of an SCB is typically either a positive or negative impulsive spike coincident with the  $H\alpha$  brightening of a couple  $\text{km s}^{-1}$ . In a little more than 10% of the cases, there is a negative-to-positive velocity reversal during the course of a brightening. The photospheric magnetic field beneath an SCB has an unsigned flux of a few gauss. Observed in AIA, a typical SCB has a peak intensity delayed by about a minute as compared to ISOON. This delay is more pronounced in the CIV and HeII images. These measurements imply that SCBs are formed in the chromosphere and propagate vertically into the transition region.

Ensemble characteristics of the SCBs as a group can be seen within each

event studied. SCBs are observed propagating away from the flare with velocities in two distinct groups: a slow group with speeds between 35 and 85 km s<sup>-1</sup>, and a fast group propagating at speeds > 150 km s<sup>-1</sup>.

A Hyder flare analyzed with the tracking algorithm observed compact brightenings that had the same characteristics as SCBs. From AIA observations, we are able to constrain the temperatures of SCBs in the Hyder flare to < 7 × 10<sup>6</sup> K. This temperature, combined with the observed Doppler velocities, imply that SCBs are not formed by shock heating, and the chromospheric heating rate in an SCB must be  $E_H \leq 10^{10}$  erg cm<sup>-2</sup> s<sup>-1</sup>.

From these measurements, we can model the triggering mechanism for SCBs. A phenomenological model of the topology of a flaring region leading to SCBs is proposed in Figure 6.1. This model describes the different propagation velocities observed in SCBs originating in different groups of coronal magnetic loops. These magnetic loops are disturbed in the eruption of a flare and allow trapped plasma to travel down the loops and impact the chromosphere, causing the observed SCBs. A PFSS model shows that the magnetic loops above SCB locations are closed and relatively low lying, primarily lying between 0.1 and 0.3  $R_\odot$  above the photosphere.

A heuristic dynamical model of SCBs is shown in Figure 6.4. This model describes the chromospheric heating and expansion that leads to the observed SCBs. Two types of chromospheric expansion are plausible in this model: low energy and high energy. In the low energy model, the chromospheric material does not have enough energy to ablate into the corona but collapses back down after cooling. The high energy model postulates a mechanism for chromospheric evaporation which also accounts for the observed H $\alpha$  velocity shifts. Both the topological model and dynamical model support the *storage and release* class of models of CME release.

### 7.1.3. Interpretation of Results

Let us now return to the two original questions posed at the outset: *What causes SCBs to appear adjacent to flares?* and *What can tracking SCBs reveal about the conditions that triggered the solar eruption?*

Addressing the first question, SCBs are a type of localized chromospheric heating and ablation due to impacting coronal plasma. SCBs are unlike flares ribbons in that they are a secondary effect of solar eruptions. Quiescent coronal magnetic loops above a chromospheric flare must be forcibly disturbed for a flare to erupt. As these coronal tethers reconfigure, trapped plasma is now free to cascade into the chromosphere causing SCBs. The corona and chromosphere are visibly disturbed by each other in this process and the progressive trains of SCBs observed are evidence of the pre-flare coronal structure.

Tracking SCBs in the chromosphere reveals two significant results about the conditions required for solar eruptions. First, SCBs are a clear chromospheric indication of an erupting CME and provide an estimate of the energy threshold needed to eject mass from the Sun. Second, this CME release threshold is not

absolute. If the flare erupts with enough energy to disrupt the coronal tethers (or mass load) but is insufficient to completely reconfigure the system, flare-heated plasma is unable to escape and tumbles back to the solar surface in a partial eruption. A complete mass ejection requires not only enough energy to eject the plasma from the Sun but also energy to destabilize the overarching coronal tethers. These two types of energy required for ejection explains why CMEs are observed with flares of significantly different magnitudes as well as non-flaring filament eruptions.

## 7.2. Extensions and Future Directions

The automated feature identifying and tracking technique provides many opportunities for extensions to this project as well as completely new applications. A natural extension to this project is to incorporate more events during the AIA-era of solar observations. This project only used one ‘standard flare’ with complementary AIA data. Better statistics of SCBs in the transition region and corona are needed to better understand how SCBs change characteristics in different layers of the atmosphere. It would also be possible to estimate the energy generated in a flare using this technique with the addition of photospheric vector magnetograms. Associating vector magnetograms with this technique and a careful consideration of the observed Doppler motions underneath the ribbons would provide a full 3D method for estimating the Lorentz force for tracked sections of a flare ribbon.

The automated feature identifying and tracking is also flexible enough to adapt it to identify new features and accept new sources of data. For example, identifying and tracking magnetic flux as it emerges and dissipates would provide an estimate of the amount of magnetic energy deposited into the atmosphere. The mechanism producing bright points in the corona has long been debated. Identifying and tracking coronal bright points would allow a similar multi-wavelength statistical analysis of these features and constraints on their physical origin.

To better understand the physical process driving SCBs, a multi-wavelength high-resolution observation campaign is needed. Images of several points along the absorption line are needed to build up better measurements of Doppler velocity. High temporal resolution is needed to resolve the impulsive brightening and decay of SCBs. True hyper-spectral imaging is needed to simultaneously observe SCBs at different emission heights in the chromosphere and constrain the formation height of SCBs. The Interferometric Bidimensional Spectrometer (IBIS) on the Dunn Solar Telescope would be capable of such observations; however, the challenge is catching a chromospheric flare and its vicinity in the relatively small field of view of IBIS.

Data driven hydrodynamic models are needed to confirm the heuristic model put forward in Figure 6.4. A 1-D model would be sufficient to show the reaction of the chromosphere to an injection of high-energy electrons. Tuning this model to reproduce the physical parameters of SCBs would provide an estimate of the energy distribution of particles driving SCBs. This would also answer the outstanding ambiguity of whether chromospheric ablation occurs in SCBs or just heating and expansion. Also the energy spectrum of the incident particles would

help answer the question of whether or not magnetic reconnection is required to form an SCB.

The method of energy deposition in the chromosphere by a beam of particles is also debated. Both collisional excitation as well as wave heating are possible methods for energy from the corona to be transmitted back down to the chromosphere. A coronal oscillatory signal in the points identified as having an SCB would provide observational evidence for wave heating. The SCBs already identified with coincident data in AIA provide a ready dataset to begin this investigation.

## REFERENCES

- Abbey, E. 1988, *Desert Solitaire*
- Allred, J. C., Hawley, S. L., Abbett, W. P., & Carlsson, M. 2005, *The Astrophysical Journal*, 630, 573
- Antiochos, S. K. 1998, *The Astrophysical Journal*, 502, L181
- Antiochos, S. K., DeVore, C. R., & Klimchuk, J. a. 1999, *The Astrophysical Journal*, 510, 485
- Antiochos, S. K., & Sturrock, P. A. 1978, *The Astrophysical Journal*, 220, 1137
- Aschwanden, M. J. 2006, *Physics of the Solar Corona* (Springer), 908
- . 2012, *The Astrophysical Journal*, 757, 94
- Avrett, E. H. 1985, in *Chromospheric diagnostics and modelling*, 67–127
- Baker, D., van Driel-Gesztelyi, L., Mandrini, C. H., Démoulin, P., & Murray, M. J. 2009, *The Astrophysical Journal*, 705, 926
- Balasubramaniam, K. S., Pevtsov, A. A., & Neidig, D. F. 2007, *The Astrophysical Journal*, 658, 1372
- Balasubramaniam, K. S., Pevtsov, A. A., Neidig, D. F., Cliver, E. W., Thompson, B. J., Young, C. A., Martin, S. F., & Kiplinger, A. 2005, *The Astrophysical Journal*, 630, 1160
- Balasubramaniam, K. S., Pevtsov, A. A., Neidig, D. F., & Hock, R. A. 2006, *Proceedings of the ILWS Workshop*, 2
- Balasubramaniam, K. S., et al. 2010, *The Astrophysical Journal*, 723, 587
- Benz, A. O. 2008, *Living Reviews in Solar Physics*, 5
- Berlicki, A., Heinzel, P., Schmieder, B., & Li, H. 2008, *Astronomy and Astrophysics*, 490, 315
- Canfield, R. C., Penn, M. J., Wulser, J.-P., & Kiplinger, A. L. 1990, *The Astrophysical Journal*, 363, 318
- Cargill, P. J., Mariska, J. T., & Antiochos, S. K. 1995, *The Astrophysical Journal*, 439, 1034
- Carrington, R. C. 1859, *Monthly Notices of the Royal Astronomical Society*, 20, 13
- Chen, P. F. 2011, *Living Reviews in Solar Physics*, 8
- Chen, P. F., Fang, C., & Shibata, K. 2005, *The Astrophysical Journal*, 622, 1202
- Crocker, J. 1996, *Journal of Colloid and Interface Science*, 179, 298

- del Toro Iniesta, José Carlos. 2003, Introduction to Spectropolarimetry
- Demoulin, P., & Priest, E. R. 1988, *Astronomy and Astrophysics*, 206, 336
- Dennis, B., & Schwartz, R. 1989, *Solar Physics*, 121, 75
- Dixon, D. 2007, *Anatomy of the Sun*
- Donne, J. 1896, in *Poems of John Donne*, ed. Chambers E. K., Vol. I (London: Lawrence and Bullen), 7
- Doschek, G. A., Feldman, U., Kreplin, R. W., & Cohen, L. 1980, *The Astrophysical Journal*, 239, 725
- Dryer, M. 1982, *Space Science Reviews*, 33, 233
- Feldman, U., Doschek, G. A., Kreplin, R. W., & Mariska, J. T. 1980, *The Astrophysical Journal*, 241, 1175
- Feynman, R. P., Leighton, R. B., & Sands, M. 1963, *The Feynman Lectures on Physics*, Vol. I: The New Millennium Edition: Mainly Mechanics, Radiation, and Heat, Volume 1 (Basic Books), 560
- Fisher, G. H., Canfield, R. C., & McClymont, A. N. 1984, *The Astrophysical Journal*, 281, L79
- Fontenla, J. M., Avrett, E. H., & Loeser, R. 1990, *The Astrophysical Journal*, 355, 700
- Forbes, T. G., & Isenberg, P. A. 1991, *The Astrophysical Journal*, 373, 294
- Fraunhofer, J. 1817, *Annalen der Physik*, 56, 264
- Gill, C. D., Fletcher, L., & Marshall, S. 2010, *Solar Physics*, 262, 355
- Giovanelli, R. G. 1978, *Solar Physics*, 59, 293
- Green, B. 2008, *Put a Little Science in Your Life*
- Grigis, P. C. 2006, PhD thesis, Eidgenössische Technische Hochschule Zürich
- Gurman, J. B. 1987, *NASA's solar maximum mission: A look at a new Sun* (Goddard Space Flight Center: NASA), 37
- Hale, G. E. 1908, *The Astrophysical Journal*, 28, 315
- Harvey, J. W., et al. 1996, *Science*, 272, 1284
- Hestroffer, D., & Magnan, C. 1998, *Astronomy and Astrophysics*, 342, 338
- Huber, M. C. E., Foukal, P. V., Noyes, R. W., Reeves, E. M., Schmahl, E. J., Timothy, J. G., Vernazza, J. E., & Withbroe, G. L. 1974, *The Astrophysical Journal*, 194, L115

- Hyder, C. L. 1967, *Solar Physics*, 2, 49
- Hyder, C. L., Epstein, G. L., & Hobbs, R. W. 1973, *The Astrophysical Journal*, 185, 985
- James, J. 2011, *Wonderful (The Way I Feel)*
- Keil, S., Rimmele, T., & Wagner, J. 2010, *Astronomische Nachrichten*, 331, 609
- Kirk, M. S., Balasubramaniam, K. S., Jackiewicz, J., McAteer, R. T. J., & Milligan, R. O. 2012, *The Astrophysical Journal*, 750, 145
- Kirk, M. S., Balasubramaniam, K. S., Jackiewicz, J., McNamara, B. J., & McAteer, R. T. J. 2011, *Solar Physics*, 345
- Kirk, M. S., Pesnell, W. D., Young, C. A., & Hess Webber, S. A. 2009, *Solar Physics*, 257, 99
- Klimchuk, J. A. 1990, *The Astrophysical Journal*, 354, 745
- Klimchuk, J. A. 2001, in *Geophysical Monograph Series*, Vol. 125, *Geophysical Monograph Series*, ed. P. Song, H. J. Singer, & G. L. Siscoe (Washington, D. C.: American Geophysical Union), 143–157
- Leenaarts, J., Carlsson, M., & Rouppe van der Voort, L. 2012, *The Astrophysical Journal*, 749, 136
- Lemen, J. R., et al. 2011, *Solar Physics*, 275, 17
- Lin, J., & Forbes, T. G. 2000, *Journal of Geophysical Research*, 105, 2375
- Lin, R. P. et al. 2002, *Solar Physics*, 3
- Lites, B. W. 1980, *Solar Physics*, 68, 327
- Lockyer, J. N. 1868, *Proceedings of the Royal Society of London*, 17, 131
- Low, B. C., & Smith, D. F. 1993, *The Astrophysical Journal*, 410, 412
- Ludwig, G., & Johnson, D. 1981, *Advances in Space Research*, 1, 23
- Maurya, R. A., & Ambastha, A. 2010, *Solar Physics*, 262, 337
- Milligan, R. O., Gallagher, P. T., Mathioudakis, M., & Keenan, F. P. 2006, *The Astrophysical Journal*, 642, L169
- Milligan, R. O., Gallagher, P. T., Mathioudakis, M., Keenan, F. P., & Bloomfield, D. S. 2005, *Monthly Notices of the Royal Astronomical Society*, 363, 259
- Milne, A. A., & Shepard, E. H. 2009, *The House at Pooh Corner* (Penguin Group USA), 180
- Moreton, G. E. 1960, *The Astronomical Journal*, 65, 494

- . 1964, *The Astronomical Journal*, 69, 145
- Nagashima, K., Sekii, T., Kosovichev, A. G., Zhao, J., & Tarbell, T. D. 2009, *The Second Hinode Science Meeting: Beyond Discovery-Toward Understanding* ASP Conference Series, 415
- Neckel, H., & Labs, D. 1994, *Solar Physics*, 153, 91
- Neidig, D., et al. 1998, in *Astronomical Society of the Pacific Conference Series*, Vol. 140, *Synoptic Solar Physics*, ed. K. S. Balasubramaniam, J. Harvey, & D. Rabin, 519
- Neupert, W. M. 1968, *The Astrophysical Journal Letters*, 153, L59+
- Newton, I. 1671, *Philosophical Transactions of the Royal Society of London*, 6, 3075
- November, L. J., & Simon, G. W. 1988, *The Astrophysical Journal*, 333, 427
- Parker, E. N. 1957, *Journal of Geophysical Research*, 62, 509
- Peirce, C. S. 1879, *American Journal of Mathematics*, 2, 394
- Pevtsov, A. A., Balasubramaniam, K. S., & Hock, R. A. 2007, *Advances in Space Research*, 39, 1781
- Pevtsov, A. A., Canfield, R. C., & Metcalf, T. R. 1995, *The Astrophysical Journal*, 440, L109
- Priest, E., & Forbes, T. 2002, *Astronomy and Astrophysics Review*, 10, 313
- Priest, E. R., & Titov, V. S. 1996, *Philosophical Transactions of the Royal Society A: Mathematical, Physical and Engineering Sciences*, 354, 2951
- Qu, M., Shih, F. Y., Jing, J., & Wang, H. 2003, *Solar Physics*, 157
- Salpeter, E. E. 1952, *The Astrophysical Journal*, 116, 649
- Santiago, J. M. B. 2004, Phd dissertation, Universität zu Göttingen
- Scherrer, P. H., et al. 1995, *Solar Physics*, 162, 129
- . 2011, *Solar Physics*, 275, 207
- Schrijver, C., & De Rosa, M. 2003, *Solar Physics*, 165
- Schrijver, C. J. 2001, *The Astrophysical Journal*, 547, 475
- Schrijver, C. J., Hagenaar, H. J., & Title, A. M. 1997, *The Astrophysical Journal*, 475, 328
- Schwabe, S. H. H. 1843, *Astronomische Nachrichten*, 20, 283
- Schwenn, R. 2006, *Living Reviews in Solar Physics*, 3

- Shibata, K., & Magara, T. 2011, *Living Reviews in Solar Physics*, 8
- Siscoe, G. 2000, *Journal of Atmospheric and Solar-Terrestrial Physics*, 62, 1223
- St. Cyr, O. C., et al. 2000, *Journal of Geophysical Research*, 105, 18169
- Stix, M. 2004, *The Sun: An Introduction*, 2nd edn. (New York: Springer), 490
- Stokes, G. G. 1852, *Philosophical Transactions of the Royal Society of London*, 142, 463
- Sturrock, P. A. 1968, *Structure and Development of Solar Active Regions*, 35, 471
- Sweet, P. A. 1958, *Electromagnetic Phenomena in Cosmical Physics*
- Uchida, Y. 1968, *Solar Physics*, 4, 30
- Unno, W. 1956, *Publications of the Astronomical Society of Japan*, 8
- Woods, T. N. 2004, *Geophysical Research Letters*, 31